



Università degli Studi di Ferrara

DOTTORATO DI RICERCA IN
SCIENZE DELLA TERRA

CICLO XXIII

COORDINATORE Prof. COLTORTI MASSIMO; Prof. GREGOIRE MICHEL

**Petrology of suprasubductive
mantle xenoliths from Estancia Sol
De Mayo (Central Patagonia,
Argentina)**

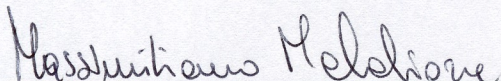
Settore Scientifico Disciplinare Geo/07

Dottorando

Dott. Melchiorre Massimiliano

Tutore

Prof. Coltorti Massimo
Prof. Gregoire Michel



(firma)



(firma)

Anni 2008/2010

Index

1. Introduction	1
1.1 <i>The incoming plate</i>	2
1.2 <i>The downgoing plate</i>	6
1.3 <i>The mantle wedge</i>	8
1.4 <i>The arc-trench complex</i>	8
2. State of the art	12
3. Cenozoic evolution of Patagonia	17
3.1 <i>Northern Patagonia and the Somoncuro Province (40°S-46°S)</i>	18
3.2 <i>Central Patagonia and the TJIgneous Province (46°S-49°S)</i>	20
3.3 <i>Southern Patagonia and the Pali Aike Volcanic Field (49°S-52°S)</i> ..	23
3.4 <i>Cenozoic geodynamic evolution of Patagonia</i>	24
4. Chemical composition of the host lavas	28
5. Petrography of the xenoliths	33
5.1 <i>Lherzolites</i>	35
5.2 <i>Harzburgites</i>	37
5.3 <i>Dunites</i>	40
5.4 <i>Wherlite</i>	42
6. Geochemistry of the mineral phases	43
6.1 Major element compositions	43
6.1.1 <i>Olivine</i>	44
6.1.2 <i>Clinopyroxene</i>	46
6.1.3 <i>Orthopyroxene</i>	51
6.1.4 <i>Spinel</i>	54
6.2 Trace element compositions	54
6.2.1 <i>Clinopyroxene</i>	57
6.2.2 <i>Orthopyroxene</i>	62
6.3 P-T estimates	67

6.4 Sr and Nd systematic	69
7. Comparisons	73
8. Discussion	83
8.1 Nature of the metasomatic liquid	84
8.2 Isotopic modelling	90
8.2.1 Isotopic composition of Patagonian clinopyroxenes	91
8.3 Considerations on the lithospheric mantle beneath Patagonia	93
9. Conclusions	95
10. References	98
Appendix: Analytical methods	112

Tables

<i>Appendix 1. Major element composition of olivines</i>	114
<i>Appendix 2. Major element composition of clinopyroxenes</i>	121
<i>Appendix 3. Major element composition of orthopyroxenes</i>	127
<i>Appendix 4. Major element composition of spinels</i>	133
<i>Appendix 5. Trace element composition of clinopyroxenes</i>	139
<i>Appendix 6. Trace element composition of orthopyroxenes</i>	143
<i>Appendix 7. P-T estimates</i>	145
<i>Appendix 8. Sr-Nd systematics</i>	147

Patagonian giants: early European perceptions

“According to Antonio Pigafetta, one of the Magellan expedition's few survivors and its published chronicler, Magellan bestowed the name "*Patagão*" (or *Patagón*) on the inhabitants they encountered there, and the name "Patagonia" for the region. Although Pigafetta's account does not describe how this name came about, subsequent popular interpretations gave credence to a derivation meaning 'land of the big feet'”.

...“However, this etymology is questionable. The term is most likely derived from an actual character name, "*Patagón*", a savage creature confronted by Primaleón of Greece, the hero in the homonymous Spanish chivalry novel (or knight-errantry tale) by Francisco Vázquez. This book, published in 1512, was the sequel of the romance "*Palmerín de Oliva*," much in fashion at the time, and a favourite reading of Magellan. Magellan's perception of the natives, dressed in skins, and eating raw meat, clearly recalled the uncivilized *Patagón* in Vázquez's book”.

The meaning of life

[...] Ma cosa stiamo combinando in realtà? Il mondo moderno è pieno di discutibili distrazioni, scadenze e priorità. Giorno e notte si confondono l'uno nell'altra. Veniamo sommersi da una valanga di paure e desideri che ci spingono in una gara impossibile da vincere. Così noi ci affrettiamo, ci affrettiamo, ci affrettiamo per raggiungere un certo punto ideale nella nostra vita, e poi che succede? [...] Molti di noi iniziano a sognare una vita meravigliosa libera e selvaggia, ma di solito lontana da quella che vivono realmente. Purtroppo scopriamo spesso questa verità proprio alla fine, quando è troppo tardi. Non si può ricominciare tutto ancora una volta. [...] niente è tanto doloroso quanto la consapevolezza di aver avuto la possibilità di fare quello che amavi veramente, e di non averla colta. Allora qual è la passione della tua vita? Che ci stai a fare su questa terra? La risposta a queste domande ti schiuderà il grande mistero della vita, tanto più profondo quanto più prepotenti ti si pongono questi interrogativi. [...] per prima cosa, nessuno ti dirà mai nulla al riguardo. [...] È anche estremamente inverosimile che un giorno ti ritrovi all'improvviso immerso in una luce intensa e che lo scopo della tua vita ti appaia chiaro in una visione mistica. [...] La maniera migliore per arrivarci è passare un po' di tempo da solo, rivolgendo a te stesso la difficile domanda. Questo esercizio non è complicato, si tratta solo di essere onesti. Basta che tu faccia così: "Alza la mano se senti di poter avere di più dalla tua vita". [...] Molto presto la "risposta" ti colpirà in piena faccia, proprio come quando sei a metà strada per la spiaggia e improvvisamente ricordi che hai lasciato il ferro da stiro acceso a casa. E quando saprai, o almeno avrai il sospetto di sapere, cosa fare della tua vita, fallo! Spicca un folle salto nel buio se è il caso, poi, non appena tocchi il suolo, corri, perché non hai un secondo da perdere. [...] Tieni a mente che qualunque cosa tu faccia, gli errori sono parte della vita. Quindi non perdere tempo a prenderti a calci per il passato. Non impantanarti o stressarti chiedendoti se stai facendo la cosa giusta. [...] Invece di scoraggiarti, ricordati sempre che il rifiuto e la resistenza sono quasi certi quando stai facendo qualcosa di molto importante e speciale. Quando comincerai a vivere i tuoi sogni, molte persone (comprese quelle che ti amano di più) cercheranno di tenerti a freno. A questo mondo ci sono molti insopportabili pessimisti che hanno abbandonato i loro sogni e ti diranno: Stai perdendo il tuo tempo, non ce la farai mai". Intorno a te potrebbero esserci persone che di nascosto desiderano che tu ottenga il meno possibile, o addirittura faccia fiasco solo per non apparire inferiori. "Scordatelo" dicono "non ne vale la pena, e comunque non è la cosa giusta per te". Quindi è importante rendersi conto che seguire il proprio cammino è incredibilmente gratificante, ma di sicuro non è semplice. Come qualsiasi altra persona, vivrai dei giorni migliori di altri. Talvolta, tutto intorno a te sembrerà un totale disastro. [...] Ma qualunque cosa succeda, *devi solo tenere duro*. Ricordati che capita a tutti di essere esausti. È incredibilmente sfiancante passare le giornate facendo qualcosa che proprio non ti piace e di cui nemmeno ti importa. Ma se segui i tuoi sogni, per lo meno sarai esausto per aver fatto quello che ami di più. [...] Quando ricavi il massimo dalla tua vita, assaporandola fino all'ultima goccia, tutto ciò che ti riguarda si trasformerà da ordinario a straordinario. [...] Il bello è che, facendo le cose che ti fanno arricciare i baffi dalla gioia (supponendo, naturalmente che tu abbia i baffi) stimolerai qualcun altro a correre dietro ai suoi sogni. [...] Sai una cosa? Anche se commetterai grossi errori, se sbaglierai su tutti i fronti, vivrai comunque un'avventura stupefacente e piena di divertimento; di notte andrai a dormire sapendo che hai dato tutto e fatto la differenza, e ti sveglierai ogni mattina attendendo con ansia il futuro, che sarà bello ed eccitante come riesci a immaginare. Sai un'altra cosa? Se darai retta al tuo cuore e userai la testa, non sbaglierai mai.

1. Introduction

Sediments, oceanic crust and mantle lithosphere return and re-equilibrate with the Earth's mantle in subduction zones (**Figure 1.1**) and for this reason they are considered the largest recycling system on Earth. Their descent and re-equilibration into the mantle, may trigger partial melting in the mantle wedge above the slab ultimately leading to the generation of new crust. The sinking of the lithosphere also provide the greatest force driving the plates and inducing the spreading of the mid-ocean ridges, although some debate is actually going on the negative buoyancy of the oceanic lithosphere (*Dogliani et al., 2007*). As proposed by *Hofmann (1997)* the material which is not recycled in the first few hundred kilometres of the upper mantle, may sink into the lower mantle down to the core-mantle boundary (CMB) where it can be reheated and possibly resurrected by a mantle plume (**Figure 1.2**).

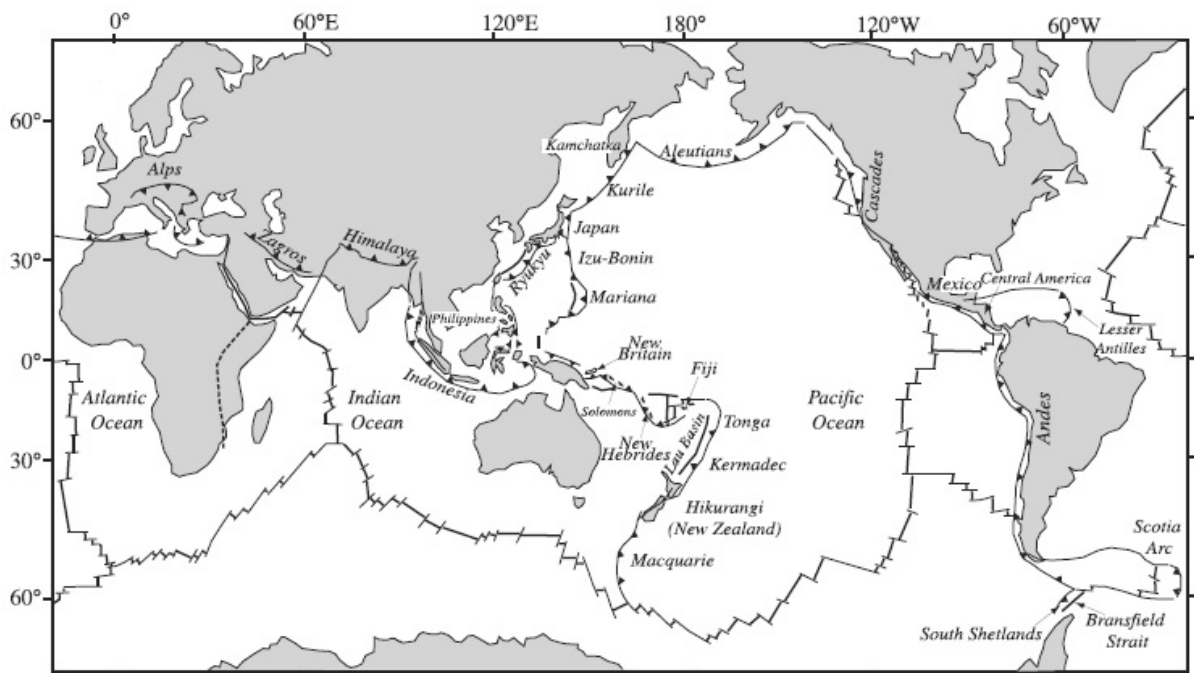


Figure 1.1: Convergent margins on Earth (from *Stern, 2002*)

A subduction environment is very complex, and the best way to describe its features is by dividing it in four main components: the incoming plate, the downgoing plate, the mantle wedge and the arc-trench complex (**Figure 1.3**).

1. Introduction

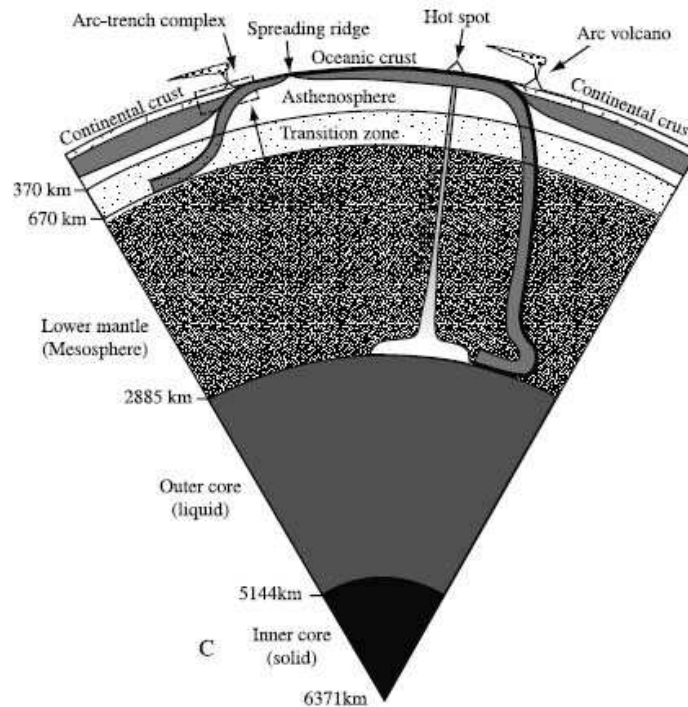


Figure 1.2: Schematic section through the center of the Earth (*Stern, 2002*), which shows the scale of subduction zones. Subducted lithosphere is shown both penetrating the 660 km discontinuity (right) and stagnating above the discontinuity (left). A mantle plume is shown ascending from the site of an ancient subducted slab.

1.1 The incoming plate

The lithosphere of the incoming plate is composed of mantle lithosphere, crust and sediments. These three elements exert fundamental controls on the behaviour of the subduction zones, but each one in a different way. In fact the mantle lithosphere controls the physics of the subduction, the sediments control the chemistry and the crust control both the physics and the chemistry.

The mantle lithosphere is slightly more dense (1-2% in excess) than the underlying asthenosphere. This excess of density powers the subduction zones and moves the plates (*Davies, 1999*). The increasing density of the plate is controlled by its thickness and age, the latter exerting also a first-order control on the trench depth (*Grellet and Dubois, 1982*). Old and dense lithosphere readily sinks, while young, buoyant lithosphere resists subduction. Subduction of old lithosphere results in relatively steep subduction zones, whereas subduction of young lithosphere is characterized by shallower dips (*Jarrard, 1986*).

The different behavior of subduction zones involving young and old lithosphere is also shown in the strain regime manifested behind the magmatic arc. In fact in some cases they affect the back arc basins with rifting or even seafloor spreading, whereas others induce folding and thrusting behind the arc. *Jarrard (1986)* subdivided subduction zones into seven strain classes, with class 1 being strongly extensional and class 7 being strongly compressional. He concluded that the strain regime in the overlying plate is correlated with the age of the subducted lithosphere and with the absolute motion of the overriding plate. A first-order differentiation of subduction zones distinguishes those subducting old lithosphere (Mariana type, class 1) from those subducting young lithosphere (Chilean type, class 7) (**Figure 1.4**).

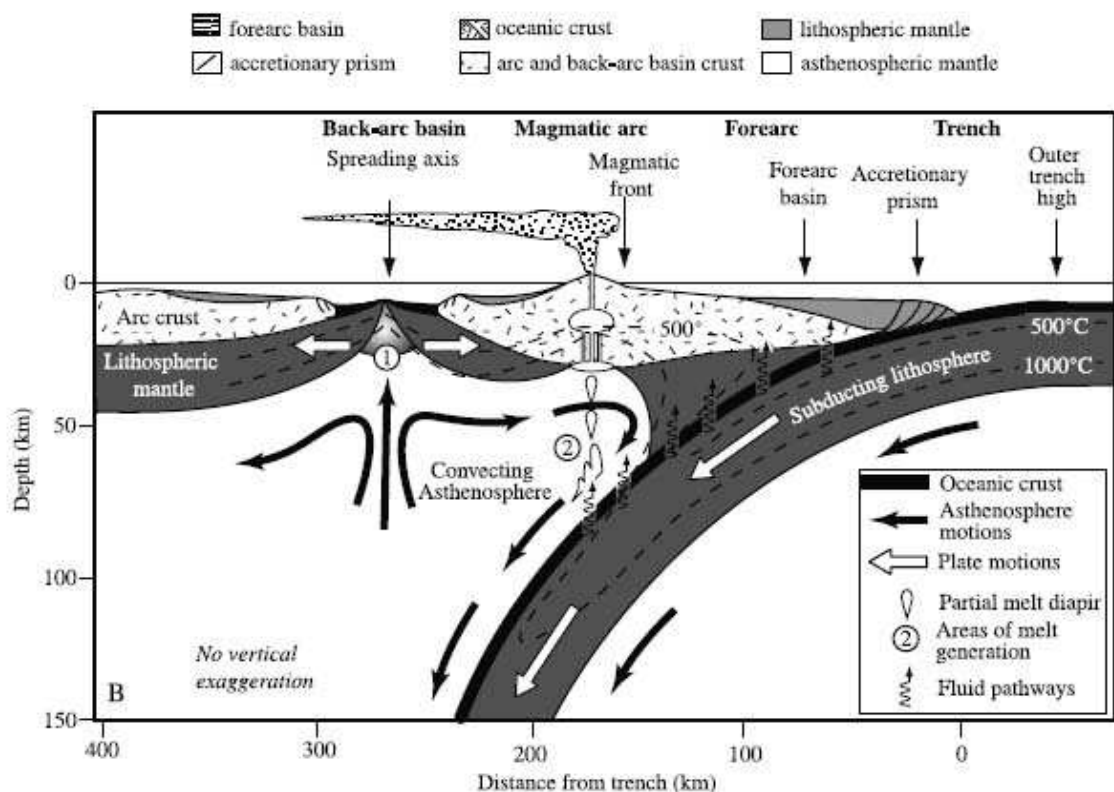


Figure 1.3: Main components of a subduction environment (from *Stern, 2002*). Note that the mantle wedge (not labelled) is the part overlying the incoming plate.

Subducted crust affects subduction zones in several ways. First of all, its density and thickness largely determine whether the subduction zone operates normally or fails.

1. Introduction

Normal oceanic crust is invariably subductable, but subduction of continental crust leads to subduction zone failure. Failure of a subduction zone happens when sufficient buoyant material is introduced into the system to disrupt downwelling. This is called collision or terrane accretion. Contrasts in lithospheric bulk density (crust plus mantle) of 0.1 gm/cm^3

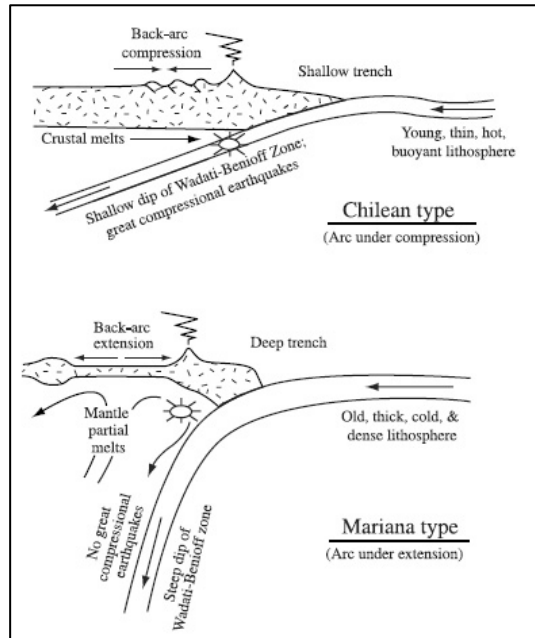


Figure 1.4: End member of Jarrard's classification of subduction environments.

which also leads to formation of amphibolites at greater depth in the crust, and seafloor weathering, that affects the uppermost 500 m of basalts, for which *Staudigel et al. (1996)* infer 2.7% H_2O , 3.0% CO_2 , and a two to threefold increase in K. Formation of amphibolites in the lower crust sequesters significant amounts of water but little else (*Carlson, 2001*). The presence of even small amounts of serpentinite in the oceanic crust is important for water cycling through subduction zones, because equal volumes of serpentinite carries an order of magnitude more water than hydrated mafic crust and because serpentinite is stable to much greater pressures (13% H_2O versus 1–2% in hydrated mafic crust and 7 GPa or more versus 3 GPa. *Pawley and Holloway, 1993; Ulmer and Trommsdorf, 1995*). Crust produced at slow and fast spreading ridges stores water, bound in minerals, in different way. Whereas fast spreading ridges are robust magmatic systems that produce crust composed almost entirely of basalt, diabase, and gabbro, slow spreading ridges have intermittent igneous activity, or it may be absent altogether, so that this crust may be largely composed of serpentinitized peridotite. Because serpentine contains more water than altered basalt or gabbro and because crust produced at slow spreading ridges contain more serpentinite with respect to that formed at fast spreading

ridges (*Karson, 1998*), slow spreading crust may carry proportionally more water into subduction zones than fast spreading crust.

Fast spreading oceanic crust is probably pervasively hydrated, but the associated peridotites are not, except at transform faults and fracture zones. Oceanic crust produced at slow spreading ridges is probably much more heterogeneous, with masses of unaltered crust (as wide as a few tens of kilometers (*Stern, 2002*)) separated by major fault zones that penetrate the full thickness of the crust and result in substantial serpentinization of mantle rocks.

From seismic velocity data for the slow spreading North Atlantic ridge *Carlson (2001)* concluded that no more than 13% of this oceanic crust could be composed of serpentinized ultramafics. It is important to know how much of the subducted lithosphere is serpentinized, in order to understand the subduction zone water budget. Deep earthquakes (up to 50 km) related to normal faulting on the outer trench rise may allow seawater to infiltrate and serpentinize mantle at much greater depths in the lithosphere than would be expected (*Peacock, 2001*). This would increase the proportion of serpentinite in the lithosphere, with the effect of significantly increasing the amount of water carried into subduction zones. Because serpentine is ductile, this would also weaken the lithosphere and greatly reduce the amount of work needed to bend the plate.

Finally sediments carried on the subducting plate play a fundamental role for element recycling. They may be the ultimate source of many of the unusual enrichments and other chemical signatures found in arc lavas. For example, the presence in some arc lavas of ^{10}Be , which is produced only in the upper atmosphere and which has a half-life of 1.6 million years, testifies to the recycling of sediments through the subduction zone (*Morris et al., 1990*). The covariation of other, fluid-mobile trace elements (such as K, Sr, Ba) has also been interpreted to indicate the importance of sediment recycling (*Plank and Langmuir, 1993*). Because of the great difference of the sediments that can be subducted in different environments, a mean composition has been calculated (GLOSS, GLOBal Subducting Sediments) (*Plank and Langmuir, 1998*). A great proportion of the GLOSS is represented by terrigenous material (76%) but it also contains significant proportions of biogenic calcium carbonate (7%) and silica (10%), along with 7% mineral-bound water.

1. Introduction

1.2 The downgoing plate.

Most of the processes associated with subduction zones happen deep below the surface and our understanding of these processes is largely based on geophysics and geochemistry of active systems, geochemistry of erupted products and on studies of exhumed old subduction zones.

The thermal structure of a subduction zone depends on many factors. Those playing the most important role are age and speed of the incoming plate, followed by shear stress across the subduction interface which induce convection in the overlying mantle wedge, geometry of subduction, fluids migrating through the subduction zone, and radioactive heating.

Models of subduction zone thermal structure are supported by seismic imaging. Two important factors for tomographic imaging of subduction zones are the presence of significant differences in material properties, manifested as seismic velocities, and the seismic “illumination” of the subduction zone by deep earthquakes. The coolness of subduction zones allows the slab to be tomographically traced to great depth. Some slabs may stagnate at the 660 km discontinuity, but most of them appear to penetrate into the lower mantle (*Stern, 2002*).

As the plate descends, it is progressively heated and squeezed, changing the mineralogy and volatile content of sediments, crust, and mantle lithosphere. The importance of kinetic effects in subduction zones are clearly demonstrated by the behavior of Mg_2SiO_4 polymorphs. Olivine and its high-pressure and hydrated polymorphs make up most of the upper mantle and the subducted lithosphere. Away from subduction zones, olivine structure change into β -spinel (wadsleyite) at ~410 km depth (boundary between the upper mantle and the transition zone with a 6% increase of density). Wadsleyite change into γ -spinel structure (ringwoodite) at ~520 km, which then should yield perovskite structure (MgSiO_3) plus magnesiowustite (MgO) at 660 km depth (it defines the transition zone–lower mantle boundary with a 8% density increasing; *Helfrich and Wood, 2001*). But things change when we consider these reactions in a subductive environment. The first reaction occur much shallower than 410 km, whereas the conversion of ringwoodite to perovskite + magnesiowustite should occur deeper than 660 km (*Irifune, 1993*). This is

because the Clapeyron slope (dP/dT) for the olivine-wadsleyite reaction is positive, while is negative for the ringwoodite to perovskite+magnesiowustite transition.

The shallower nature of the first conversion increases the density of the subducting lithosphere, favoring continued sinking, while the deeper nature of the second conversion decreases the slab density. These predictions are consistent with the observation that deep earthquakes first appear at ~325 km depth, about where the olivine-wadsleyite phase change is first expected, and cease at ~700 km depth, where the ringwoodite-perovskite + magnesiowustite change should be complete.

Numerical models of mantle convection suggest that the 660 km discontinuity generally should not act as a barrier to continued slab sinking (*Davies, 1995*). This conclusion is also supported by mantle tomography, suggesting that some slabs can be traced down well beyond 660 km (**Figure 2**).

Another important reaction in subducted lithospheric mantle is the breakdown of serpentinite to olivine, orthopyroxene, and water, which results in a very large density increase as it releases a lot (13 wt %) of water. Depending on temperatures, antigorite (a variety of serpentine) is stable up to pressure of 8 GPa, ~250 km deep in a subduction zone (*Ulmer and Trommsdorf, 1995*), providing an effective way to transport water to great depths.

Subducted sediments transport most of their incompatible elements budget into subduction zones. Although many uncertainties remain about the changes that accompany subduction of sediments due to their variable bulk composition from one arc to another, it is possible to put forward some general observations about their behaviour. First of all the progressive heating and squeezing of sediments causes progressive transformations that increase density and decrease water content. Second, the solubility of cations in hydrous fluids increases rapidly with temperature and pressure; for example, SiO_2 in aqueous fluid increases from 1000 to 100,000 times as pressure increases from 0 to 2 GPa (*Manning, 1996*), corresponding to a depth of 70 km. Third, fluid-mobile elements and light isotopes fractionate as subduction and dewatering proceeds, so that light element isotope ratios of sediments before these enter the trench should not characterize sediments beneath arc volcanoes. Fourth, clay-rich sediments melt at temperatures similar to mafic crust and at comparable pressures corresponding to depths greater than ~50 km (700°– 800°C at 120

1. Introduction

km, *Nichols et al., 1996; Johnson and Plank, 1999*). Trace element systematics of some arc lavas associated with cold subduction zones have led some authors to conclude that sediment melting generally occurs (*Elliott et al., 1997*).

1.3 The mantle wedge

The mantle wedge is the part of the mantle that overlies the subduction zone, and where subducting materials are mixed with convecting mantle to generate magmas, fluids, and ultimately continental crust. In this scenario one of the most important roles is played by the convecting asthenosphere, because it is able to interact with slab-derived fluids and melts to generate arc magmas. The dynamics of magma generation in subduction environment is different from the two other magma-producing tectonic settings, i.e. intraplate and divergent environments. In fact while for hot spots and ridges melts are linked to mantle upwelling, the mantle wedge melts are associated with cold thermal regime.

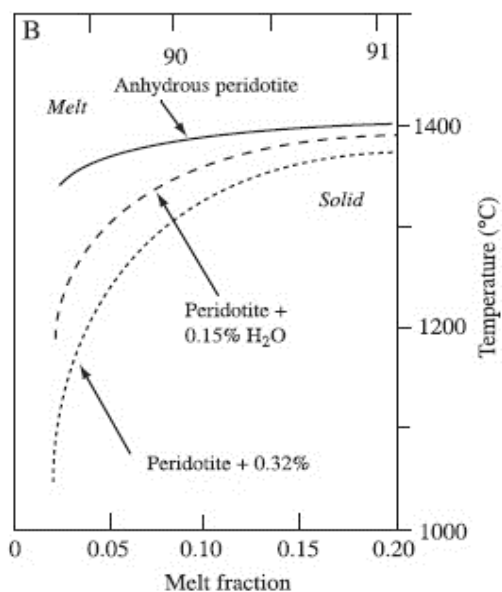


Figure 1.5: Plot of melt fraction versus temperatures of hydrous batch melts from peridotite containing 0.15% and 0.32% H₂O (*Stolper and Newman, 1994*). Upper axis shows forsterite content of equilibrium olivine.

The generation of magmas is due to the interaction of the aqueous fluids and melts released by the slab with the overlying mantle, whose melting temperature can be lowered by several hundred degrees with respect to dry melting (**Figure 1.5**). Melting due to fluid addition to the mantle wedge is thought to be responsible for $10 \pm 5\%$ melting of the mantle, with 10% melting for every 0.2% water added (*Pearce and Peate, 1995*).

1.4 The arc-trench complex

A mature and stable subduction zone causes magmatic and tectonic phenomena in the overlying lithosphere, which can be recognized as arc-trench complexes, where subduction zone products can be studied directly.

Arc-trench complexes differ fundamentally depending on whether they are built on continental lithosphere (Andean-type arcs) or oceanic lithosphere (intraoceanic or primitive arcs). The crust of Andean-type arcs can be up to 80 km thick, about twice that of normal continental crust (*Allmendinger et al., 1997; Yuan et al., 2000*), while intraoceanic arc crusts are typically 20–35 km thick. Three main components characterized the arc-trench systems: the forearc, the magmatic arc and the back arc.

The forearc lies between the trench and the magmatic front and is 166 ± 60 km wide (*Gill, 1981*). Two types of forearc can be distinguished: the accretionary and non-accretionary (**Figure 1.6**), depending on the thickness of the sediments subducted. When the thickness of sediments is greater than 400–1000 m, they will be scraped off the downgoing plate and transferred to the overriding plate to form an accretionary prism (*Dahlen, 1990; von Huene and Scholl, 1991; Le Pichon et al., 1993*). Furthermore the high sedimentation rates associated with accretionary forearcs produce also forearc basins forming between the accretionary prism and the magmatic arc (**Figure 1.6a**) (*Dickinson, 1995*). Non-accretionary forearcs (**Figure 1.6b**) form where the amount of sediment available on the subducting plate is low, typically distant from continents. Therefore neither an accretionary prism nor forearc basins are recognized. As a consequence, the igneous infrastructure of the forearc is exposed. Non-accretionary forearcs provide unique insights into how subduction zones begin and their early history, the significance of ophiolites, and the nature of fluids released from relatively shallow parts of subduction zones.

The magmatic arc is generally characterized by an igneous activity concentrated near the magmatic front, decreasing with the distance from the trench. Arc magmas are generally fractionated, porphyritic, and wet (*Perfit et al., 1980; Ewart, 1982; Tatsumi and Eggins, 1995*), especially when compared to mid-ocean ridge or hot spot magmas. Arcs are also characterized by crustal thickening with respect to the other magmatic environments, because of the relatively fix position of the mantle that is melting as well as the overlying lithosphere (mantle and crust). Consequently, mafic magmas tend to stagnate, giving rise to fractional crystallization and assimilation processes. Arc lavas are dominantly silica-oversaturated and subalkaline and are further subdivided into volumetrically predominant calc-alkaline and tholeiitic suites and less common shoshonitic suites.

Water content in arc melt inclusions varies widely, from 5 to 6 wt.% H₂O for inclusions from Nicaragua (Cerro Negro), central Mexico, and the Marianas, to <0.5 wt.% for

1. Introduction

Galunggung, Indonesia (Wallace, 2005). Values as high as 8–10 wt.% H₂O have been found in melt inclusions in high-Mg andesites from the Shasta region of California (Grove *et al.*, 2002). The H₂O variations appear in some cases to be related to primary factors such as the proximity to the arc front or the relationship with the amount of subducted material. In assessing variations with distance from the trench, it is important to note that the lower end of the H₂O range for arc basalts overlaps the values of submarine basaltic glasses from back-arc basins such as the Marianas back arc and Lau Basin, in which H₂O contents vary from 0.5 to 2 wt.% (Stolper and Newman, 1994; Kent *et al.*, 2002). This is consistent with the interpretation that subduction input of H₂O into the mantle wedge decreases with increasing slab depth and distance from the trench.

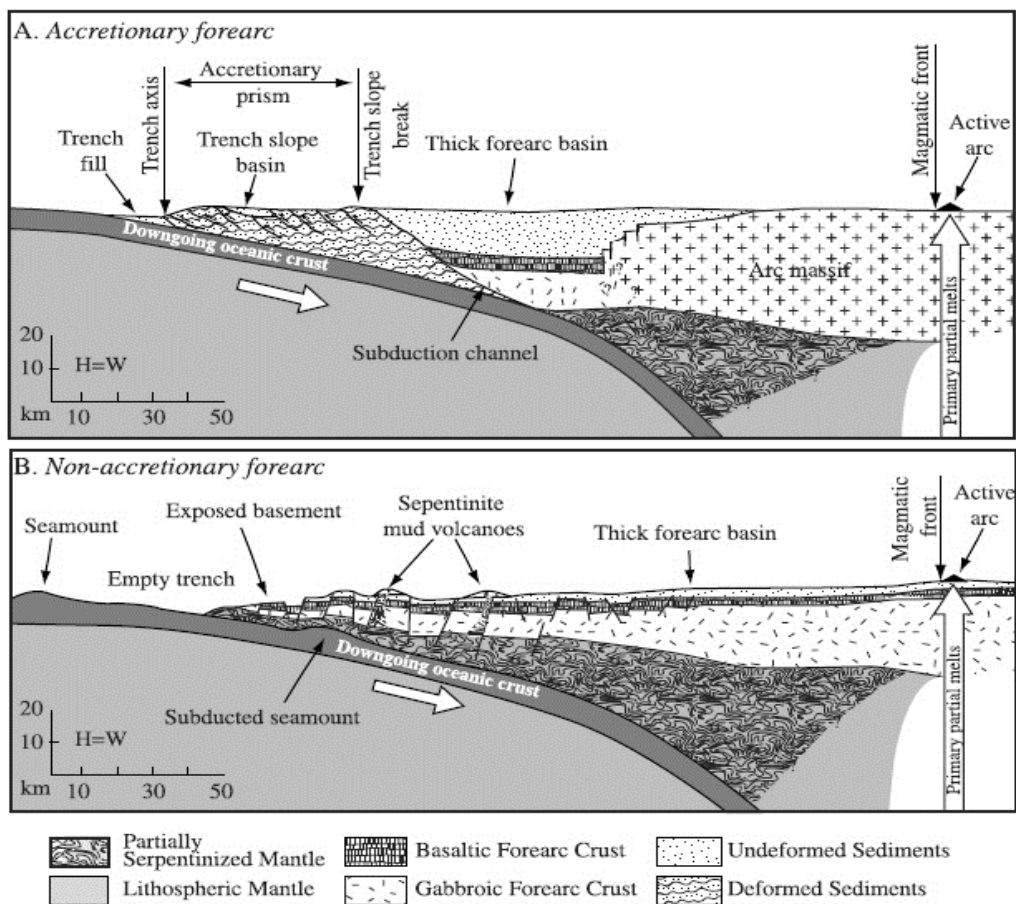


Figure 1.6: End-member forearc types: (a) accretionary forearc and (b) nonaccretionary forearc.

Finally, the back arc region lies behind the magmatic arc, and it can show a wide range of magmatic and tectonic styles, depending on strain class (Jarrard, 1986). Low-strain arcs

(strain classes 1 or 2) are associated with back arc extension, whereas arcs with high strain (strain classes 6 or 7) may be associated with back arc thrusting. Intermediate strain classes may be associated with a back arc region showing little or no tectonic and magmatic activity. Active extension, rifting and seafloor spreading, characterize the back arc regions above several subduction zones: the best examples are represented by the Mariana Trough behind the Mariana arc (spreading rate of 4 cm yr⁻¹, *Bibee et al., 1980*), the Lau-Havre Trough behind the Tonga-Kermadec arc (spreading rate of 16 cm yr⁻¹, *Bevis et al., 1995*), the North Fiji Basin behind the Vanuatu (New Hebrides) arc, the Manus Basin NE of New Guinea, and the East Scotia Sea behind the South Sandwich. Extensional back arcs may rift as well as spread.

Rifting is observed where the extensional regime propagates along the strike of the arc system, such as the northern Mariana Trough (*Martinez et al., 1995*) and the Havre Trough (*Fujiwara et al., 2001*), as well as for back arc basins that are in the initial stages of development like Okinawa Trough (SW of Japan, *Fabbri and Fournier, 1999*) and the Sumisu Rift in the Izu arc (*Taylor et al., 1991*). Lavas erupted at back arc basins are commonly referred to as back arc basin basalts (BABB). BABB erupted from spreading ridges are dominated by pillowed basalts that are compositionally similar to MORB (*Hawkins and Melchior, 1985*) but contain more water and a significant “subduction component” (*Gribble et al., 1998; Newman et al., 2000*). BABB from back arc rifts, however, may be compositionally similar to those erupted from the affected arc. Furthermore back arc regions of high-strain convergent margins can be affected by crustal shortening and compression leading to the development of a system of back-arc basins behind the magmatic arc. The best Cenozoic example is found behind the present Andean arc (*Jordan, 1995*). This is a fold-and-thrust belt formed in response to subduction of young, buoyant lithosphere.

2. State of the art

Samples of the sub-arc mantle, represented by peridotite xenoliths entrained in arc magmas, are rare relative to mantle samples from non-arc settings, i.e. from oceanic hotspots and continental rift zones (Nixon, 1987). This means that there is a paucity of xenolith-based direct petrological information about the mantle wedge relative to other tectonic settings. Hence the rare examples of arc-derived peridotite xenoliths need to be investigated systematically and in detail to explore the nature of mantle-wedge materials and processes.

Peridotite xenoliths of mantle-wedge origin have been described from various localities worldwide, for example those from the Japanese island arcs (Takahashi, 1978; Aoki, 1987; Abe, 1997; Abe et al., 1998; Arai et al., 1998, 2000), the Colorado Plateau (Smith and Riter, 1997; Smith et al., 1999), the Cascades, USA (Brandon and Draper, 1996; Ertan and Leeman, 1996), Mexico (Luhr and Aranda-Gomez, 1997), Papua New Guinea (Gregoire et al., 2001; McInnes et al., 2001; Franz et al., 2002) and Kamchatka (Kepenzhiskas et al., 1995; Arai et al., 2003; Ionov, 2010).

Mantle xenoliths entrained in alkali basalts occur also in several localities from Patagonia, most of them situated between 40 and 52°S in intra-arc to back-arc positions with respect to the Andean volcanic arc. This material represent a peculiar, transitional type between the two above-described categories. They come in fact from a back-arc setting, but are entrained in alkali basalts similar to those found in intra-plate settings. Ntaflos et al. (2006) investigated a suite of unmetasomatized anhydrous spinel lherzolite and harzburgite from Tres Lagos (situated within the Volcanic Gap). Their Sr- and Nd-isotopic ratios have been affected by host basalt infiltration, whereas their high Sr-isotopic ratios point to subsequent contamination by ground-water and/or Ca-rich surface solutions. The authors speculated a two-stage partial melting process responsible for the origin of the Tres Lagos xenoliths. A first step should have been occurred in the garnet stability field (2% of batch melting) and subsequently the residue experienced 2–8% batch melting in the spinel peridotite field. They finally concluded that Tres Lagos peridotites were not been affected by subduction-related metasomatic processes and they could represent an old lithospheric mantle.

Conceição et al. (2005) published a paper on the isotopic composition (whole rock Sr and Nd) of mantle xenoliths sampled all over Patagonia. They showed that the majority of the

samples analyzed fall on the mantle array, but some of them exhibited radiogenic Sr enrichments without dramatic changing of the Nd isotopic composition. These isotopic features plot those samples on the right side of the mantle array and the authors explained these data as result of three possible processes: i) a mixture of a depleted mantle with an enriched source (EM-2) for those samples affected by high $^{87}\text{Sr}/^{86}\text{Sr}$ and low $^{143}\text{Nd}/^{144}\text{Nd}$; ii) a mixture of a depleted mantle with a mixture of mantle-derived and slab-derived melts for the samples characterized by high Sr/Nd ratios but low $^{87}\text{Sr}/^{86}\text{Sr}$ ratios and iii) chromatographic processes for those samples exhibiting enrichment of radiogenic Sr without dramatic change of Nd isotopic composition.

Another work (also in this case mainly isotopic) is that of *Schilling et al. (2005)* on spinel-bearing lherzolites and harzburgites entrained in alkaline lavas erupted by the cinder cone of Cerro Redondo. Based on P-T estimates (indicating T between 823 °C and 1043 °C and P ranging from 12.4 kb to 21.4 kb), petrographic, geochemical, and isotopic characteristics, they concluded that Cerro Redondo xenoliths came from a thick homogeneous mantle column (36 km to 63 km depth) characterized by different degrees of basalt infiltration. Using a simple mixing model based on Sr isotopes, they quantify the host basalt infiltration, calculating a contamination value between 0.2% and 12%. As the interaction with the host basalt increased, xenoliths showed a gradual increase of disequilibrium textures such as reaction rims and exsolution lamellae in orthopyroxene and clinopyroxene, and increase of TiO_2 , CaO, Al_2O_3 , Na_2O , K_2O , P_2O_5 , LREE, and incompatible element concentrations.

One of the most important studied locality in Patagonia is Gobernador Gregores (Santa Cruz Province, Argentina). The most interesting debate concerning the mantle nodules carried on by Plio-Pleistocene alkali basalts in this area is the presence of carbonatitic fluids that metasomatize the mantle wedge. As already explained at the beginning of this chapter the occurrence of mantle xenoliths in subduction regions is rare, but the presence of carbonatitic metasomatizing fluids is even rarer. *Laurora et al. (2001)* tried to investigate the origin of these fluids in Gobernador Gregores studying a suite of spinel-facies mantle xenoliths. They were characterized by higher $\text{CaO}/\text{Al}_2\text{O}_3$ whole-rock ratios with respect to other Southern Patagonian mantle xenoliths occurrences and in some samples by TiO_2 enrichments. They described three different occurrences: i) anhydrous lherzolites and harzburgites, containing clinopyroxene with a depleted major element

2. State of the art

composition; ii) formation of new phases such as amphibole±phlogopite±Cl-apatite-bearing during a metasomatic episode and iii) pockets of Na-Si-rich glass and carbonate drops, with amphibole as residual phase, due a decompressional event during the xenoliths uplift to the surface, that caused a closed system disequilibrium melting of the second assemblage (mainly the amphibole). The carbonated silicate melt underwent liquid immiscibility, products of which are represented by the carbonated drops and the silicate glass. Because of the different flow rates of carbonate and silicate melt, the xenoliths became enriched in carbonate (found in vein) during their migration. Therefore they finally hypothesized an aqueous slab derived Cl-rich fluids metasomatic agent and concluded that the origin of the carbonated silicate melt was the merely result of decompression melting during the uplift of the xenoliths to the surface.

Scambelluri et al. (2008) on the same suite of xenoliths recognized carbonic fluid inclusions, glass and carbonate in several textural domains on which they focused their attention. The high densities preserved by a number of CO₂ inclusions indicated that fluid infiltration took place at mantle depths. The low densities pertaining to the majority of analyzed fluid inclusions derived from inclusion re-equilibration during xenolith ascent. The glasses analyzed (occurring mainly as reaction haloes around clinopyroxene, amphibole and phlogopite, with microlites of new pyroxene, olivine and locally carbonate) varied widely their compositions in terms of both major (SiO₂ = 47.0 – 68.3 wt%; Na₂O+K₂O = 5.8 – 12.2 wt%) and trace elements. Incompatible trace element patterns of glasses in anhydrous xenoliths were similar to those of the host alkali basalts, whereas the compositions of interstitial and vein glasses in the hydrous xenoliths indicated that a compositional control has been exerted by the local mineral assemblage (mainly amphibole). The combined textural and microthermometric investigations clearly showed that the carbonic fluid and glass post-dated a stage of hydrous metasomatism of this mantle wedge: CO₂ and siliceous glass formed immediately before and/or during breakdown of the hydrous mantle assemblage. The microstructural and chemical data let the authors asses a close relationship between (i) infiltration of the host alkali basalt together with CO₂-fluid and (ii) partial melting of hydrous rock-forming minerals favoured by high-CO₂ contents of the ambient fluid phase. The presence of carbonic fluid was likely due to a decrease of CO₂ solubility in the uprising basaltic melt. At the xenolith scale, hydrous phase breakdown produced a reactive percolating melt that progressively increased its

silica and alkali content due to interaction with the host peridotite minerals. They finally concluded that the Si- and alkali-rich glasses could be due to a reaction between the host (or similar) magma and xenolith minerals. These reactions most probably occurred at mantle depths in the presence of significant amounts of exsolved CO₂, immediately before and/or after the early entrainment of the xenoliths into the host magma, producing a variety of textures and chemical compositions depending on the local assemblages and physico-chemical parameters of melt/peridotite reactions.

Rivalenti et al. (2004) investigated the mantle xenoliths entrained in the lavas of nine Patagonian localities comprised between 40°S and 52°S. The most common texture in the xenoliths was the re-crystallized granular or porphyroblastic one. As far as the xenoliths studied could represent the whole Patagonia mantle, these textures suggest that the mantle wedge experienced a regional, pervasive re-crystallisation that left only a few relics of the preceding mantle (in fact the authors found only six samples characterized by protogranular or porphyroclastic texture). They divided the lithotypes observed for all the localities in two groups: the first comprises anhydrous lherzolites and harzburgite, rare dunites. Their bulk-rock and clinopyroxene trace element profiles varied from slightly LREE-depleted to LREE-enriched. The second group was composed of lherzolites, harzburgites and rare wehrlites containing hydrous phases (amphibole ± phlogopite ± apatite), abundantly represented at Gobernador Gregores. With respect to the anhydrous group these samples were characterized in both bulk-rock and clinopyroxene by a convex upwards trace element pattern resembling that of peridotites affected by alkali basalt metasomatism, and by variable, and sometimes high Ti, Hf and Zr depletion and Nb enrichment. The composition of calculated melts in equilibrium with clinopyroxene resulted similar to the Patagonia arc magmas closer to the trench, but in the region South of latitude 46.30°S, it changed eastwards to an E-MORB-like melt. The authors interpreted the textural and geochemical bulk-rock and clinopyroxene features of the xenoliths as controlled by two main processes: (1) melting in the region of thermal inversion of the wedge, triggered by infiltration of hydrous components; (2) reactive porous flow of the melts into the overlying mantle. The component triggering melting is inferred to be slab-derived in the western occurrences and a garnet-facies, asthenosphere-derived melt in the eastern occurrences as a consequence of wedge thickening. Differences between northern and southern Patagonia were interpreted to be due to variable contribution of slab

2. State of the art

components to the wedge. Compared to the southern region, slab-derived melts are tentatively attributed to the subduction of older and colder segments of the Nazca plate in the North.

Finally, another interesting work carried out on a suite of spinel-facies mantle xenoliths (lherzolites, harzburgites and dunites) entrained in the alkali basalts of the Cerro de los Chenques Quaternary back-arc volcano (200 km E of the volcanic arc) has been published by Rivalenti et al. (2007). The clinopyroxene geochemistry indicated that the pristine mantle was a lherzolite with Depleted Mantle (DM) composition, recording either melting episodes triggered by infiltration of a metasomatic agent or only enrichment of highly incompatible elements in those sectors where percolation occurred under decreasing fluid volume. Metasomatism was operated by a fluid originated in garnet-bearing assemblages that induced olivine and clinopyroxene dissolution, variations in the Sr and Nd isotopic signatures (i.e. pre-metasomatic mantle: $^{87}\text{Sr}/^{86}\text{Sr}=0.702712$ and $^{143}\text{Nd}/^{144}\text{Nd}=0.513495$; xenoliths recording the highest metasomatism: $^{87}\text{Sr}/^{86}\text{Sr} =0.704234$ and $^{143}\text{Nd}/^{144}\text{Nd} =0.512870$), and increase in LILE and LREE, but not in Nb and Ti. The authors ruled out several hypothesis on the origin of the metasomatic agent, such as a metasomatism induced by the entraining alkali basalt. They also excluded a possible subarc origin of the mantle beneath Los Chenques subsequently transported by reversed corner flow 200 km to the East (the distance between arc and Los Chenques). They finally concluded that the features of the mantle xenoliths studied could be reasonably related to the fluids released by the slab and consistent with the signature and basalts forming the upper part of the subducted Nazca plate.

3. Cenozoic evolution of Patagonia.

In Patagonia the Andean volcanic arc is distinguished into a Southern Volcanic Zone (SVZ; Thorpe *et al.*, 1982) and an Austral Volcanic Zone (AVZ; Stern and Kilian, 1996) separated by a volcanic gap occurring between 46.3 and 49°S latitude (**Figure 3.1**).

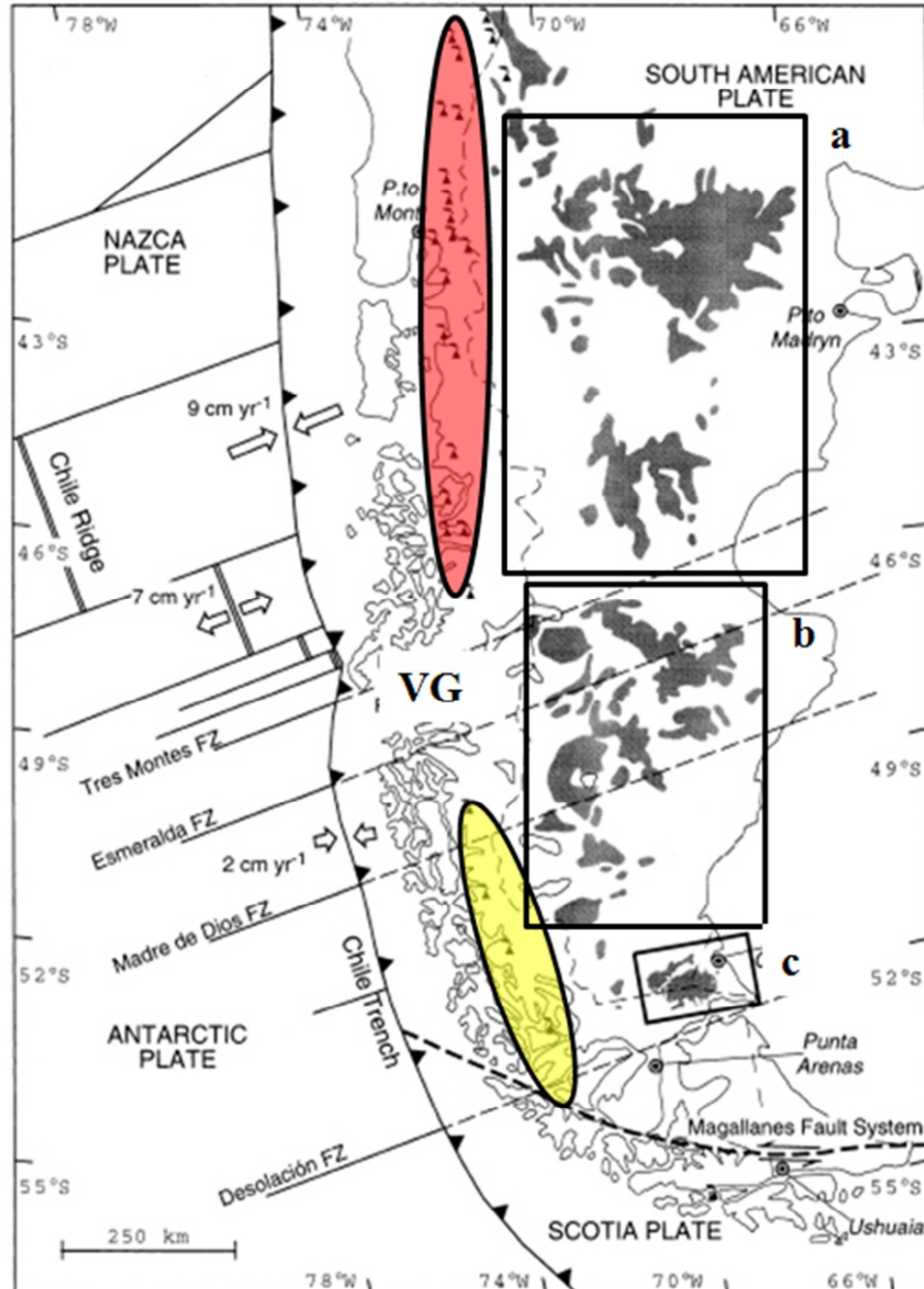


Figure 3.1: Sketch map of Patagonia (after *D’Orazio et al.*, 2000). The light red and yellow circles indicate respectively the SVZ and the AVZ. VG is “Volcanic Gap”. (a), (b) and (c) indicate the back-arc volcanic fields respectively of Northern Patagonia, Central Patagonia and Southern Patagonia.

3. Cenozoic evolution of Patagonia

The geological history during the Cenozoic of both SVZ and AVZ is related to the subduction of the Nazca and Antarctic plates respectively, beneath the South American plate. The average convergence rate over this period has been of 10 cm/yr for the Nazca plate and of 2 cm/yr for the Antarctic plate. The two plates are separated by the Chile ridge, and the present day position of the triple point between the Nazca, South America and Antarctic plates (Chile Triple Junction, CTJ) occur at 46.3°S. (*Cande and Leslie, 1986; Forsythe et al., 1986*).

A peculiar feature of Patagonia is the presence of several continental mafic volcanic plateaux ranging in age from late Paleocene to Recent time (*Ramos and Kay, 1992*). They are the Eocene Posadas Formation (located between 46 to 50°S), the late Oligocene to early Miocene Somoncuro magmatic province (41 to 43°S and similar age magmas erupted up to 46°S) and the late Miocene to Pliocene Triple Junction (TJ) province east of the CTJ (46 to 49°S). The Posadas and the TJ provinces have been respectively associated with Eocene and Miocene-Recent collision of the Farallon-Aluk (*Ramos and Kay, 1992; Kilian et al., 1997; Ramos and Aleman, 2000*) and the Nazca-Antarctica (*Ramos and Kay, 1992; Gorrington et al., 1997*) spreading ridges with the Chile trench, while the Somoncuro province with a mantle thermal anomaly linked to the late Oligocene/early Miocene changes in plate convergence vectors (*Kay et al., 1993, 2007*).

Because of the vastness of Patagonia (extending for more than 2000 km from north to south), and to simplify the back arc geological description I will divide the area in “Northern Patagonia” (extending from 40°S to 46°S), “Central Patagonia” (from 46°S to 49°S) and “Southern Patagonia” (from 49°S to 52°S), focusing more attention on the Central Patagonia, since most of the studied samples have been collected from post plateau volcanics of this area.

3.1 Northern Patagonia and the Somoncuro Province (40°S-46°S).

Between 40°S and 46°S occurs the largest post-Eocene mafic volcanic field of the Northern Patagonia, the Somoncuro igneous province (**Figure 3.2**). It consists of a series of Oligocene to early Miocene volcanic fields that cover more than 55 000 km² in the Meseta

de Somuncura and surrounding region (Meseta de Cari Laufquen and Meseta de Canquel), overlying a late Precambrian to Paleozoic magmatic and metamorphic basement itself covered by the extensive Jurassic silicic volcanic rocks of the Chon Aike province (Kay *et al.*, 1989; Pankhurst and Rapela, 1995) as well as Cretaceous to Tertiary volcanic and sedimentary rocks (Rapela and Kay, 1988; Rapela *et al.*, 1988; Ardolino *et al.*, 1999).

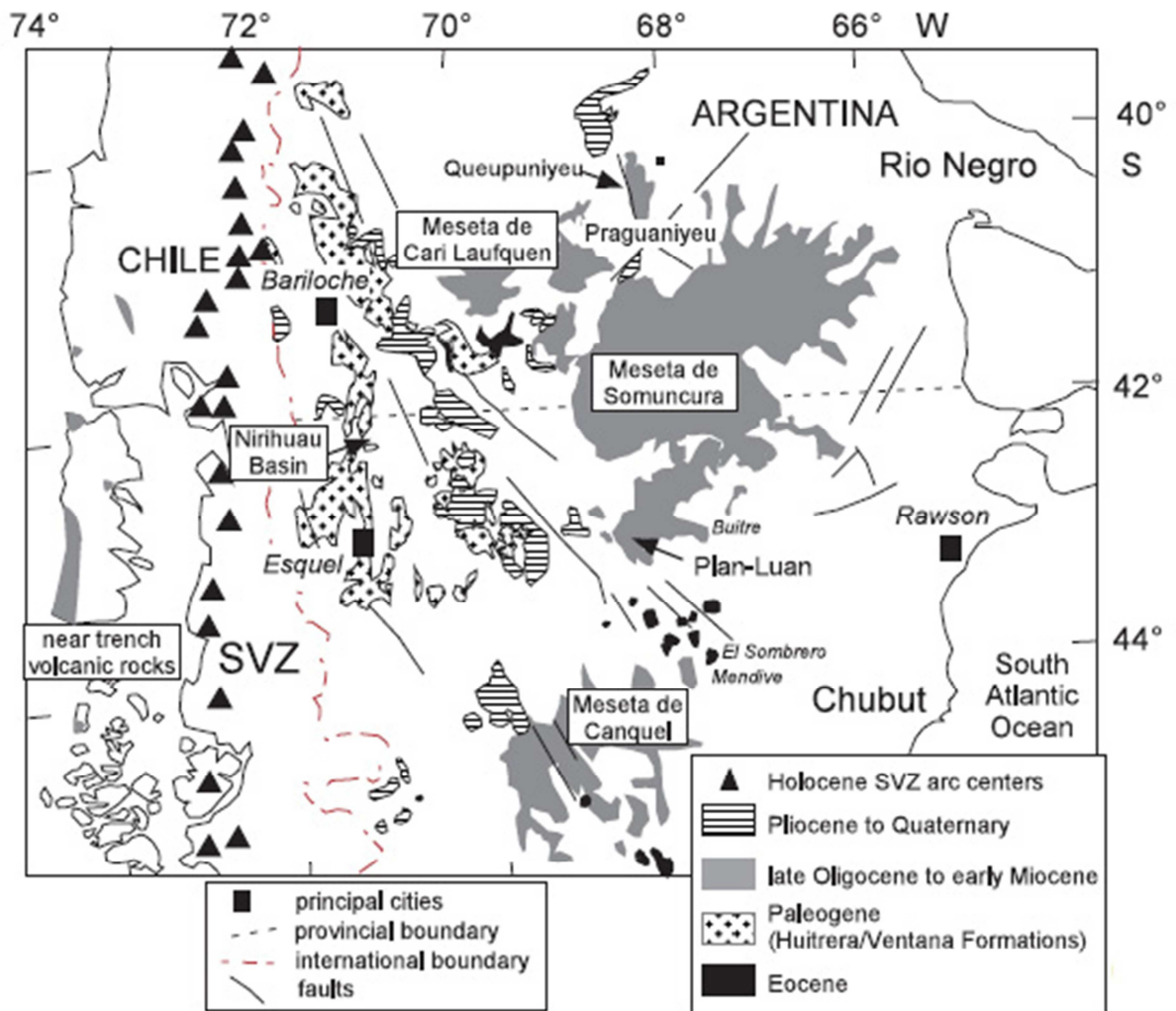
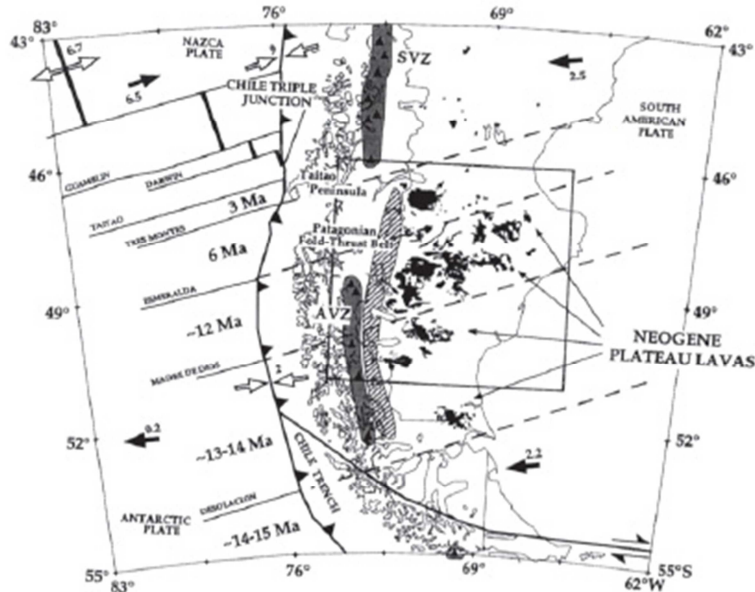


Figure 3.2: Sketch map of Northern Patagonia (from Kay *et al.*, 2007) showing the Somuncura igneous province, comprising from North to South the Meseta de Cari de Laufquen, the Meseta de Somuncura and the Meseta de Canquel. Symbols indicating the timing of magmatism are reported in legend.

3. Cenozoic evolution of Patagonia

Somuncura province volcanic rocks can be divided into pre-plateau, plateau and post-plateau groups. Low-volume late Oligocene pre-plateau flows are typically intraplate alkaline basalts and hawaiites, with depleted isotopic compositions ($^{87}\text{Sr}/^{86}\text{Sr} < 0.704$; $\epsilon\text{Nd} > +2$) and enriched trace element compositions. Voluminous $\sim 27 \pm 2$ Ma plateau flows are dominantly hypersthene normative basalts and basaltic andesites with flat REE patterns ($\text{La}/\text{Yb} = 4\text{--}12$), relatively low LILE abundances, transitional to arc-like Ba/La , Sr/La , Th/Ta and U/Ta ratios, intraplate La/Ta ratios and enriched Nd–Sr isotopic compositions ($^{87}\text{Sr}/^{86}\text{Sr} > 0.7043$; $\epsilon\text{Nd} < +1.3$). Finally intermediate to low-volume $\sim 23\text{--}17$ Ma post-plateau flows are dominantly alkali olivine basalts and hawaiites with steep REE patterns



($\text{La}/\text{Yb} > 15$), high LILE abundances, high Ba/La ratios, intraplate Sr/La and U/Ta ratios, and depleted isotopic compositions ($^{87}\text{Sr}/^{86}\text{Sr} = 0.7034\text{--}0.7046$; ϵNd ranging between $+0.9$ and $+4.5$).

Figure 3.3: Sketch map of Central Patagonia (from *Gorring et al., 1997*). In black the Neogene plateau.

3.2 Central Patagonia and the TJ igneous province (46°S-49°S)

In central Patagonia (**Figure 3.3**) the middle Miocene to Recent northwards migration of the CTJ from approximately 50°S (*Cande and Leslie, 1986; Forsythe et al., 1986*) to 46.3°S, has generated unique geodynamic, structural, and magmatic features (*Gorring et al., 1997*), namely the modern volcanic arc gap between the SVZ and the AVZ, the eruption of arc adakitic magmas (*Kay et al., 1993*) and in the AVZ (*Stern and Kilian, 1996*) and finally the extensive late Miocene to Pleistocene magmatism that originated the TJ province.

The TJ province can be subdivided into a voluminous, late Miocene to early Pliocene main plateau sequence, and a less voluminous, latest Miocene to Plio-Pleistocene post plateau sequence (Gorring *et al.*, 1997). Main plateau sequence forms the smaller mesetas to the northeast (called “northeastern region”) and the large and elevated plateaux of de la Muerte (MM), Belgrano (MB), Central (MC) and del Lago Buenos Aires (MLBA) Mesetas (Figure 3.4).

Main plateaux lavas of MM, MB and MC are tholeiitic basalts and basaltic andesites (Ramos and Kay, 1992; Gorring and Kay, 1993, 1994), whereas those from the “northeastern region” and MLBA are alkaline basalt and hawaiite (Baker *et al.*, 1981; Stern *et al.*, 1990; Ramos and Kay, 1992; Gorring and Kay, 1993, 1994). Post plateaux lavas are typically alkaline basalt and

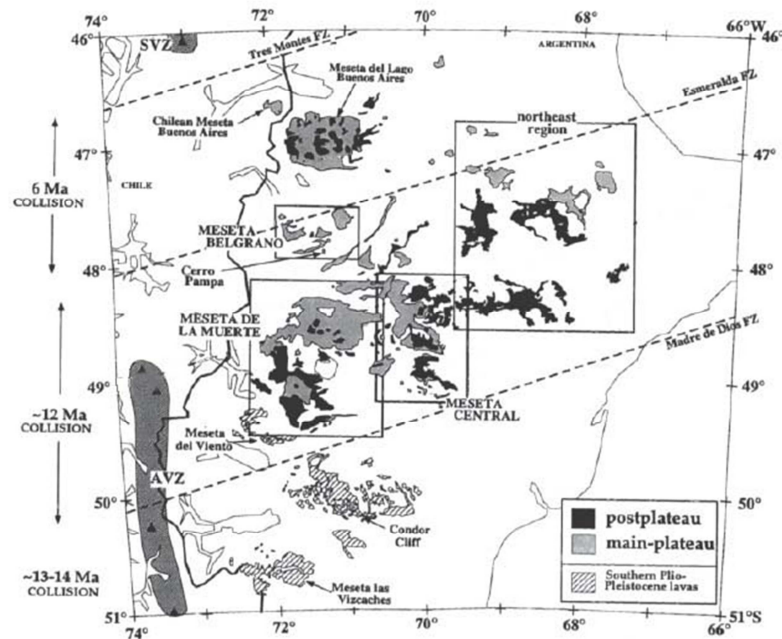


Figure 3.4: Map showing the occurrence of the different plateau of Central Patagonia (from Gorring *et al.*, 1997). In grey and black are represented the main and post-plateau sequences respectively.

hawaiite (Ramos and Kay, 1992; Gorring and Kay, 1993, 1994), except in MLBA where strongly alkaline lavas, basically basanites, are recognized. Post-plateaux volcanics generally occur as small cones, pyroclastic debris on the top of large plateaux and as flows, filling paleovalleys and forming small hills. Total estimated volumes for the main and post-plateau sequences for all mesetas are $\sim 1000 \text{ km}^3$ and $\sim 100 \text{ km}^3$ respectively (Ramos and Kay, 1992).

3. Cenozoic evolution of Patagonia

Main plateau and post-plateau lavas are characterized by a strong OIB affinity, in terms of trace element and isotopic composition. In fact they have OIB-like ratios and concentrations of LILE, LREE and HFSE, and relatively enriched Sr and depleted Nd isotopic signature ($^{87}\text{Sr}/^{86}\text{Sr}$ ranging from 0.7034 to 0.7046 with ϵNd between +5 and 0). Slightly higher LILE/HFSE and LREE/HFSE ratios of the western plateaux lavas (MM, MC, MB) by comparison to those of the “northeastern region” and MLBA indicate the presence of minor arc components in these latter.

$^{40}\text{Ar}/^{39}\text{Ar}$ radiometric ages (**Figure 3.5 and 3.6**) for the main plateaux lavas of the western back-arc range from 12 to 7 Ma, whereas those from further northeast are between 7 and 2 Ma. Post-plateaux lavas are generally 5 to 2 Ma younger than those of the main plateaux.

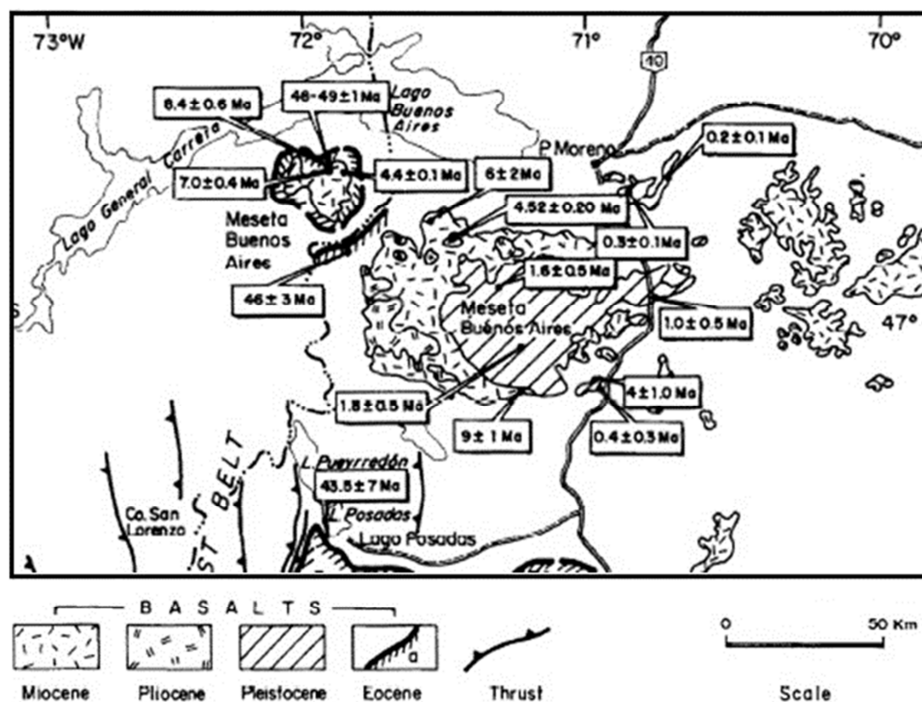


Figure 3.5: Distribution of the MLBA plateau basalts (from Ramos and Kay, 1992). K/Ar ages are from Charrier et al., 1978, 1979; Sinito, 1980; Baker et al., 1981; Ramos, 1982; Busteros and Lapido, 1983; Ramos and Drake, 1987.

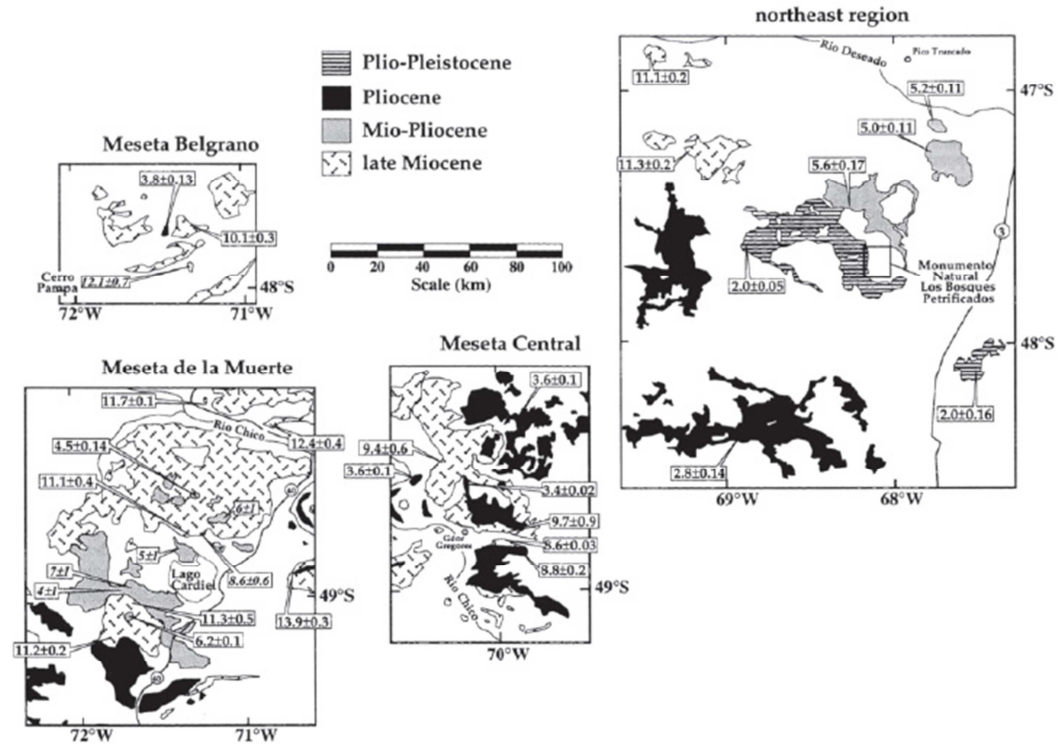


Figure 3.6: $^{40}\text{Ar}/^{39}\text{Ar}$ ages of the MB, MC, MM, and the northeast region (from *Gorring et al., 1997*) with light grey indicating the main plateau sequence and black the post plateau volcanic.

3.3 Southern Patagonia and the Pali Aike Volcanic Field (49°S-52°S)

This area is characterized by the occurrence of the southernmost and youngest Cenozoic back-arc Patagonian plateau lavas, represented by the Pali Aike Volcanic Field (PAVF). It covers an area of about 4500 km² north of the Magallanes fault system and is situated 200 km east of the Andean Cordillera. More than 80% of the totality of the volcanic products consist of an extensive succession of plateau-like basaltic lava flows, while the remaining 20% consists of more than 450 monogenetic structures represented by maars, tuff-rings, scoria and spatter cones, and by associated lava flows (*D'Orazio et al., 2000*). *D'Orazio et al. (2000)* observed two main elongation trends of the cones, one with an ENE direction and another with a NW direction, the first being linked to the still active Magallanes Strait Rift System described by *Diraison et al. (1997)* while the second is probably connected with the Mesozoic Patagonian Austral Rift (*Corbella et al., 1996*).

3. Cenozoic evolution of Patagonia

The erupted products are basically alkaline and olivine basalts and basanites. Trace element distribution is relatively homogenous and reveals a typical within-plate OIB-like signature, with high LREE/HREE ratios. Sr and Nd isotopic compositions are close to the MORB values, and are the most depleted among the whole set of Cenozoic Patagonian plateaux lavas.

Available $^{40}\text{Ar}/^{39}\text{Ar}$ ages (*Mercerer, 1976; Linares and Gonzales, 1990; Meglioli, 1992; Singer et al., 1997; Corbella, 1999*) indicate an age for the erupted lavas between 3.78 and 0.17 Ma, with the oldest rocks cropping out in the western sector of the volcanic field.

3.4 Cenozoic geodynamic evolution of Patagonia

As already noticed at the beginning of this chapter, one of the largest Cenozoic back-arc continental basaltic provinces of the world occurs in Patagonia. A major question remains: why these Patagonian magmatic events, which are not tied to major times of back-arc extension, occurred (*Kay, 2002a*)? Part of the explanation seems to lie in the fact that oceanic ridges and young oceanic crust have been subducted at the Chilean trench located to the west throughout much of the Cenozoic. As a result, the spatial and temporal pattern of some major events have been associated with slab-windows formed in conjunction with collisions of spreading ridges with the Chile trench (*Ramos and Kay 1992; Gorrying et al. 1997; D’Orazio et al. 2001*). The slab-window model has been proposed to explain the plateaux lavas generated in Central (the four mesetas, MM, MC, MB, MLBA and the “northeastern region”) and Southern (PAVF) Patagonia. Those from Central Patagonia were originally interpreted as due to an extensional regime (*Baker and Rea, 1978*), or related to a mantle plume, but the two hypothesis were abandoned after the work of *Ramos and Kay (1992)*. In fact they showed the lack of significant Neogene extension and pointed out the absence of topographic swells or hotspot tracks in central Patagonia, linking the emplacement of the plateaux with the opening of a slab window between the subducted Nazca and Antarctic plates as a result of late Miocene to Pliocene ridge collisions. Based of $^{40}\text{Ar}/^{39}\text{Ar}$ radiometric age dating *Ramos and Kay (1992), Gorrying et al. (1997)* and *D’Orazio et al. (2000)* highlighted a spatial and temporal link between the ridge-trench collision, the slab window and the eruption of the plateaux lavas. Northeast of where the ridge collided ~12 Ma ago most lavas are syncollisional or postcollisional in

age. Trace element and isotopic data indicate that main plateau lavas formed by a higher percentage of melting of a garnet-bearing, OIB-like mantle than post plateau lavas. The highest volume of melts were erupted in the western and central plateaus. According to *Gorring and Kay (1997)* in a migrating slab window model, main plateau lavas can be explained by melts that formed from upwelling, subslab asthenosphere which flowed around the trailing edge of the descending Nazca Plate and then interacted with subduction-metasomatized asthenospheric wedge and continental lithosphere. Alkaline, post-plateau lavas can be explained as melts generated by weaker upwelling of subslab asthenosphere through the open slab window.

The slab window model has been also proposed by *D'Orazio et al. (2000, 2001)* in order to explain the Southern Patagonian volcanic province of Pali Aike. They concluded that geochemical features of the plateau lavas of this area indicate a fertile garnet-bearing asthenospheric source. The model they proposed (**Figure 3.7**) referred always to the collision of the Chile Ridge with the Chile Trench at 14 Ma proposed by *Gorring et al. (1997)*, attributing to the prominent change in the kinematics of the South America–Scotia plate boundary the 8–6 m.y. delay between the passage of the trailing edge of the Nazca Plate beneath the PAVF area and the subsequent volcanic activity.

Further north in Patagonia, between 40 and 46°S, the origin of the Somuncura igneous province is still matter of debate. Some authors associated the plateau events to thermal anomalies correlated with a major late Oligocene/early Miocene change in plate convergence vectors (*Kay et al., 1993; Muñoz et al., 2000; de Ignacio et al., 2001*) and the aftermath of shallow subduction events (*Kay 2001, 2002b*), but the problem with this explanation is that the volume of magma erupted in plateau events is greater than those expected as a thermal consequence of these events (*Gorring et al., 1997; Kay, 2001*).

The 29 to 26 Ma tholeiitic to mildly alkaline mafic flows that built most of the plateau have an intraplate-like chemistry with a number of striking isotopic and chemical parallels to oceanic intraplate magmas from the Hawaiian Islands (*Kay et al. 1993*). As in Hawaii, the main plateau (shield stage) lavas can be modeled as the deepest and highest percentage melts from the most isotopically enriched mantle source. These similarities are consistent with the Somuncura magmas having a link to a mantle thermal anomaly or “hotspot”-like mantle. Most trace element and isotopic differences between Somuncura and Hawaiian lavas can be related to interaction of the Somuncura magmas with an arc-like component

3. Cenozoic evolution of Patagonia

inherited from lithospheric or upper asthenospheric mantle sources. Evidence for such an arc-like component is strongest in western plateau flows which have transitional arc-like trace elements (La/Ta ratios = 20-25) and enriched isotopic signatures. Further east, a transition to higher $^{87}\text{Sr}/^{86}\text{Sr}$ ratios at a given ϵNd and higher Ba/La ratios in plateau compared to pre-plateau magmas indicate the participation of this component into the mantle magma source during plateau formation (*Kay et al. 1993*). High Ba/La ratios in the plateau flows are consistent with a subcrustal origin. The simplest explanation is that this high Ba/La component is derived from the involvement of the subducted slab that gave rise to Paleocene arc lavas (*Rapela et al. 1988*) to the west. A problem in explaining the Somuncura plateau magmas is the cause of such a “hotspot-like” mantle thermal anomaly. Oceanic plate and paleogeographic reconstructions show that this event was not contemporaneous with important arc volcanism or ridge collision to the west. The lack of any clear tectonic cause led *Kay et al. (1993)* to suggest an association with a ‘hot-spot’-like thermal instability generated by mantle disturbances related to major late Oligocene plate reorganization. Subsequently, *de Ignacio et al. (2001)* amplified this suggestion by arguing that the Somuncura magmas were generated by asthenospheric corner flow that lead to a transient thermal anomaly above the subducting plate at the time of plate reorganization. They suggested that the intake of hot asthenosphere was induced by slab rollback and was focused by assumed favorable concave-up geometry of the subducting plate. Near the same time, *Muñoz et al. (2000)* argued that ~ 29 to 19 Ma lava flows to the west in Chile (38°S to 43°S) were related to extensional lithospheric thinning. This event was attributed to asthenospheric upwelling in a slab window that formed in response to changes in subduction zone geometry and that also produced the Somuncura magmas. Problems with this model include creating a slab window in the absence of ridge collision or other evidence for a gap in the subducting plate, lack of evidence for major extension in the Somuncura region, and the volume of the Somuncura flows. *Kay et al. (2004)* have argued that the formation of the Somuncura plateaux magmas may be related to a change in the rate of motion of the South American plate relative to the “hot-spot” mantle reference frame. *Silver et al. (1998)* argued that the Andean deformation cycle beginning at ~25 Ma was driven by an increase in the relative motion of South America with respect to Africa. *O’Connor et al. (1999)* have shown that the motion of Africa was faster relative to hotspots after 20 Ma than before 45 Ma. Unfortunately, there are still no reliable constraints on relative rates between 45 and 20 Ma, but there is an age correspondence

between the eruption of the Somuncura province and the upsurge of the African plate hotspots between 30 and 19 Ma (*O'Connor et al., 1999*).

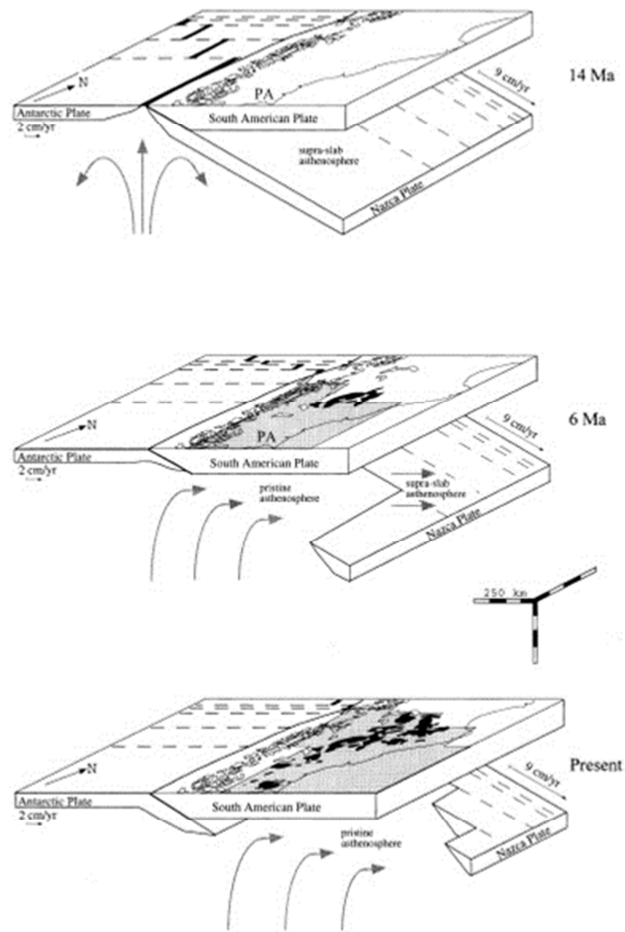


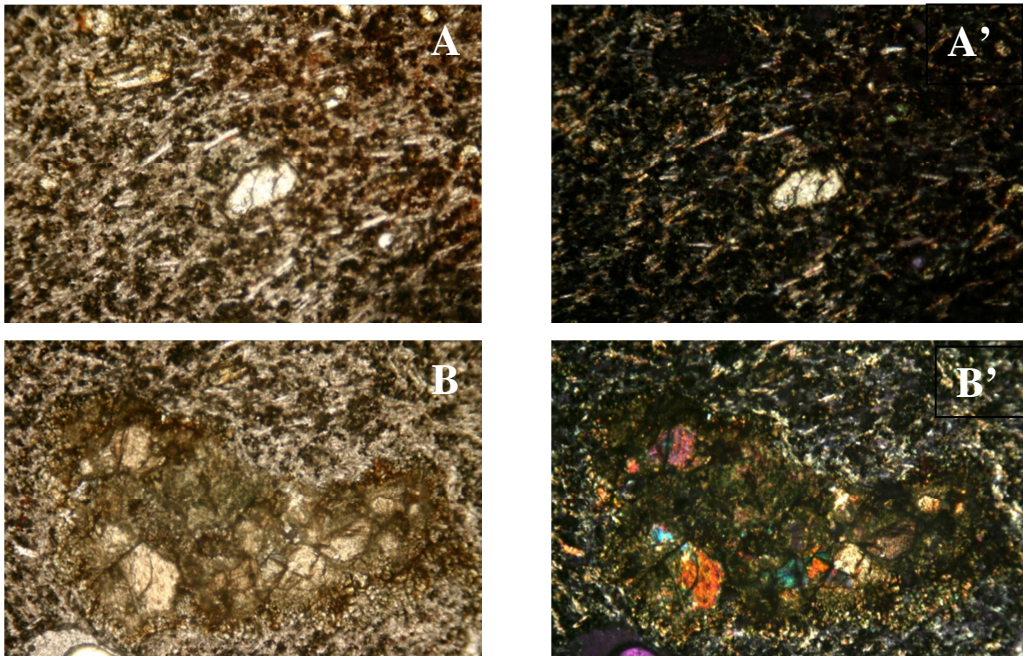
Figure 3.7: Slab window opening beneath Pali Aike according to *D'Orazio et al. (2000)*.

4. Chemical composition of the host lavas

4. Chemical composition of the host lavas

The mantle xenoliths from this study are entrained in the alkaline post-plateau lavas of the MLBA. As already described in the geological setting MLBA lavas can be subdivided in two sequences related to the main and to the post-plateau event respectively. $^{40}\text{Ar}/^{39}\text{Ar}$ radiometric ages (**Figure 3.6**) from MLBA main plateau lavas range from 10 to 4.5 Ma (Sinito, 1980; Baker et al., 1981; Mercer and Sutter, 1982; Thon-That et al., 1999) with the oldest lavas exposed on the southeast edge of the plateau. Post plateau lavas range from 3.4 to 0.125 Ma an age, but most are ≤ 1.8 Ma (Baker et al., 1981; Thon-That et al., 1999).

Samples represent the host rock of the xenoliths, thus they do not represent an extensive ad hoc sampling. Lavas are quite fresh, characterized by a porphyritic texture with 2 to 5% phenocrysts overwhelming dominated by euhedral olivine (**Figure 4.1 A-A'**). Sometimes is possible to observe glomerophiric assemblage of olivine (in some cases surrounded by marked rim of reaction) that probably have a mantle origin (**Figure 4.1 B-B'**). The groundmass is microcrystalline indicating a rapid magma cooling, with abundant acicular plagioclase (**Figure 4.1 C-C'**), associated to clinopyroxenes, olivine and Fe-Ti oxides.



4. Chemical composition of the host lavas

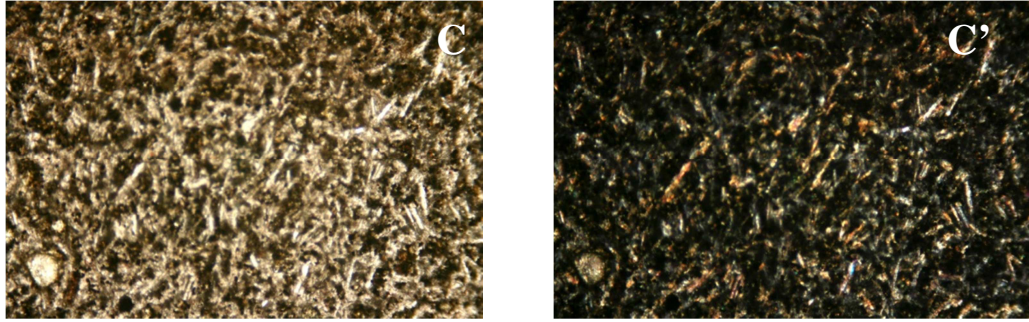


Figure 4.1: Microphotographs in plane polarized light (A, B, C) and cross polarized light (A', B', C') of the MLBA lavas. A-A' microphotographs show a crystal of euhedral olivine (MGP4). B-B' represent a glomerophiric assemblage of olivine (MGP2). C-C' microphotographs showing the groundmass of sample MGP1.

	MGP1	MGP2	MGP3	MGP4	MGP5	MGP6
SiO ₂	50.83	50.52	50.65	50.73	50.56	50.82
TiO ₂	2.13	2.15	2.14	2.10	2.13	2.14
Al ₂ O ₃	16.38	16.36	16.41	16.55	16.41	16.29
Fe ₂ O ₃ Tot	9.28	9.57	9.43	9.31	9.52	9.49
MnO	0.15	0.16	0.16	0.16	0.16	0.15
MgO	3.93	4.02	4.13	4.00	4.11	4.04
CaO	7.52	7.62	7.48	7.46	7.45	7.42
Na ₂ O	5.69	5.59	5.45	5.64	5.57	5.63
K ₂ O	2.65	2.58	2.51	2.55	2.57	2.55
P ₂ O ₅	1.09	1.08	1.07	1.07	1.06	1.07
LOI	0.35	0.36	0.56	0.43	0.45	0.40
TOTAL	100	100	100	100	100	100
mg#	48.65	48.45	49.51	49.05	49.15	48.79
Rb	32	32	31	31	32	32
Ba	398	393	376	390	387	387
Th	5	4	5	5	6	3
Nb	49	49	50	47	50	48
La	27	27	29	29	26	26
Ce	92	92	97	98	88	79
Sr	682	689	681	674	685	678
Nd	38	39	36	38	36	38
Zr	256	256	253	251	254	252
Y	20	21	20	21	21	20
Co	24	24	26	26	25	27
Cr	195	182	210	173	174	164
Ni	46	45	47	47	47	45
Pb	9	10	7	11	12	12
V	157	157	161	155	158	158
Zn	66	70	67	66	67	68
Cu	40	38	40	39	39	40
Ga	30	35	29	27	28	28
Sc	20	20	20	19	21	19

Table 4.1: Major and trace element composition of the six lavas analyzed by XRF. Mg# (MgO/(MgO+FeO) mol %) is calculated with Fe₂O₃=0.15*FeO

4. Chemical composition of the host lavas

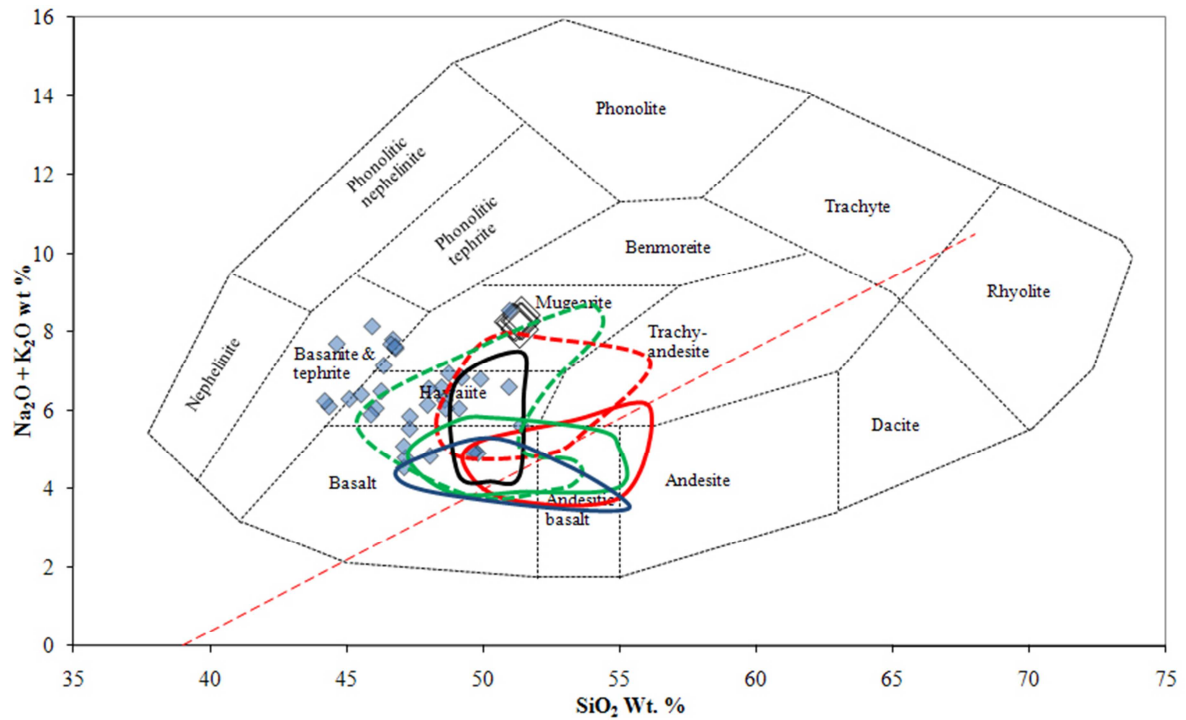


Figure 4.2: Total Alkali vs. Silica diagram of *Cox et al. (1979)*. Empty diamonds indicate the samples analyzed in this work, while light blue diamonds are MLBA post plateau lavas from *Gorring et al. (2003)*. Solid black line indicates the field of the Somoncuro pre-plateau lavas; solid and dashed red line indicate the Somoncuro main plateau and post plateau lavas respectively (*Kay et al., 2007*). Solid and dashed green line indicate the field of the main and post plateau lavas of the TJ Province respectively (*Gorring and Kay, 1997*). Blue line is the PAVF field (*D’Orazio et al., 2001*). Dashed red line separates the alkaline and subalkaline domains.

The geochemical compositions of MLBA lavas analyzed in this study are given in **Table 4.1**. MLBA post plateau lavas are sodic alkaline (~ 50 wt.% SiO_2 ; ~ 8 wt.% $\text{Na}_2\text{O} + \text{K}_2\text{O}$, with $\text{Na}_2\text{O} / \text{K}_2\text{O} > 2$), plotting in the mugearite field on a total alkali–silica classification diagram (**Figure 4.2**). They have low MgO content (~ 4 wt%) as well as Ni and Cr, the first being ~ 45 ppm and the second varying from 164 to 210 ppm. This characteristics can be explained by a differentiation suffered by these samples with respect to the other Neogene Patagonian post plateau lavas, as well as those coming from the same locality. As shown in **Figure 4.2** most of MLBA post plateau lavas are in fact basanites/tephrites and hawaiites (*Gorring et al., 2003*).

In **Figure 4.3** some variation diagrams are reported. SiO_2 is always on the x axis, while CaO, K_2O , MgO and Na_2O are plotted on the y axis. MLBA samples from this study fall in the field of the post plateau lavas of both the Somoncuro and TJ Provinces for CaO (~ 7.50 wt%), MgO and K_2O (~ 2.50 wt%) contents, while they are outside any field for Na_2O . In fact the value of ~ 5.60 wt% is very high with respect to MBLA post plateau lavas, as well

as to the main and post plateau lavas from the other localities. The Na₂O enrichment of xenolith-bearing lavas can be related to a higher differentiation degree, although the capacity of carrying heavy mantle rocks is highly reduced by differentiation. The tendency for MBLA lavas to be more alkaline in nature (as also testified by the absence of tholeiitic product in the main plateau stage) may be instead an indication for a substantially lower degree of partial melting and/or higher Na₂O content in the source region of these basalts.

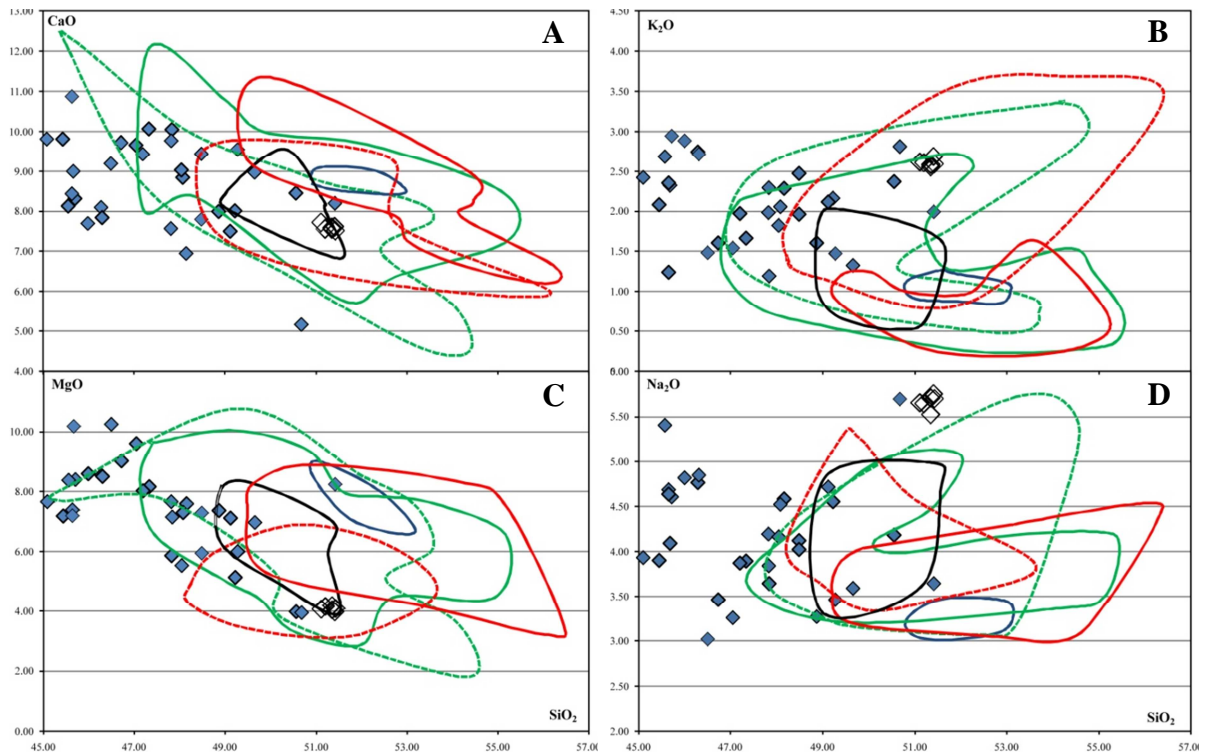


Figure 4.3: Harker type variation diagrams for major element concentration (wt%) plotting SiO₂ on the x axis vs. CaO (A), K₂O (B), MgO (C) and Na₂O (D).

Chondrite normalized trace element concentrations of the samples are reported in **Figure 4.4**. In the spider diagram are also reported the fields of the main and post plateau lavas from the TJ province (MM, MB, MC and the northeastern region, from *Gorring and Kay (2001)*), and the composition of the OIB and the N-MORB from *Sun and Mcdonough (1989)*. The patterns of the lavas of this work resemble that of the OIB, as those of the main and post plateau from the TJ province, the latter having a slightly higher incompatible trace element concentrations with respect to those of the main plateau. Moreover the OIB signature of the samples is also highlighted by the Ba vs. Nb diagram

4. Chemical composition of the host lavas

proposed in **Figure 4.5**, in which the samples clearly fall in the field of the within plate composition, together with those of all the other localities belonging to the TJ province.

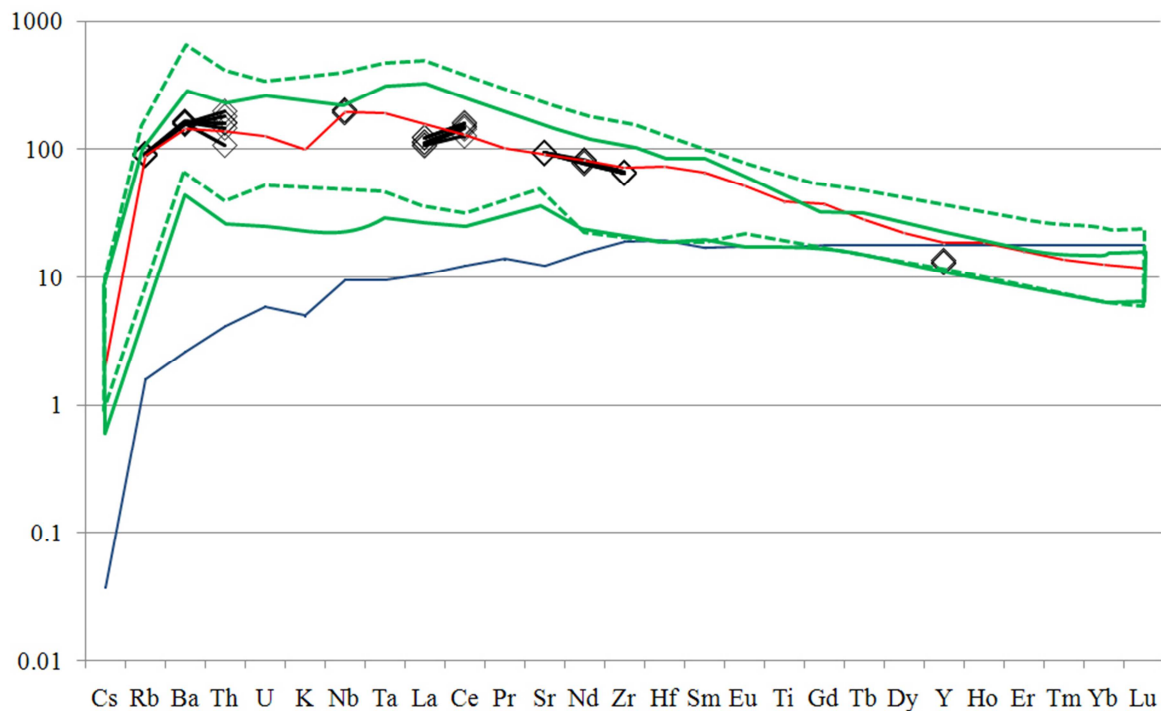


Figure 4.4: Chondrite normalized trace element compositions of MLBA post plateau lavas. Solid and dashed green line fields represent the main and post plateau lavas respectively from TJ province. Red and blue lines are OIB and N-MORB compositions respectively (from *Sun and McDonough, 1989*)

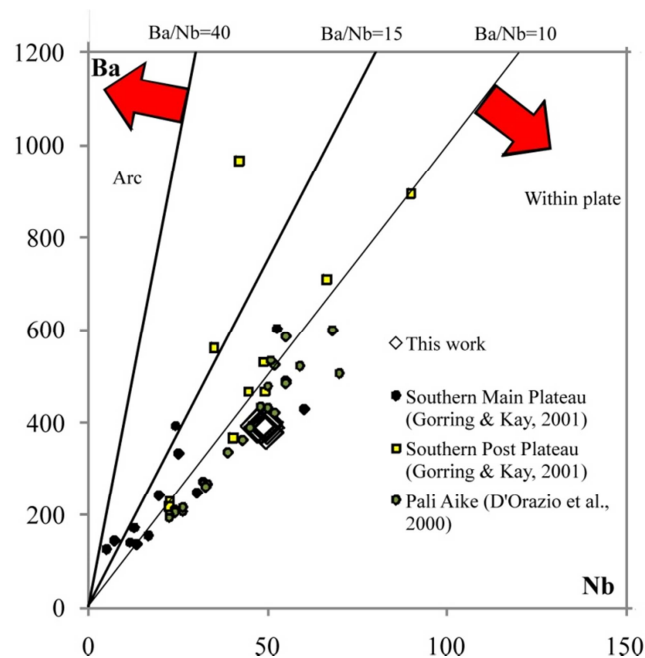


Figure 4.5: Nb vs. Ba plot. Empty black diamonds are the samples of this work.

5. Petrography of the xenoliths.

15 xenoliths occurring in the post plateau lavas of the MLBA have been studied. Most of them are very small in size (few centimeters across) and rounded in shape. Their modal composition (**Table 5.1**) has been calculated by counting over 1,000 point per each thin section.

	olivine	orthopyroxene	clinopyroxene	spinel	Total
MPG 1b	56.2	34.2	5.0	4.6	100
MPG 1c	68.4	30.2		1.4	100
MPG 1d	72.5		12.8	14.7	100
MPG 1h	91.7	5.2	1.4	1.7	100
MPG 2a	80.6	3.1	3.9	12.4	100
MPG 2b	71.4	13.1	9.5	6.0	100
MPG 2b2	59.0	22.7	13.3	5.0	100
MPG 3a	77.3	16.7	3.0	3.0	100
MPG 4b	60.8	29.7	2.0	7.5	100
MPG 4c	51.0	40.4	2.3	6.3	100
MPG 5a	89.5	0.6	2.9	7.0	100
MPG 1g	84.4	12.2		3.4	100
MPG 4e	87.8	7.9	0.2	4.1	100
MPG 3b	73.6	20.5	4.0	1.9	100
MPG 4a	94.7		1.0	4.3	100

Table 5.1: Modal composition of the mantle xenoliths from Estancia Sol de Mayo.

The xenoliths are mainly represented by anhydrous spinel-bearing harzburgites (7) and dunites (5), with minor lherzolites (2) and one wehrlite (**Figure 5.1**). They are characterized by a coarse grained protogranular texture (*Mercier and Nicolas, 1975*) and they are devoid of metasomatic features, such as spongy rims, reaction rims around spinel and/or orthopyroxene, glassy patches, as well as any hydrous minerals.

The most common feature is the presence of two textural kinds of clinopyroxenes (cpx) and three types of orthopyroxenes (opx). The former generally occur as protogranular in the peridotitic matrix (cpx1) or growing around the spinel (spl, cpx2); opx is present as i) large protogranular crystals with exsolution lamellae (opx1), ii) small clean and undeformed grains without exsolution lamellae (opx2) and iii) as smaller grains arranged in vein (opx3).

5. Petrography of the xenoliths

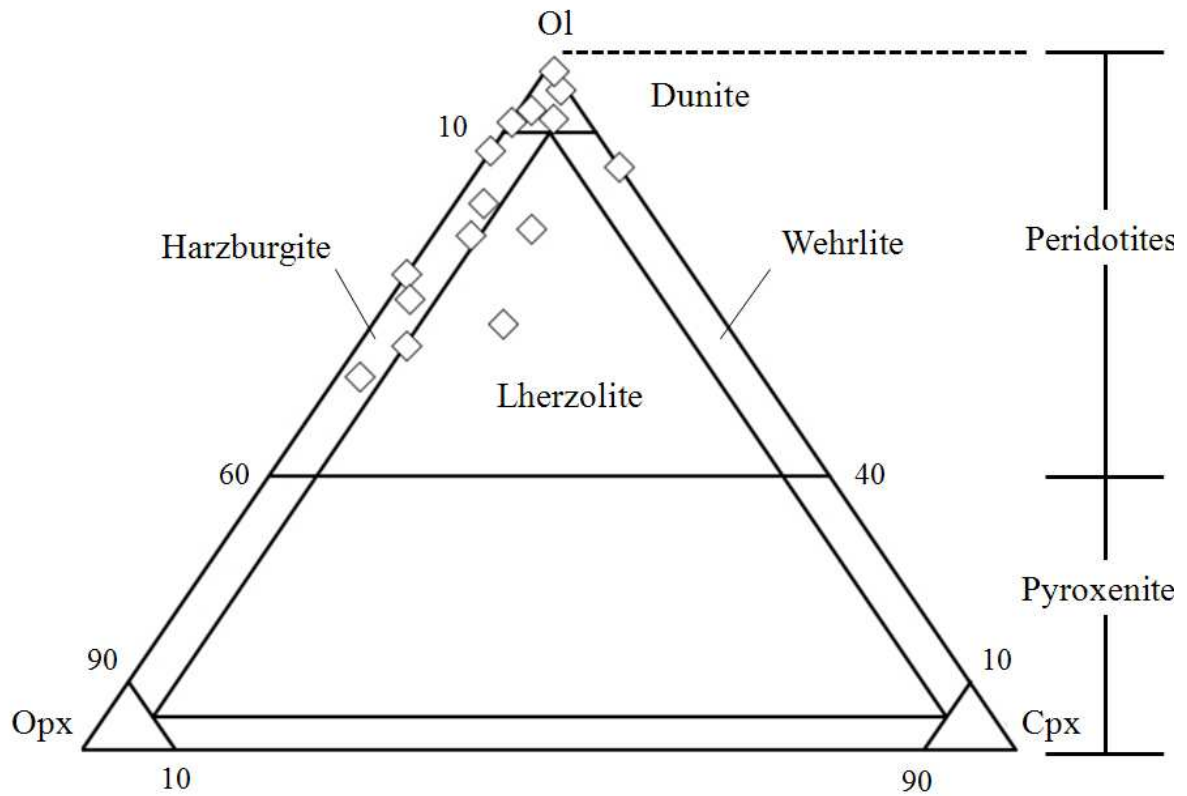


Figure 5.1: Ultramafic classification diagram (after Streckeisen, 1976).

5.1 Lherzolites

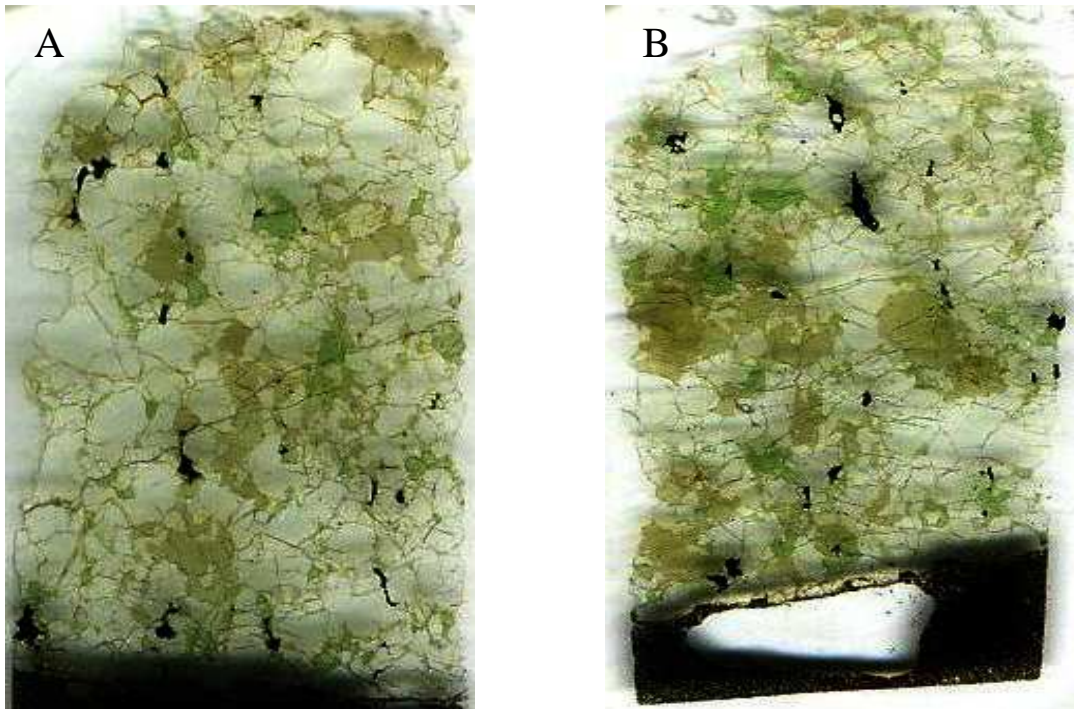


Figure 5.2: Thin sections microphotograph of two lherzolite samples. Samples MGP2b (A) and MGP2b2 (B).

Two samples (MGP2b and MGP2b2, **Figure 5.2**) fall in the lherzolite field. Olivine is the most abundant mineral (71.4 and 59% respectively); it has variable dimensions, reaching in some cases 1 cm. It is often characterized by 120° triple junctions (**Figure 5.3 A**), as well as strong kink banding.

Opx (13.1 and 22.7% respectively) is recognized as both opx1 and opx2. Opx1 has generally smaller dimension with respect to the olivine, sometimes intensely fractured, especially when close to the xenolith/host lava boundary. The biggest grains are often characterized by exsolution lamellae. Opx2 is less abundant and smaller when compared to opx1. It does not show exsolution lamellae or any sign of deformation as in the case of opx1. Furthermore they are clearly recognizable for their shiny brown colour.

In both samples cpx (9.5 and 13.3% respectively) is found as cpx1 and cpx2 (**Figure 5.3 B and C**). The latter is generally much smaller than cpx1, and its common texture is represented in **Figure 5.3 C**, where the cpx2 envelops the spinel.

5. Petrography of the xenoliths

Finally the spl (6 and 5% respectively) always occurs as the smallest mineral. It is always almost totally black, in some cases showing a brown colour along the rim (**Figure 5.3 D**). It can have tabular or elongated shape.

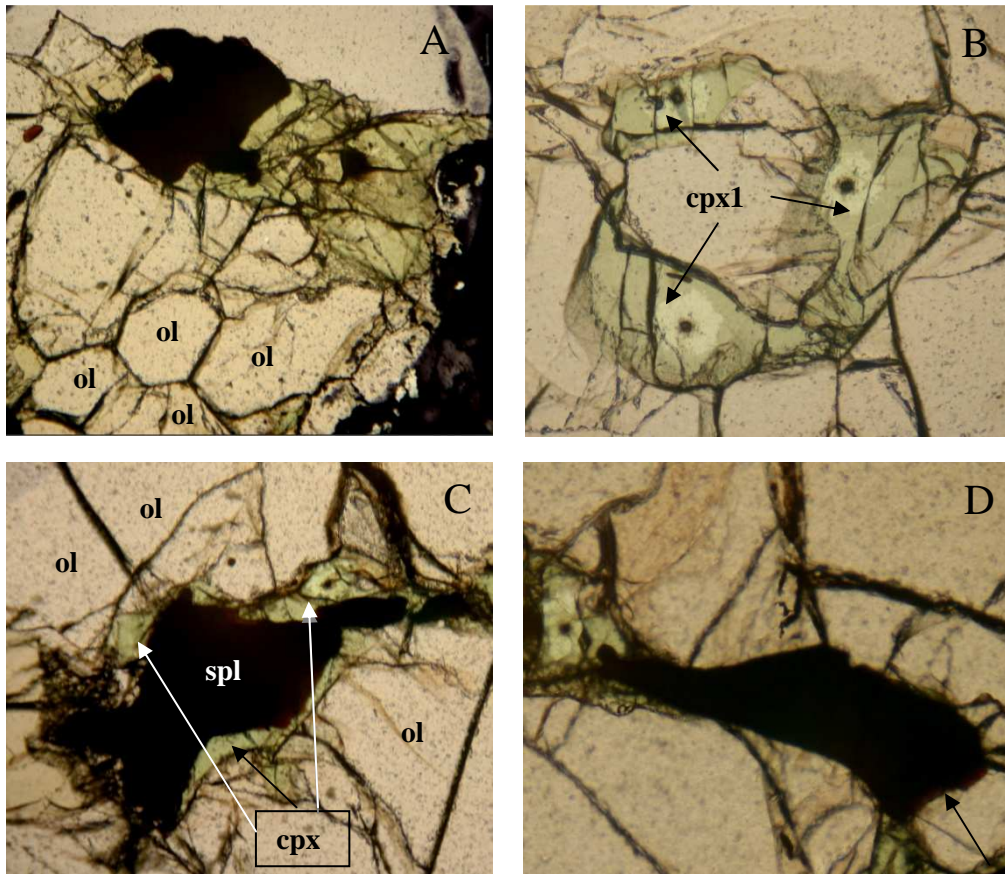


Figure 5.3: Microphotographs from the two lherzolite samples. (A) 120° triple junctions of a group of olivines in sample MGP2b2; (B) three cpx1 from MGP2b2 sample; (C) example of cpx2 growing around the spl in sample MGP2b; (D) spl preserving the brown color (indicated by the black arrow) along the rim in sample MPG2b.

5.2 Harzburgite

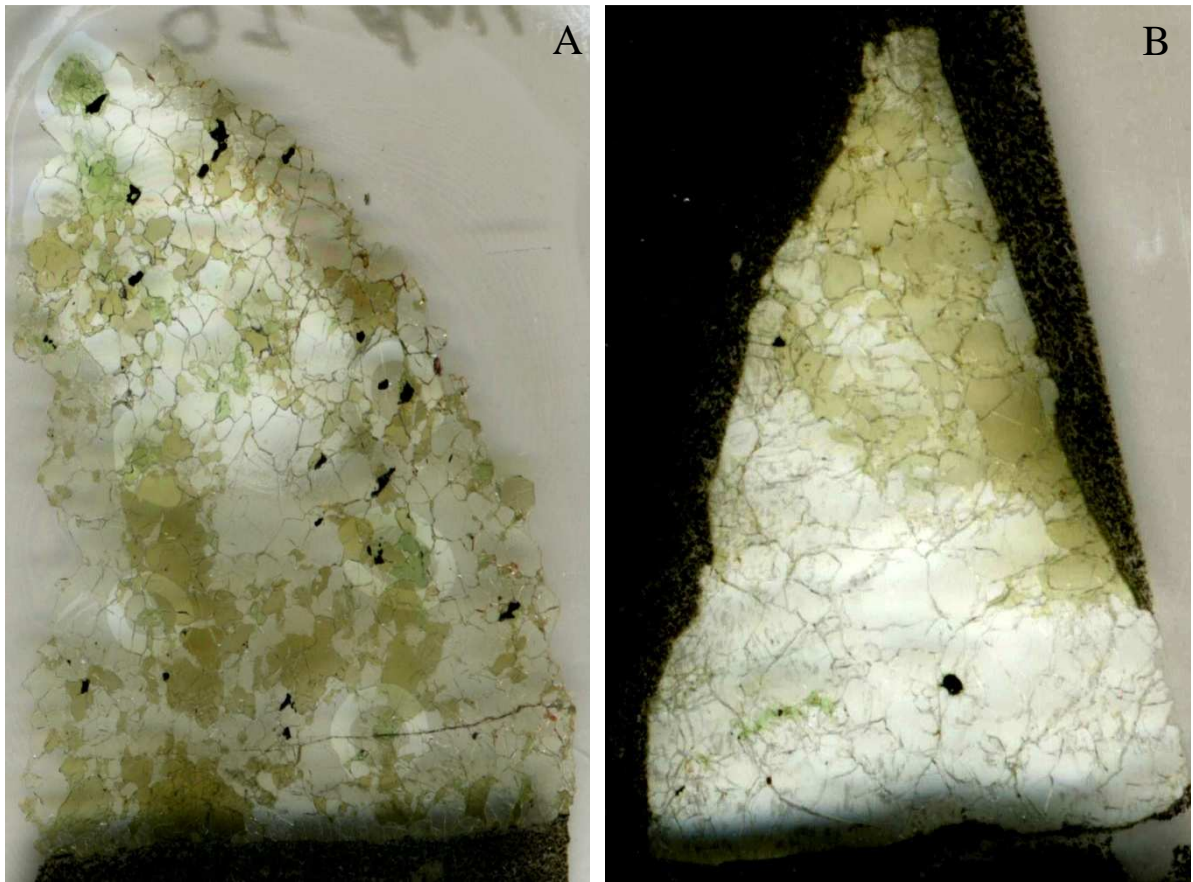


Figure 5.4: Thin section photomicrograph of two representative harzburgite thin sections. (A) sample MGP1b; (B) sample MGP1c.

With 7 samples (MGP1b, MGP1c, MGP1g, MGP3a, MGP3b, MGP4b, MGP4c) harzburgite is the most represented lithotype of the Estancia Sol de Mayo suite. One sample (MGP1b, **Figure 5.4A**) fall on the boundary separating harzburgites from lherzolites, but considering its low cpx percentage (only 5%) with respect to the previously illustrated two lherzolites I prefer to classify it as harzburgite.

The most abundant mineral is olivine, varying its modal content from 51% (MGP4c) to 84.4% (MGP1g), followed by orthopyroxene ranging from 12.2% (MGP1g) to 40.4% (MGP4c), spinel ranging from 1.4% (MGP1c) to 7.5% (MGP4b) and finally clinopyroxene comprised between 2% (MGP4b) and 5% (MGP1b).

Olivine has an average size of several millimetres. The biggest grains are generally marked by strong kink-banding, as in sample MGP4b, MGP1g and MGP1b, but it is common also

5. Petrography of the xenoliths

in the small sample MGP1c. As for lherzolites, olivines in harzburgites show 120° triple junction.

In all samples orthopyroxene is observed as opx1 and opx2. The former is characterized by variable dimensions, ranging from several microns up to ~1 mm. Only in one sample (MGP1b) the biggest opx1 present strong king-banding and exsolution lamellae. In two samples two peculiar textural features are recognized: in MGP1g a group of big and equidimensional opx1 is concentrated in a cluster (**Figure 5.5A**), well separated from other few smaller opx, and variable in dimension and shape; in MGP1c almost all the opx are located in the tip of the sample that has a triangular shape (**Figure 5.4B**). As for the lherzolites, also opx2 in the harzburgites are recognizable for their smaller dimension and their shiny colour. Also in this case they do not present neither kink banding nor exsolution lamellae.

Both cpx1 and cpx2 are present in MGP1b and MGP4b. While in the first sample the two cpx generations are equally distributed, in the second cpx2 prevails. In samples MGP3B and MGP1c only one generation of cpx is observed: cpx1 in the former, cpx2 in the latter. In MGP1g cpx is completely absent. The dimension and the shape are the main differences between cpx1 and cpx2. The former is always bigger and tabular, while the second has a typical elongated shape, resembling in some cases that of the spinel (as shown in **Figure 5.5B**).

Finally the spinel is always black, generally very little (few mm in size) and with an elongated shape when linked to the growth of the cpx2. Otherwise it is bigger and tabular in shape.

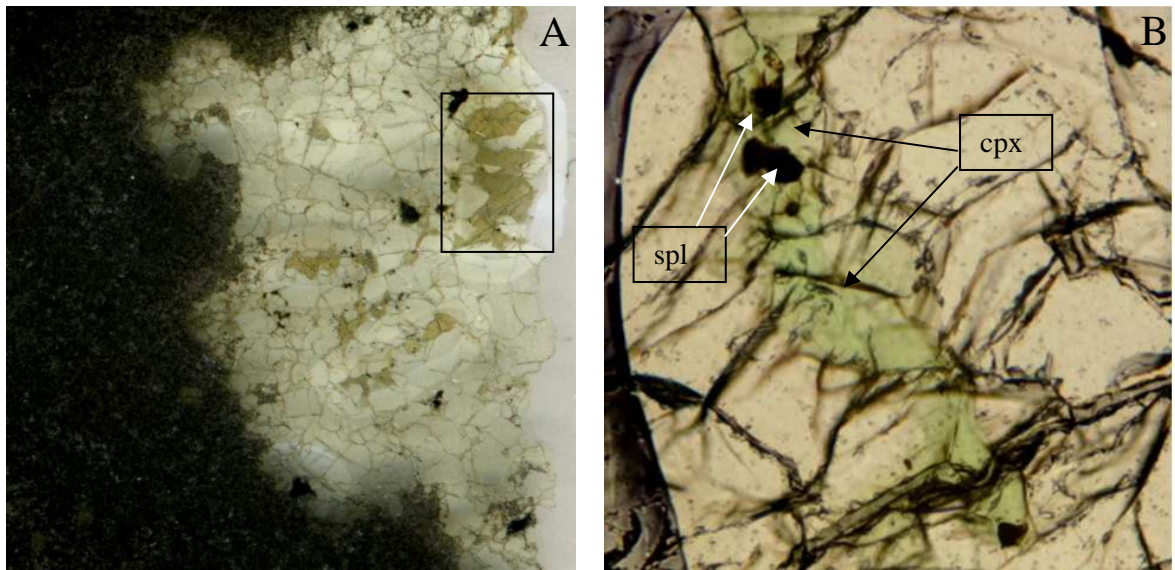


Figure 4.5: (A) Thin section photomicrograph of harzburgite MGP1g. In the black square is shown the cluster of opx; (B) elongated cpx2 from sample MGP1c, preserving two little spinels in the centres.

5.3 Dunites

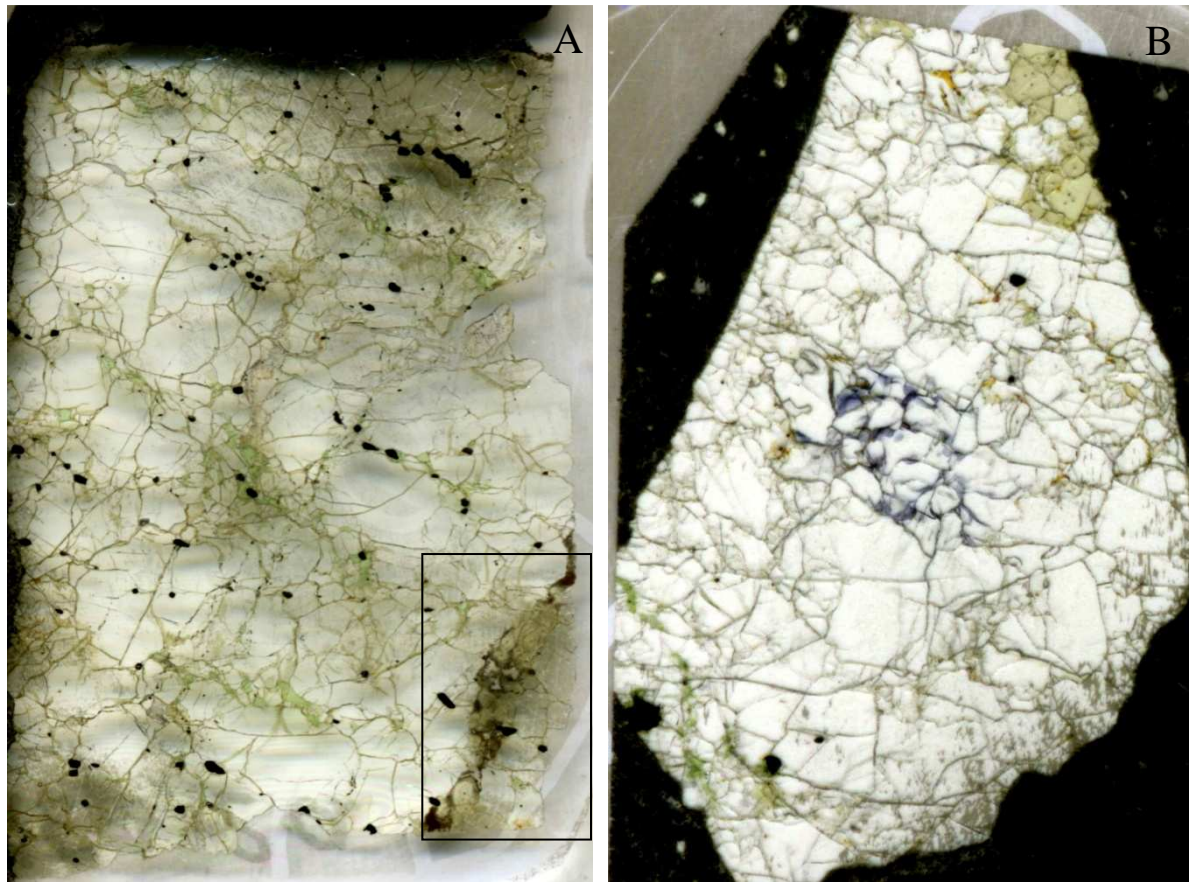


Figure 5.6: Thin section photomicrograph of two representative dunites. (A) sample MGP2a; in the black square there is the opx2 vein, shown in the next figure; (B) MGP1h.

Five samples (MGP1h, MGP2a, MGP4a, MGP4e and MGP5a) are classified as dunites. They have a modal composition dominated by olivine (varying from 80.6 up to 94.7%), followed by orthopyroxene, spinel and clinopyroxene (comprised between 0.6 and 7.9%; 1.7 and 8%; 0.2 and 3.9 % respectively).

Olivine is always of big dimensions (up to ~1 cm), often fractured even when observed far from the contact with the host lava and characterized by kink banding and 120° triple junctions.

Orthopyroxene is observed as opx3 only in sample MGP2a, where the crystals are clearly arranged in vein. Here they have dimension comprised between few millimetres up to ~0,5

cm, and they are surrounded by a microcrystalline groundmass mainly composed of plagioclase (**Figure 5.7**).

Both generations of cpx are equally represented in dunites. Cpx1 is generally bigger than cpx2, the latter observed always with an elongated shape. In sample MGP1h only small cpx2 are recognized, some of them preserving in the centre a relict of the aluminiferous phase. Otherwise the spinel can be completely absent, but the shape of the cpx suggest it growth at the expense of the spinel.

Finally the spinel is always black and small, and in some cases it can be very abundant (like in sample MGP2a).

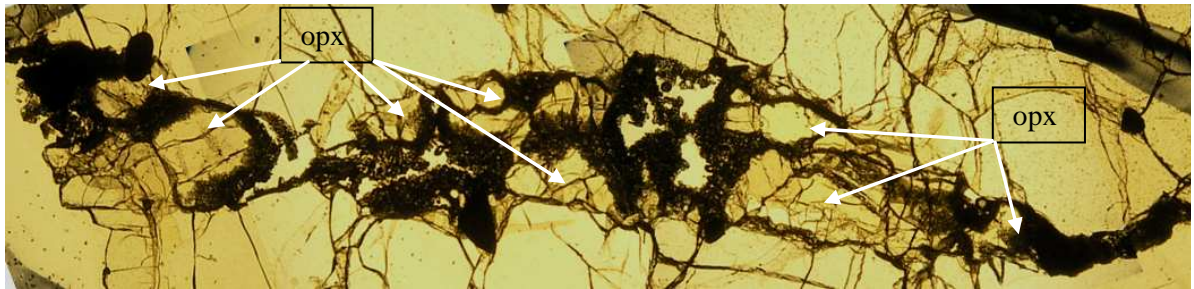


Figure 5.7: Opx3 arranged in vein in sample MGP2a.

5.4 Wehrlite

One sample is classified as wehrlite (MGP1d, **Figure 5.8**). Its modal composition is shown in **Table 5.1**.

It is characterized by abundant olivine, that frequently reaches the dimension of ~1 cm. 120° junctions are often observed, while kink banding is quite rare.

Big crystals of clinopyroxene occur in all the thin section analyzed, with one grain reaching up to 2 cm in size. The others are smaller even if they are among the largest cpx observed in all the samples of the Estancia Sol de Mayo suite. All the clinopyroxenes can be described as cpx₂. Generally the associated spinel is found within the clinopyroxenes, but sometimes it is situated along the rim of the cpx.

The spinel (always black) is generally of several millimetres in size. Its shape is mainly tabular, even if few elongated crystals may be found.

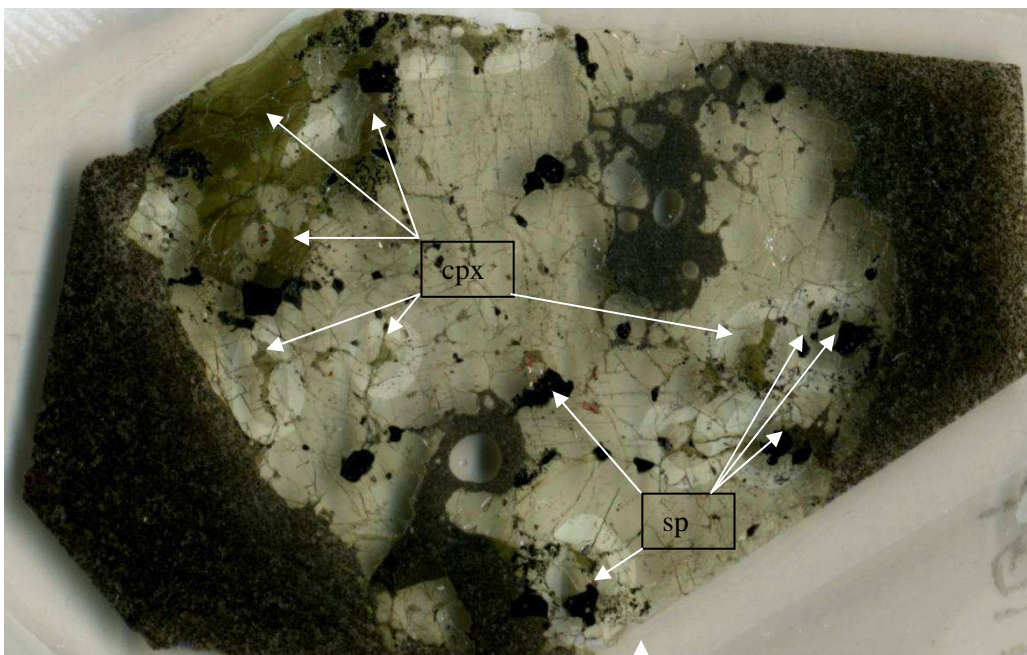


Figure 5.8: This section photomicrograph of the wehrlite MGP1d.

6. Geochemistry of the mineral phases

In this chapter the major and trace element compositions of the mineral phases observed within the Estancia Sol de Mayo mantle xenoliths are described. The former have been measured using an Electron Microprobe (EMP) on olivines, clinopyroxenes, orthopyroxenes and spinels, while the latter have been acquired only for pyroxenes using a Femto-Laser Ablation Inductively Coupled Plasma Mass Spectrometer (LA-ICP-MS). Both major and trace elements have been performed at the Observatoire Midi Pyrenees - CNRS of the University of Toulouse (see Appendix for analytical methods).

6.1 Major element compositions

In the following diagrams the various lithotypes are illustrated by different symbols: diamond identifies the lherzolites, circles the harzburgites, triangles the dunites, and finally asterisk the wehrlite. Furthermore each sample is identified by a different colour. When two types of clinopyroxene or spinel occur in the same sample the symbols for secondary cpx or spl are empty but the line have the colour of the sample. The legend is shown in **Figure 6.1**.

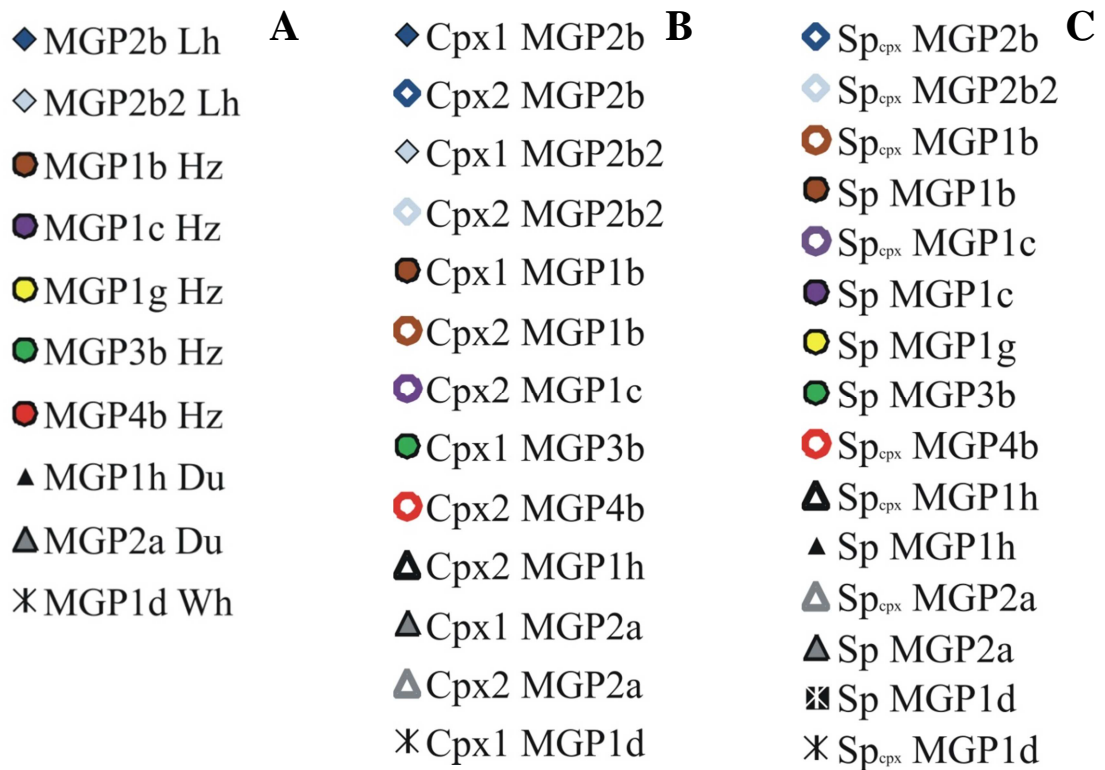


Figure 6.1: Legend for the olivine and orthopyroxene (A), clinopyroxene (B) and spinel (C) diagrams.

6. Geochemistry of the mineral phases

6.1.1 Olivine

In the following chapter the major element composition of olivines will be discussed. The complete set of analyses are reported in **Appendix 1**.

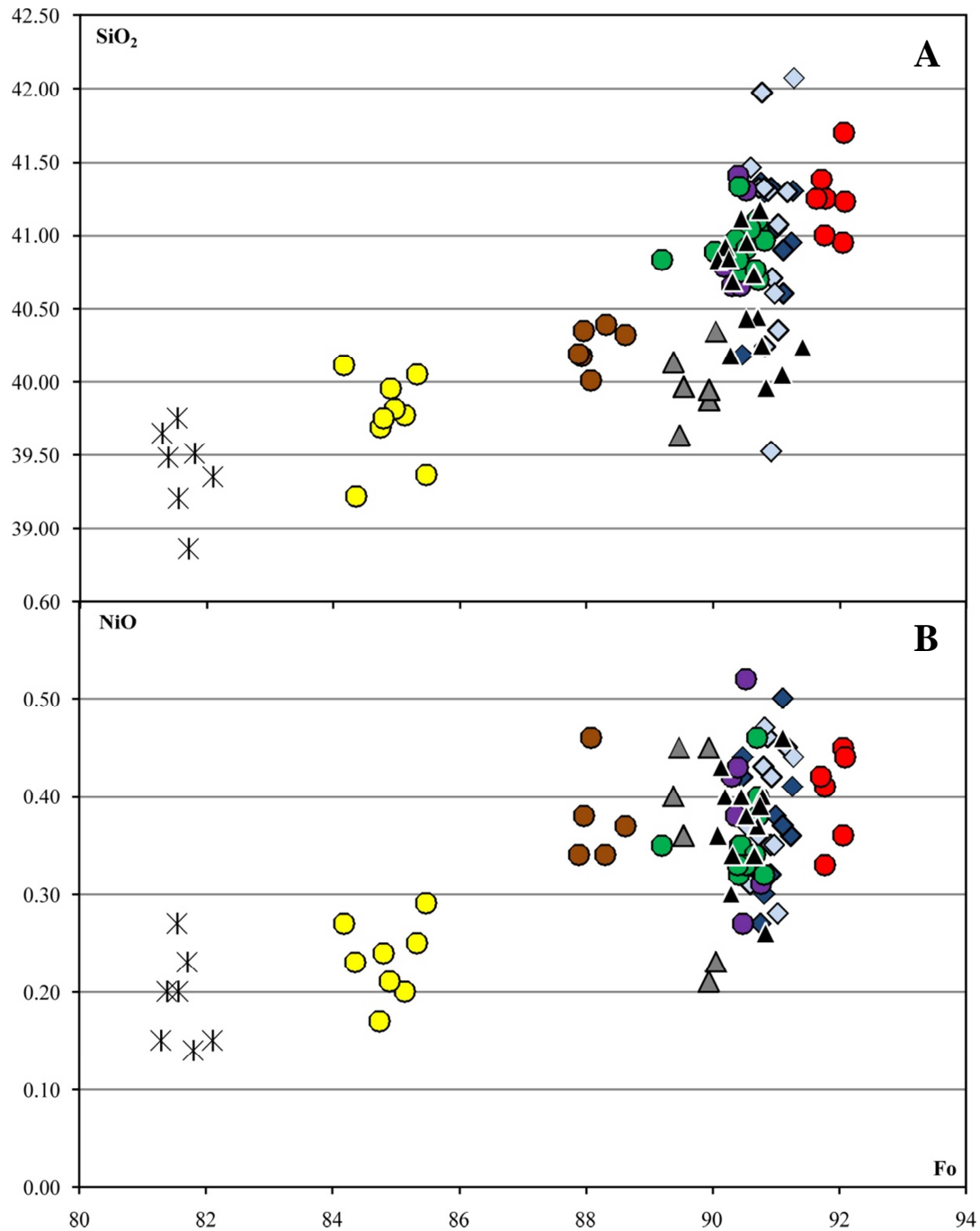


Figure 6.2: Fo vs. SiO₂ (A) and NiO (B).

As illustrated in **Figure 6.2** olivines of the lherzolites have a Fo content ranging from 90.47 to 91.29. The two samples are characterized by a wide range of SiO₂ content, with

MGP2b2 (39.52-42.07 wt%) showing a higher variation than MGP2b (40.18-41.36 wt%). The two samples present a rather narrow but similar range of NiO (0.27-0.50 wt%). Olivines in harzburgites (five samples over the total of 7 described in the petrography chapter) have Fo content varying from 84.18 up to 92.09. Apart from sample MGP4b which present Fo content (91.71-92.06) higher than those of lherzolitic olivines and a narrow range of variation of SiO₂ (40.95-41.70 wt%) and NiO (0.33-0.45 wt%), the remaining harzburgites have comparable or lower Fo content (89.20-90.82). Olivines of samples MGP1b and MGP1g have particularly low Fo in olivine (84.18-88.62) as well as SiO₂ and NiO contents, the former varying from 39.22 to 40.39 wt% and the latter from 0.17 to 0.46 wt%. The dunites (MGP1h and MGP2a) are characterized by Fo (89.37-91.42) contents comparable to those of lherzolites with sample MGP1h (90.07-91.42) showing a range slightly higher than the one of MGP2a (89.37-90.05). Also the SiO₂ and NiO content variations are comparable to those of lherzolites, varying from 39.63 to 41.17 wt% and from 0.21 to 0.46 wt% respectively. Finally, olivines of the wehrlite show the lowest Fo values, ranging from 81.29 to 82.10. They also show low SiO₂ and NiO values, but comparable to those of the harzburgite MGP1g, ranging respectively from 38.86 to 39.75 wt% and 0.14 to 0.20 wt%.

6.1.2 Clinopyroxene

As already described, a further classification of clinopyroxenes (**Appendix 2**) is necessary. In the following description they will be classified not only based on lithotype and sample, but also according to their textural position, i.e. primary those occurring as protogranular (cpx1) and secondary those linked to spinel (cpx2).

Cpx1 from lherzolites have mg# ranging from 91.4 to 94. that are comparable to those of the cpx2 (91.6-93.9). The latter show slightly higher Al₂O₃ and Cr₂O₃ (**Figure 6.3**) contents (4.01-4.31 wt% and 1.19-1.45 wt% respectively) with respect to the former (3.21-4.12 wt% (with only one reaching 4.52 wt%) and 0.56-1.02 wt% respectively). They have comparable CaO (20.92-21.59 wt%), Na₂O (0.76-1.02 wt%) and TiO₂ (0.12-0.39 wt% with a couple of cpx1 having 0.05 and 0.08 wt%) contents, while SiO₂ varies widely for both types of cpx, with cpx2 marked by lower values (50.03-53.12 wt% for cpx2 and 51.11-53.66 wt% for cpx1).

Mg# of cpx1 from harzburgites vary from 89.9 up to 93; they have an Al₂O₃ content (1.75-3.56 wt%) lower than those of the lherzolites, but comparable Cr₂O₃ (0.57-1.45 wt%), as well as Na₂O, and CaO (**Figure 6.4**), the former varying from 0.71 to 1 wt% and the latter from 20.77 to 21.72 wt%. They are characterized by much lower TiO₂ (0.05-0.2 wt%) contents, but higher SiO₂ (51.83-54.05 wt%) (**Figure 6.5**). Except the one of sample MGP1b (mg# 88.9-90.1), the secondary cpx show a range of mg# (91.2-93.5) similar to those of lherzolite cpx2, falling in the same field in terms of Al₂O₃ (3.46-4.34 wt%), Cr₂O₃ (1.26-1.59 wt%), CaO (21.02-21.33), and TiO₂ (0.12-0.31 wt%) contents. Moreover they show a narrower range of SiO₂ (52.25-53.05 wt%) and a higher content of Na₂O (0.95-1.18 wt%). Cpx2 from sample MGP1b do not show any compositional differences with the primary cpx from the same sample.

Cpx1 from dunites have a very narrow mg# range, from 91.2 to 92.4 comparable with that of harzburgite MGP3b. It also displays the same Al₂O₃ content, ranging from 1.75 to 3.12 wt%, but slightly lower Cr₂O₃ (from 0.73 to 1.2 wt%). At comparable mg# values they are characterized by higher TiO₂ (0.07-0.3 wt%) and Na₂O (0.74-1.13 wt%) contents with respect to their equivalent in harzburgites (but similar to those of lherzolites) and lower SiO₂ (52.12-53.37 wt%) and CaO (20.49-21.77 wt%) contents. Secondary cpx have mg# (90-92) similar to that of the primary, but have higher Al₂O₃ (2.65-4.03 wt%) and Na₂O (1-

6. Geochemistry of the mineral phases

1.27 wt%), slightly higher Cr_2O_3 (0.91-1.36) and TiO_2 (0.24-0.51 wt%) and slightly lower SiO_2 and CaO contents (varying from 51.62 to 52.77 and from 19.86 to 21.07 respectively). All these features collocate the cpx2 of dunites in the same field of those previously described and belonging to the Iherzolites and the Harzburgites (with the exception of cpx2 from sample MGP1b).

Finally clinopyroxenes of the wehrlite show the lowest mg# ranging from 82.3 to 86.6. They are characterized by the highest Al_2O_3 and TiO_2 contents, the former comprised between 5.13 and 7.3 wt% and the second between 0.63 and 1.12 wt%. At the same time they are characterized also by the lowest values of Cr_2O_3 (0.37-0.86 wt%), CaO (12.4-21.38 wt%), Na_2O (0.32-0.96 wt%) and SiO_2 (49.43-51.62 wt%).

6. Geochemistry of the mineral phases

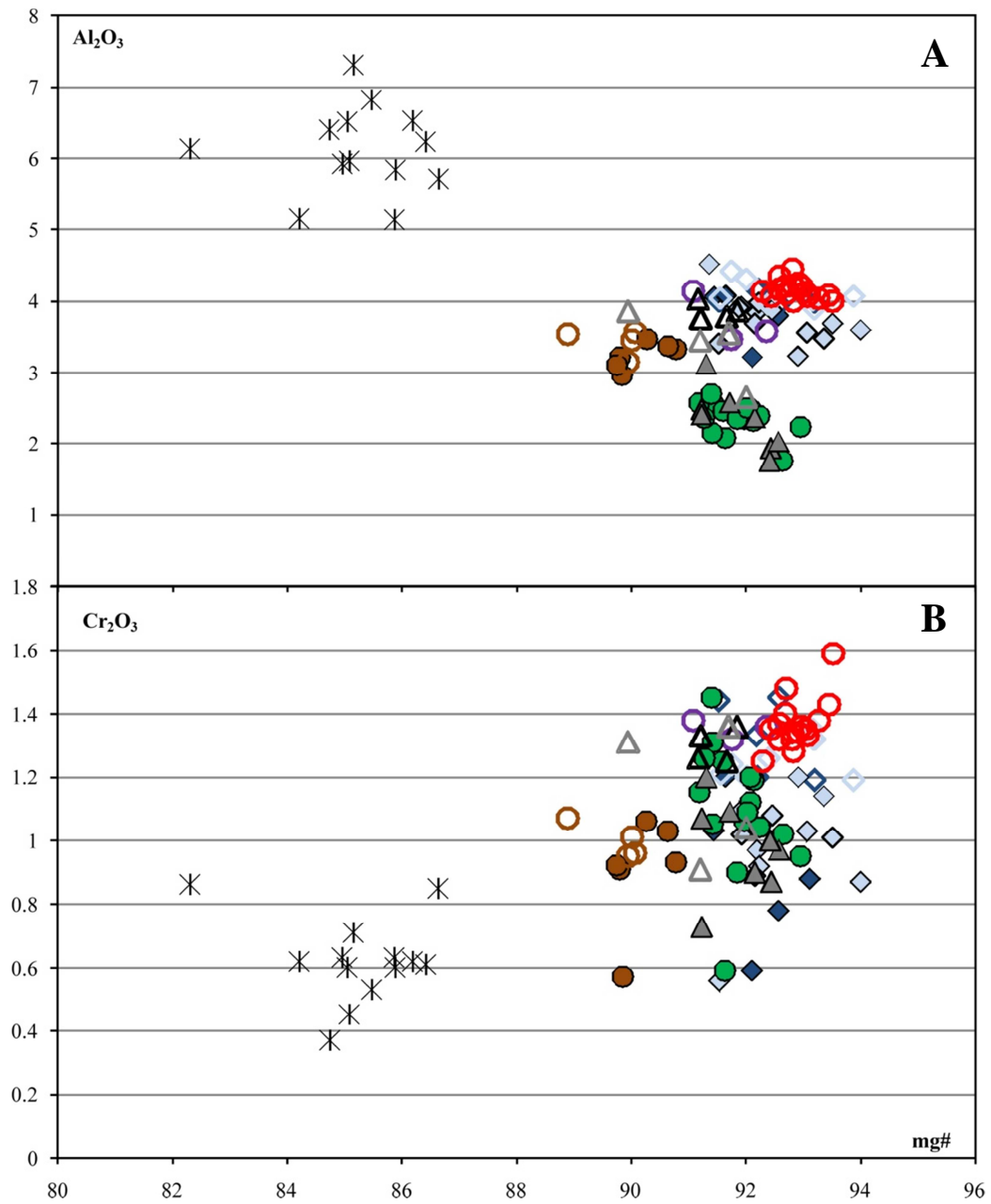


Figure 6.3: Al₂O₃(A) and Cr₂O₃ (B) vs mg#.

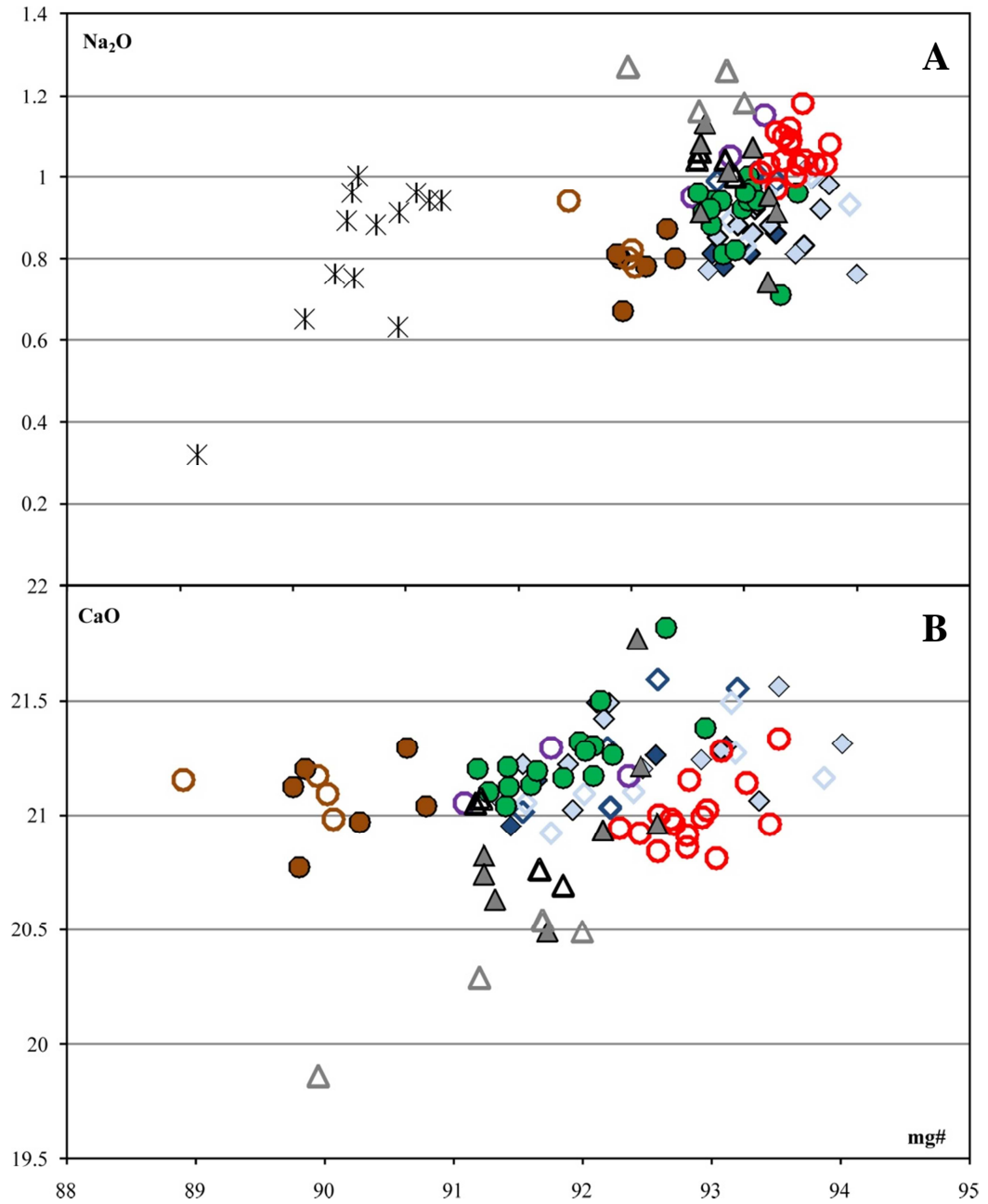


Figure 6.4: Na₂O (A) and CaO (B) vs mg#.

6. Geochemistry of the mineral phases

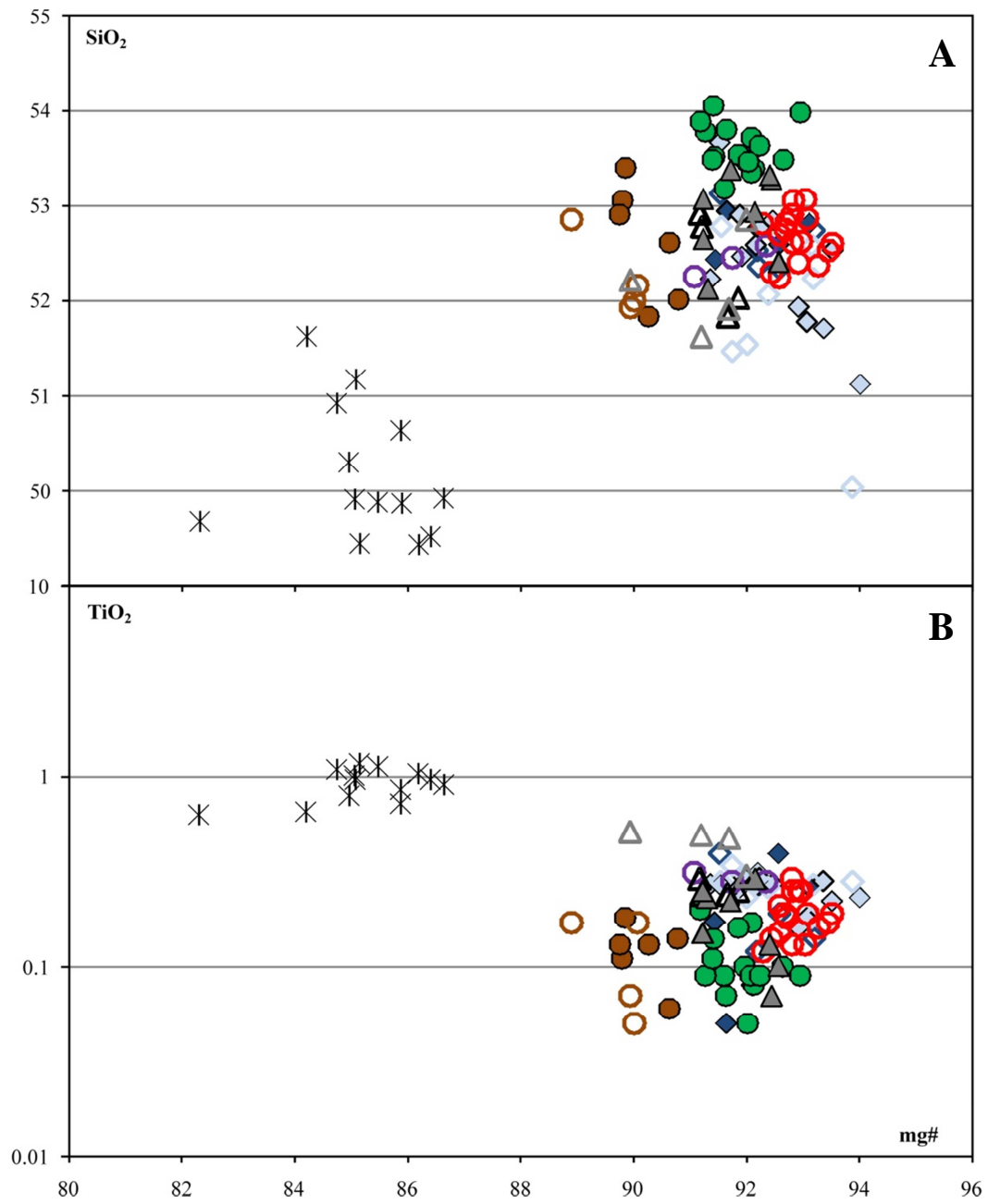


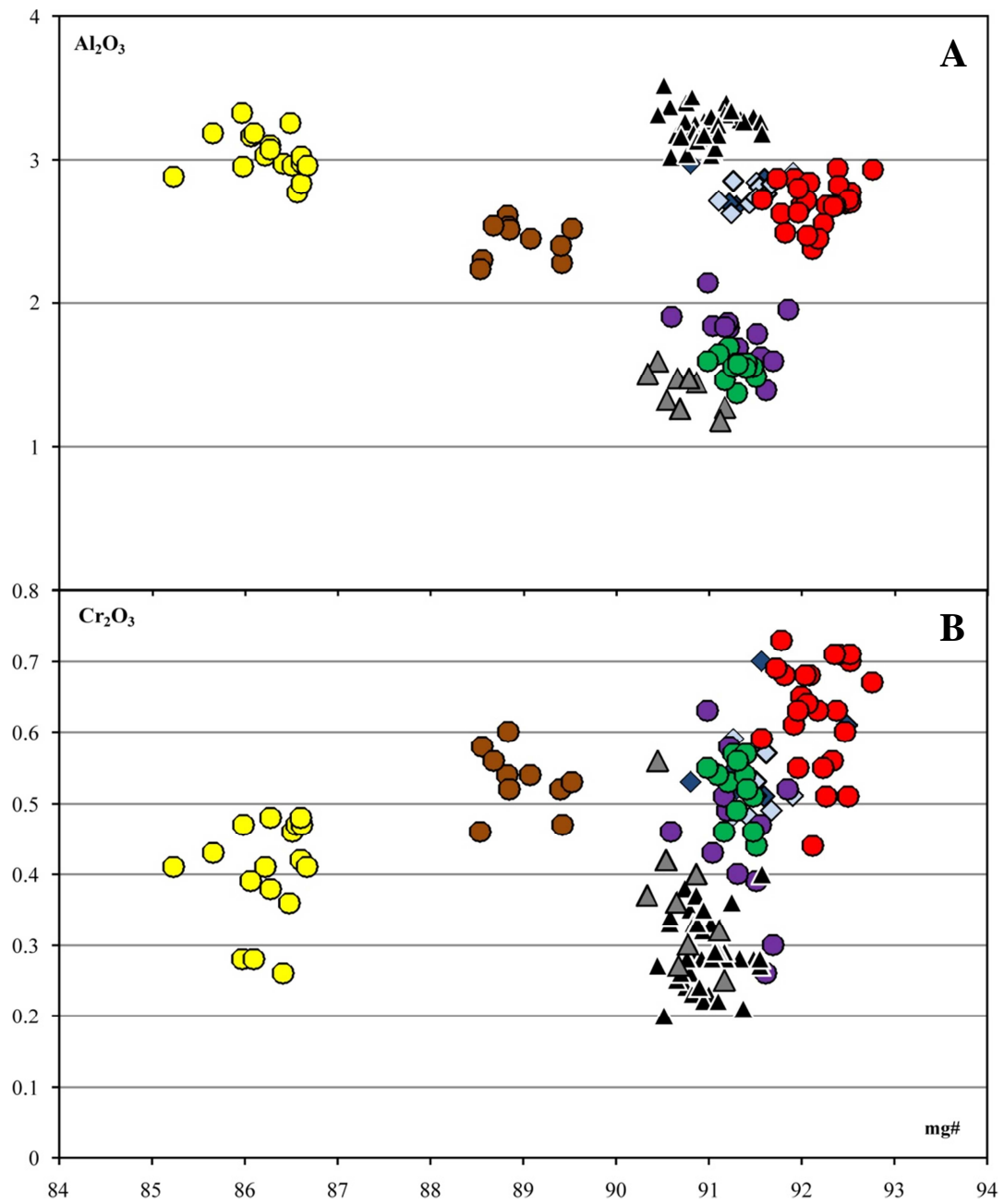
Figure 6.5: SiO₂ (A) and TiO₂ (B) vs mg#. Y axis of (B) is in logarithmic scale.

6.1.3 Orthopyroxene

As described above (Chapter 5), orthopyroxenes have been divided in three groups on the basis of their textural position and optical features. However no difference between opx1 and opx2 have been found in terms of major element composition, while opx arranged in vein (opx3, sample MGP2a) is always quite well discriminated.

Orthopyroxenes (**Appendix 3** and **Figure 6.6**) from lherzolites have mg# ranging from 90.8 to 92.49 with an Al₂O₃ content comprised in the range 2.62-2.97 wt%. They also show high and quite variable Cr₂O₃, SiO₂ and CaO contents, with the first varying from 0.48 to 0.7 wt%, the second from 55.33 to 56.4 wt% and the last from 0.84 to 0.99 wt%. Orthopyroxenes of harzburgites are characterized by a wide mg# range, from 85.24 to 92.76. Two samples (MGP3b and MGP1c) have mg# (90.59-91.56) comparable to those of lherzolites, with lower Al₂O₃ (1.37-2.14 wt%), slightly lower Cr₂O₃ (0.26 to 0.63 wt%), similar CaO (0.82 and 0.97 wt% (with one sample having 0.72 wt%)) and higher SiO₂ contents (55.84-57.15 wt%). Opx from the other two samples (MGP1b and MGP1g) have Al₂O₃ (2.3-3.32 wt%) contents comparable (or slightly higher) to those of lherzolites but lower mg#, ranging from 85.24 to 89.53. They are also marked by similar CaO contents (0.79-0.98 wt%) but lower SiO₂ (54.1-55.91 wt%) and Cr₂O₃ (0.26-0.6 wt%) contents. Finally orthopyroxenes from sample MGP4b are characterized by a very high mg# (91.6-92.76), and by Al₂O₃, SiO₂ and CaO comparable to those of lherzolites. In fact Al₂O₃ varies from 2.38 to 2.94 wt%, SiO₂ from 55.76 to 57.23 wt% and CaO from 0.85 to 1 wt%. Cr₂O₃ content is slightly higher, ranging from 0.44 to 0.73 wt%. As it can be appreciated from the proposed diagrams, the opx3 (those arranged in vein in the dunitic sample MGP2a) are always distinguished from all the others. They have a mg# analogous to those of opx from lherzolites and harzburgites MGP1c and MGP3b, comprised between 90.45 and 91.49, but they have (at comparable mg#) higher Al₂O₃ content (3.02-3.52 wt%), and lower CaO (0.76-0.89 wt%), SiO₂ (54-55.47 wt%) and Cr₂O₃ (0.2-0.4 wt%) contents. Opx1 from the other dunitic sample (MGP1h) have comparable Cr₂O₃ (comprised in the range 0.25-0.42 wt% except one analyses up to 0.56 wt%) and CaO (0.8-0.96 wt%) contents to those of opx3 of sample MGP2a, but they show much higher SiO₂ (57.29-57.88 wt%) and lower Al₂O₃ (1.18-1.59 wt%) contents.

6. Geochemistry of the mineral phases



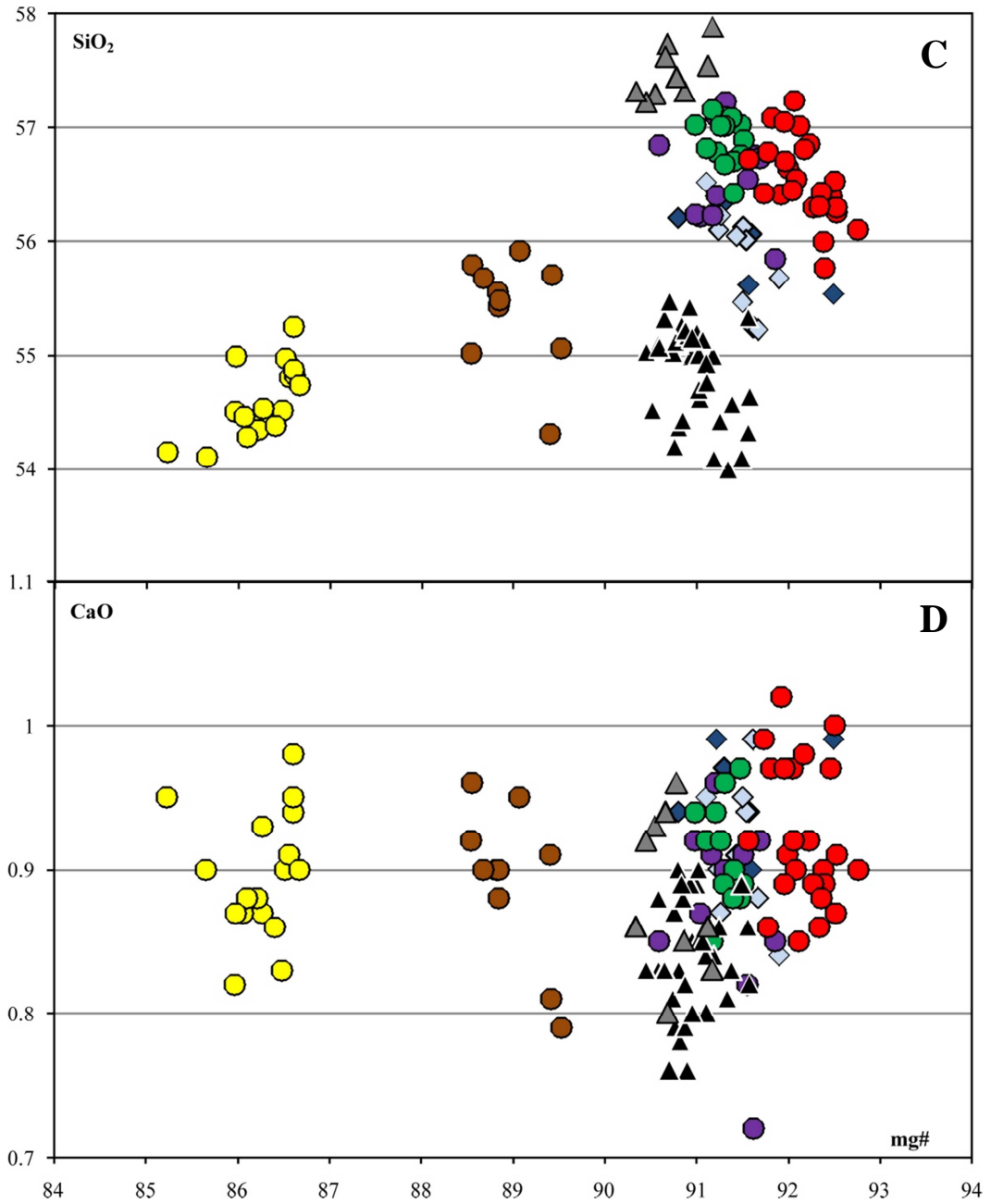


Figure 6.6: Al₂O₃ (A), Cr₂O₃ (B), SiO₂ (C), CaO (D) vs mg# for orthopyroxenes.

6.1.4 Spinel

As for the clinopyroxenes, spinels (**Appendix 4**) have been further classified according to their textural position in “Sp_{cpx}” and “Sp”: the former are those occurring close to a cpx, while the latter is not related to any pyroxene. The legend of the following diagrams showing the composition of the spinel is the same than that of **Figure 6.1**.

In **Figure 6.7** are plotted the data according to the spinel textural positions. It is possible to highlight the presence of three groups. One is composed of the Sp_{cpx} that have a large range of mg# (61.19-77.18) and low cr# (37.06-50.97), indicating that these spinels have a higher Al₂O₃ content with respect to Cr₂O₃ (Group I). All the other spinels (those not related to the cpx) fall in the second group (Group II), at higher cr# (49.21-60.60) and lower mg# (61.95-67.36) comparable only with that of few Sp_{cpx}. The third group (Group III) is composed of few spinels of both Sp and Sp_{cpx}, at very low cr# (17.48-26.50) and mg# (54.96-64.86).

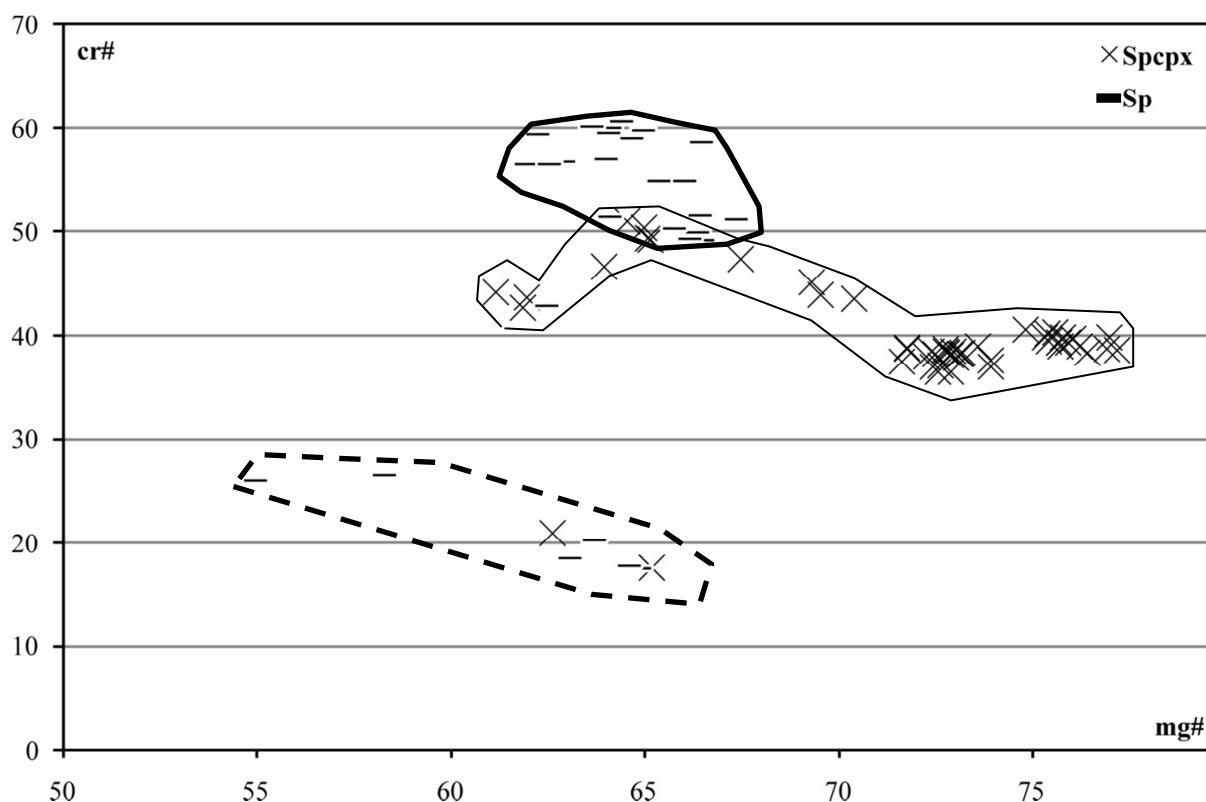
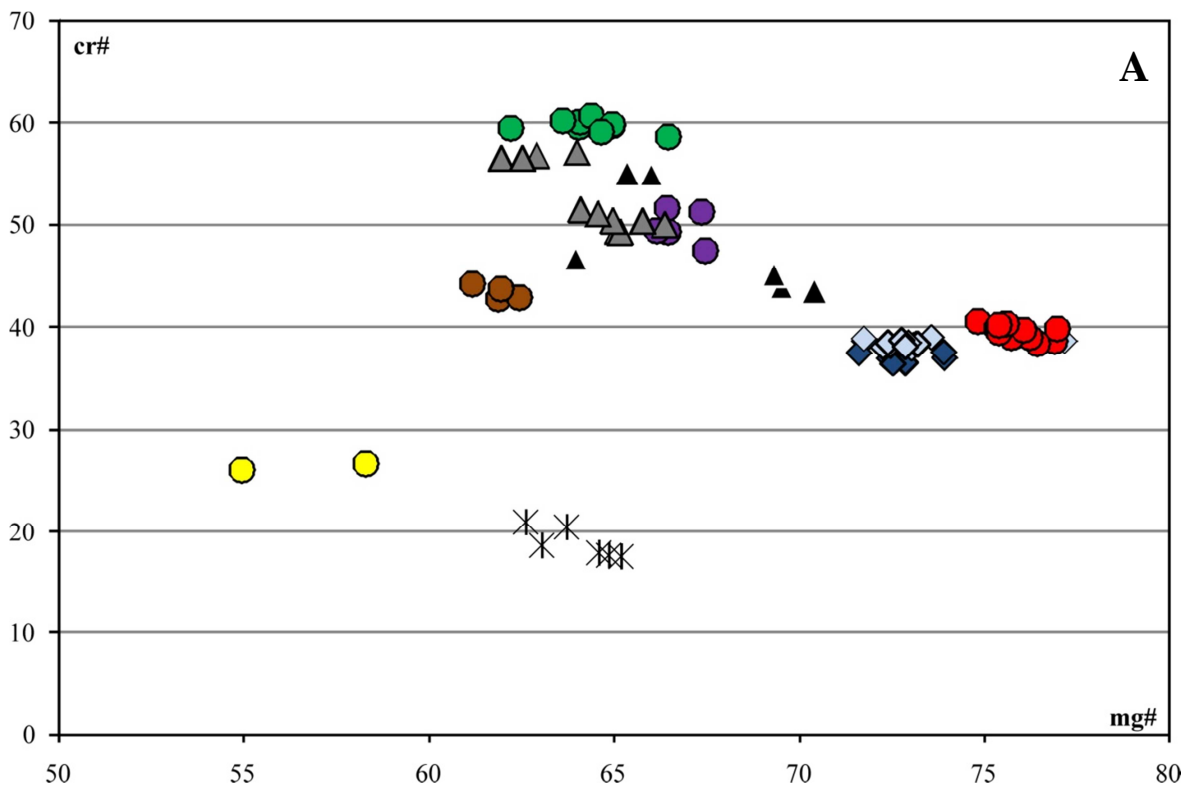


Figure 6.7: cr# vs. mg# for spinels. The two symbols indicate their different textural position. The thin black line indicates Group I, the bold black line Group II and the dashed bold black line Group III.

6. Geochemistry of the mineral phases

Also if we take into account the lithotype, in **Figure 6.8 A and B** it is possible to observe that spinel from lherzolites have mg# and cr# ranging from 72.28 to 73.13, and from 37.06 to 38.15 respectively, with only one sample falling outside these ranges (mg#=77.18 and cr#=38.53). Those belonging to harzburgites have quite different geochemical composition, with one sample (MGP4b) having the highest mg# (74.83-76.91) and cr# comparable to that of lherzolites; three samples (MGP1b, MGP1c and MGP3b) characterized by higher cr# with respect to MGP4b and lherzolites (42.63-59.97) and lower mg# (61.19-67.48), and two spinels of sample MGP1g with very low mg# and cr#. Spinel of dunites fall in the field defined by the three harzburgites MGP1b, MGP1c and MGP3b, with mg# ranging from 61.95 to 66.36 and cr# from 46.64 to 57.05. Three Sp_{cpx} from dunite MGP1h plot outside this group, having slightly higher mg# (69.55-70.42) and lower cr# (43.46-43.89). Finally spinels of the wehrlite are the most aluminiferous (cr# 17.48-20.82) and have mg# ranging from 62.63 up to 64.86.



6. Geochemistry of the mineral phases

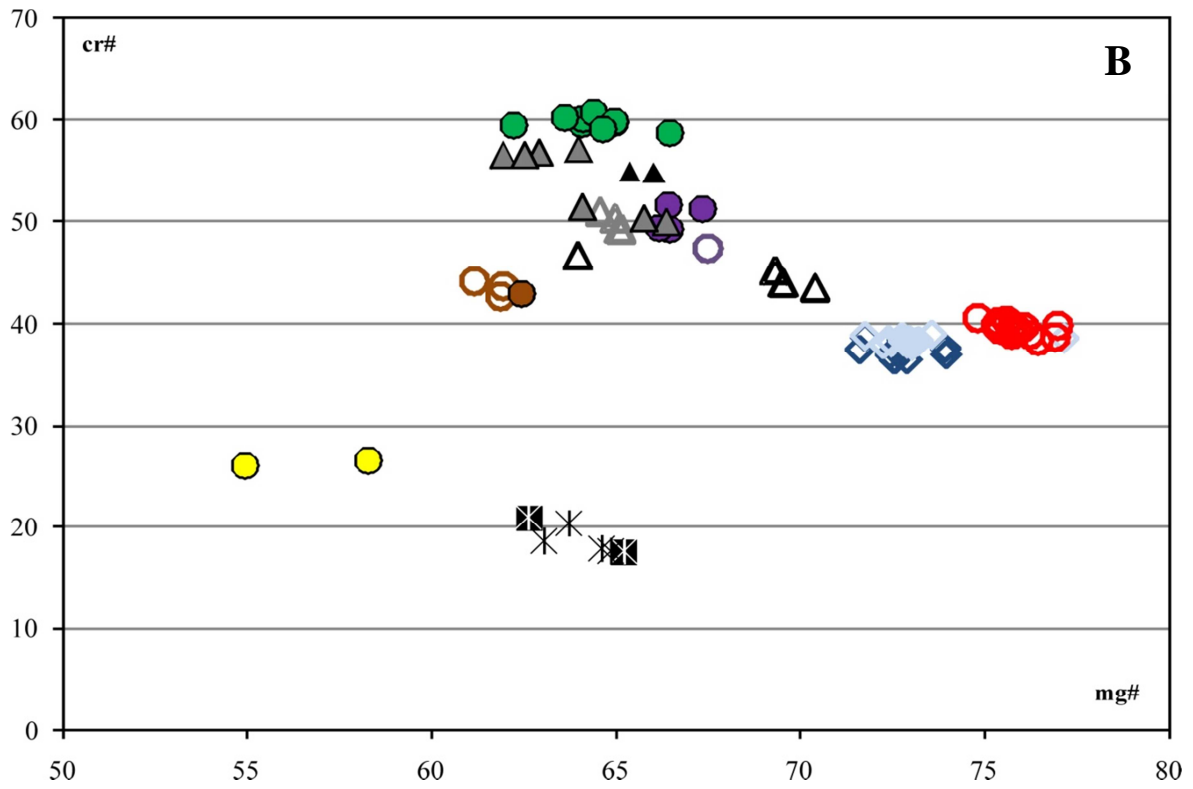


Figure 6.8: cr# vs. mg# for spinels. In (A) spinels are subdivided only for lithotype, while in (B) both for lithotype and textural position.

6.2 Trace element compositions

6.2.1 Clinopyroxene

Trace element compositions of clinopyroxenes are reported in **Appendix 5**. All the patterns do not show any correlation neither with the textural position (**Figure 6.9**) nor the lithotype. Thus cpx1 and cpx2 are practically indistinguishable solely on the base of trace element composition. Chondrite-normalized trace element and REE (Rare Earth Elements) compositions for each sample are proposed in **Figure 6.10** and **6.11**. Symbols representing the samples are shown in **Figure 6.1 B**.

Cpx from lherzolites are characterized by a strong positive Th anomaly, a strong negative Nb anomaly, and negative Zr and Ti anomalies. Most of them are LREE (Light REE) enriched with $(La/Yb)_N$ ranging from 2.09 to 5.57. Few grains are marked by a lower $(La/Yb)_N$ ratio comprised between 1.55 and 1.96, corresponding to an increase of the HREE (Heavy REE) content. Clinopyroxenes from harzburgites show similar positive Th and negative Nb anomalies to those highlighted for the lherzolites, but they are also characterized by more pronounced negative Ti anomaly and by a very variable, but always negative, Zr anomaly. In fact, while sample MGP1c (and few grains of MGP4b) show a slightly negative Zr anomaly, cpx from MGP1b, MGP3b and MGP4b are marked by a strong negative Zr anomaly. The REE patterns resemble those of the lherzolites, with an enrichment in LREE, most of the cpx having a $(La/Yb)_N$ comprised between 2.09 and 7.28. Some of them are characterized by a contemporaneous HREE enrichment, leading to a decrease of the $(La/Yb)_N$ ratio (0.87-1.68).

Only one clinopyroxene from the dunite MGP2a (the sample with the vein of orthopyroxene) has been analyzed. It shows a more fractionated incompatible trace element pattern, always characterized by the prominent positive Th and negative Nb anomalies. It has also marked Zr and Ti negative anomalies, and a steep REE pattern, with a $(La/Yb)_N$ equal to 4.11.

As described for lherzolites, harzburgites and dunite, clinopyroxenes of the wehrlite are also characterized by the negative Nb and positive Th anomalies, even if the last one is less marked than that of the other cpx because of the lower Th content. Indeed while in the Lh it varies from 0.235 up to 14.7 ppm, in the Hz from 0.706 to 14.2 ppm, and in the Du it is

6. Geochemistry of the mineral phases

equal to 2 ppm, Th content of the cpx of the wehrlite ranges from 0.12 and 0.41 ppm. Also the two negative Zr and Ti anomalies are present in the wehrlitic clinopyroxenes, the former being generally marked and the second varying from slightly to strong. Based on REE patterns two different kind of cpx can be highlighted, one with a convex upward pattern and a $(La/Yb)_N$ ranging from 0.79 and 1.04 and another that show LREE enrichment with a $(La/Yb)_N$ varying from 2.87 up to 5.26. These two compositions, however, are not related to different textural position.

Finally in **Figure 6.12** two binary diagrams are proposed. In this case the trace elements are correlated with the Al_2O_3 content of the samples (as index of depletion). As it can be observed the $(La/Yb)_N$ (**Figure 6.12 A**) and the Sr_N content (**Figure 6.12 B**) increase with the decreasing of the Al_2O_3 . This behaviour rules out a relation of the composition of the samples to a depletion evolution, because in this case we should observe an inverse trend, i.e. a decreasing of the LREE with the decreasing of the Al_2O_3 content.

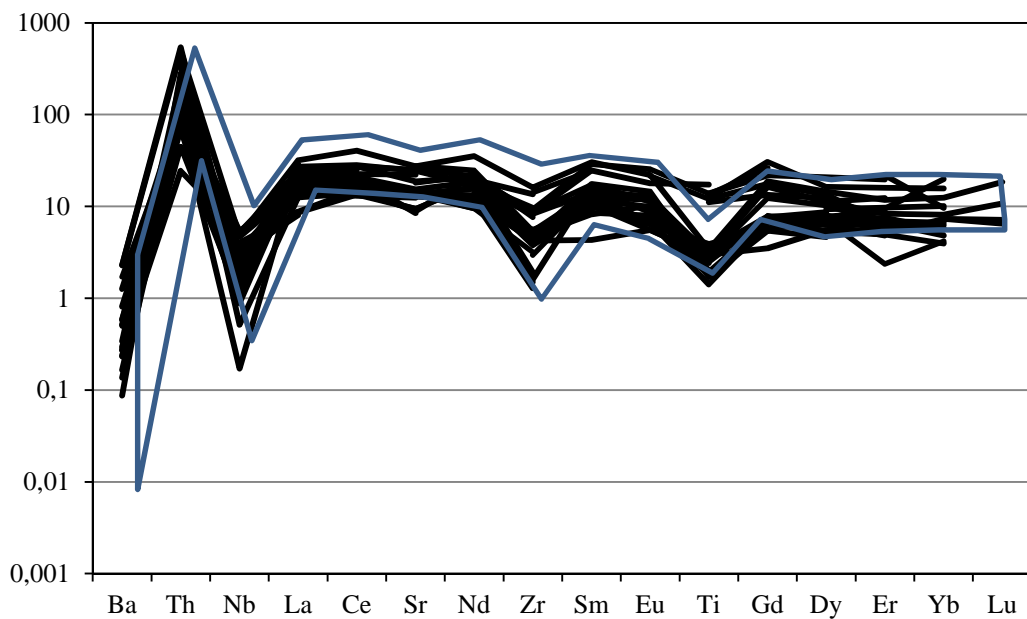


Figure 6.9: Chondrite-normalized trace element compositions of clinopyroxenes. The blue field encompasses the patterns of cpx2, while cpx1 are all represented by black lines.

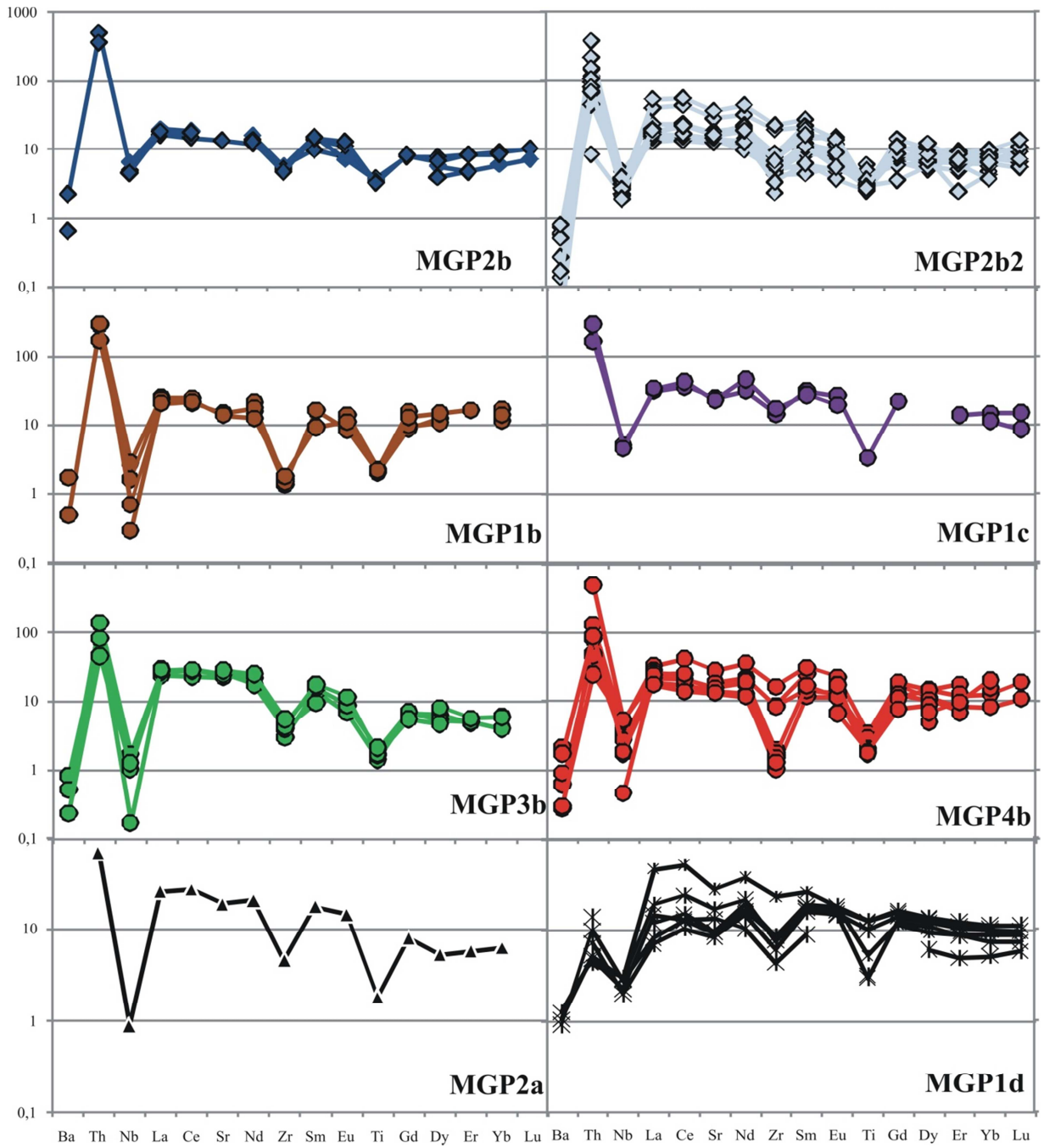


Figure 610: Chondrite-normalized trace element compositions of clinopyroxenes from Estancia Sol de Mayo.

6. Geochemistry of the mineral phases

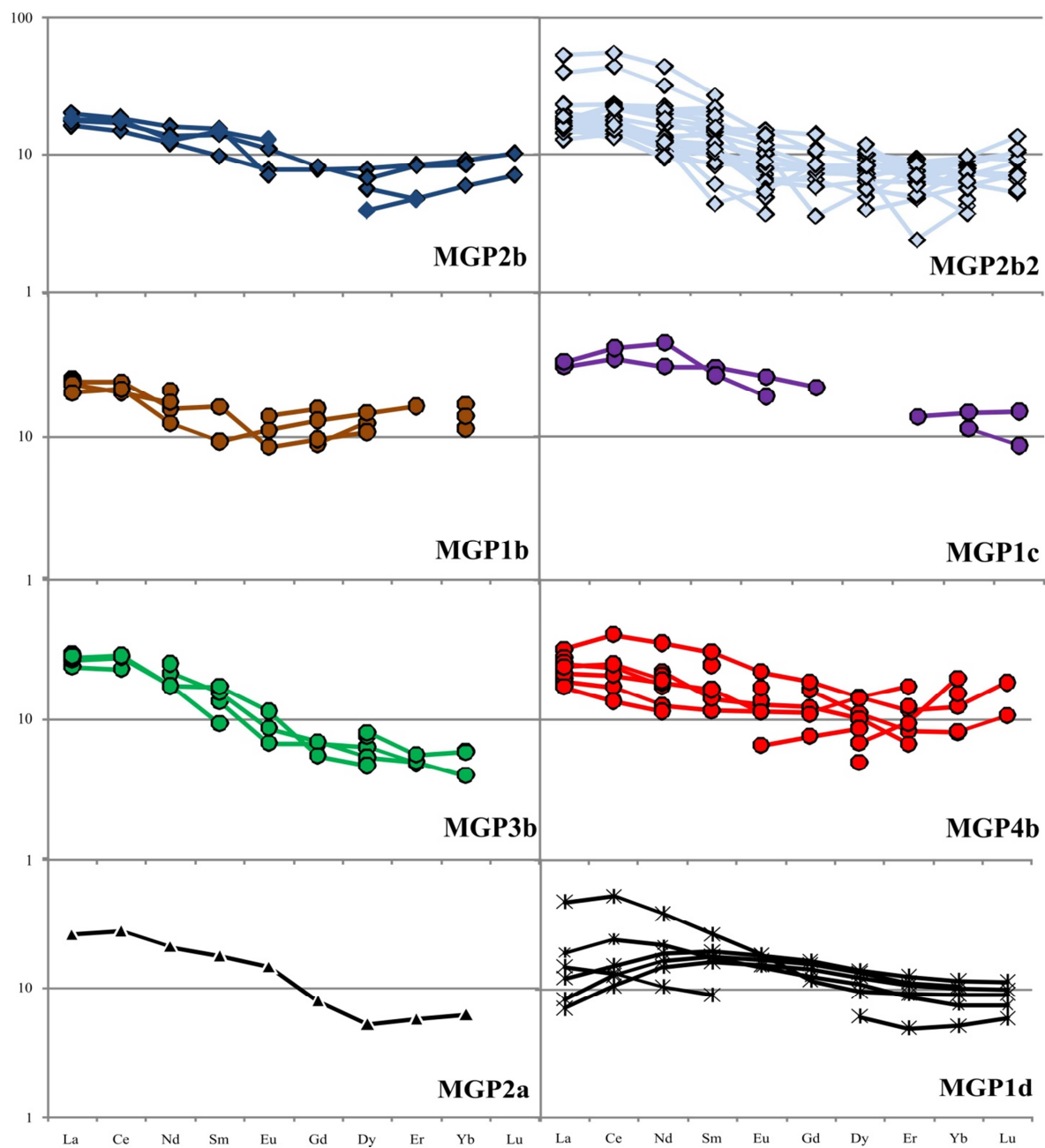
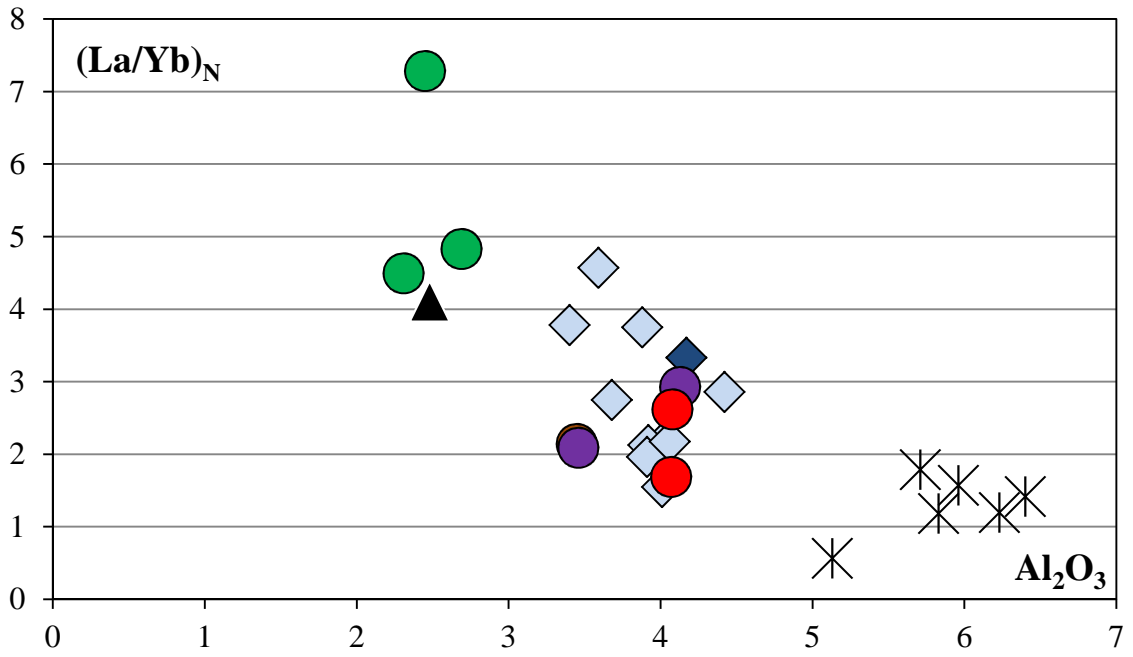


Figure 6.11: Chondrite-normalized REE patterns of clinopyroxenes from Estancia Sol de Mayo.

A



B

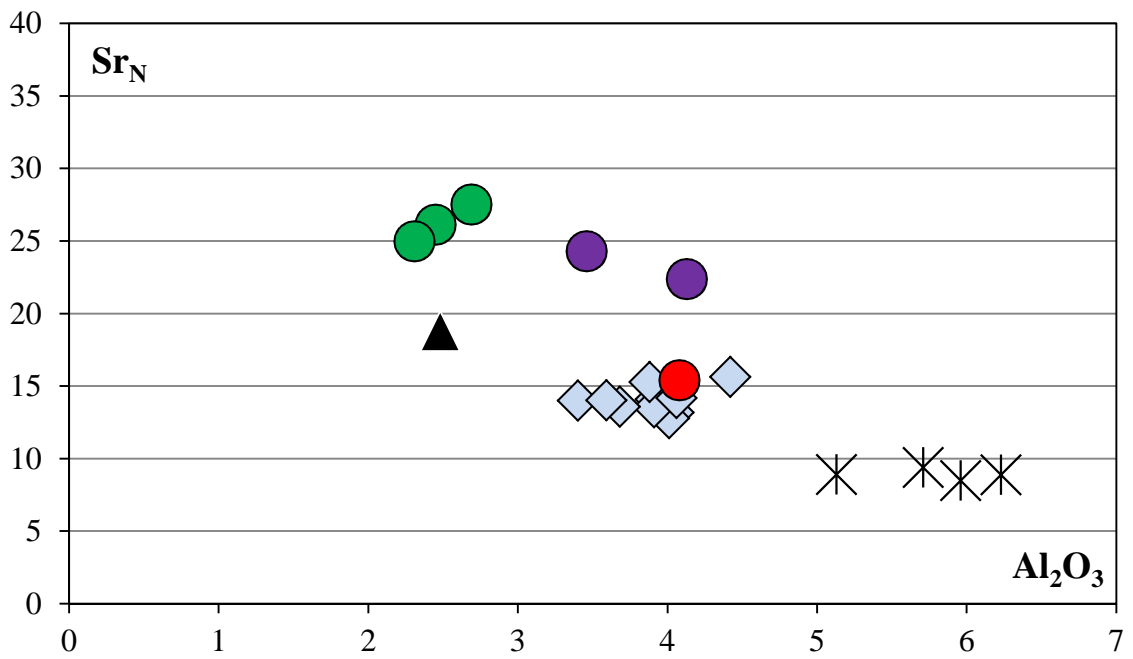


Figure 6.12: $(La/Yb)_N$ (A) and Sr_N (B) vs. Al_2O_3 .

6.2.2 Orthopyroxene

Trace elements compositions of orthopyroxenes are shown in **Appendix 6**, while the chondrite-normalized trace elements and REE patterns are shown in **Figure 6.13** and **Figure 6.14** respectively. Orthopyroxenes from the two lherzolites are characterized by a prominent positive Th and negative Sr, Zr and Ti anomalies. MGP2b and MGP2b2 show flat MREE (Medium REE) and HREE at about 5X chondritic, and depleted LREE with a negative Ce anomaly. The $(La/Yb)_N$ ratio varies between 0.06 and 0.3.

Orthopyroxenes from harzburgites MGP1b and MGP1c display the same prominent positive Th and negative Sr, Zr and Ti anomalies similar to those from the lherzolites. Also their REE patterns show flat MREE and HREE slopes with a drastic LREE depletion with a $(La/Yb)_N$ ratio ranging from 0.14 to 0.18. The other three harzburgites (MGP1g, MGP3b and MGP4b) are characterized by the strong positive Th and negative Sr anomalies but slightly negative Zr and Ti anomalies. The REE patterns show flat HREE and depleted LREE and MREE, with $(La/Yb)_N$ ranging from 0.16 and 0.74.

Finally orthopyroxenes analysed in the two dunites MGP1h and MGP2a show always marked positive Th and negative Sr anomalies, but while the former has slightly negative Zr and Ti anomalies, the latter (opx3 in vein) display a positive Zr and a prominent negative Ti anomalies. The REE patterns are similar, with flat MREE and HREE and a depletion in LREE evidenced also in this case by the low $(La/Yb)_N$ ratio between 0.21 and 0.36.

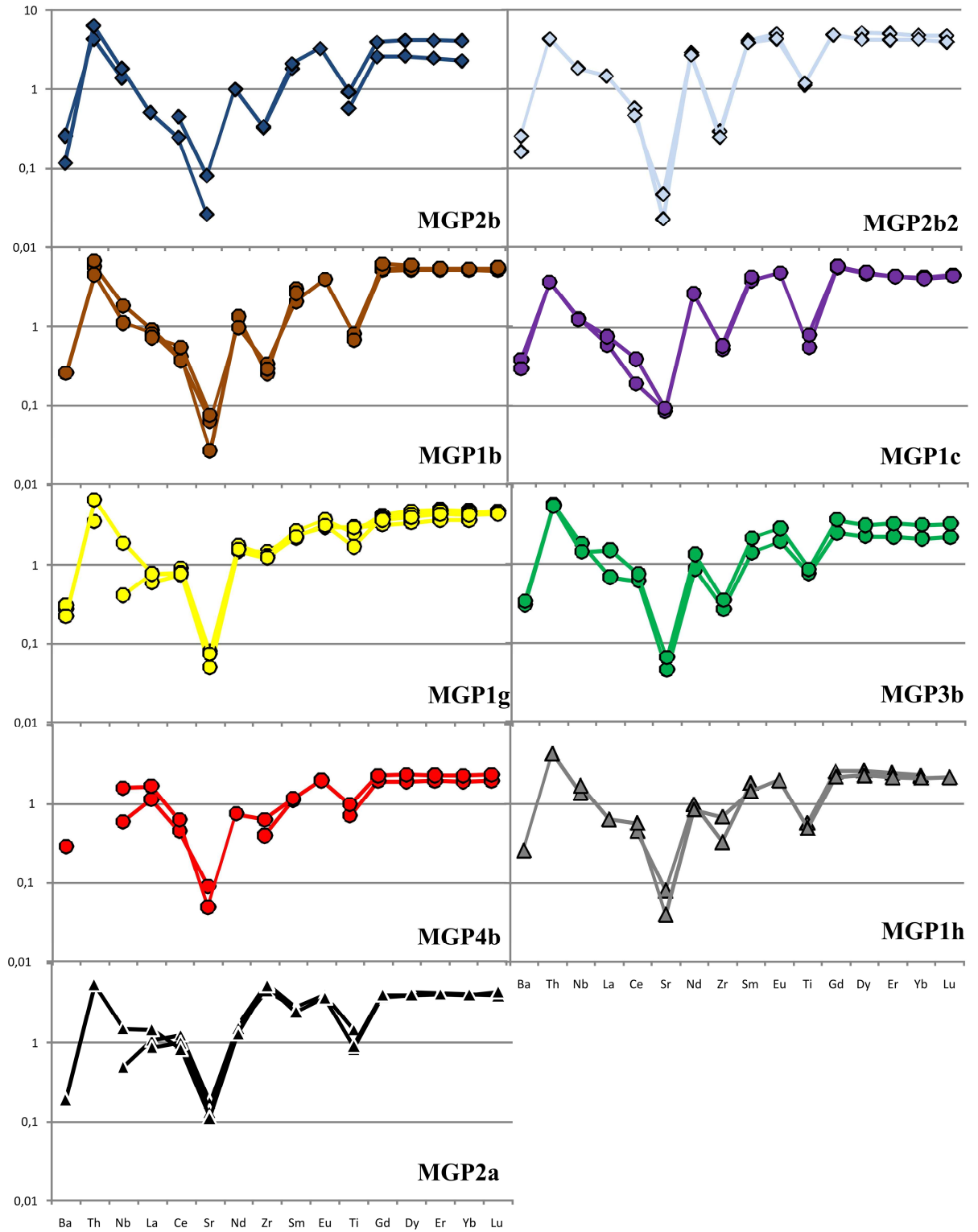


Figure 6.13: Chondrite-normalized trace element patterns of orthopyroxenes from Estancia Sol de Mayo.

6. Geochemistry of the mineral phases

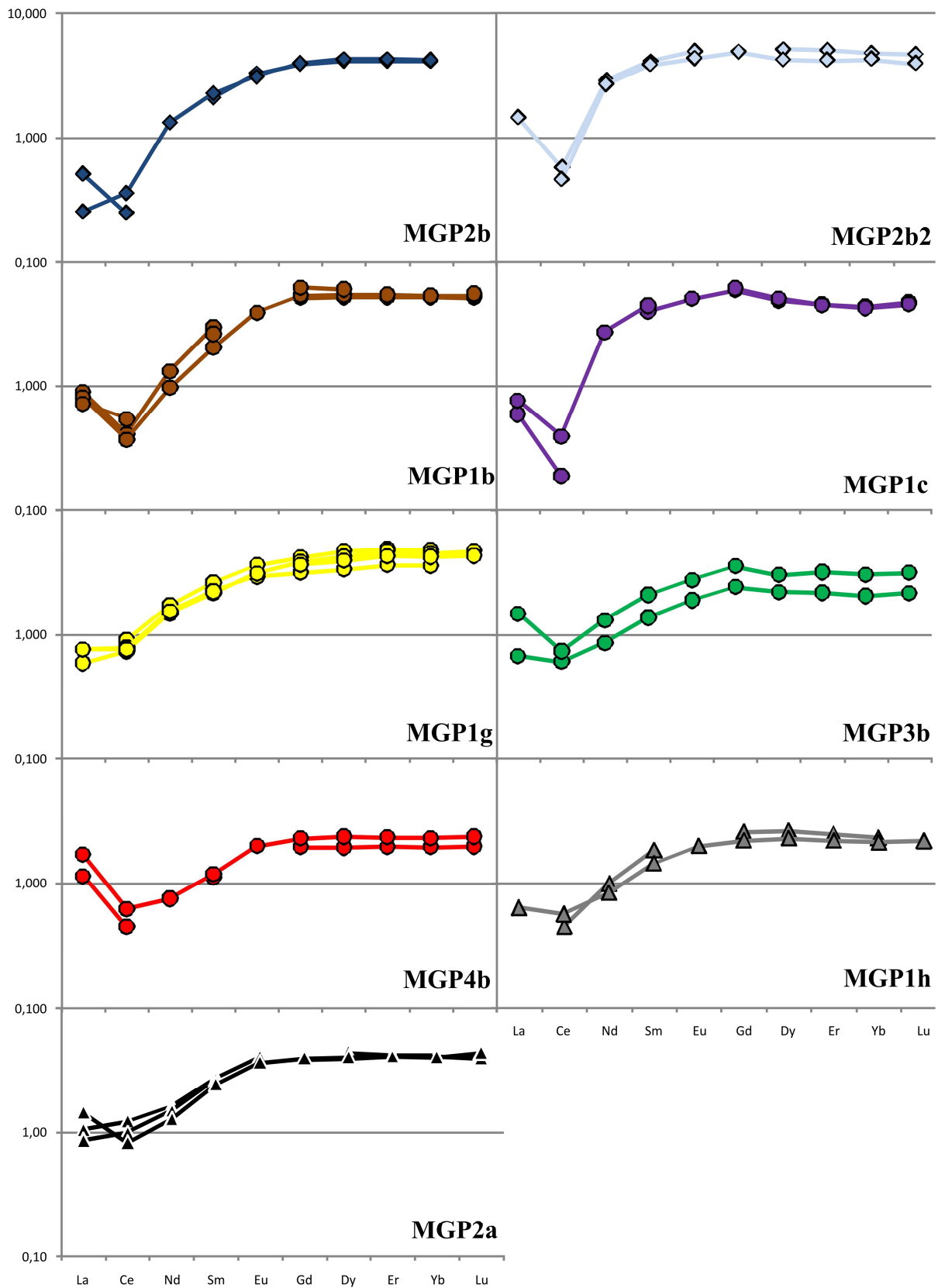


Figure 6.14: Chondrite-normalized REE patterns of clinopyroxenes from Estancia Sol de Mayo.

On the basis of this preliminary description of the incompatible trace element concentrations of orthopyroxenes from Estancia Sol de Mayo it is quite clear that on the contrary of what observed for clinopyroxenes, two different groups of pattern could be distinguished. This is highlighted by the difference in the negative Zr (that become positive in the case of the orthopyroxenes from the vein of sample MGP2a) and Ti anomalies that is possible to observe and by the different REE patterns. Hence **Figure 6.15** allows to better distinguish the different groups of orthopyroxenes. **Figure 6.15A** show Ti^* [$Ti_N/((Eu_N+Gd_N)/2)$] vs $(Ce/Yb)_N$. This diagram clearly distinguishes two groups of orthopyroxenes, one at low Ti^* (i.e. prominent Ti negative anomaly) and $(Ce/Yb)_N$ (the lherzolites MGP2b and MGP2b2 and the harzburgites MGP1b and MGP1c, **Group I**) and one at higher values of both $(Ce/Yb)_N$ and Ti^* (three harzburgites MGP1g, MGP3b and MGP4b, and the two dunites MGP1h and MGP2a, **Group II**). **Figure 6.15B** better constrains this subdivision by taking into account the Zr anomaly (expressed in the diagram as Zr^* , [$Zr_N/((Sm_N+Nd_N)/2)$]) that, as described previously, can be slightly to prominent negative, but also positive in one case. Once again it is possible to observe the two groups, but the orthopyroxenes in vein of sample MGP2a clearly plot outside **Group II** due to their positive Zr anomaly, forming **Group III**.

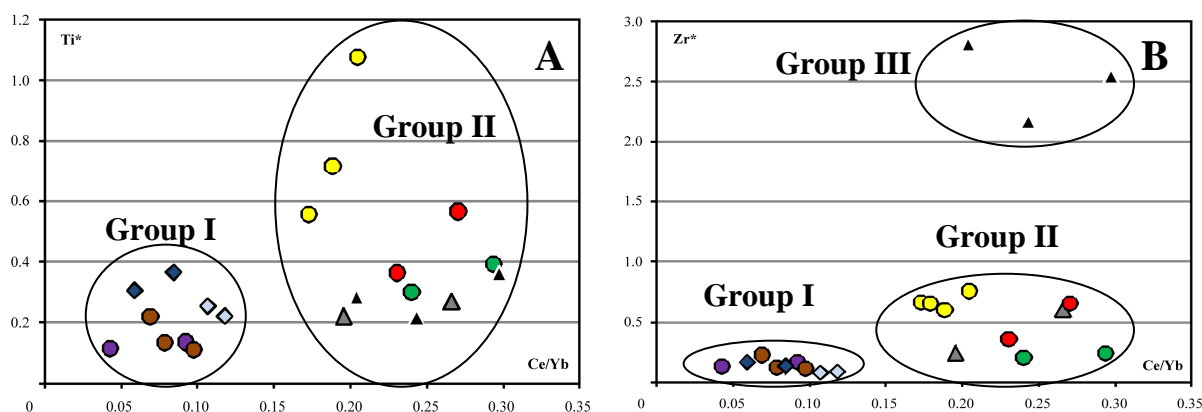


Figure 6.15: Ti^* (A) and Zr^* (B) vs. $(Ce/Yb)_N$ for orthopyroxenes. Zr^* is calculated as $Zr_N/[(Nd_N+Sm_N)/2]$, while Ti^* is calculated as $Ti_N/[(Eu_N+Gd_N)/2]$.

6. Geochemistry of the mineral phases

The complete trace element patterns of the three groups are shown in **Figure 6.16**.

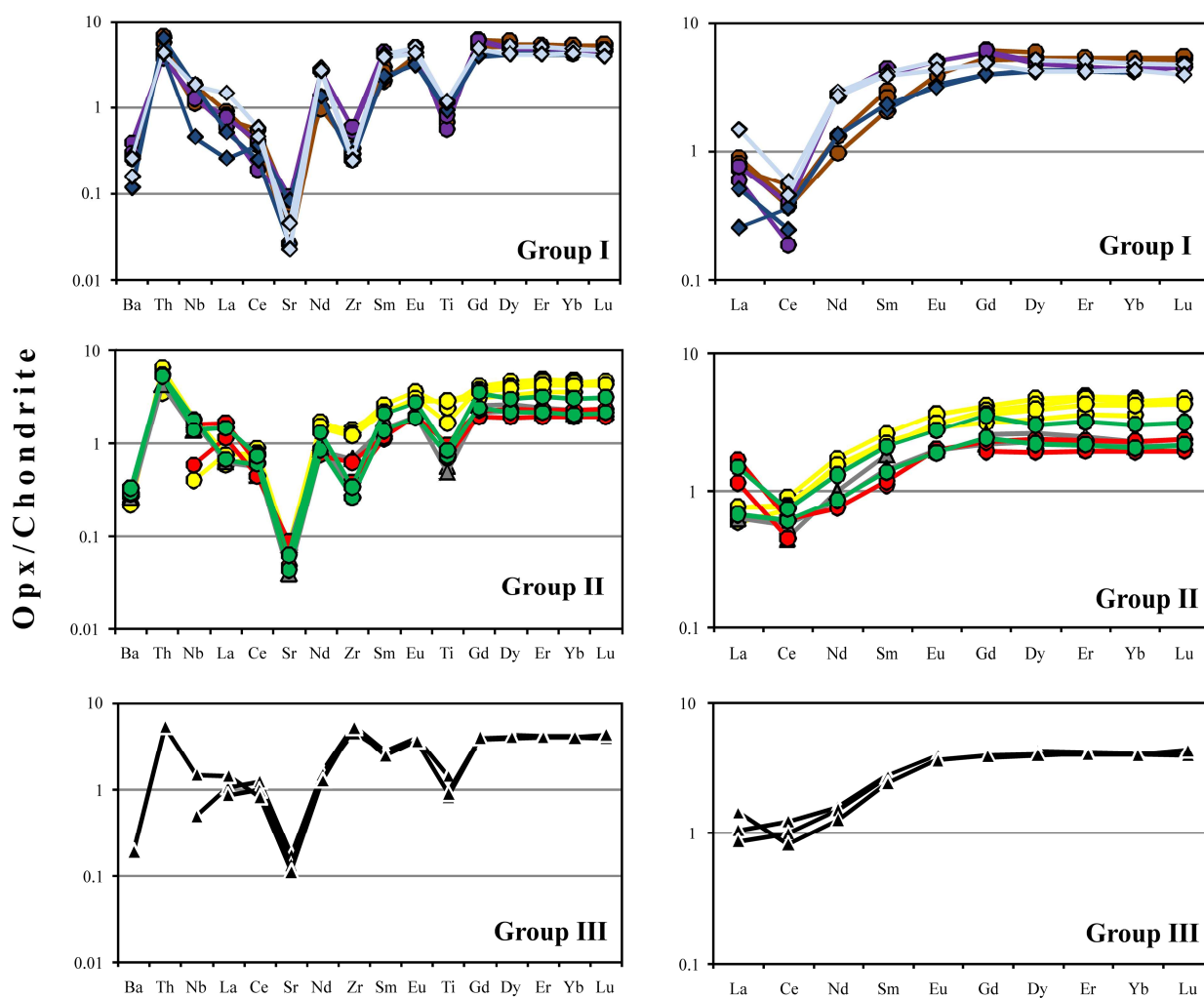


Figure 6.16: Trace element compositions (A, C and E) and REE (B, D, and F) of the three groups of orthopyroxenes.

6.3 P-T estimates

Temperature and pressure estimates (**Appendix 7**) of the spinel-bearing ESM peridotites have been calculated using the two pyroxenes geothermometer of *Brey and Köhler (1990)* and the geobarometer of *Köhler and Brey (1991)*. The former is based on the Fe exchange between the two pyroxenes for a fixed pressure of 1.5 GPa while the latter uses the Ca exchange between olivine and clinopyroxene. Unfortunately the measurements of the CaO content of the olivines have been performed only by Electron Microprobe, hence they are not so precise to guarantee reasonable and useful results. For this reason some care is needed looking at the diagram of **Figure 6.17** particularly regarding those pressures exceeding 2 GPa. Notwithstanding the diagram indicate that most of the samples fall in the spinel stability field, with the temperature ranging from 1011 to 1044 °C and a pressure comprised between 1.2 and 2 GPa. A second group of samples fall in the plagioclase stability field and show a narrower range of pressure (0.15-0.54 GPa) and a wider range of temperature (943-1037 °C). Finally three P-T estimates fall in the garnet field (with temperature and pressure comprised between 1026 and 1055°C and between 2.4 and 3.7 GPa respectively).

Because of the poor constrained equilibration pressures for Patagonian mantle xenoliths available in literature, only the T estimates of this suite of mantle nodules have been compared to those studied by *Dantas (2007)*. As shown by the histogram proposed in **Figure 6.18** the T obtained for the ESM mantle xenoliths fit well with those estimated for other localities from central Patagonia that show two picks, one at 1020-1040 °C (the majority of the samples) and another at 820-840 °C. Also Pali Aike (southern Patagonia) show almost the same T of ESM, with a major pick at 980-1000 °C. On the other hand, the localities from northern Patagonia show a very wide range of T of equilibration of the mantle nodules, varying from 780 up to 1200 °C

6. Geochemistry of the mineral phases

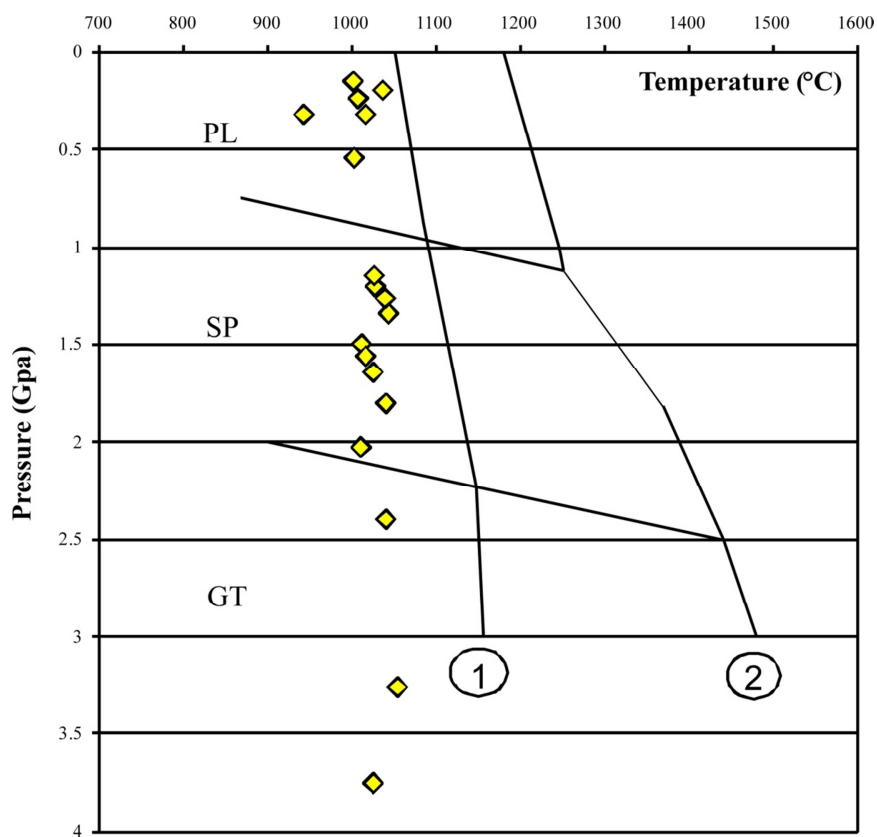


Figura 6.17: P-T estimates of Estancia Sol de Mayo peridotites. PL, SP and GT stand for plagioclase, spinel and garnet respectively. 1 is the hydrous solidus, while 2 is the anhydrous solidus.

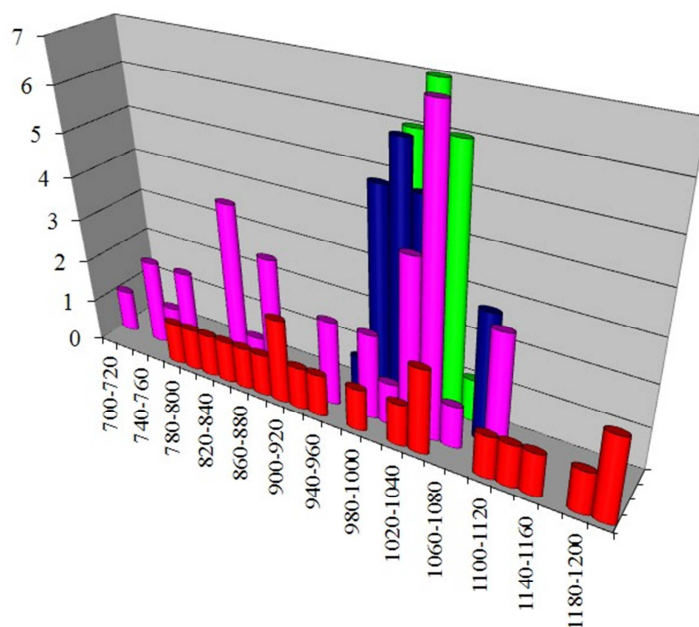


Figura 6.18: Histogram of the T estimates of Estancia Sol de Mayo peridotites (green cylinders) and of peridotites from northern (red cylinders), central (pink cylinders) and south (blue cylinders) Patagonia (Dantas, 2007).

6.4 Sr and Nd systematics

Separated clinopyroxenes from four samples from Estancia Sol de Mayo (two lherzolites and two harzburgites) have been analyzed by TIMS for the acquisition of the Sr and Nd isotopic ratios. The results are given in **Table 6.1**

	MGP1-A	MGP2-A	MGP2-B	MGP4-A
Rb (ppm)	-	-	-	-
Sr (ppm)	138	99	100	125
$^{87}\text{Sr}/^{86}\text{Sr}$	0.70386	0.70371	0.70374	0.70368
2σ	0.00001	0.00001	0.00001	0.00001
Nd (ppm)	9.11	4.92	5.81	11.2
Sm (ppm)	2.37	1.37	1.70	2.97
$^{147}\text{Sm}/^{144}\text{Nd}$	0.15662	0.16811	0.17595	0.16022
$^{143}\text{Nd}/^{144}\text{Nd}$	0.51276	0,51279	0,51279	0,51269
2σ	0,00001	0,00002	0,00001	0,00003

Table 6.1: Sr and Nd isotopic compositions of the four Estancia Sol de Mayo samples.

In the $^{143}\text{Nd}/^{144}\text{Nd}$ vs. $^{87}\text{Sr}/^{86}\text{Sr}$ diagrams proposed in **Figure 6.19 A** and **B** the analysed samples plot in the field of the mantle-derived basalts from the Southern Volcanic Zone (**A**), close to the HIMU field (**B**) described by *Zindler and Hart (1986)*. They have a quite high $^{87}\text{Sr}/^{86}\text{Sr}$ ratio ranging from 0.70368 up to 0.70386, and low $^{143}\text{Nd}/^{144}\text{Nd}$ (0.51269-0.51279).

Figure 6.20 A and **B** shows the variation of the two isotopic ratios related to the inverse of the concentration of Sr and Nd respectively. It is clear that the negative correlation existing between $^{87}\text{Sr}/^{86}\text{Sr}$ ratio with $1/\text{Sr}$ (i.e. a contemporaneous increasing of the isotopic ratio with the concentration of Sr) and the positive correlation between $^{143}\text{Nd}/^{144}\text{Nd}$ and $1/\text{Nd}$, are characterized by an increasing of the isotopic ratio correlated to a decreasing of Nd content.

Finally in **Figure 6.21** is shown the relationship between $^{143}\text{Nd}/^{144}\text{Nd}$ and $^{147}\text{Sm}/^{144}\text{Nd}$ ratios. The latter have been calculated as $0,1435 * ([\text{Sm}]/[\text{Nd}] * (3,69014 + ^{143}\text{Nd}/^{144}\text{Nd}))$. The

6. Geochemistry of the mineral phases

behaviour of the samples is the same already shown for **Figure 6.20 B**, i.e. a positive correlation between the two ratios, with an increasing of the $^{143}\text{Nd}/^{144}\text{Nd}$ related to an increasing of $^{147}\text{Sm}/^{144}\text{Nd}$ ratios with one sample (MGP4-A) that fall outside this trend.

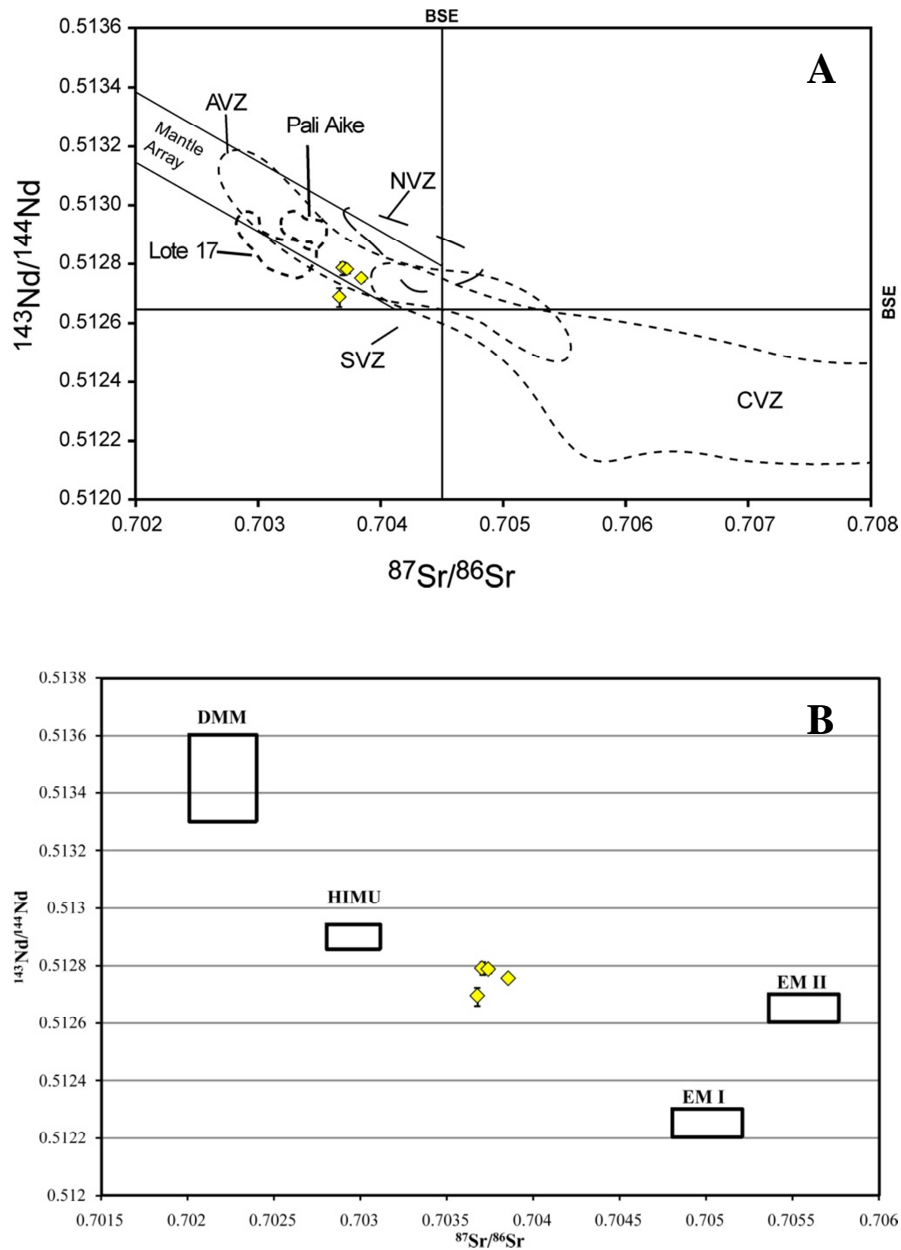


Figure 6.19: Sr–Nd isotopic composition of Estancia Sol de Mayo xenoliths (represented by the yellow diamonds). In (A) for comparison the fields of mantle derived basalt from volcanic zones from South America (NVZ, CVZ, SVZ from *Conceicao et al., 2005*) and Pali Aike (*Stern et al., 1999*) and Estancia Lote 17 (*Gorring and Kay, 2000*), while in (B) are plotted the fields of DMM, HIMU, EM I and EM II from *Zindler and Hart (1986)*.

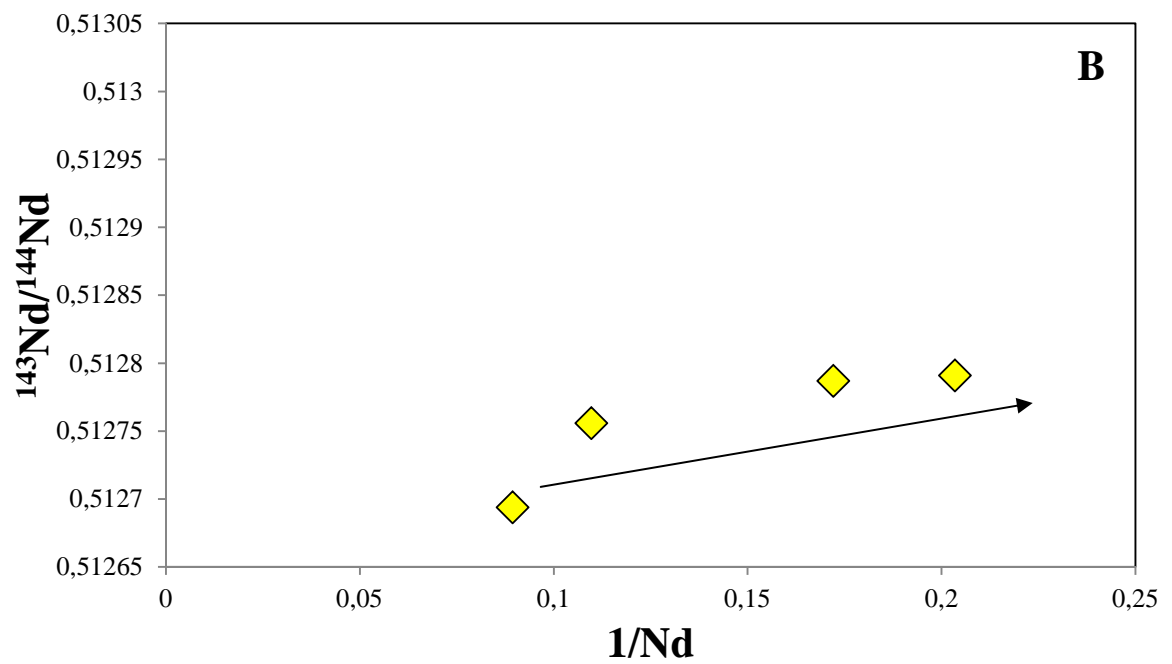
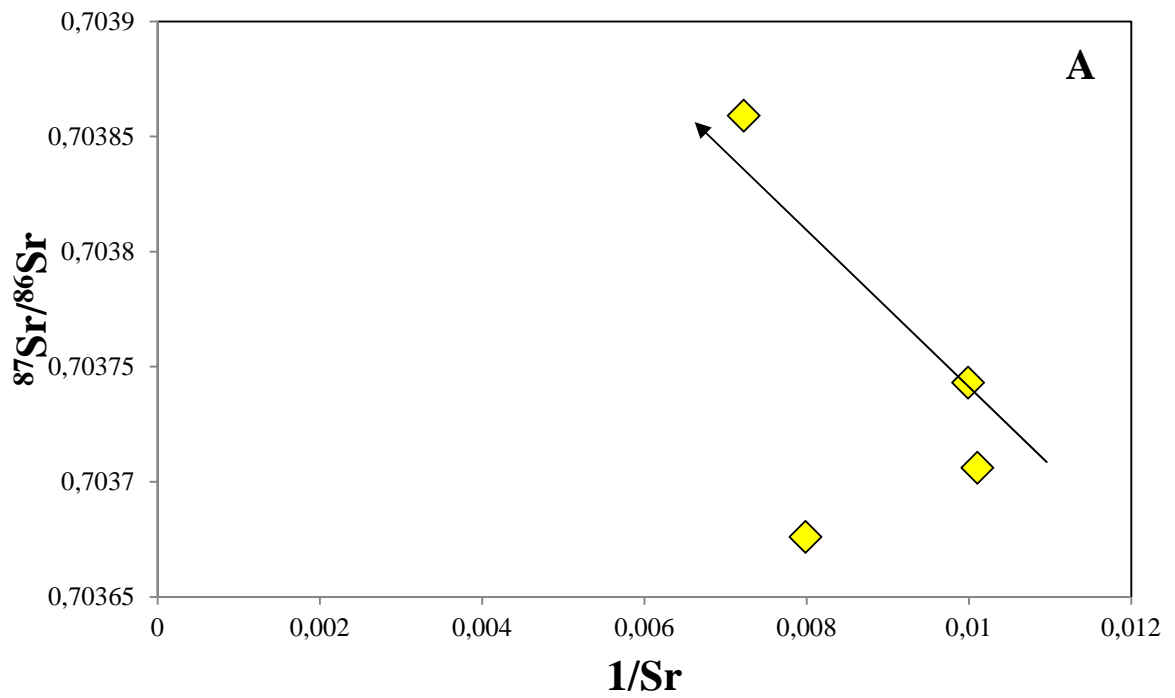


Figure 6.20: $^{87}\text{Sr}/^{86}\text{Sr}$ vs. $1/\text{Sr}$ (A) and $^{143}\text{Nd}/^{144}\text{Nd}$ vs. $1/\text{Nd}$ (B).

6. Geochemistry of the mineral phases

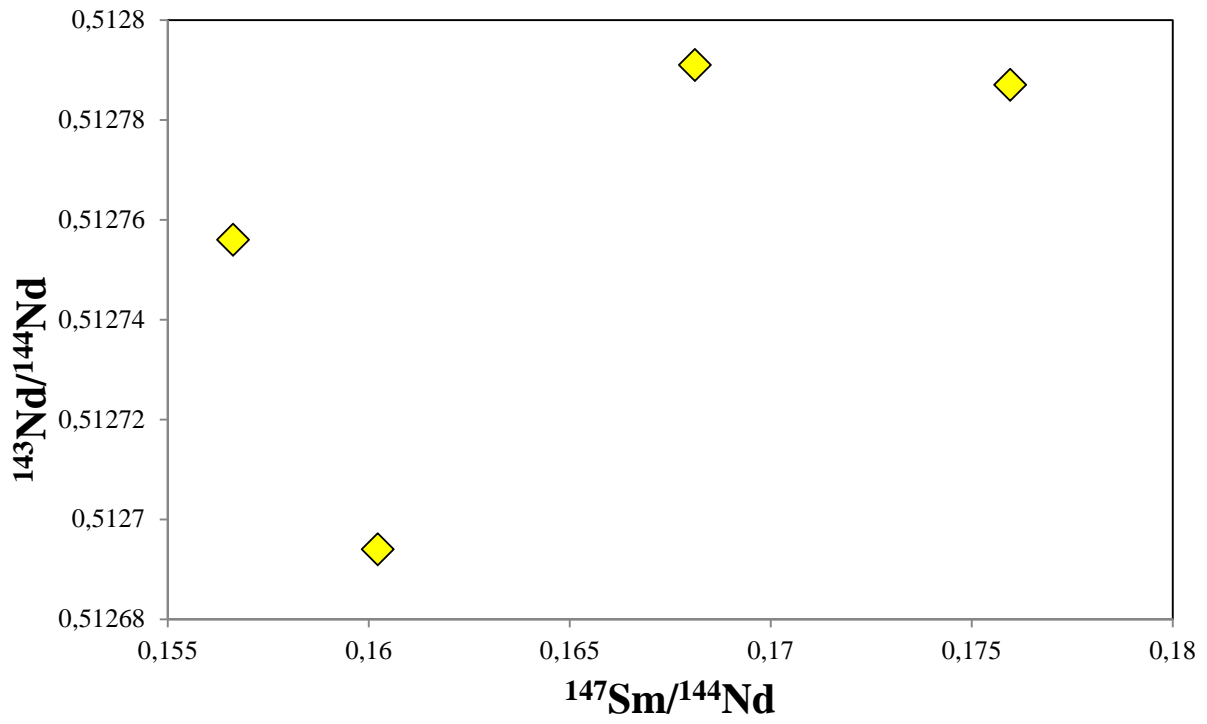


Figure 6.21: $^{143}\text{Nd}/^{144}\text{Nd}$ vs. $^{147}\text{Sm}/^{144}\text{Nd}$ for Estancia Sol de Mayo xenoliths.

7. Comparisons

The aim of this chapter is to compare major and trace elements contents of mineral phases of the xenoliths from Estancia Sol de Mayo, illustrated in **Chapters 6**, to other Patagonian localities studied mainly by *Dantas (2007)*. In her work six localities (**Table 7.1** and **Figure 7.1**) covering a length from North to South of about 1000 Km have been investigated (four from Northern Patagonia and two from Central Patagonia). To simplify the following discussion and to a better understanding of the proposed diagrams, the localities belonging to the same part of Patagonia will be represented by one symbol, full when referred to peridotites, and empty for the pyroxenites. For all the other symbols used refer to **Figure 6.1**.

Northern Patagonia				
Area	Meseta Somoncura		Meseta Canquel	
Locality	Cerro Aznare	Praguaniyeu	Cerro Rio Chubut	Cerro de los Chenques
Age of volcanism	~20-29 Ma	~20-29 Ma	~49-52 Ma	~20-25 Ma

Central Patagonia		
Area	Northeastern region	Meseta Central
Locality	Cerro Clark	Gobernador Gregores
Age of volcanism	~11-2 Ma	~3,4-3,6 Ma

Table 7.1: List of the localities compared with Estancia Sol de Mayo.

7. Comparisons

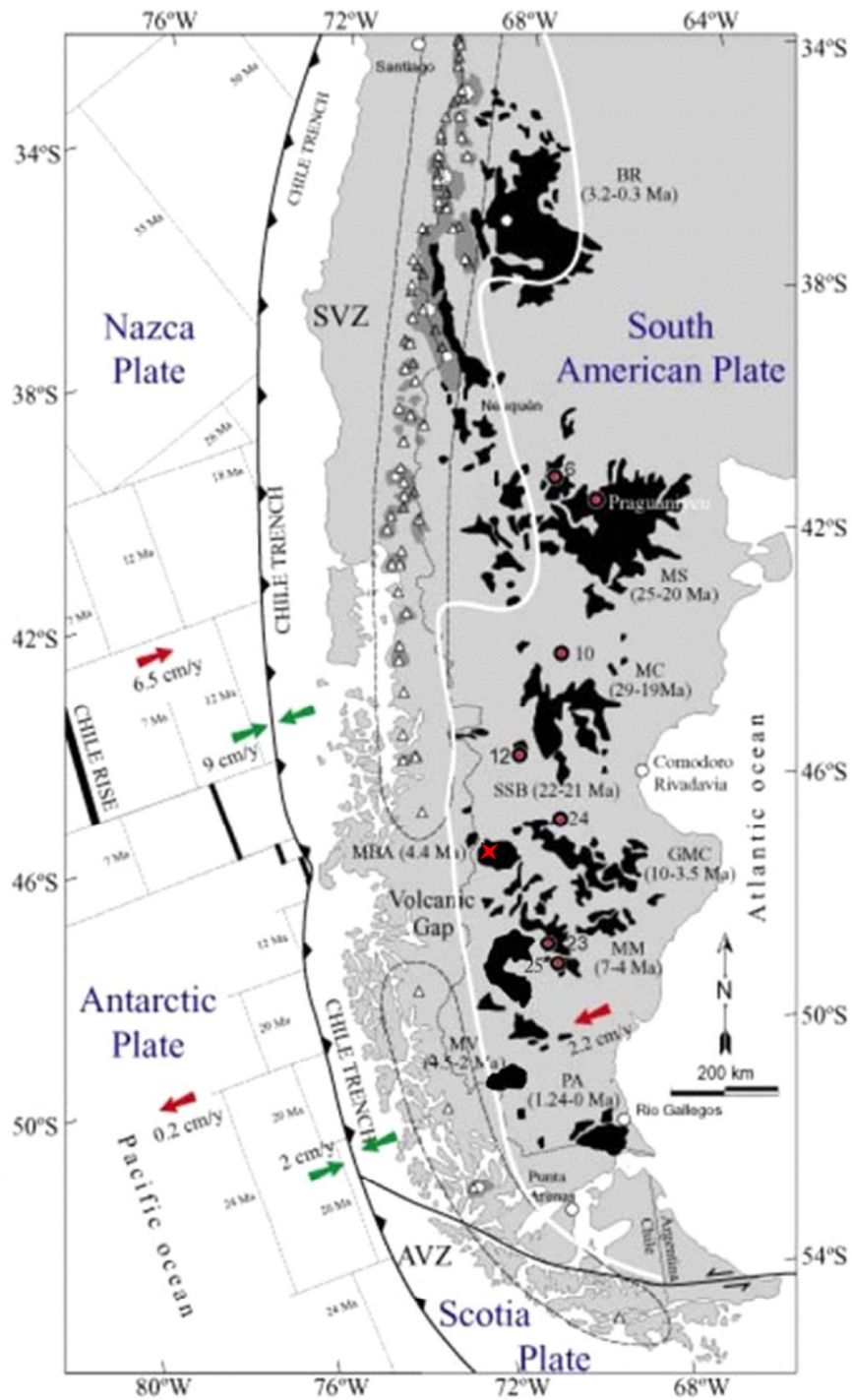


Figure 7.1: Sketch map of Patagonia (from *Dantas, 2007*) showing the position of the localities (red dots) chosen for the comparison with the samples from Estancia Sol de Mayo (represented by the red star). Dot numbers represent: 6 Cerro Aznare (*Dantas, 2007*), 10 Cerro Rio Chubut (*Bjerg, 2005; Aliani, 2009*), 12 Cerro de los Chenques (*Dantas, 2007; Rivalenti 2004, 2007*), 23 Gobernador Gregores (*Dantas, 2007; Rivalenti, 2004*), 24 Cerro Clark (*Dantas, 2007; Rivalenti, 2004*), 25 Tres Lagos (*Ntaflos, 2006; Rivalenti, 2004*). Red arrows indicate the absolute movement of the plates, while green arrows the relative one (*Corvolàn, 1981; Ramos and Kay, 1992*). The dashed white line represents the limit between the arc and back-arc.

The comparison of the clinopyroxenes from Estancia Sol de Mayo to those analyzed in other suites of mantle xenoliths highlights, as shown in **Figure 7.2**, the presence of three different trends. The two groups of cpx from ESM described in the Geochemistry chapter, the first characterized by mg# varying from 91.2 to 94, and high Al_2O_3 contents ranging from 4.52 to 3.22 wt. %, and the second with mg# ranging from 82.3 to 93 and Al_2O_3 from 7.3 wt. to 1.93 %, plot respectively along the trends that are defined as **trend 1 and trend 2**. Also the cpx of peridotites from Northern Patagonia plot along the trend 1, with Al_2O_3 contents ranging from 2.28 to 6.60 wt. % at mg# comprised between 94.98 and 89.38, while those from Central Patagonia are the most scattered, with almost an equal number of cpx plotting in the two groups (Al_2O_3 from 2.45 wt. % up to 8.17 wt. % with a mg# variable between 86.48 and 94.21). Cpx of wehrlites from Central Patagonia clearly plot along **trend 2**, and are characterized by Al_2O_3 contents ranging from 2.47 wt. % to 9.30 wt. %, and mg# varying between 82.01 and 93.19. Cpx from pyroxenites of Northern Patagonia are clearly divided into two groups: one fall in the same field of those belonging to the first trend (Al_2O_3 ranging from 2.66 wt. % to 8.09 wt. %, and mg# comprised between 89.48 and 92.69), while the second is not aligned neither with the first nor the second trend. In fact these cpx plot on a third trend (**trend 3**) with mg# varying from 84.56 to 89.79 with low Al_2O_3 contents (2.65-4.43).

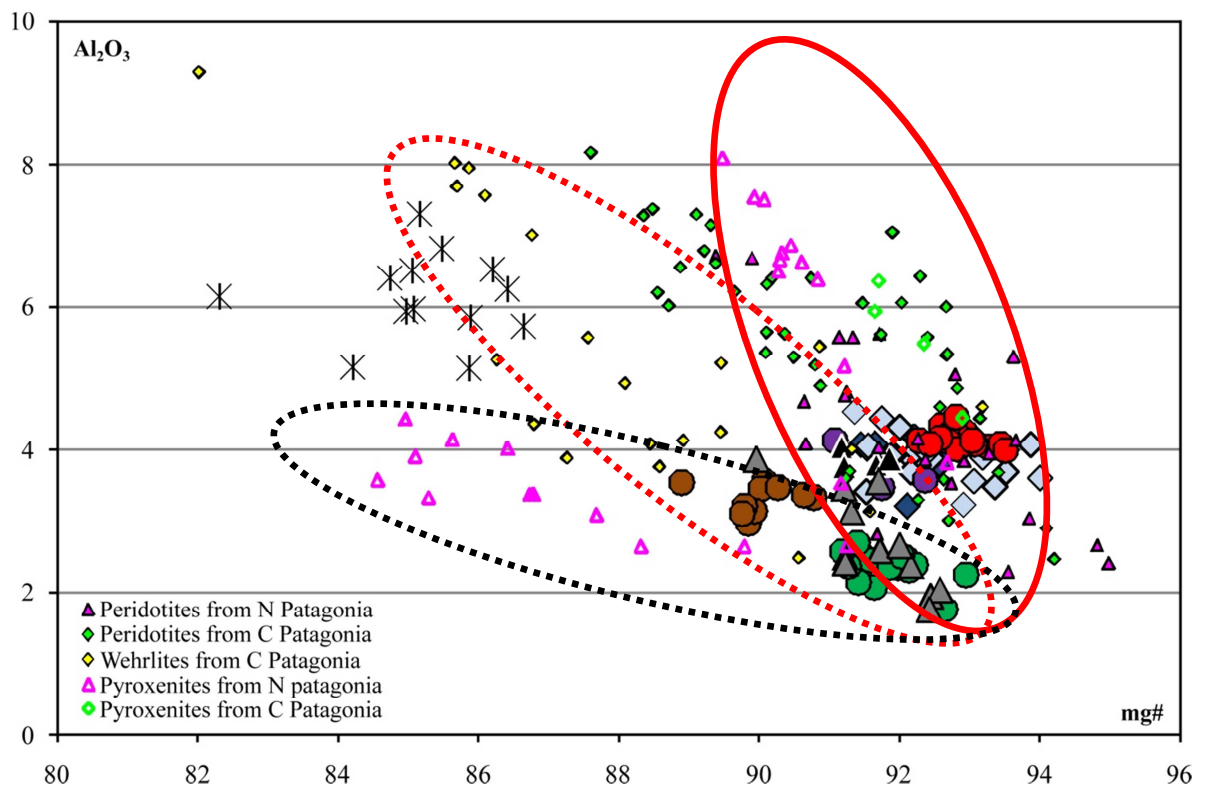


Figure 7.2: Al_2O_3 vs. mg# diagram for clinopyroxenes of Estancia Sol de Mayo (for legend see **Figure 6.1**) and other localities from Patagonia (legend in the inset). Bold red line identifies “**trend 1**”, dashed bold red line “**trend 2**”, dashed bold black line “**trend 3**”.

7. Comparisons

The orthopyroxenes from Estancia Sol de Mayo also define two trends, one that can be linked to **trend 1** and the second to **trend 3** defined by cpx. The lack of **trend 2** is due to the fact that it is defined by the cpx analyzed in the wehrlites, where opx is very rare. As reported in **Figure 7.3 A** and **B** the samples from Estancia Sol de Mayo described as enriched in Al_2O_3 and depleted in Cr_2O_3 (MGP2b, MGP2b2, MGP4b and MGP2a) plot along **trend 1** together with the opx from the peridotites (Al_2O_3 and mg# varying between 1.51 wt. % to 6.04 wt. % and 86.43 to 92.03 respectively) and pyroxenites (characterized by Al_2O_3 contents ranging from 2.97 wt. % to 4.85 wt. % and mg# comprised into a narrow range, from 90.15 to 90.60) from the Central Patagonia and a group of websterites from Northern Patagonia (Al_2O_3 and mg# varying between 3.56 wt. % to 4.62 wt. % and 89.74 to 90.95 respectively). On the other hand, opx from harzburgites MGP1b, MGP1c, MGP1g and MGP3b, plot along **trend 3** together with the second group of websterites from Northern Patagonia, characterized by Al_2O_3 contents varying from 1.90 wt. % to 3.62 wt. % and a mg# ranging from 80.43 to 88.34. The increasing of the mg# of the opx from ESM is linked to a decreasing of the Al_2O_3 content and an increasing of Cr_2O_3 .

The definition of similar trends to those defined by clinopyroxenes and orthopyroxenes is less clear when observing the cr# vs. mg# of spinels. As described in **section 6.1.4** the spinels can be also divided into two groups, one comprising the majority of the phases analyzed crystals and characterized by a decreasing of the cr# (i.e. increasing of the Al_2O_3) with an increasing of the mg#, and a second group composed of very few grains (the spinels of the wehrlite MGP1d and the harzburgite MGP1g) that plot outside the mantle array at very low cr# (17.53-26.50) and mg# ranging from 54.96 to 64.86. In **Figure 7.4** the data from *Dantas (2007)* are plotted: it can be observed that spinels from the peridotites (characterized by cr# ranging from 11.80 to 34.79 and mg# comprised between 69.33 and 77.73) and pyroxenites (with cr# and mg# varying from 9.54 to 22.97 and from 74.67 to 77.82 respectively) from Northern Patagonia are aligned with those of ESM falling on the mantle array, but at lower cr# and higher mg#. Also the spinels of peridotites from the Central Patagonia (cr# ranging from 9.33 to 60.35 and mg# from 55.57 to 81.35) plot in the same field, even if they are more scattered (as also observed in **Figure 7.3** for the clinopyroxenes belonging to the samples of the same area) and some of them are aligned with the spinels from the samples MGP1d and MGP1g.

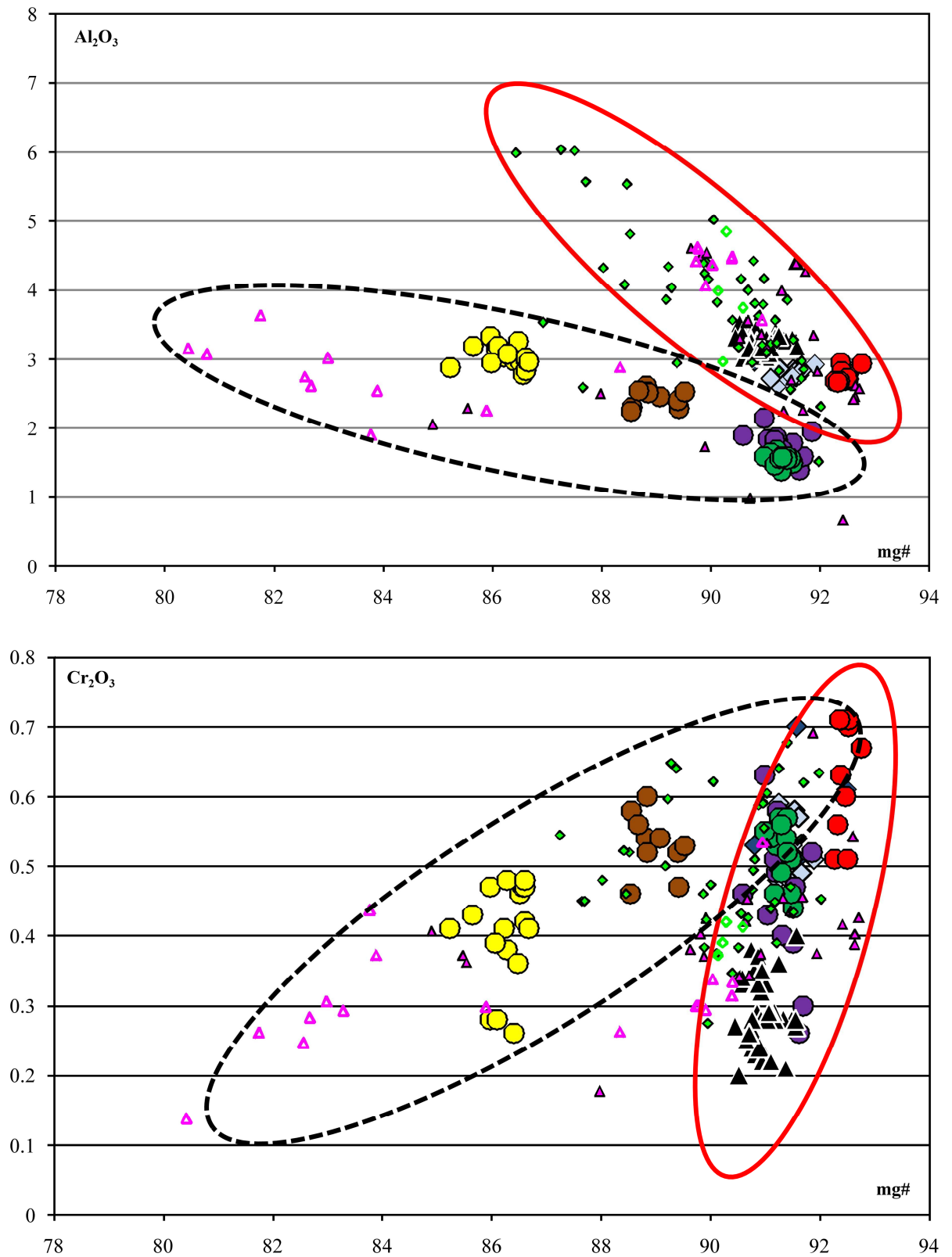


Figure 7.3: Al₂O₃ vs. mg# diagram (A) and Cr₂O₃ vs. mg# (B) for orthopyroxenes of Estancia Sol de Mayo (for legend see **Figure 6.1**) and other localities from Patagonia (legend in the inset of **Figure 7.2 A**); the two fields represented by the bold red line and the dashed bold black line correspond to **trend 1** and **trend 3** as in **Figure 7.2**.

7. Comparisons

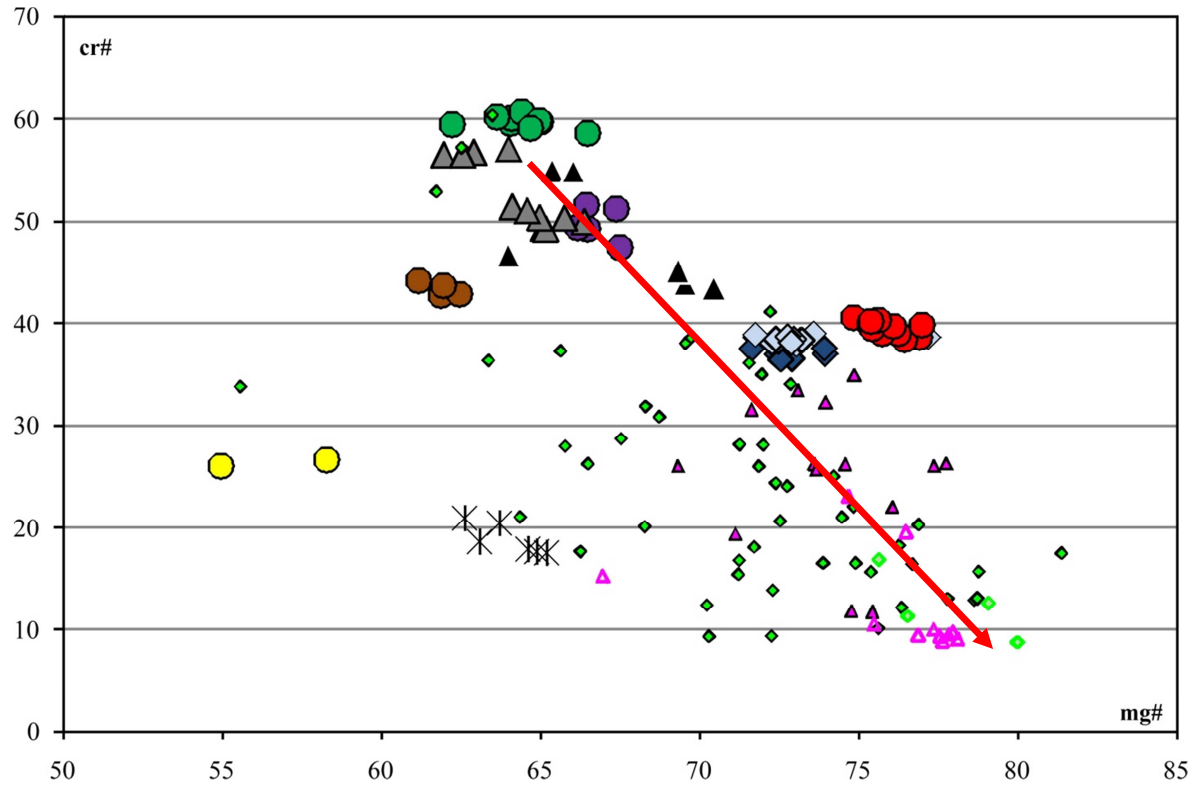


Figure 7.4: cr# vs. mg# for the spinels of Estancia Sol de Mayo. For comparison also spinels of peridotites and pyroxenites from Northern and Central Patagonia are plotted. Symbols are shown in **Figure 6.1** and **7.2**.

As already shown in **Figure 6.12** the clinopyroxenes from ESM are characterized by LREE enrichment related to an Al_2O_3 depletion. This is true not only for the Estancia Sol de Mayo suite, but also for other Patagonian mantle xenoliths suites. The diagrams proposed in **Figure 7.5** evidence the same situation for mantle peridotites from Cerro de los Chenques and Cerro del Fraile (**Figure 7.5 A** and **A'**) characterized by an increase of $(\text{La}/\text{Yb})_N$ and the Sr_N when the Al_2O_3 content decreases. On the other hand, Cerro Rio Chubut and Tres Lagos (**Figure 7.5 B** and **B'**) are characterized by a decreasing of the two parameters correlated to a decreasing of the Al_2O_3 content. This is the typical situation in which a portion of mantle that underwent partial melting has not been subsequently affected by metasomatism. Finally a more complex situation is observed at Gobernador Gregores. As it can be appreciated from (**Figure 7.5 C** and **C'**) both the situations described for the other localities are recognized: in fact a group of sample clearly record only a depletion event, while a second is affected by metasomatism that affect the REE and the Sr contents.

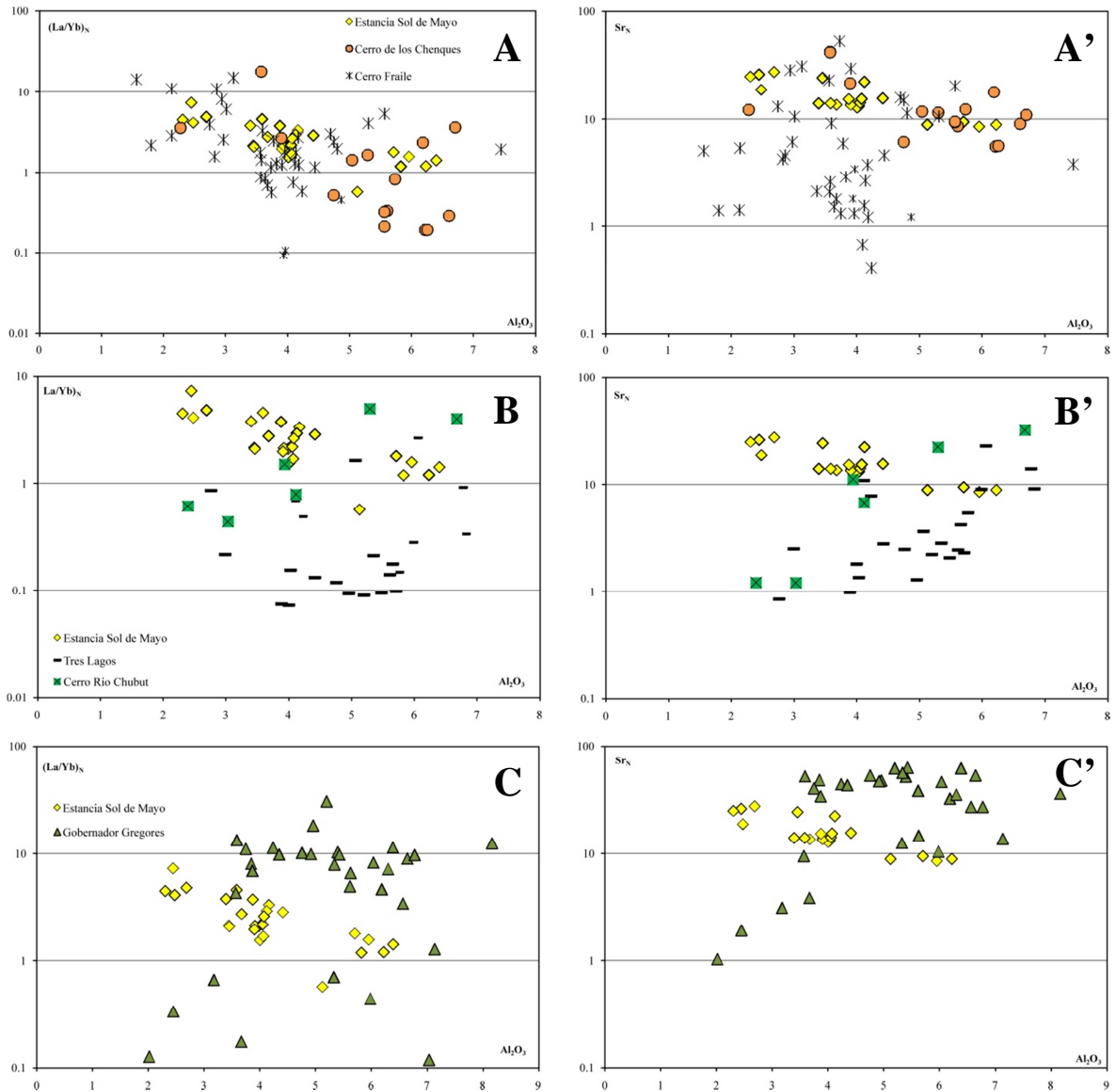


Figure 7.5: $(\text{La}/\text{Yb})_N$ (A, B, C) and Sr_N (A', B', C') (normalized to Chondrite) vs. Al_2O_3 content of clinopyroxenes from Estancia Sol de Mayo and other eight localities taken for comparison.

Finally the isotopes from Estancia Sol de Mayo described in **Chapter 6.4** have been compared to other samples (**Appendix 8, Figure 7.6 and 7.7**), chosen on the basis of the lithotype and the modal content of the clinopyroxenes. Most of them belong to the suite of mantle xenoliths studied by *Dantas (2007)*, the others come from three suites studied by *Bjerg et al. (2005)*, *Faccini (2008)* and *Aliani et al. (2009)*.

7. Comparisons

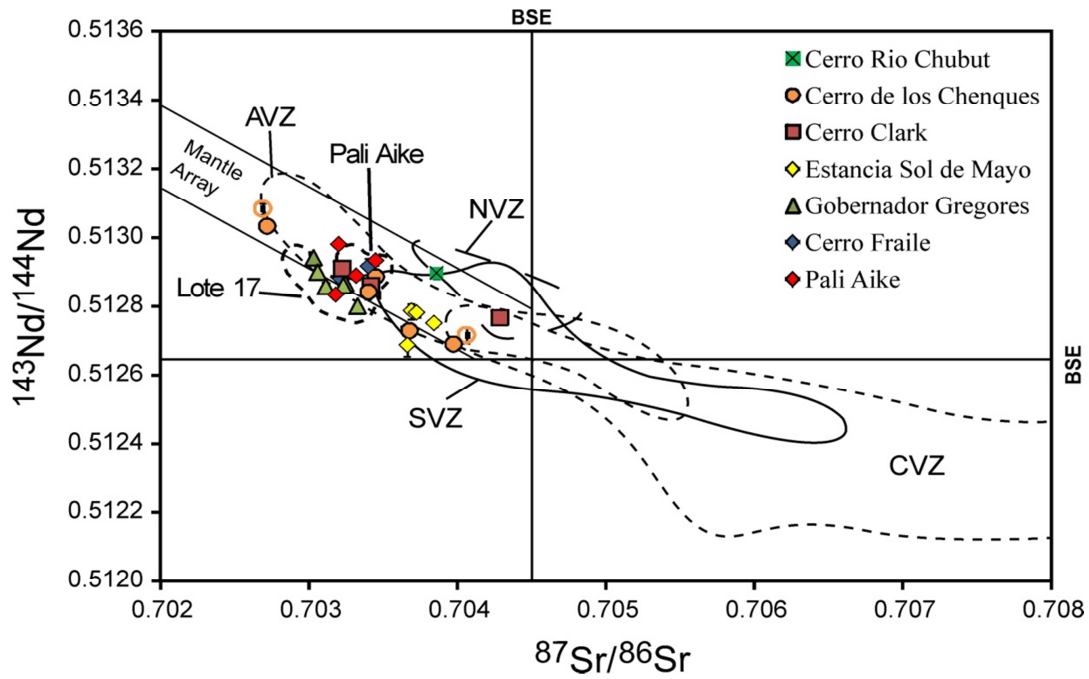


Figure 7.6: $^{143}\text{Nd}/^{144}\text{Nd}$ vs $^{87}\text{Sr}/^{86}\text{Sr}$ plot. Symbols for each locality are reported in the inset. The full symbols represent peridotitic samples (Iherzolites, harzburgites, wehrlites), while empty symbols indicate pyroxenites. For the comparison fields refer to **Figure 6.19**.

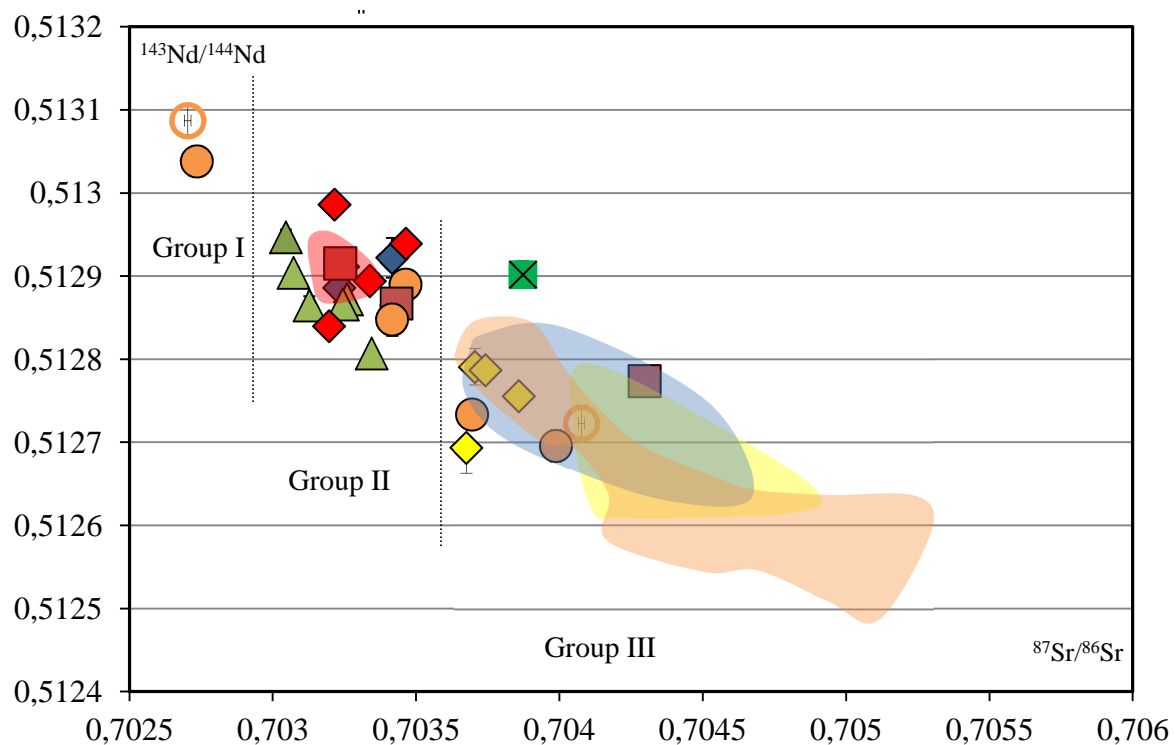


Figure 7.7: $^{143}\text{Nd}/^{144}\text{Nd}$ vs $^{87}\text{Sr}/^{86}\text{Sr}$ plot. Symbols are the same that in **Figure 7.6**. Sr-Nd of the plateau lavas are also plotted. The Somoncuro Province is represented by the light orange field (Kay *et al.*, 2004), the Triple Junction Province by the blue field (Gorring *et al.*, 1997, Gorring and Kay, 2001), Meseta Lago Buenos Aires by the yellow field (Gorring *et al.*, 2003) and Pali Aike by the red field (D'Orazio *et al.*, 2000, 2001).

As it is possible to observe, the samples (that plot all on the mantle array) can be divided into three different groups: the first group (**Group I**) is represented by a couple of samples from Cerro de los Chenques, one peridotite and one pyroxenite, having an isotopic composition close to the depleted mantle (DM). The most depleted has a $^{87}\text{Sr}/^{86}\text{Sr}$ and $^{143}\text{Nd}/^{144}\text{Nd}$ ratios of 0.702704 and 0.513087 respectively, while the second has $^{87}\text{Sr}/^{86}\text{Sr}$ of 0.702736 and $^{143}\text{Nd}/^{144}\text{Nd}$ of 0.513038. The second group (**Group II**) of samples comprises all those analyzed from Gobernador Gregores, those from Pali Aike, two from Cerro de los Chenques, two from Cerro Fraile and two from Cerro Clark. They are all peridotites, and they are characterized by a typical HIMU signature, varying the $^{87}\text{Sr}/^{86}\text{Sr}$ ratio from 0.703046 to 0.703464 and the $^{143}\text{Nd}/^{144}\text{Nd}$ between 0.512807 and 0.512986. Finally the last group (**Group III**) comprises the four samples from Estancia Sol de Mayo, three from Cerro de los Chenques, and one from Cerro Rio Chubut and Cerro Clark. Except one mantle xenolith from Cerro de los Chenques that is classified as websterite, all the others are peridotites. These samples are clearly aligned toward the Enriched Mantle I (EM I) composition. They show a wider range in the isotopic composition of both the $^{87}\text{Sr}/^{86}\text{Sr}$ and the $^{143}\text{Nd}/^{144}\text{Nd}$ ratio being the first comprised between 0.703676 and 0.704297, while the second ranging from 0.512694 and 0.512902.

The samples from the different groups are also characterized by different trace element patterns. As highlighted by **Figure 7.8** the samples are characterized by an increasing of the LREE contents proceeding from Group I to Group III, being the most depleted those belonging to the first one.

7. Comparisons

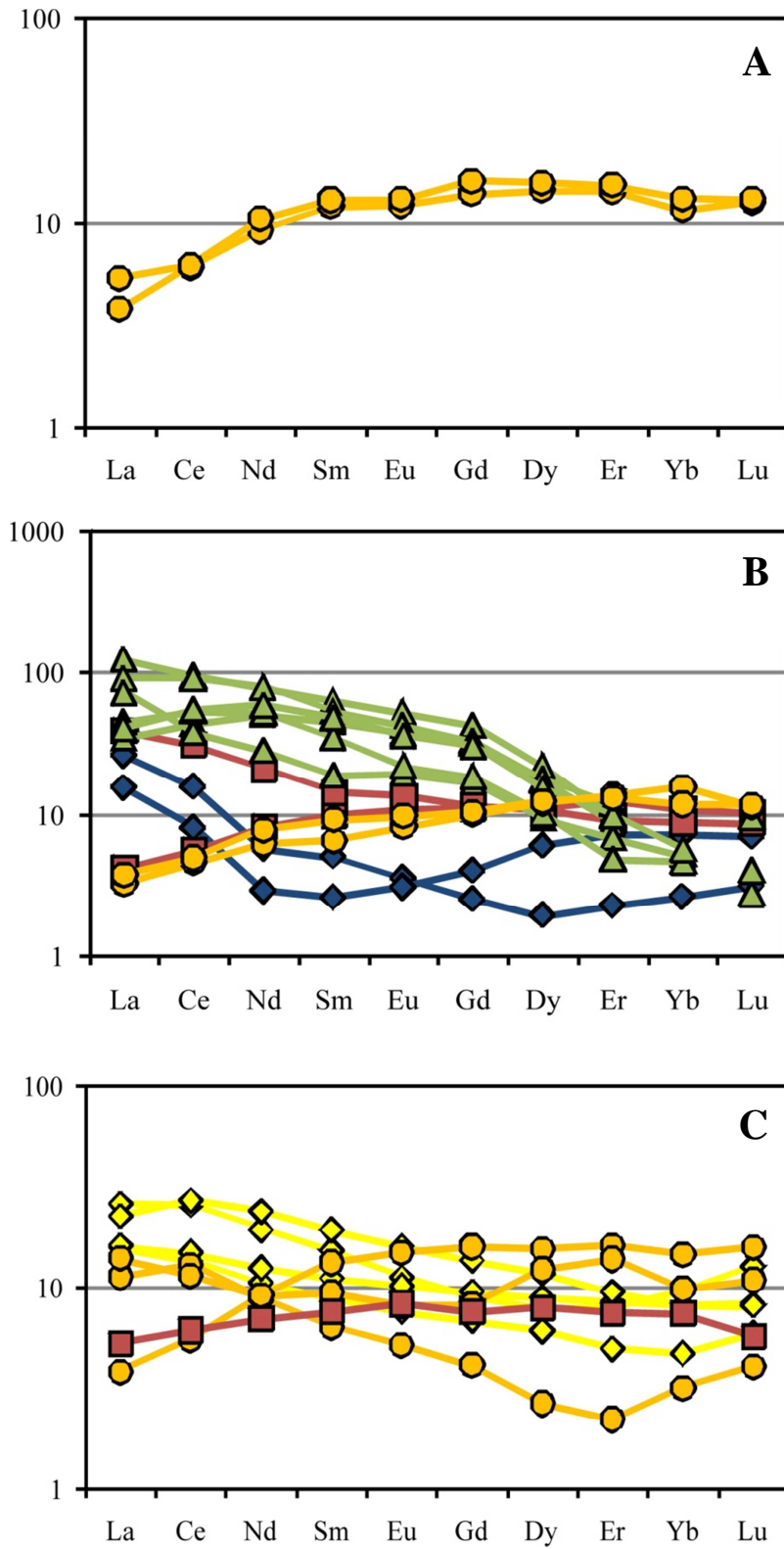


Figure 7.8: Chondrite-normalized trace element patterns of Group I (A), Group II (B) and Group III (C) clinopyroxenes. For the symbols refer to the inset of Figure 7.6.

8. Discussion

In this section the results obtained and described in the previous chapter will be discussed. First of all I will discuss those from Estancia Sol de Mayo and then I will try to focus the attention on all the other localities used for the comparison and of which some isotopic analysis have been performed.

The geochemical features of the clinopyroxenes and orthopyroxenes analyzed at Estancia Sol de Mayo and shown in Chapter 6, highlight the presence of three different evolutionary trends showing a decrease in Al_2O_3 content with the increasing of the mg# (**Figure 6.3 A** and **6.6 A**). The difference among the trends could be supported by the partial melting of three different sources, that have almost the same mg# but a different Al_2O_3 content. If we consider this kind of evolution for the ESM xenoliths, we should observe a correlation between the increasing of the mg# and the nature of the lithotype left from the partial melting, i.e. the gradual passage from lherzolites to harzburgites to dunites. This is not the case for the xenoliths of this suite, because as the proposed diagrams suggest, no correlations can be established among the variation of the mg# and the lithotypes. The hypothesis of an origin of the xenoliths linked to a simple partial melting is also ruled out by the trace element composition (**Figure 6.12 A** and **B**). In the first diagram $(\text{La}/\text{Yb})_N$ vs. Al_2O_3 if we assume to melt a fertile lherzolite, the residue left would have a minor Al_2O_3 content (what we observe from the major elements) coupled with a decreasing of the LREE, i.e. in this case a decreasing of the ratio $(\text{La}/\text{Yb})_N$. Indeed the diagram clearly show a negative correlation between these two parameters, with an increasing of the LREE linked to a decreasing of the aluminum content. The same is observed from **Figure 6.12 B** in which Sr is correlated with Al_2O_3 . Sr should behave as the LREE, i.e. it should decrease when Al_2O_3 decrease. But it shows the same feature than the $(\text{La}/\text{Yb})_N$, it increases when Al_2O_3 decreases. These geochemical features as well as the presence also of two texturally different cpx and opx observed in thin sections highlight a metasomatic/refertilization event affecting the upper mantle beneath Estancia Sol de Mayo.

8.1 Nature of the metasomatic liquid

One of the major problem when dealing with mantle xenoliths metasomatism/refertilization is to identify the nature of the liquid that could have affected the portion of mantle considered. As far as ESM suite is concerned, in **Figure 8.1** is proposed the Al_2O_3 vs. mg# diagram for the clinopyroxenes (already shown in **Figure 7.2**) in which the three trends highlighted by the cpx from pyroxenites and wehrlites from northern and central Patagonia (*Dantas, 2007*) are plotted together with their REE patterns (in the three insets and in **Figure 8.2**).

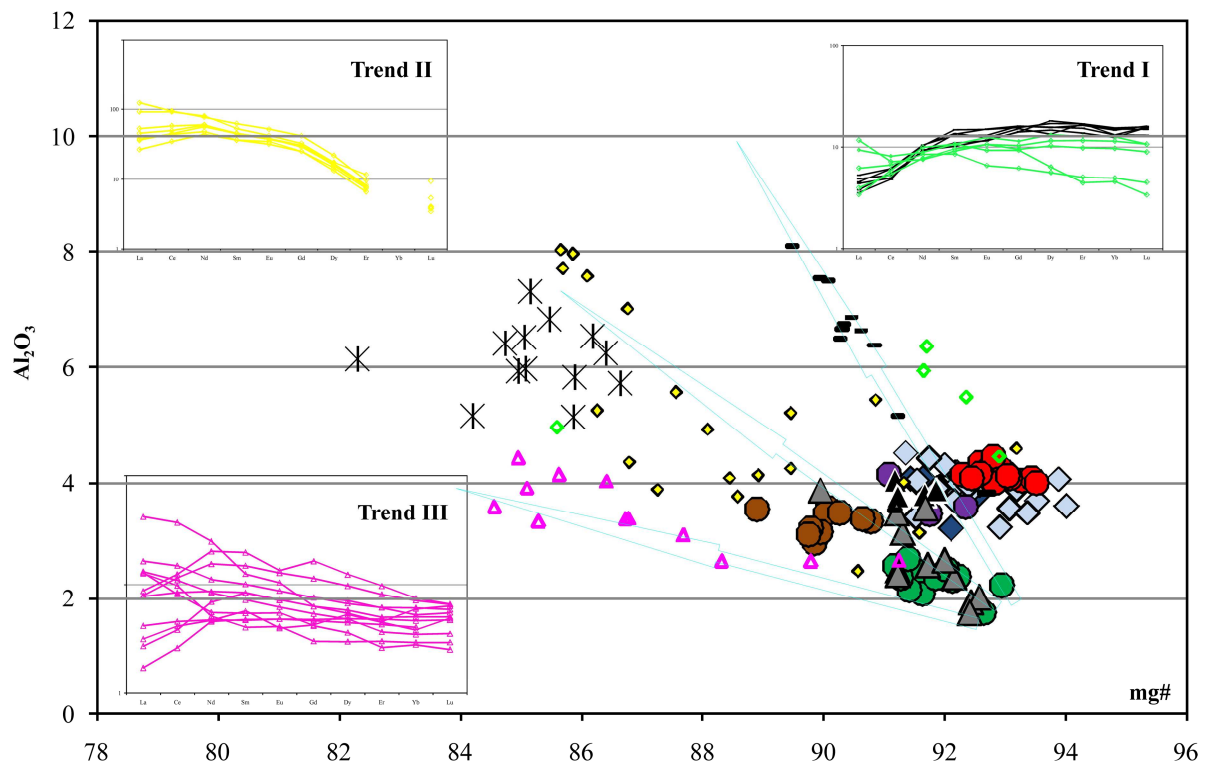


Figure 8.1: Al_2O_3 vs. mg# for ESM clinopyroxenes and REE (insets) compositions of clinopyroxenes of pyroxenites and wehrlites from northern and central Patagonia (*Dantas, 2007*). Symbols are the same of **Figure 7.2**.

It is clear that the three groups have different trace element compositions (better highlighted by **Figure 8.2**): pyroxenites from northern Patagonia (**trend 1**) are characterized by prominent Nb and slightly negative Ti anomalies, depleted LREE and from enriched to flat MREE and HREE. The same feature can be observed also for the clinopyroxenes of the pyroxenites of central Patagonia that fall in the same group, except for a slightly negative Zr anomaly and for less enriched REE patterns. Wehrlites from

central Patagonia that belong to **trend 2** show the highest trace elements concentrations, with prominent negative Nb and Ti

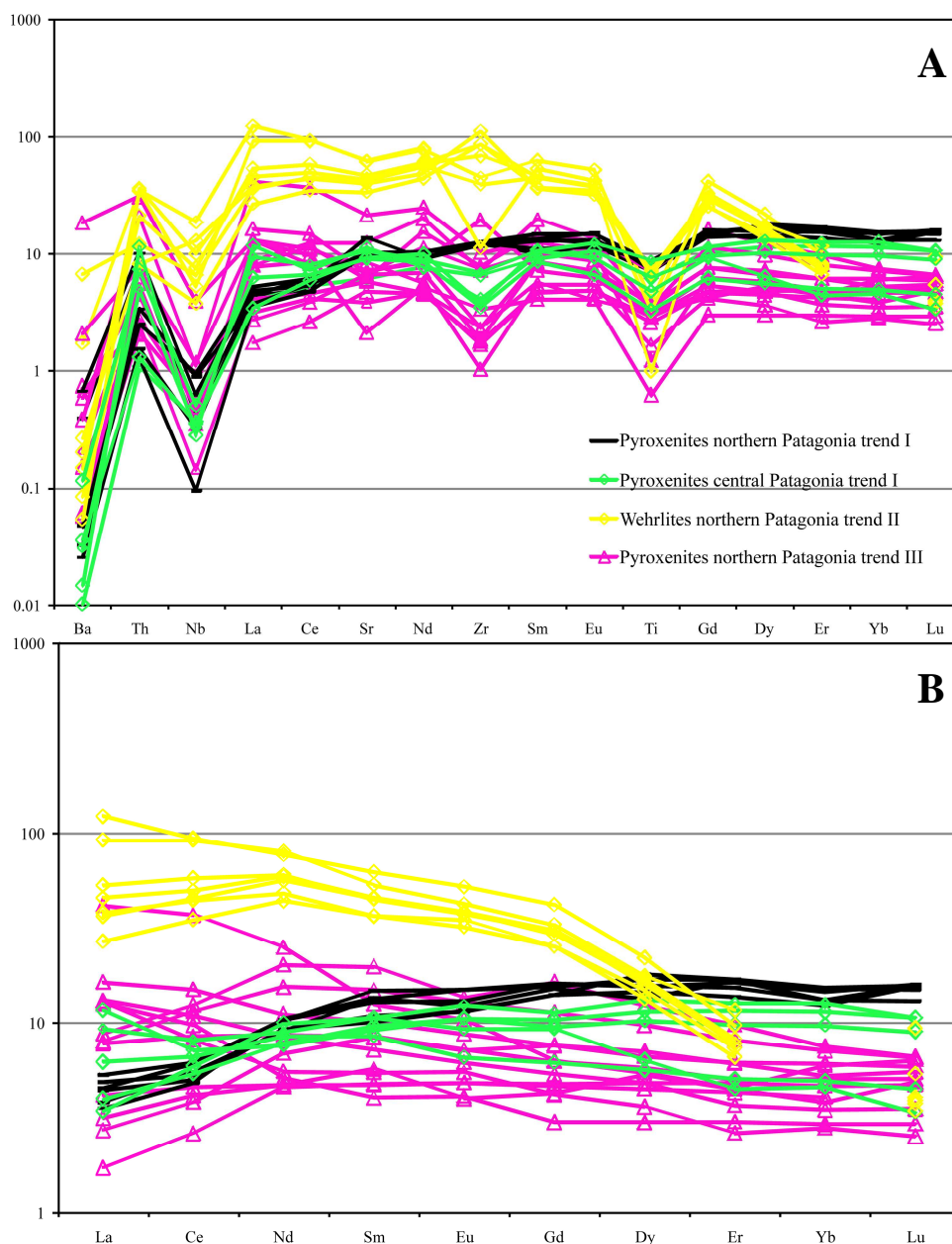


Figure 8.2: Chondrite-normalized trace elements compositions (A) and REE (B) of pyroxenites and wehrlites from northern and central Patagonia (*Dantas, 2007*).

anomalies, negative to positive Zr anomaly, enriched LREE and fractionated HREE. Finally clinopyroxenes of pyroxenites from northern Patagonia that form **trend 3** are characterized by the wider range of trace elements concentrations, with negative Nb, Zr and Ti anomalies. LREE contents vary from depleted to slightly enriched and fractionated

8. Discussion

to flat HREE. The REE patterns of the cpx from peridotites from Estancia Sol de Mayo clearly resemble those of the cpx from pyroxenites of the **trend 3** as it is possible to observe from **Figure 8.3**.

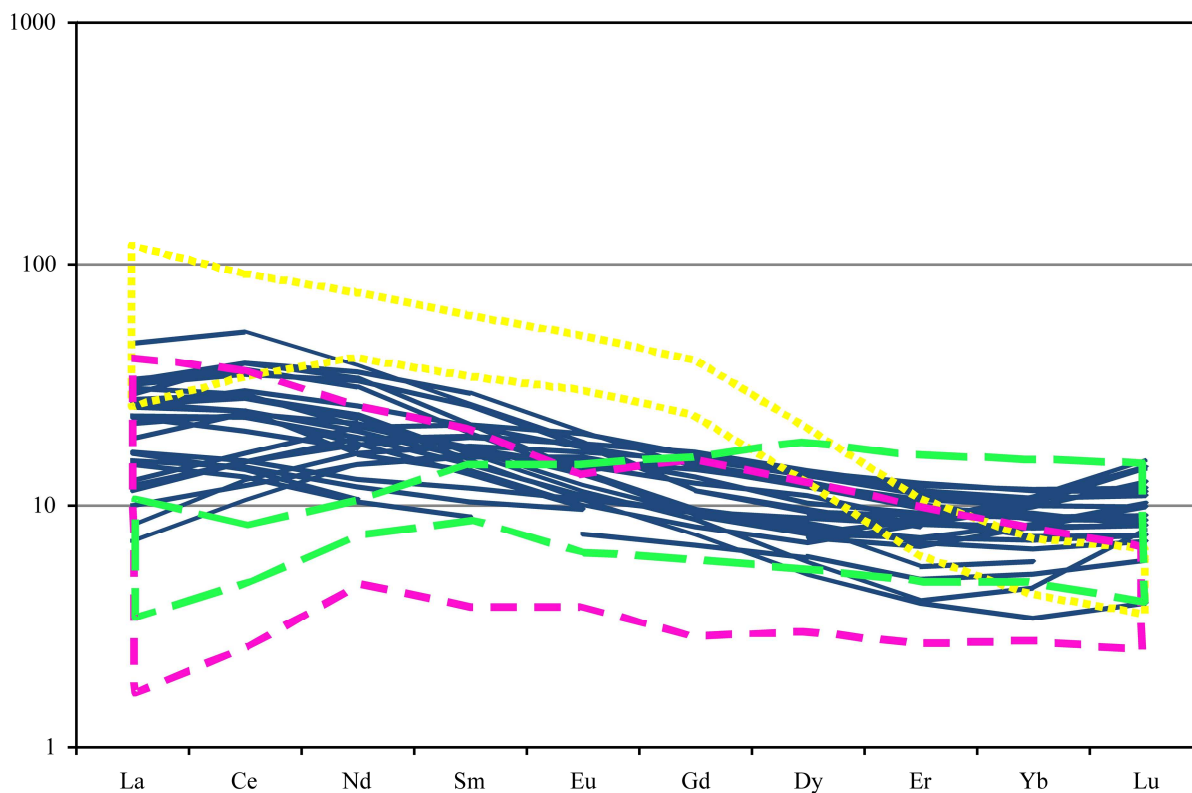


Figure 8.3: Chondrite-normalized REE compositions of ESM peridotites. The green line identifies **trend 1**, the yellow line **trend 2** and the pink line **trend 3**.

The next step consists in understanding the origin of the clinopyroxenes from ESM (those belonging to **trend 3**) and also constrain the possible evolution of those belonging to the other two trends. As already said, from the major element compositions the ESM samples identified two trends, **trend 1** and **trend 2**, but from **Figure 8.2** and **8.3** it is possible to observe that their trace element compositions resemble those of the cpx belonging to **trend 3**. The REE patterns of the clinopyroxenes from **trend 3** are similar to those of the transitional/alkaline lavas from the Somoncura Province, as shown in **Figure 8.4 A** and **B**. Starting from these compositions, and using the partition coefficient between clinopyroxene and transitional melts (the data from GERM, <http://earthref.org/GERM/>) and considering the most and the least LREE-enriched Somoncura lavas, the clinopyroxenes in equilibrium with these lavas have been calculated. The results are shown

in **Figure 8.5**: the two patterns represented by the white asterisks with a black background are the clinopyroxenes calculated from the two selected Somoncuro lavas. They clearly fall in the field represented by the pink dashed line (clinopyroxenes of pyroxenites from northern Patagonia, **trend 3**) and their patterns are exactly the same than those of the clinopyroxenes from the peridotites of ESM (blue lines), confirming that a transitional/alkaline metasomatism event has affected the mantle beneath ESM.

Furthermore, while the clinopyroxenes of **trend 2** are clearly related to an alkaline metasomatic event, for those belonging to **trend 1** is feasible to infer a metasomatism/refertilization event related to tholeiitic melts. **Figure 8.6** supports this hypothesis: the REE patterns of phenocryst cpx from tholeiitic lavas from literature have been plotted together with those of the clinopyroxenes of **trend 1**. The two suites of clinopyroxenes show exactly the same patterns, supporting the evidence of the percolation in the ESM mantle of a tholeiitic melt. The same kind of process can be envisaged also for some ESM cpx, that fall on **trend 1** (**Figure 8.2**). What can be speculated is that the ESM mantle portion suffered a tholeiitic refertilization process, notwithstanding the complete absence within the Meseta Lago Buenos Aires of tholeiitic lavas, being typical eruptive products of the main plateau sequences of all the other Triple Junction Province mesetas. This refertilization process with respect to “normal” metasomatism is characterized by a much higher melt/rock ratio. The tholeiitic refertilization has been followed by a transitional/alkaline metasomatic event (as shown by the calculation of the clinopyroxenes in equilibrium with the lavas of Somoncuro) as suggested by the succession recorded in all plateaux. The large difference in trace element contents between the two melts caused a substantial enrichment of the source, not associated to an analogous increase in major element, i.e. Al_2O_3 , which are much more similar. In order to have this last event recorded by cpx, it should have been occurring some time before the entrainment and the uprising of the xenoliths.

The possible involvement of a tholeiitic melt as refertilization agent can be put forward also considering the textural and geochemical features of orthopyroxenes. From the petrographic study of the samples three generations of orthopyroxenes are recognized. They have been classified mainly as protogranular with exsolution lamellae (opx1), or smaller (with respect to opx1) protogranular without exsolution lamellae (opx2), with some grains arranged in a vein (opx3). The latter is a clear evidence of a metasomatic event, that

8. Discussion

has affected the sample very recently. Because of the new crystallization of opx, it is easy to support and confirm the idea that a SiO₂-saturated (or oversaturated) melt (such as a tholeiite) percolate the mantle.

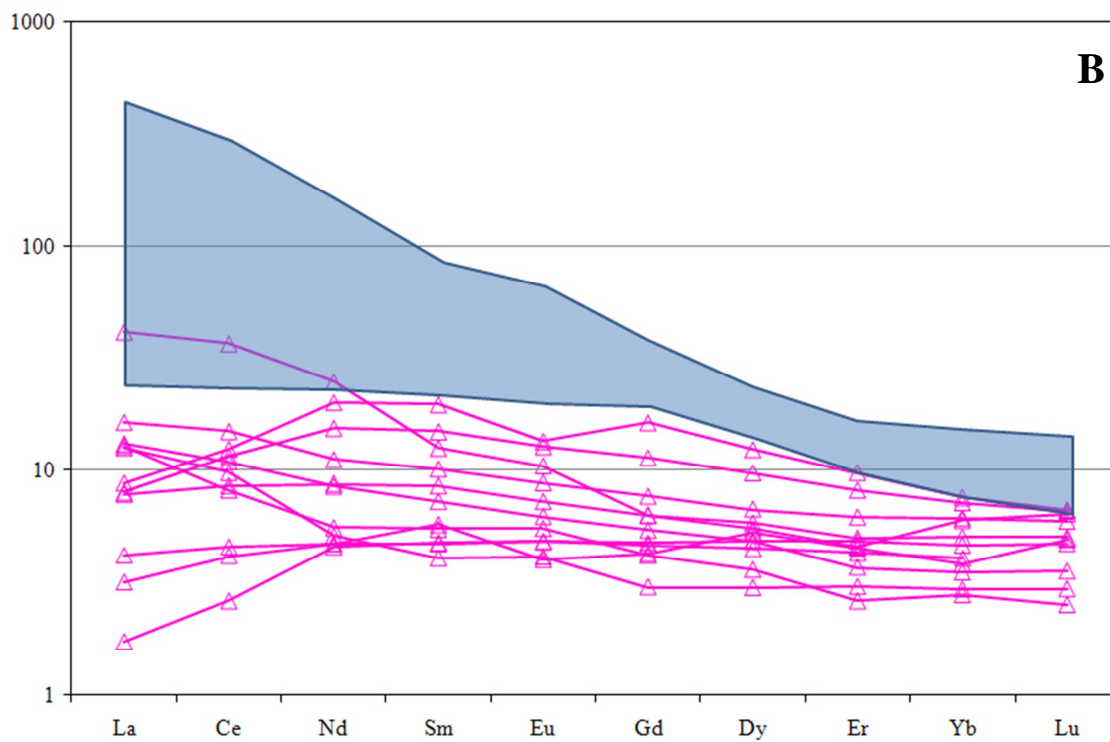
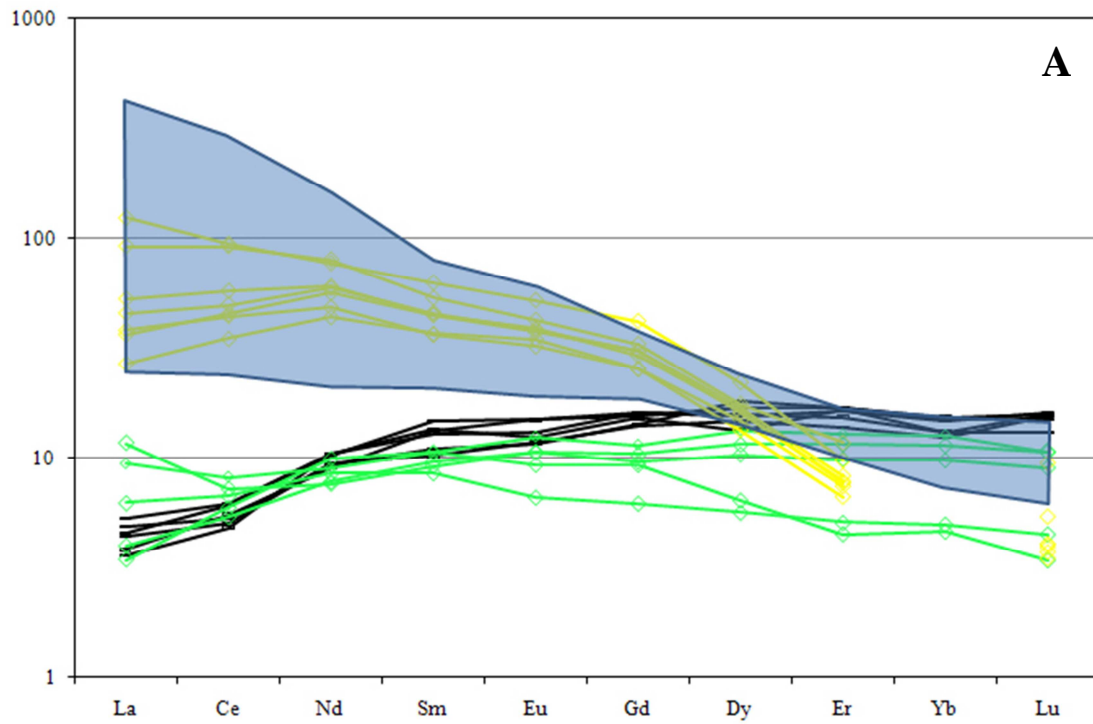


Figure 8.4: Chondrite-normalized REE of **trend 1** and **trend 2** clinopyroxenes (**A**) and **trend 3** (**B**) of peridotites and pyroxenites from northern and central Patagonia (*Dantas, 2007*) with the blue field representing in both the diagrams the tholeiitic lavas of Somoncurea.

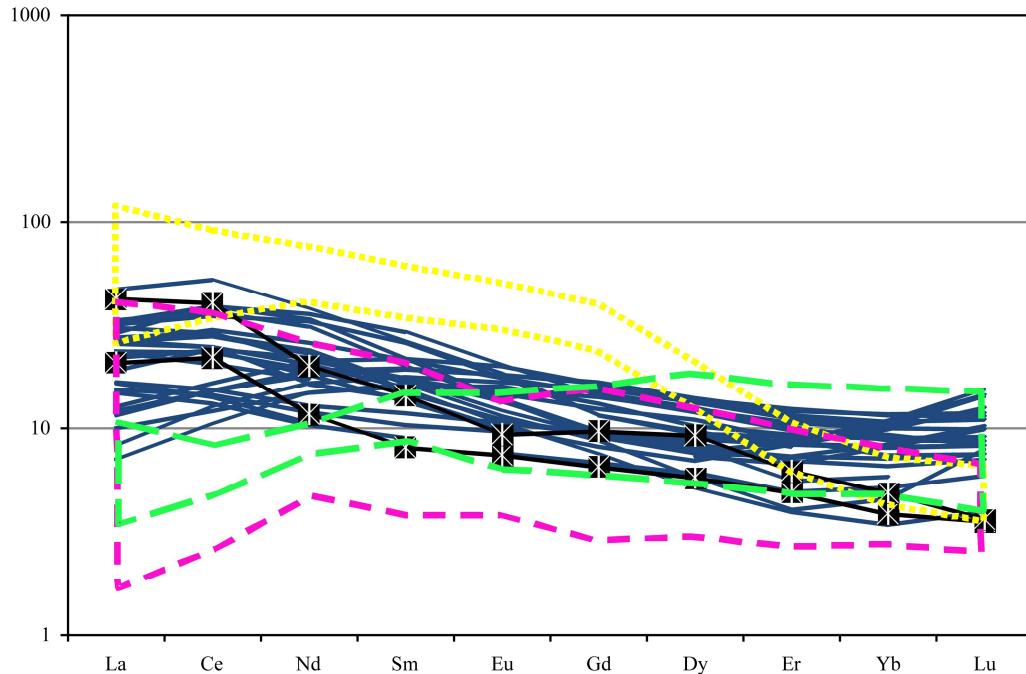


Figure 8.5: Chondrite-normalized REE of calculated clinopyroxenes (white asterisk with black background) in equilibrium with a tholeiitic melt. For the blue patterns and the three different fields refer to **Figure 8.3**

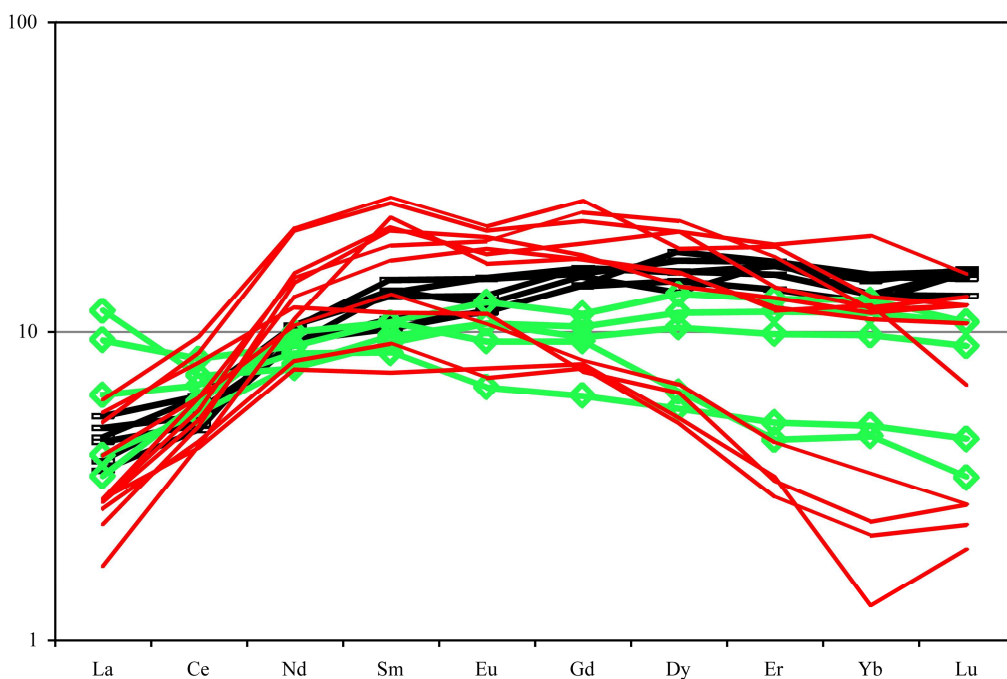


Figure 8.6: Chondrite-normalized REE clinopyroxenes belonging to **trend 1** (for symbols see the previous **Figures**) and of phenocrysts of clinopyroxenes of tholeiitic lavas from Ethiopia (*Beccaluva et al., 2009*).

8. Discussion

If this will be the case the contemporaneous presence of tholeiitic and transitional/alkaline melts in the ESM mantle has to be inferred, contrary of what it is observed in the lava succession of the plateaux where tholeiitic magmas always anticipate those transitional or alkaline.

8.2 Isotopic modelling

Many natural processes on Earth cause mixing of two or more components having different chemical and/or isotopic compositions. The chemical and isotopic compositions of two-component mixtures are expressed by simple linear or hyperbolic patterns. When two components (A and B) mix, the chemical composition of the mixture (M) vary systematically depending on the relative abundances of the end members. With this aim f_A is defined as the mixing parameter: $f_A = W_A/(W_A + W_B)$ where W_A and W_B are the weights (or volumes) of the components A and B in the mixture. As it is possible to understand f_A is a dimensionless number, that can vary from 0 and 1. Obviously it will be 0 when the mixture M is composed only by component B and 1 when only component A is present in the mixture. Hence the mixing parameter f_A is the “weight fraction” or “volume fraction” of component A in two component mixtures. That means that the complementary weight fraction of B (f_B) is equal to $1 - f_A$, i.e. equal to $W_B/(W_A + W_B)$. The concentration of any element (X) in a binary mixture of A and B depends on the concentration of that element in the components A and B. Therefore the concentration of element X in a mixture (M) of components A and B is: $(X)_M = (X)_A f_A + (X)_B (1 - f_A)$, where the parentheses mean “concentration”. By rearranging the last equation it is possible to obtain that $(X)_M = f_A [(X)_A - (X)_B] + (X)_B$, that represents the equation of a straight line with slope m equal to $(X)_A - (X)_B$ and intercept q equal to $(X)_B$.

The isotope composition of some elements are variable because some of their isotopes are the products of naturally occurring radioactive parents or because of isotope fractionation. Therefore it is possible to consider cases where mixing occurs between two materials that contain the same element but with different isotopic compositions. Imagine that we want to mix two components that have different $^{87}\text{Sr}/^{86}\text{Sr}$ ratios. For what has been said above, the concentration of Sr of a mixture of two components A and B is given by $(\text{Sr})_M = (\text{Sr})_A f_A + (\text{Sr})_B (1 - f_A)$ [1]. If the end members have different $^{87}\text{Sr}/^{86}\text{Sr}$ ratios, then the isotopic

composition of any mixture must be the weighted sum of the $^{87}\text{Sr}/^{86}\text{Sr}$ ratios where the weighting factors are $(\text{Sr})_A/(\text{Sr})_M$ and $(\text{Sr})_B/(\text{Sr})_M$ (a detailed derivation is given by *Faure, 1986*). Therefore the equation for the $^{87}\text{Sr}/^{86}\text{Sr}$ ratio of a binary mixture is:

$$\left(\frac{^{87}\text{Sr}}{^{86}\text{Sr}}\right)_M = \left(\frac{^{87}\text{Sr}}{^{86}\text{Sr}}\right)_A f_A \frac{(\text{Sr})_A}{(\text{Sr})_M} + \left(\frac{^{87}\text{Sr}}{^{86}\text{Sr}}\right)_B (1 - f_A) \frac{(\text{Sr})_B}{(\text{Sr})_M} \quad [2]$$

When two components having different Sr concentrations and isotopic compositions are mixed in varying proportions, the resulting mixtures differ from the end members both in terms of Sr concentration and $^{87}\text{Sr}/^{86}\text{Sr}$ ratio. Both these values can be calculated from the previously defined equations for selected values of the mixing parameter f_A . However most of the times the problem that the geologists have is the opposite, that means that we measure the Sr concentration and $^{87}\text{Sr}/^{86}\text{Sr}$ ratio of a suite of samples and then we wish to test the hypothesis that they derive from the mixing of two components. The desired isotopic mixing equation is derived by solving equation [1] and [2] for f_A and equating the results. The outcome of this algebraic manipulation is: $(^{87}\text{Sr}/^{86}\text{Sr})_M = [a/(\text{Sr})_M] + b$ [3],

where a is equal to $\frac{(\text{Sr})_A(\text{Sr})_B \left[\left(\frac{^{87}\text{Sr}}{^{86}\text{Sr}}\right)_B - \left(\frac{^{87}\text{Sr}}{^{86}\text{Sr}}\right)_A \right]}{(\text{Sr})_A - (\text{Sr})_B}$ and b is $\frac{(\text{Sr})_A \left(\frac{^{87}\text{Sr}}{^{86}\text{Sr}}\right)_A - (\text{Sr})_B \left(\frac{^{87}\text{Sr}}{^{86}\text{Sr}}\right)_B}{(\text{Sr})_A - (\text{Sr})_B}$

Equation [3] is a hyperbola in coordinates of $(\text{Sr})_M$ (x-coordinate) and $(^{87}\text{Sr}/^{86}\text{Sr})_M$ (y-coordinate) whose position and curvature are defined by the numerical values of a and b , which depend entirely on the compositions of the end members.

8.2.1 Isotopic composition of Patagonian clinopyroxenes

The isotopic results measured on separated cpx from four samples of Estancia Sol de Mayo (**Figure 6.19**) and from 29 samples from other localities of Patagonia (**Figures 7.6 and 7.7**), support the idea of the presence of a transitional/alkaline percolating fluid in the peridotitic matrix as previously put forward. Using the equations described in **Chapter 8.2** the mixing percentage of two components, DMM and EM II have been calculated. The compositions of these two end members have been selected on the basis of previous works: the depleted mantle composition is the same used by *Ionov et al., (2002)* and corresponds

8. Discussion

to a residue of about 5% partial melting of a primitive spinel lherzolite; its $^{87}\text{Sr}/^{86}\text{Sr}$ and $^{143}\text{Nd}/^{144}\text{Nd}$ ratios are of 0.70263 and 0.51313 respectively, while the Sr and Nd concentrations are 14.72 and 0.581 ppm respectively. The enriched mantle component is an average of the Kerguelen OIB alkaline basalts (data from GEOROC, <http://georoc.mpch-mainz.gwdg.de/georoc/>). $^{87}\text{Sr}/^{86}\text{Sr}$ ratio is 0.705479 and $^{143}\text{Nd}/^{144}\text{Nd}$ ratio is 0.512634, while its Sr and Nd concentrations are 235 and 14.78 ppm respectively.

In **Figures 8.7** is reported the same figure already presented in Chapter 7 with the mixing hyperbola superimposed. As it is possible to observe the samples do not fall on the mixing line, but they are aligned just below it. Furthermore in the diagram f_A are also indicated. A couple of samples from Cerro de Los Chenques fall very close the DMM composition, while for the other four samples it is possible to infer a mixing with the EM II ranging between 3% and 8%. At Gobernador Gregores and Pali Aike the percentage of EM II involved in the mixing is around 2%, less than that of Cerro de Los Chenques. Cerro Clark is the locality that show the major influence of an enriched component added to the system: it goes from 2-3% up 9%. Finally Estancia Sol de Mayo is characterized by high percentage of the EM II mixed with the DMM, that has been calculated around 5-6%.

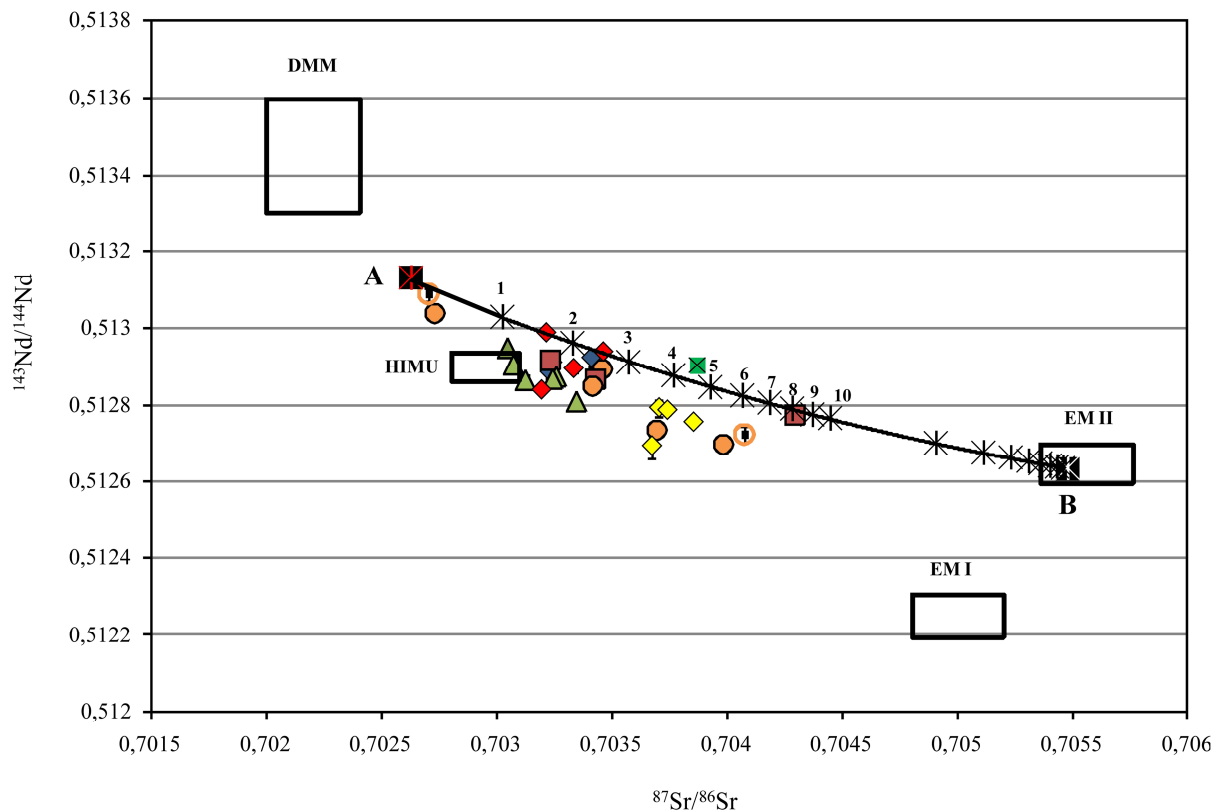


Figure 8.7: $^{143}\text{Nd}/^{144}\text{Nd}$ vs. $^{87}\text{Sr}/^{86}\text{Sr}$ for the 33 samples analyzed. Fields are from Zindler and Hart (1986). The red (A) and white (B) asterisks with black background represent the DMM and EM II compositions of the end-members chosen for the mixing. The solid black line represents the mixing hyperbola. Numbers are the percentages of the EM II component in the mixture. Black asterisks represent the different isotopic compositions of the mixtures.

8.3 Considerations on the lithospheric mantle beneath Patagonia

From the comparison of Chapter 7 it is possible to have an overview of a large area of Patagonia. From the clinopyroxenes study, three different trends are recognized. The cpx from Estancia Sol de Mayo plot along two of these trends together with those from peridotites and pyroxenites from Northern and Central Patagonia. The third trend is that composed of the cpx from the pyroxenites from Northern Patagonia. Furthermore the two diagrams shown in **Figure 7.5** highlight the behaviour of the trace element compositions that are plotted versus Al_2O_3 content. Not only the samples from Estancia Sol de Mayo show a negative correlation between LREE/Sr and Al_2O_3 . Also those from Cerro de los Cenques, Cerro Clark, Praguanyieu and Cerro Fraile are characterized by enrichment in LREE and Sr related to a decrease of the aluminum content, that as explained for the cpx of ESM, can be related to a metasomatic event affecting the mantle. At Gobernador Gregores the situation is more complex, because one group of cpx shows the typical correlation related to partial melting processes, while another group is characterized by the same trend observed for ESM. That means that at Gobernador Gregores there is a clear evidence of a mantle that underwent partial melting, followed by metasomatic event able to increase the LREE/Sr contents. Two localities (Cerro Rio Chubut and Tres Lagos) clearly evidence only to partial melting events, showing a positive correlation between $(\text{La}/\text{Yb})_{\text{N}} - \text{Sr}_{\text{N}}$ and Al_2O_3 . For the latter locality Ntaflos *et al.* (2006) consider this mantle portion as a residuum after partial melting event starting within the garnet stability field and ending within the spinel stability field. No evidence of metasomatic process were detected by the same authors in this locality.

Also the orthopyroxenes from the different localities define two trends, that are the same of those observed for the clinopyroxenes. The story of the cpx can be linked to that of the orthopyroxenes. In fact if we consider, for example, at the mantle xenoliths from ESM the samples containing the cpx affected by the increasing of the Al_2O_3 content, they also

8. Discussion

display the opx characterized by the same enrichment. The same happens for those Al_2O_3 depleted samples.

Finally from the isotopic results shown in the previous Chapters and from the data reported above it is possible to point out a mixing between a depleted and an enriched mantle beneath Patagonia. Although for two investigated localities (Gobernador Gregores and Pali Aike) the percentage of the EM II is very low (around 2%), for Estancia Sol de Mayo, Cerro de Los Chenques and Cerro Clark a mixing of up to 9% of an EM II component has to be considered.

9. Conclusions

A new suite of mantle xenolites from Patagonia has been studied. They have been sampled at the south western corner of the Meseta Lago Buenos Aires, one of the five mesetas comprised in the Triple Junction Province together with the Meseta de la Muerte, Belgrano, Central and the northeastern region and are entrained in the alkaline post-plateau lavas of the MLBA. As described in the geological setting MLBA lavas can be subdivided in two sequences related to the main and to the post-plateau event respectively. $^{40}\text{Ar}/^{39}\text{Ar}$ radiometric ages (**Figure 3.6**) from MLBA main plateau lavas range from 10 to 4.5 Ma with the oldest lavas exposed on the southeast edge of the plateau, while post-plateau lavas range from 3.4 to 0.125 Ma, but most are ≤ 1.8 Ma in age. Chondrite-normalized trace element patterns of the lavas resemble those of the OIB, as well as those of the main and post-plateau from the TJ province, the latter having a slightly higher incompatible trace element concentrations with respect to those of the main plateau. The OIB signature of the samples is also highlighted by the Ba vs. Nb diagram proposed in **Figure 4.5**, in which the samples clearly fall in the field of the within plate composition, together with those of all the other localities belonging to the TJ province.

The xenoliths are represented by anhydrous spinel-bearing harzburgites and dunites, with minor lherzolites and one wehrlite. They are characterized by a coarse grained protogranular texture and they are devoid of modal metasomatic features. They show two texturally different clinopyroxenes. One is protogranular, defined cpx 1, while the second is linked to the spinel (cpx 2). Also three different orthopyroxenes are recognized: one is represented by large protogranular crystals with exsolution lamellae (opx1); the second by small clean and undeformed grains without exsolution lamellae (opx2) and the last occurs as smaller grains arranged in vein (opx3).

On the whole the geochemical features of clinopyroxenes and orthopyroxenes major element compositions highlight three different trends. Two of them are shared by cpx and opx: the first is characterized by high Al_2O_3 content at almost constant mg# (**trend 1**) and the second by a slight increase of the Al_2O_3 content with a decreasing of the mg# (**trend 2**). A third one is observed only for the cpx and is situated in between the other two trends: it comprises the clinopyroxenes of the wehrlites. The trace element concentrations normalized to those of the Chondrite do not show any difference between cpx 1 and cpx 2 (characterized by prominent to slightly negative Nb, Zr and Ti anomalies and LREE

9. Conclusions

enriched), but discriminate the three groups of the orthopyroxenes: one is represented by the opx 3 (those arranged in vein) characterized by a prominent positive Zr anomaly, while the other two show always prominent to slightly negative Ti and Zr anomalies and LREE depleted.

The correlation between incompatible trace elements ($(\text{La/Yb})_N$ and Sr_N) and Al_2O_3 features of the cpx highlight the presence of a refertilization/metasomatic events affecting the Estancia Sol de Mayo upper mantle, evidenced by the enrichment of the LREE and Sr correlated to a decreasing of the Al_2O_3 content. The melt accounted for the refertilization process has a tholeiitic affinity: the hypothesis is supported by the major element compositions of some clinopyroxenes falling in **trend 1** and by the occurrence of secondary orthopyroxene arranged in vein that need a SiO_2 -saturated (or oversaturated) parental melt to crystallize. Because of the lack on the ESM field of tholeiitic lavas, and taking into account the large amount of melt involved in tholeiitic magmatic activity, the most feasible process which can be envisaged is refertilization, i.e. with a melt/rock ratio higher than metasomatism.

A further metasomatic event occurred within the ESM mantle. The interaction affected the trace element compositions of the clinopyroxenes (as described in **chapter 8.1**). The metasomatizing agent is transitional/alkaline in affinity and analogous to the lavas occurring within the various plateaux. This conclusion has been reached by reconstructing the REE pattern of a clinopyroxene in equilibrium with a selected lava from the Somoncuro Province that resemble those of the clinopyroxenes from Estancia Sol de Mayo. This metasomatic event is also evidenced by the isotopic data for some separated ESM cpx that are characterized by high $^{87}\text{Sr}/^{86}\text{Sr}$ and low $^{143}\text{Nd}/^{144}\text{Nd}$ ratios, plotting close to the HIMU field.

From the comparison with other localities already studied it is evident that the Al_2O_3 enrichment observed for both the cpx and the opx is common all over Patagonia. Also the cpx from other Patagonian localities are aligned on the same trends than those defined by the cpx and opx of Estancia Sol de Mayo. Moreover the trace elements features of mantle xenoliths evidence the occurrence in some localities of metasomatic events affecting the upper mantle. Other localities only evidence mantle partial melting events.

Sr-Nd systematic performed for all the localities show a large range of both $^{87}\text{Sr}/^{86}\text{Sr}$ and $^{143}\text{Nd}/^{144}\text{Nd}$ isotopic ratios. This large range is also observed in xenoliths from a same locality (i.e. Cerro de Los Chenques and Cerro Clark). Because some of the samples fall close to the DMM field and the other are aligned toward the EM II end member, some calculations of isotopic mixing have been performed. It has been possible to asses that for the most radiogenic samples up to 9% of an EM II has to be considered in order to account for the samples with the highest Sr and the lowest Nd isotopic ratios.

10. References

- Abe, N., 1997. *Petrology of mantle xenoliths from the arcs: implications for the petrochemical evolution of the wedge mantle*. Ph.D. thesis, Kanazawa University, Kanazawa.
- Abe, N., Arai, S., Yurimoto, H., 1998. *Geochemical characteristics of the uppermost mantle beneath the Japan island arc: implications for upper mantle evolution*. *Physics of the Earth and Planetary Interiors* 107, 233-248.
- Aliani, P., Ntaflos, T., Bjerg, E.A., 2009. *Origin of melt pockets in mantle xenoliths from Southern Patagonia, Argentina*. *Journal of South American Earth Science* 28, 419-428.
- Allmendinger, R. W., Jordan, T. E., Kay, S. M., Isacks, B. L., 1997. *The evolution of the Altiplano-Puna Plateau of the central Andes*. *Annual Reviews of Earth and Planetary Science* 25, 139–174.
- Aoki, K., 1987. *Japanese Island arc: xenoliths in alkali basalts, high-alumina basalts, and calc alkaline andesites and dacites*. In *Mantle Xenoliths*, edited by P. H. Nixon, 319–33, John Wiley & Sons, New York.
- Arai, S., Hirai, H., ABE, N., 1998. *Petrological characteristics of the sub-arc mantle: An overview on petrology of peridotite xenoliths from the Japan arc*. *Trends in Mineralogy (India)* 2, 39–55.
- Arai, S., Ishimaru, S., Okrugin, V. M., 2003. *Metasomatized harzburgite xenoliths from Avacha volcano as fragments of mantle wedge of the Kamchatka arc: an implication for the metasomatic agent*. *Island Arc* 12, 233-246.
- Arai, S., KIDA, M., 2000. *Origin of fine-grained peridotite xenoliths from Iraya volcano of Batan Island, Philippines: Deserpentinization or metasomatism at the wedge mantle beneath an incipient arc?* *The Island Arc* 9, 458–71.
- Ardolino, A., Franchi, M., Remesal, M., Salini, F., 1999. *El volcanismo en la Patagonia extrandina*. In *Geologia Argentina*, edited by R. Caminos. Servicio Geologico Nacional Anales 29, 579–612.

- Baker, P.E., Rea, W.J., 1978. *Compositional variations in the Patagonian plateau basalts. Paper presented at the International Geodynamics Conference, Tokyo.*
- Baker, P.E., Rea, W.J., Skarmeta, J., Caminos, R., Rex, D.C., 1981. *Igneous history of the Andean Cordillera and Patagonian Plateau around latitude 46°S. Philosophical Transaction of the Royal Society of London 303, 105-149.*
- Beccaluva, L., Bianchini, G., Natali, C., Siena, F., 2009. *Continental flood basalts and mantle plume: a case study of the Northern Ethiopian Plateau. Journal of Petrology 50, 1377-1403.*
- Benoit, M., Ceuleneer, G., Polve, M., 1999. *The remelting of hydrothermally altered peridotite at mid-ocean ridges by intruding mantle diapirs. Nature 402, 514 – 518.*
- Bevis, M., 1995. *Geodetic observations of very rapid convergence and back-arc extension at the Tonga arc. Nature 374, 249–251.*
- Bibee, L. D., Shor, J. G. G., Lu, R. S., 1980. *Inter-arc spreading in the Mariana Trough, Marine Geology 35, 183–197.*
- Bjerg, E.A., Ntaflou, T., Kurat, G., Dobosi, G., Labudis, C.H., 2005. *The upper mantle beneath Patagonia, Argentina, documented by xenoliths from alkali basalts. Journal of South American Earth Science 18, 125-145.*
- Brandon, A. D., Draper, D. S., 1996. *Constraints on the origin of the oxidation state of mantle overlying subduction zones: An example from Simcoe, Washington, USA. Geochimica et Cosmochimica Acta 60, 1739–49.*
- Brey, G. P., Köhler, T., 1990. *Geothermobarometry in four-phase lherzolites II. New thermobarometers and practical assessment of existing thermobarometer. Journal of Petrology 31, 1353-1378*
- Busteros, A., Llapido, O., 1983. *Rotas básicas en la vertiente occidental de la meseta Lago Buenos Aires, provincia de Santa Cruz. Revista de la Asociación Geológica Argentina 38, 427-436.*
- Cande, S.C., Leslie, R.B., 1986. *Late Cenozoic tectonics of the Southern Chile Trench. Journal of Geophysical Research 91, 471-496.*

10. References

- Carlson, R. L., 2001. *The abundance of ultramafic rocks in Atlantic Ocean crust. Geophysical Journal International* 144, 37–48.
- Charrier, R., Linares, E., Niemeyer, H. and Skarmeta, J., 1979. *K-Ar ages of basalt flows of the Meseta Buenos Aires in Southern Chile and their relation to the southeast Pacific triple junction. Geology* 7, 436-439.
- Charrier, R., Linares, E., Niemeyer, H., Skarmeta, J., 1978. *Edades Potasio-Argon de vulcanitas mesozoicas y cenozoicas del sector chileno de la meseta Buenos Aires, Aysen, Chile, y su significado tectónico. VII Congreso Geológico Argentino, (Neuquén) Actas II, 23-41.*
- Cloos, M., 1993. *Lithospheric buoyancy and collisional orogenesis: Subduction of oceanic plateaus, continental margins, island arcs, spreading ridges, and seamounts. Geological Society of American Bulletin* 105, 715–737.
- Conceição, R. V., Mallmann, G., Koester, E., Schilling, M., Bertotto, G.W., Rodriguez-Vargas A., 2005. *Andean subduction-related mantle xenoliths: Isotopic evidence of Sr–Nd decoupling during metasomatism. Lithos* 82, 273-287.
- Conceição, R.V., Mallmann, G., Koester, E., Schilling, M., Bertotto, G.W., Rodriguez-Vargas, A., 2005. *Andean subduction-related mantle xenoliths: Isotopic evidence of Sr–Nd decoupling during metasomatism. Lithos* 82, 273-287.
- Corbella, H., 1999. *Dataciones radimétricas en Pali Aike, Patagonia Austral. In: XIV Congreso Geológico Argentino, Actas II, 265–268.*
- Corbella, H., Chelotti, L., Pomposiello, C., 1996. *Neotectónica del rift Jurásico austral en Pali Aike, Patagonia Extranjera, Santa Cruz, Argentina. In: XIII Congreso Geológico Argentino y III Congreso de Exploración de Hidrocarburos, Actas II, 383–393.*
- Corvalán, J., 1981. *Plate tectonic map of the Circum-Pacific region, Southeast Quadrant. Tulsa, OK. American Association of Petroleum Geologists.*
- Cox, K.G., Bell, J. D., Pankhurst, R. J., 1979. *The interpretation of igneous rocks. George Allen and Unwin, London. 450 pp.*

- D’Orazio M., Agostini S., Innocenti F., Haller M., Manetti P., Mazzarini F., 2001. *Slab window-related magmatism from southernmost South America: the Late Miocene mafic volcanics from the Estancia Glencross Area (~52°S, Argentina–Chile)*.
- D’Orazio M., Agostini S., Mazzarini F., Innocenti F., Manetti P., Haller M., Lahsen A., 2000. *The Pali Aike Volcanic Field, Patagonia: slab-window magmatism near the tip of South America. Tectonophysics 321, 407-427.*
- Dahlen, F. A., 1990. *Critical taper model of fold-and-thrust belts and accretionary wedges. Annual Reviews of Earth and Planetary Science 18, 55–99.*
- Dantas, C., 2007. *Caractérisation du manteau supérieur patagonien: les enclaves ultramafiques et mafiques dans les laves alcalines. PhD thesis.*
- Davies, G. F., 1995. *Penetration of plates and plumes through the mantle transition zone, Earth and Planetary Science Letters, 133, 507– 516.*
- Davies, G. F., 1999. *Dynamic Earth, Cambridge University Press, New York.*
- de Ignacio, C., Lopez, I., Oyarzun, R., Marquez, A., 2001. *The northern Patagonia Somuncura plateau basalts: a product of slabinduced, shallow asthenospheric upwelling? Terra Nova 13, 117–121.*
- Dickinson, W. R., 1995. *Forearc basins, in Tectonics of Sedimentary Basins, edited by C. J. Busby and R. V. Ingersoll, 221–261, Blackwell Science, Malden, Mass.*
- Diraison, M., Coppold, P.R., Gapais, D., Rossello, E.A., 1997. *Magellan Strait: part of a Neogene rift system. Geology 25, 703–706.*
- Doglioni, C., Carminati, E., Cuffaro, M., Scrocca, D., 2007. *Subduction kinematics and dynamic constraints. Earth-Science Reviews 83, 127-175.*
- Elliott, T., Plank, T., Zindler, A., White, W., Bourdon, B., 1997. *Element transport from slab to volcanic front at the Mariana arc. Journal of Geophysical Research 102, 14.991–15.019.*
- Ertan, I. E., Leeman, W. P., 1996. *Metasomatism of Cascades subarc mantle: Evidence from a rare phlogopite orthopyroxenite xenolith. Geology 24, 451–4.*

10. References

- Ewart, A., 1982. *The mineralogy and petrology of Tertiary-Recent orogenic volcanic rocks; With special reference to the andesitic-basaltic compositional range*, in *Andesites: Orogenic Andesites and Related Rocks*, edited by R. S. Thorpe, 25–95, John Wiley, New York.
- Fabbri, O., Fournier, M., 1999. *Extension in the southern Ryukyu arc (Japan): Link with oblique subduction and back arc rifting*. *Tectonics* 18, 486–497.
- Faure, G., 1986. *Principles of isotope geology*. Edited by John Wiley and Sons, 606 pages, New York.
- Forsythe, R., Nelson, E., Carr, M.J., Keading, M.E., He & M., Mpodozis, C., Soffia, J.M. and Harnbour, S., 1986. *Pliocene near trench magmatism in Southern Chile: a possible manifestation of ridge collision*. *Geology*, 14: 23-27.
- Franz, L., Becker, K. P., Kramer, W., Herzig, P. M., 2002. *Metasomatic mantle xenoliths from the Bismark microplate (Papua New Guinea) - thermal evolution, geochemistry and extent of slab-induced metasomatism*. *Journal of Petrology* 43, 315-343.
- Fujiwara, T., Yamazaki, T., Joshima, M., 2001. *Bathymetry and magnetic anomalies in the Havre Trough and southern Lau Basin; From rifting to spreading in back-arc basins*. *Earth and Planetary Science Letters* 185, 253–263.
- Gill, J. B., 1981. *Orogenic Andesites and Plate Tectonics*. Springer-Verlag, New York, 1981.
- Gorring, M. L., Kay, S. M., 2000. *Carbonatite metasomatized peridotite xenoliths from southern Patagonia: implications for lithospheric process and Neogene plateau magmatism*. *Contribution to Mineralogy and Petrology* 140, 55-72.
- Gorring, M. L., Kay, S. M., 2001. *Mantle processes and sources of Neogene slab window magmas from Southern Patagonia, Argentina*. *Journal of Petrology* 42, 1067-1094.
- Gorring, M. L., Kay, S. M., Zeitler, P. K., Ramos, V. A., Rubiolo, D., Fernandez, M. I., Panza, J. L., 1997. *Neogene patagonian plateau lavas: continental magmas associated with ridge collision at the Chile Triple Junction*. *Tectonics* 16, 1-17.

Gorring, M. L., Singers, B., gowers, J., Kay, S. M., 2003. *Plio–Pleistocene basalts from the Meseta del Lago Buenos Aires, Argentina: evidence for asthenosphere–lithosphere interactions during slab window magmatism. Chemical Geology 193, 215-235.*

Gorring, M.L., Kay, S.M., 1993. *Temporal and spatial trace element and isotopic variations in Miocene to Recent Patagonian plateau basalts southeast of the Chile Triple Junction (46.5° to 49°S) (abstract). Eos Trans. AGU 74 (16), Spring Meet. Suppl., 324.*

Gorring, M.L., Kay, S.M., 1994. *Isotopic evidence for an OIB-like mantle source for southern Patagonian plateau basalts between 46.50 and 49°S. Geological Society of America, Abstracts Programs 26, A-293.*

Gregoire, M., McInnes, B. I. A., O'Reilly, S. Z., 2001. *Hydrous metasomatism of oceanic sub-arc mantle, Lihir, Papua New Guinea. Part 2. Trace element characteristics of slab-derived fluids. Lithos 59, 91-108.*

Grellet, C., Dubois, J., 1982. *The depth of trenches as a function of the subduction rate and age of the lithosphere. Tectonophysics 82, 45–56.*

Gribble, R. F., Stern, R. J., Newman, S., Bloomer, S. H., O'Hearn, T., 1998. *Chemical and isotopic composition of lavas from the northern Mariana Trough: Implications for magmagenesis in back-arc basins. Journal of Petrology 39, 125–154.*

Grove, T. L., Parman, S. W., Bowring, S. A., Price, R. C., Baker, M. B., 2002. *The role of an H₂O-rich fluid component in the generation of primitive basaltic andesites and andesites from the Mt. Shasta region, N. California. Contribution to Mineralogy and Petrology 142, 375–396.*

Hawkins, J. W., Melchior, J. T., 1985. *Petrology of Mariana Trough and Lau Basin basalts. Journal of Geophysical Research 90(B13), 11.431–11.468.*

Helfrich, G. R., Wood, B. J., 2001. *The Earth's mantle. Nature 412, 501–507.*

Hofmann, A. W., 1997. *Mantle geochemistry: The message from oceanic volcanism. Nature 385, 219–229.*

10. References

- Ionov, D. A., Mukasa, S. B., Bodinier, J. L., 2002. Sr–Nd–Pb isotopic composition of peridotite xenoliths from Spitsbergen: numerical modeling indicates Sr–Nd decoupling in the mantle by melt percolation metasomatism. *Journal of Petrology* 43, 2261–2278.
- Ionov, D. A., 2010. Petrology of Mantle Wedge Lithosphere: New Data on Supra-Subduction Zone Peridotite Xenoliths from the Andesitic Avacha Volcano, Kamchatka. *Journal of Petrology* 51, 327-361.
- Irfune, T., 1993. Phase transformations in the Earth's mantle and subducting slabs: Implications for their compositions, seismic velocity and density structures and dynamics. *Island Arc* 2, 55–71.
- Jarrard, R. D., 1986. Relations among subduction parameters. *Review of Geophysics* 24(2), 217–283.
- Johnson, M. C., Plank, T., 1999. Dehydration and melting experiments constrain the fate of subducted sediments, *Geochemistry Geophysics Geosystems* 1,1007.
- Jordan, T. E., 1995. Retroarc foreland and related basins, in *Tectonics of Sedimentary Basins*, edited by C. J. Busby and Ingersoll, R. V., 331–362, Blackwell, Malden, Mass.
- Karson, J. A., 1998. Internal structure of oceanic lithosphere: A perspective from tectonic windows, in *Faulting and Magmatism at Mid-Ocean Ridges. Geophysical Monograph Series 106*, 177–218. Edited by W. R. Buck et al., AGU, Washington D. C..
- Kay, S. M., Ardolino, A., Gorring, M. L., Ramos, V. A., 2007. The Somoncuro large igneous province in Patagonia: interaction of a trancient mantle thermal anomaly with a subducting slab. *Journal of Petrology* 48, 43-77.
- Kay, S. M., Gorring, M. L., Ramos, V. A., 2004. Magmatic sources, setting and causes of Eocene to Recent Patagonian plateau magmatism (36°S to 52°S latitude). *Revista de la Asociacion Geologica Argentina* 59, 556-568.
- Kay, S. M., Ramos, V. A., Mpodozis, C., Sruoga, P., 1989. Late Paleozoic to Jurassic silicic magmatism at the Gondwanaland margin: analogy to the Middle Proterozoic in North America? *Geology* 17, 324–328.

Kay, S. M., 2001. *Magmatic and tectonic setting of the Neuquén Basin, Argentina, Final Report to Repsol-YPF, (unpublished), 215 pp, Buenos Aires.*

Kay, S. M., 2002a. *Magmatic sources, setting and causes of Eocene to Recent Patagonian plateau magmatism (36°S to 52°S latitude). XV° Congreso Geológico Argentino, Actas 3, 95-100.*

Kay, S. M., 2002b. *Tertiary to Recent transient shallow subduction zones in the central and Southern Andes. XV° Congreso Geológico Argentino, Actas 3, 282-283.*

Kay, S.M., Ramos, V.A., Marquez, M., 1993. *Evidence in Cerro Pampa volcanic rocks for slab-melting prior to ridge-collision in southern South America. Journal of Geology 101, 703- 714.*

Kent, A. J. R., Elliot, T. R., 2002. *Melt inclusions from Marianas arc lavas: implications for the composition and formation of island arc magmas. Chemical Geology 183, 263–286.*

Kepezhinskas, P. K., Defant, M. J., Drummond, M. S., 1995. *Na metasomatism in the island-arc mantle by slab melt-peridotite interaction: evidence from mantle xenoliths in the north Kamchatka arc. Journal of Petrology 36, 1505-1527.*

Kilian, R., Weigand, O., Altherr, R., 1997. *Tertiary to Quaternary Chemical Trends of Basalts from the Cordillera Baguales (50°S): Constraints on the Geotectonic Evolution of the Southernmost Andes. Final Symposium IGCP 345 Evolucion Litosférica de los Andes. Actas VIII Congreso Geológico Chileno 3, 1666–1670.*

Köhler, T., Brey, G. P., 1991. *Ca-exchange between olivine and clinopyroxene as a geothermobarometer calibrated from 2 to 60 kbar in primitive natural lherzolites. Geochimica et Cosmochimica acta 54, 2375-2388*

Lachance, G.R., Trail, R.J., 1966. *Practical solution to the matrix problem in X-ray analysis. Can. Spectr. 11, 43-48.*

Laurora, A., Mazzucchelli, M., Rivalenti, G., Vannucci, R., Zanetti, A., Barbieri, M. A., Cingolani, C. A., 2001. *Metasomatism and melting in carbonatade peridotite xenoliths from the mantle wedge: the Gobernador Gregores case (Southern Patagonia). Journal of Petrology 42, 69-87.*

10. References

- Le Pichon, X., Henry, P., Lallemand, S., 1993. Accretion and erosion in subduction zones: The role of fluids. *Annual Reviews of Earth and Planetary Science* 21, 307–331.
- Linares, E., Gonzalez, R.R., 1990. Catalogo de edades radiometricas de la Republica Argentina 1957–1987. In: *Asociacion Geologica Argentina Publicaciones Especiales, Serie B* 19, 628 pp.
- Luhr, J. F., ARANDA-GOMEZ, J. J., 1997. Mexican peridotite xenoliths and tectonic terranes: Correlations among vent location, texture, temperature, pressure, and oxygen fugacity. *Journal of Petrology* 38, 1075–112.
- Manning, C. E., 1996. Effect of sediment on aqueous silica transport in subduction zones, in *Subduction: Geophysical Monograph Series 96*, edited by G. E. Bebout et al., 277–284, AGU, Washington, D. C..
- Martinez, F., Fryer, P., Baker, N. A., Yamazaki, T., 1995. Evolution of backarc rifting: Mariana Trough, 20°–24°N. *Journal of Geophysical Research* 100(B3), 3807–3828.
- McInnes, B. I. A., Gregoire, M., Binns, R. A., Herzig, P. M., Hannington, M. D., 2001. Hydrous metasomatism of oceanic subarc mantle, Lihir, Papua New Guinea: petrology and geochemistry of fluid-metasomatised mantle wedge xenoliths. *Earth and Planetary Science Letters* 188, 169–183.
- Meglioli, A., 1992. *Glacial geology and geochronology of southernmost Patagonia and Tierra del Fuego, Argentina and Chile. Ph.D. dissertation, Leigh University, Bethlehem, PA.*
- Mercer, J., Sutter, J.F., 1982. Late Miocene–Earliest Pliocene glaciations in southern Argentina: implications for global ice-sheet history. *Palaeogeography, Palaeoclimatology, Palaeoecology* 38, 185–206.
- Mercer, J.H., 1976. Glacial history of southernmost South America. *Quaternary Research* 6, 125–166.
- Mercier, J.C., Nicolas, A., 1975. Textures and fabrics of upper mantle peridotites as illustrated by xenoliths from basalts. *J. Petrol.* 16, 454–487.

- Morris, J. D., Leeman, W. P., Tera, F., 1990. *The subducted component in island arc lavas: Constraints from Be isotopes and B-Be systematic.* *Nature* 344, 31–36.
- Muñoz, J., Troncoso, R., Duhart, P., Crignola, P., Farmer, L., Stern, C. R., 2000. *The relation of the mid-Tertiary coastal magmatic belt in south-central Chile to the late Oligocene increase in plate convergence rate.* *Revista Geologica de Chile* 27, 177–203.
- Newman, S., Stolper, E., Stern, R. J., 2000. *H₂O and CO₂ in magmas from the Mariana arc and back arc systems.* *Geochemistry, Geophysics, Geosystems* 1, (1999GC000027).
- Nichols, G. T., Wyllie, P. J., Stern, C. R., 1996. *Experimental melting of pelagic sediment, constraints relevant to subduction, in Subduction: Top to Bottom, Geophysical Monograph Series 96, edited by G. E. Bebout et al., 293–298, AGU, Washington D. C..*
- Nixon, P. H., 1987. *Mantle Xenoliths.* John Wiley & Sons, New York.
- Ntaflos, T., Bjerg, E. A., Labudia, C. H., Kurat, G., 2006. *Depleted lithosphere from the mantle wedge beneath Tres Lagos, southern Patagonia, Argentina.* *Lithos* 94, 46-65.
- Ntaflos, T., Bjerg, E.A., Labudia, C.H., Kurat, G., 2006. *Depleted lithosphere from the mantle wedge beneath Tres Lagos, Southern Patagonia, Argentina.*
- O'Connor, J. M., Stouffers, P., van den Bogaard, P., McWilliams, M., 1999. *First seamount evidence for significantly slower African plate motion since 19 to 30 Ma.* *Earth and Planetary Science Letters* 171, 575-589.
- Pankhurst, R. J., Rapela, C. W., 1995. *Production of Jurassic rhyolite by anatexis of the lower crust of Patagonia.* *Earth and Planetary Science Letters* 134, 223–236.
- Pawley, A. R., Holloway, J. R., 1993. *Water sources for subduction zone volcanism: New experimental constraints.* *Science* 260, 664–667.
- Peacock, S. M., 2001. *Are the lower planes of double seismic zones caused by serpentine dehydration in subduction oceanic mantle?.* *Geology* 29, 299–302.
- Pearce, J. A., Peate, D. W., 1995. *Tectonic implications of the composition of volcanic arc magmas.* *Annual Reviews of Earth and Planetary Science* 23, 251–285.

10. References

- Perfit, M. R., Gust, D. A., Bence, A. E., Arculus, R. J., Taylor, S. R., 1980. Chemical characteristics of island-arc basalts; implications for mantle sources. *Chemical Geology* 30, 227–256.
- Pike, N.J.E., Schwartzam, E.C., 1977. Classification textures in ultramafic xenoliths. *Journal of Geology* 85, 49–61.
- Plank, T., Langmuir, C. H., 1993. Tracing trace elements from sediment input to volcanic output at subduction zones. *Nature* 362, 739–742.
- Plank, T., Langmuir, C., 1998. The chemical composition of subducting sediment and its consequence for the crust and mantle. *Chemical Geology* 145, 325–394.
- Pouchou, J. L., Pichoir, F. 1984. A new model for quantitative X-ray microanalysis. Part 1: application to the analysis of homogeneous samples. *Recherche Aérospatiale* 5, 13–38.
- Ramos, V.A., 1982. Geologia de la region del lago Cardiel, provincia de Santa Cruz. *Revista de la Asociación Geológica Argentina* 37, 23-49.
- Ramos, V.A., 1989. Foothills structure in Northern Magallanes Basin, Argentina. *American Association of Petroleum Geologist* 73, 887-903.
- Ramos, V.A., Aleman, A., 2000. Tectonic Evolution of the Andes. In: *Tectonic Evolution of South America*, edited by U.G., Cordani, E.J., Milani, A., Thomas Filho, D.A., Campos, 635–685. *International Geological Congress, Rio de Janeiro*.
- Ramos, V.A., Drake, R., 1987. Edad y significado tectónico de la Formación Rio Tarde (Cretácico) Lago Posadas, provincia de San Cruz. *X Congreso Geológico Argentino, Actas I*, 143-148.
- Ramos, V.A., Kay, S.M., 1992. Southern Patagonia plateau basalts and deformation: backarc testimony of ridge collisions. *Tectonophysics* 205, 261–282.
- Rapela, C. W., Spalletti, L. A., Merodio, J. C., Aragon, E., 1988. Temporal evolution and spatial variation of lower Tertiary volcanism in the Patagonian Andes (40°–42°30'S). *Journal of South American Earth Sciences* 1, 75–88.
- Rapela, C. W., Kay, S. M., 1988. Late Paleozoic to Recent magmatic evolution of northern Patagonia. *Episodes* 11, 175-182.

- Rivalenti, G., Mazzucchelli, M., Laurora, A., Ciuffi, S. I. A., Zanetti, A., Vannucci, R., Cingolani, C. A., 2004. The backarc mantle lithosphere in Patagonia, South America. *Journal of South American Earth Science* 17, 121-152.
- Rivalenti, G., Mazzucchelli, M., Zanetti, A., Vannucci, R., Bollinger, C., Hemond, C., Bertotto, G. W., 2007. Xenoliths from Cerro de los Chenques (Patagonia): An example of slab-related metasomatism in the backarc lithospheric mantle. *Lithos* 49, 45-67
- Scambelluri, M., Vannucci, R., De Stefano, A., Preite-Martinez, M., Rivalenti, G., 2008. CO₂ fluid and silicate glass as monitors of alkali basalt/peridotite interaction in the mantle wedge beneath Gobernador Gregores, Southern Patagonia. *Lithos* 107, 121-133.
- Schilling, M., Conceição, R.V., Mallmann, G., Koester, E., Kawashita, K., Hervé, F., Morata, D., Motoki, A., 2005. Spinel-facies mantle xenoliths from Cerro Redondo, Argentine Patagonia: Petrographic, geochemical, and isotopic evidence of interaction between xenoliths and host basalt. *Lithos* 82, 485-502.
- Silver, P.G., Russo, R. M., Lithgow-Bertelloni, C., 1998. Coupling of South American and African plate motion and plate deformation. *Science* 279, 60-63.
- Singer, B.S., Ton-That, T., Vincze, T., Rabassa, J., Roig, C., Brunstad, K., 1997. Timescale of late Cenozoic climate change in the southern hemisphere from ⁴⁰Ar/³⁹Ar dating of Patagonia lavas. *Terra Abstracts, European Union Geoscience* 9, 65–66.
- Sinito, A.M., 1980. Edades geológicas, radiométricas y magnéticas de algunas vulcanitas cenozoicas de las provincias de Santa Cruz y Chubut. *Revista de la Asociación Geológica Argentina* 35, 332-339.
- Smith, D., Riter, J. C. A., 1997. Genesis and evolution of low-Al orthopyroxene in spinel peridotite xenoliths, Grand Canyon field, Arizona, USA. *Contributions to Mineralogy and Petrology* 127, 391–404.
- Smith, D., Riter, J. C. A., Mertzman, S. A., 1999. Erratum to 'Water-rock interactions, orthopyroxene growth and Si-enrichment in the mantle: Evidence in xenoliths from the Colorado Plateau, southwestern United States'. *Earth and Planetary Science Letters* 167, 347–56.

10. References

- Snow, J.E., Hart, S.R., Dick, H.J.B., 1994. Nd and Sr isotope evidence linking mid-ocean-ridge basalts and abyssal peridotites. *Nature* 371, 57 – 60.
- Staudigel, H., Plank, T., White, B., Schmincke H. U., 1996. Geochemical fluxes during seafloor alteration of the basaltic upper oceanic crust: DSDP sites 417 and 418, in *Subduction: Top to Bottom. Geophysical Monograph Series 96*, 19–38. Edited by G. E. Bebout et al., AGU, Washington D. C..
- Stern, C.R., Frey, F.A., Futa, K., Zartman, R.E., Peng, Z., Kyser, T.K., 1990. Trace element and Sr, Nd, Pb, and O isotopic composition of Pliocene and Quaternary alkali basalts of the Patagonian Plateau lavas of southernmost South America. *Contribution to Mineralogy and Petrology* 104, 294-308.
- Stern, C.R., Killian, R., 1996. Role of the subducted slab, mantle wedge, and continental crust in the generation of adakites from the Andean Austral Volcanic Zone. *Contribution to Mineralogy and Petrology* 123, 263- 281.
- Stern, C.R., Killian, R., Olker, B., Hauri, E. H., Kyser, T.K., 1999. Evidence from mantle evolution for relatively thin (<100 km) continental lithosphere below the Phanerozoic crust of southernmost South America. *Lithos* 48, 217-235.
- Stern, R. J., 2002. Subduction zones. *Review of Geophysics* 40, 1-38.
- Stolper, E. M., Newman, S., 1994. The role of water in the petrogenesis of Mariana trough magmas. *Earth and Planetary Science Letters* 121, 293– 325.
- Streckeisen, A. L., 1976. Classification of the common igneous rocks by means of their chemical composition: a provisional attempt. *Neues Jahrbuch für Mineralogie, Monatshefte*, 1976, H. 1, 1-15.
- Sun, S., McDonough, W. F., 1989. Chemical and isotopic systematics of oceanic basalts: implications for mantle composition and processes. In: *Magmatism in the ocean basins*, edited by Saunders, A. D., Norry, M. J., Geological Society of London, London, 313-345.
- Takahashi, E., 1978. Petrologic model of the crust and upper mantle of the Japanese island arcs. *Bulletin Volcanologique* 41, 529–47.
- Tatsumi, Y., Eggins, S., 1995. *Subduction Zone Magmatism*, Blackwell, Malden, Mass.

- Taylor, B., Klaus, A., Brown, G. R., Moore, G. F., Okamura, Y., Murakami, F., 1991. *Structural development of Sumisu Rift, Izu-Bonin arc*, *Journal of Geophysical Research* 96, 113–129.
- Thon-That, T., Singer, B., Mörner, N. A., Rabassa, J., 1999. *Datacion de lavas basálticas por $^{40}\text{Ar}/^{39}\text{Ar}$ y geología glacial de la region del lago Buenos Aires, provincia de Santa Cruz, Argentina*. *Revista de la Asociación Geológica Argentina* 54, 333–352.
- Thorpe, R. S., Francis, P. W., Hamill, M., Baker, M. C. W., 1982. *The Andes, in Andesite: orogenic andesites and related rocks*, edited by R. S. Thorpe, 187-205, Chichester: Wiley.
- Ulmer, P., Trommsdorf, V., 1995. *Serpentine stability to mantle depths and subduction-related magmatism*, *Science* 268, 858–861.
- von Huene, R., Scholl, D. W., 1991. *Observations at convergent margins concerning sediment subduction, subduction erosion, and the growth of continental crust*. *Reviews of Geophysics* 29, 279–316.
- Wallace, P. J., 2005. *Volatiles in subduction zone magmas: concentration and fluxes based on melt inclusion and volcanic gas data*.
- Yuan, X., 2000. *Subduction and collision processes in the central Andes constrained by converted seismic phases*. *Nature* 408, 958–961.
- Zindler, A., Hart, S. R., 1986. *Chemical geodynamics*. *Annual Reviews of Earth and Planetary Science* 14, 493-571.



Your E-Mail Address

mlcsm1@unife.it

Subject

Dichiarazione di conformità

Io sottoscritto Dott. (Cognome e Nome)

Melchiorre Massimiliano

nato a

Mesagne

Provincia

Brindisi

il giorno

16/07/1982

avendo frequentato il corso di Dottorato di Ricerca in:

Scienze della Terra

Ciclo di Dottorato

XXIII

Titolo della tesi in Italiano

Petrologia degli xenoliti di mantello soprasubduttivo di Estancia Sol de Mayo (Patagonia Centrale, Argentina)

Titolo della tesi in Inglese

Petrology of suprasubductive mantle xenoliths from Estancia Sol De Mayo (Central Patagonia, Argentina)

Titolo della tesi in altra Lingua Straniera

Tutore - Prof:

Massimo COLTORTI, Michel GREGOIRE

Settore Scientifico Disciplinare (SSD)

GEO/07

Parole chiave (max 10)

Patagonia, xenoliti di mantello, metasomatismo, rifertilizzazione

Consapevole - Dichiaro

CONSAPEVOLE --- 1) del fatto che in caso di dichiarazioni mendaci, oltre alle sanzioni previste dal codice penale e dalle Leggi speciali per l'ipotesi di falsità in atti ed uso di atti falsi, decade fin dall'inizio e senza necessità di alcuna formalità dai benefici conseguenti al provvedimento emanato sulla base di tali dichiarazioni; -- 2) dell'obbligo per l'Università di provvedere al deposito di legge delle tesi di dottorato al fine di assicurarne la conservazione e la consultabilità da parte di terzi; -- 3) della procedura adottata dall'Università di Ferrara ove si richiede che la tesi sia consegnata dal dottorando in 4 copie di cui una in formato cartaceo e tre in formato .pdf, non modificabile su idonei supporti (CD-ROM, DVD) secondo le istruzioni pubblicate sul sito : <http://www.unife.it/dottorati/dottorati.htm> alla voce ESAME FINALE – disposizioni e modulistica; -- 4) del fatto che l'Università sulla base dei dati forniti, archiverà e renderà consultabile in rete il testo completo della tesi di dottorato di cui alla presente dichiarazione attraverso l'Archivio istituzionale ad accesso aperto "EPRINTS.unife.it" oltre che attraverso i Cataloghi delle Biblioteche Nazionali Centrali di Roma e Firenze. --- DICHIARO SOTTO LA MIA RESPONSABILITA' --- 1) che la copia della tesi depositata presso l'Università di Ferrara in formato cartaceo, è del tutto identica a quelle presentate in formato elettronico (CD-ROM, DVD),

a quelle da inviare ai Commissari di esame finale e alla copia che produrrò in seduta d'esame finale. Di conseguenza va esclusa qualsiasi responsabilità dell'Ateneo stesso per quanto riguarda eventuali errori, imprecisioni o omissioni nei contenuti della tesi; -- 2) di prendere atto che la tesi in formato cartaceo è l'unica alla quale farà riferimento l'Università per rilasciare, a mia richiesta, la dichiarazione di conformità di eventuali copie; -- 3) che il contenuto e l'organizzazione della tesi è opera originale da me realizzata e non compromette in alcun modo i diritti di terzi, ivi compresi quelli relativi alla sicurezza dei dati personali; che pertanto l'Università è in ogni caso esente da responsabilità di qualsivoglia natura civile, amministrativa o penale e sarà da me tenuta indenne da qualsiasi richiesta o rivendicazione da parte di terzi; -- 4) che la tesi di dottorato non è il risultato di attività rientranti nella normativa sulla proprietà industriale, non è stata prodotta nell'ambito di progetti finanziati da soggetti pubblici o privati con vincoli alla divulgazione dei risultati, non è oggetto di eventuali registrazioni di tipo brevettale o di tutela. --- PER

ACCETTAZIONE DI QUANTO SOPRA RIPORTATO

Firma Dottorando

Ferrara, li 16/02/2011 Firma del Dottorando

Massimiliano Melchiorri

Firma Tutore

Visto: Il Tutore Si approva Firma del Tutore

[Signature]

Appendix: Analytical methods

This study is based on the major and trace elements characterization of the mineral phases of Patagonian mantle xenoliths measured in Electron Microprobe (EMP) and major and trace element compositions of the entraining lavas performed with X-Ray Fluorescence (XRF). Furthermore $^{87}\text{Sr}/^{86}\text{Sr}$ and $^{143}\text{Nd}/^{144}\text{Nd}$ have been measured on separated clinopyroxenes with Thermal Ionization Mass Spectrometer (TIMS). All the analysis have been performed at the UMR 5563 (LMTG, Observatoire Midi-Pyrenees) of the University Paul Sabatier (Toulouse III), except the bulk rock composition of the lava, performed at the University of Ferrara.

Major element compositions of minerals were determined with the CAMECA SX50 electron microprobe and a standard program: beam current of 20 nA and an acceleration voltage of 15 kV, 10 – 30 s of peak counting, 10 s of background counting, and natural and synthetic minerals as standards. Nominal concentrations were subsequently corrected using the PAP data reduction method (*Pouchou & Pichoir 1984*). The theoretical lower limits of detection are about 100 ppm (0.01%).

Concentrations of REE and trace elements in clinopyroxene and orthopyroxene were determined in situ using the Agilent 7500 ICP – MS instrument (Observatoire Midi Pyrénées, University Toulouse III) coupled either to CETAC laser ablation module that uses a 266 nm frequency-quadrupled Nd-YAG laser or either to a commercial femtosecond Ti : Sa laser system (Amplitude Technologies Pulsar 10) based on the Chirped-pulse amplification (CPA) technique. Pulses are amplified in this set-up by a regenerative and a multipass amplifier up to 12 mJ. This system provides laser pulses at 800 nm with a variable pulse energy and a pulse duration as short as 50 fs. Its contrast on 10 ps is of the order of 10^{-7} . Its repetition rate can be varied between 1 Hz and 10 Hz. The shot-to-shot stability (RMS) is 2 %. The linearly polarized laser beam is injected in a BX51 microscope (Olympus). The beam is reflected by a 45° dielectric mirror and focused down to the sample placed in an ablation cell mounted on a XY stage, using a 0.9 Cassegrain objective. The NIST 610 and NIST 612 glass standards were used to calibrate relative element sensitivities. Each analysis was normalized using CaO values first determined by electron microprobe. A beam diameter of 50 – 100 μm and a scanning rate of 20 $\mu\text{m}/\text{s}$ were used.

The theoretical limits of detection range from 10 – 20 ppb for REE, Ba, Th, U, Zr to 2 ppm for Ti. The accuracy on a typical laser analysis is between 1 and 10%.

Whole-rock major and some trace elements (Zn, Cu, Sc, Ga, Ni, Co, Cr, V, Rb, Ba, Th, Nb, Sr, Zr, and Y) were obtained by X-ray fluorescence (XRF) on pressed-powder pellets, using an ARL Advant-XP automated X-ray spectrometer. Calibration was performed using international reference samples (some of which were also run as unknowns in order to determine accuracy and detection limits), and the matrix correction method proposed by *Lachance and Trail (1966)* was applied. Mean accuracies were generally better than 2% for major oxides, and 5% for trace element determinations, while the detection limits for trace elements were: Zn, Ba, Cu, Sc = 5 ppm; Ni, Co, Cr, V, Rb, Y, Th, Nb = 1 ppm; and Sr, Zr, Ga = 2 ppm. Volatile contents were determined as loss on ignition at 1000 °C.

Measurements of Sr and Nd isotopic ratios were realised on leached hand picked clinopyroxenes, following the method described in *Snow et al. (1994)* and used in *Benoit et al. (1999)*, in order to reduce the effect of the hydrothermal fluid-rocks interactions which affect principally the $^{87}\text{Sr}/^{86}\text{Sr}$ ratios. Leached clinopyroxenes underwent acid digestion with a mixture of HF–HClO₄ at 140 °C, to prevent the formation of Ca fluorides which trap REE. Drying of the samples was made at the same temperature until the complete evaporation of HClO₄. Chemical separation was performed on combined Sr-Spec/Thru-Spec columns. The Sr cut was processed again through the same column to efficiently separate Sr from Rb and Ca while Nd was further eluted on LnSpec Eichrom resin. Isotopic measurements were conducted on a Finnigan Mat 261 for all measurements. Sr was run on a single W filament with Ta activator, while Nd was run on a Re double filament. The NBS 987 (for Sr) and La Jolla (for Nd) standards were run regularly to check the measurements: average value $^{87}\text{Sr}/^{86}\text{Sr} = 0.710248 \pm 0.000020$ (n = 17, Triton mass spectrometer), average value $^{87}\text{Sr}/^{86}\text{Sr} = 0.710246 \pm 0.000012$ (n = 23, Mat 261 mass spectrometer), and average value $^{143}\text{Nd}/^{144}\text{Nd} = 0.511853 \pm 0.000010$ (n = 16, Triton mass spectrometer). Blanks were <650 pg for Sr and <350 pg for Nd.

Sample Area	MG2b2 Lh												MG1b Hz											
	Area 3		Area 3		Area 4		Area 4		Area 5		Area 6		Area 3		Area 4		Area 4		Area 5		Area 8		Area 8	
	5	7	8	ol	rim	ol	rim	ol	rim	ol	rim	ol	core	ol	core	ol	core	ol	core	ol	rim	ol	core	ol
Host rock	Lh	Lh	Lh	Lh	Lh	Lh	Lh	Lh	Lh	Lh	Lh	Lh	Lh	Hz	Hz	Hz	Hz	Hz	Hz	Hz	Hz	Hz	Hz	Hz
SiO ₂	42,07	41,97	40,96	41,07	41,46	40,35	40,70	40,24	39,52	40,60	40,32	40,01	40,17	40,35	40,39	40,19	0,00	0,00	0,00	0,00	0,00	0,00	0,00	0,00
ThO ₂	0,00	0,00	0,00	0,00	0,00	0,02	0,02	0,00	0,00	0,00	0,00	0,00	0,00	0,00	0,00	0,00	0,00	0,00	0,00	0,00	0,00	0,00	0,00	0,00
Al ₂ O ₃	0,00	0,00	0,00	0,00	0,00	0,00	0,00	0,00	0,00	0,00	0,00	0,00	0,00	0,00	0,00	0,00	0,00	0,00	0,00	0,00	0,00	0,00	0,00	0,00
FeO	8,70	9,12	9,21	8,71	9,28	8,81	8,94	8,88	8,86	8,83	11,13	11,60	11,55	11,73	11,25	11,71	0,22	0,17	0,11	0,24	0,22	0,17	0,17	0,17
MnO	0,11	0,10	0,15	0,11	0,14	0,14	0,09	0,12	0,07	0,15	48,63	48,08	47,18	48,11	47,68	47,67	0,05	0,09	0,11	0,10	0,09	0,09	0,09	0,09
MgO	51,13	50,35	49,74	49,65	50,17	50,20	50,32	49,35	49,79	49,95	0,00	0,00	0,00	0,00	0,00	0,00	0,00	0,00	0,00	0,00	0,00	0,00	0,00	0,00
CaO	0,09	0,05	0,07	0,07	0,05	0,06	0,07	0,12	0,12	0,10	0,00	0,00	0,00	0,00	0,00	0,00	0,00	0,00	0,00	0,00	0,00	0,00	0,00	0,00
Na ₂ O	0,00	0,00	0,00	0,00	0,00	0,00	0,00	0,00	0,00	0,00	0,00	0,00	0,00	0,00	0,00	0,00	0,00	0,00	0,00	0,00	0,00	0,00	0,00	0,00
K ₂ O	0,00	0,00	0,00	0,00	0,00	0,00	0,00	0,00	0,00	0,00	0,00	0,00	0,00	0,00	0,00	0,00	0,37	0,46	0,00	0,38	0,34	0,34	0,34	0,34
NiO	0,44	0,00	0,00	0,00	0,31	0,28	0,42	0,47	0,35	0,35	0,03	0,11	0,17	0,04	0,12	0,00	0,03	0,11	0,17	0,04	0,12	0,00	0,00	0,00
Cr ₂ O ₃	0,06	0,03	0,03	0,07	0,02	0,00	0,00	0,00	0,02	0,00	100,75	100,52	99,29	100,95	100,09	100,17	0,996	0,988	0,992	0,997	0,998	0,993	0,993	0,993
Tot	102,60	101,62	100,16	99,68	101,43	99,86	100,56	99,18	98,73	99,98	0,000	0,000	0,000	0,000	0,000	0,000	0,000	0,000	0,000	0,000	0,000	0,000	0,000	0,000
Si	1,039	1,037	1,012	1,015	1,024	0,997	1,005	0,994	0,976	1,003	0,996	0,988	0,992	0,997	0,998	0,993	0,000	0,000	0,000	0,000	0,000	0,000	0,000	0,000
Ti	0,000	0,000	0,000	0,000	0,000	0,000	0,000	0,000	0,000	0,000	0,000	0,000	0,000	0,000	0,000	0,000	0,000	0,000	0,000	0,000	0,000	0,000	0,000	0,000
Al6	0,000	0,000	0,000	0,000	0,000	0,000	0,000	0,000	0,000	0,000	0,000	0,000	0,000	0,000	0,000	0,000	0,000	0,000	0,000	0,000	0,000	0,000	0,000	0,000
Fe2	0,180	0,188	0,190	0,180	0,192	0,182	0,185	0,183	0,183	0,182	0,230	0,240	0,239	0,242	0,232	0,242	0,005	0,004	0,002	0,005	0,005	0,005	0,004	0,004
Mn	0,002	0,002	0,003	0,002	0,003	0,003	0,002	0,003	0,001	0,003	1,791	1,770	1,737	1,772	1,756	1,755	0,001	0,002	0,003	0,003	0,002	0,002	0,002	0,002
Mg	1,883	1,854	1,832	1,828	1,847	1,849	1,853	1,817	1,833	1,839	0,000	0,000	0,000	0,000	0,000	0,000	0,000	0,000	0,000	0,000	0,000	0,000	0,000	0,000
Ca	0,002	0,001	0,002	0,002	0,001	0,002	0,002	0,003	0,003	0,003	0,000	0,000	0,000	0,000	0,000	0,000	0,000	0,000	0,000	0,000	0,000	0,000	0,000	0,000
Na	0,000	0,000	0,000	0,000	0,000	0,000	0,000	0,000	0,000	0,000	0,000	0,000	0,000	0,000	0,000	0,000	0,000	0,000	0,000	0,000	0,000	0,000	0,000	0,000
K	0,000	0,000	0,000	0,000	0,000	0,000	0,000	0,000	0,000	0,000	0,000	0,000	0,000	0,000	0,000	0,000	0,000	0,000	0,000	0,000	0,000	0,000	0,000	0,000
Ni	0,009	0,000	0,000	0,000	0,006	0,006	0,008	0,009	0,007	0,007	0,007	0,009	0,000	0,008	0,007	0,007	0,000	0,000	0,000	0,000	0,000	0,000	0,000	0,000
Cr	0,001	0,000	0,000	0,001	0,000	0,000	0,000	0,000	0,000	0,000	0,000	0,001	0,002	0,000	0,001	0,000	0,000	0,001	0,002	0,000	0,001	0,001	0,001	0,000
totale	3,116	3,083	3,039	3,028	3,074	3,038	3,056	3,010	3,005	3,037	3,030	3,015	2,975	3,026	3,001	3,003	88,62	88,08	87,92	87,97	88,31	87,89	87,89	87,89
Fo	91,29	90,77	90,59	91,04	90,60	91,04	90,94	90,83	90,92	90,98	11,38	11,92	12,08	12,03	11,69	12,11	88,62	88,08	87,92	87,97	88,31	87,89	87,89	87,89
Fa	8,71	9,23	9,41	8,96	9,40	8,96	9,06	9,17	9,08	9,02	11,38	11,92	12,08	12,03	11,69	12,11	11,38	11,92	12,08	12,03	11,69	12,11	12,11	12,11

Appendix 1: Major element composition of olivines

Sample Area	MGPIc Hz										MGPIg Hz									
	Area 1		Area 2		Area 3		Area 4		Area 4		Area 1		Area 2		Area 3		Area 4		Area 5	
	5	6	3	4	7	8	9	10	3	4	5	6	3	3	3	3	10	11	3	4
point	ol	ol	ol	ol	ol	ol	ol	ol	ol	ol	ol	ol	ol	ol	ol	ol	ol	ol	ol	ol
phase	rim	core	rim	core	core	rim	rim	core	core	core	core	core	core	core	core	core	core	core	core	core
rim/core	Hz	Hz	Hz	Hz	Hz	Hz	Hz	Hz	Hz	Hz	Hz	Hz	Hz	Hz	Hz	Hz	Hz	Hz	Hz	Hz
Host rock																				
SiO ₂	41,00	40,65	41,00	40,80	41,41	41,30	40,78	40,65		39,22	39,77	39,81	39,95	39,69	40,05	39,75				
TiO ₂	0,00	0,00	0,00	0,00	0,00	0,00	0,00	0,00		0,00	0,00	0,00	0,00	0,00	0,00	0,00				
Al ₂ O ₃	0,00	0,00	0,00	0,00	0,00	0,00	0,00	0,00		0,00	0,00	0,00	0,00	0,00	0,00	0,00				
FeO	9,39	9,59	9,15	9,49	9,55	9,41	9,74	9,47		15,28	14,35	14,52	14,61	14,67	14,14	14,63				
MnO	0,13	0,12	0,14	0,14	0,16	0,18	0,10	0,11		0,32	0,21	0,23	0,16	0,22	0,16	0,20				
MgO	50,08	50,11	50,43	49,94	50,47	50,43	50,16	50,23		45,61	46,13	46,05	46,11	45,74	46,15	45,81				
CaO	0,08	0,05	0,07	0,05	0,08	0,03	0,05	0,07		0,09	0,08	0,12	0,07	0,07	0,13	0,07				
Na ₂ O	0,00	0,00	0,00	0,00	0,00	0,00	0,00	0,00		0,00	0,00	0,00	0,00	0,00	0,00	0,00				
K ₂ O	0,00	0,00	0,00	0,00	0,00	0,00	0,00	0,00		0,00	0,00	0,00	0,00	0,00	0,00	0,00				
NiO	0,27	0,42	0,31	0,38	0,43	0,52	0,00	0,35		0,27	0,23	0,20	0,21	0,17	0,25	0,24				
Cr ₂ O ₃	0,00	0,00	0,08	0,00	0,04	0,00	0,02	0,07		0,03	0,00	0,00	0,09	0,02	0,06	0,01				
Tot	100,95	100,94	101,18	100,80	102,14	101,87	100,85	100,95		101,71	100,13	100,74	101,20	100,58	100,94	100,71				
Si	1,013	1,004	1,013	1,008	1,023	1,020	1,007	1,004		0,991	0,969	0,983	0,987	0,981	0,989	0,982				
Ti	0,000	0,000	0,000	0,000	0,000	0,000	0,000	0,000		0,000	0,000	0,000	0,000	0,000	0,000	0,000				
Al6	0,000	0,000	0,000	0,000	0,000	0,000	0,000	0,000		0,000	0,000	0,000	0,000	0,000	0,000	0,000				
Fe2	0,194	0,198	0,189	0,196	0,197	0,194	0,201	0,196		0,316	0,310	0,296	0,302	0,303	0,292	0,302				
Mn	0,003	0,003	0,003	0,003	0,003	0,004	0,002	0,002		0,007	0,004	0,004	0,003	0,005	0,003	0,004				
Mg	1,844	1,845	1,857	1,839	1,858	1,857	1,847	1,850		1,679	1,673	1,699	1,698	1,684	1,699	1,687				
Ca	0,002	0,001	0,002	0,001	0,002	0,001	0,001	0,002		0,002	0,001	0,002	0,002	0,002	0,003	0,002				
Na	0,000	0,000	0,000	0,000	0,000	0,000	0,000	0,000		0,000	0,000	0,000	0,000	0,000	0,000	0,000				
K	0,000	0,000	0,000	0,000	0,000	0,000	0,000	0,000		0,000	0,000	0,000	0,000	0,000	0,000	0,000				
Ni	0,005	0,008	0,006	0,008	0,009	0,010	0,000	0,007		0,005	0,005	0,004	0,004	0,003	0,005	0,005				
Cr	0,000	0,000	0,001	0,000	0,000	0,000	0,000	0,001		0,000	0,000	0,000	0,001	0,000	0,001	0,000				
totale	3,061	3,060	3,071	3,055	3,093	3,087	3,059	3,061		3,001	2,962	2,988	2,997	2,978	2,993	2,982				
Fo	90,48	90,30	90,76	90,37	90,40	90,52	90,18	90,43		84,18	84,36	85,14	84,91	84,75	85,33	84,80				
Fa	9,52	9,70	9,24	9,63	9,60	9,48	9,82	9,57		15,82	15,64	14,86	15,03	15,25	14,67	15,20				

Sample Area	MGP3b Hz																																
	Area 1			Area 2			Area 3			Area 4			Area 5			Area 6			Area 7														
	3	4	ol	9	ol	rim	10	ol	core	9	ol	rim	10	ol	core	5	ol	rim	6	ol	core	3	ol	rim	4	ol	core	3	ol	rim	4	ol	core
point	ol	core	Hz	ol	rim	Hz	ol	core	Hz	ol	rim	Hz	ol	core	Hz	ol	rim	Hz	ol	core	Hz	ol	rim	Hz	ol	core	Hz	ol	rim	Hz	ol	core	Hz
rim/core	core	Hz		rim	Hz		core	Hz		rim	Hz		core	Hz		rim	Hz		core	Hz		rim	Hz		core	Hz		rim	Hz		core	Hz	
Host rock	Hz			Hz			Hz			Hz			Hz			Hz			Hz			Hz			Hz			Hz			Hz		
SiO ₂	39,36	40,89	40,83	40,75	41,03	40,69	40,76	40,95	41,33	41,10	40,96	41,04	40,97	40,91	40,83																		
TiO ₂	0,01	0,00	0,00	0,00	0,01	0,00	0,00	0,00	0,00	0,00	0,00	0,01	0,00	0,00	0,00																		
Al ₂ O ₃	0,00	0,00	0,00	0,00	0,00	0,00	0,00	0,00	0,00	0,00	0,00	0,00	0,00	0,00	0,00																		
FeO	13,97	9,74	10,60	9,45	9,10	9,12	9,09	9,29	9,42	9,10	8,98	9,20	9,44	9,36	9,45																		
MnO	0,27	0,12	0,20	0,08	0,13	0,15	0,08	0,18	0,11	0,06	0,27	0,13	0,21	0,21	0,13																		
MgO	46,11	49,36	49,13	50,17	49,91	50,01	49,54	50,08	49,89	49,84	49,83	49,70	49,66	50,23	49,97																		
CaO	0,05	0,04	0,08	0,07	0,07	0,07	0,07	0,06	0,07	0,08	0,11	0,03	0,06	0,07	0,09																		
Na ₂ O	0,00	0,00	0,00	0,00	0,00	0,00	0,00	0,00	0,00	0,00	0,00	0,00	0,00	0,00	0,00																		
K ₂ O	0,00	0,00	0,00	0,00	0,00	0,00	0,00	0,00	0,00	0,00	0,00	0,00	0,00	0,00	0,00																		
NiO	0,29	0,00	0,35	0,35	0,40	0,38	0,34	0,33	0,32	0,46	0,32	0,00	0,00	0,33	0,33																		
Cr ₂ O ₃	0,03	0,08	0,07	0,02	0,04	0,00	0,03	0,07	0,00	0,05	0,03	0,05	0,00	0,00	0,03																		
Tot	100,09	100,23	101,26	100,89	100,69	100,42	99,91	100,96	101,14	100,69	100,50	100,16	100,34	101,11	100,83																		
Si	0,972	1,010	1,009	1,007	1,014	1,005	1,007	1,012	1,021	1,015	1,012	1,014	1,012	1,011	1,009																		
Ti	0,000	0,000	0,000	0,000	0,000	0,000	0,000	0,000	0,000	0,000	0,000	0,000	0,000	0,000	0,000																		
Al6	0,000	0,000	0,000	0,000	0,000	0,000	0,000	0,000	0,000	0,000	0,000	0,000	0,000	0,000	0,000																		
Fe2	0,289	0,201	0,219	0,195	0,188	0,188	0,188	0,192	0,195	0,188	0,186	0,190	0,195	0,193	0,195																		
Mn	0,006	0,003	0,004	0,002	0,003	0,003	0,002	0,004	0,002	0,001	0,006	0,003	0,004	0,004	0,003																		
Mg	1,698	1,818	1,809	1,847	1,838	1,842	1,824	1,844	1,837	1,835	1,835	1,830	1,829	1,850	1,840																		
Ca	0,001	0,001	0,002	0,002	0,002	0,002	0,002	0,002	0,002	0,002	0,003	0,001	0,002	0,002	0,002																		
Na	0,000	0,000	0,000	0,000	0,000	0,000	0,000	0,000	0,000	0,000	0,000	0,000	0,000	0,000	0,000																		
K	0,000	0,000	0,000	0,000	0,000	0,000	0,000	0,000	0,000	0,000	0,000	0,000	0,000	0,000	0,000																		
Ni	0,006	0,000	0,007	0,007	0,008	0,008	0,007	0,007	0,006	0,009	0,006	0,000	0,000	0,007	0,007																		
Cr	0,000	0,001	0,001	0,000	0,000	0,000	0,000	0,001	0,000	0,000	0,000	0,000	0,000	0,000	0,000																		
totale	2,972	3,033	3,051	3,060	3,053	3,048	3,030	3,060	3,063	3,052	3,048	3,038	3,042	3,066	3,056																		
Fo	85,47	90,03	89,20	90,44	90,72	90,72	90,67	90,57	90,42	90,71	90,82	90,59	90,36	90,53	90,41																		
Fa	14,53	9,97	10,80	9,56	9,28	9,28	9,33	9,43	9,58	9,29	9,18	9,41	9,64	9,47	9,59																		

Sample Area	MGP1h Du										MGP2a Du									
	Area 3		Area 4		Area 4		Area 4		Area 5		Area 3		Area 1		Area 2		Area 2		Area 4	
	3	4	4	5	4	6	4	5	4	5	3	4	3	4	3	4	3	4	7	8
point	ol	ol	ol	ol	ol	ol	ol	ol	ol	ol	ol	ol	ol	ol	ol	ol	ol	ol	ol	ol
phase	core	rim	core	core	core	core	core	rim	core	core	rim	rim	rim	core	rim	core	rim	core	rim	core
rim/core	Du	Du	Du	Du	Du	Du	Du	Du	Du	Du	Du	Du	Du	Du	Du	Du	Du	Du	Du	Du
Host rock																				
SiO ₂	40,68	40,92	40,43	40,18	40,83	41,11	40,95	40,84	40,84	40,84	39,87	39,63	39,96	40,13	39,94	40,34	39,94	40,34	40,34	40,34
TiO ₂	0,00	0,00	0,00	0,00	0,00	0,00	0,00	0,00	0,00	0,00	0,03	0,00	0,00	0,01	0,00	0,01	0,00	0,00	0,00	0,01
Al ₂ O ₃	0,00	0,00	0,00	0,00	0,00	0,00	0,00	0,00	0,00	0,00	0,00	0,00	0,00	0,00	0,00	0,00	0,00	0,00	0,00	0,00
FeO	9,48	9,55	9,14	9,52	9,76	9,34	9,20	9,51	9,51	9,51	9,76	10,32	10,16	10,30	9,75	9,67	9,75	9,67	9,67	9,67
MnO	0,17	0,13	0,17	0,17	0,14	0,21	0,19	0,14	0,14	0,14	0,14	0,24	0,23	0,12	0,21	0,15	0,21	0,15	0,15	0,15
MgO	49,59	49,27	49,01	49,63	49,69	49,61	49,41	49,40	49,40	49,40	48,94	49,20	48,77	48,61	48,91	49,08	48,91	49,08	49,08	49,08
CaO	0,05	0,08	0,00	0,09	0,00	0,00	0,04	0,04	0,04	0,04	0,08	0,05	0,06	0,07	0,08	0,07	0,08	0,07	0,07	0,07
Na ₂ O	0,00	0,00	0,00	0,00	0,00	0,00	0,00	0,00	0,00	0,00	0,00	0,00	0,00	0,00	0,00	0,00	0,00	0,00	0,00	0,00
K ₂ O	0,00	0,00	0,00	0,00	0,00	0,00	0,00	0,00	0,00	0,00	0,00	0,00	0,00	0,00	0,00	0,00	0,00	0,00	0,00	0,00
NiO	0,34	0,40	0,38	0,30	0,36	0,40	0,00	0,00	0,00	0,00	0,21	0,45	0,36	0,40	0,45	0,23	0,40	0,45	0,23	0,23
Cr ₂ O ₃	0,00	0,02	0,16	0,01	0,05	0,01	0,01	0,07	0,07	0,07	0,00	0,03	0,00	0,01	0,00	0,04	0,01	0,00	0,04	0,04
Tot	100,31	100,37	99,29	99,90	100,83	100,68	99,80	100,00	100,00	100,00	99,03	99,92	99,54	99,65	99,34	99,59	99,65	99,34	99,34	99,59
Si	1,005	1,011	0,999	0,993	1,009	1,016	1,012	1,009	1,009	1,009	0,985	0,979	0,987	0,991	0,987	0,997	0,991	0,987	0,987	0,997
Ti	0,000	0,000	0,000	0,000	0,000	0,000	0,000	0,000	0,000	0,000	0,001	0,000	0,000	0,000	0,000	0,000	0,000	0,000	0,000	0,000
Al6	0,000	0,000	0,000	0,000	0,000	0,000	0,000	0,000	0,000	0,000	0,000	0,000	0,000	0,000	0,000	0,000	0,000	0,000	0,000	0,000
Fe2	0,196	0,197	0,189	0,197	0,202	0,193	0,190	0,196	0,196	0,196	0,202	0,213	0,210	0,213	0,201	0,200	0,213	0,201	0,201	0,200
Mn	0,004	0,003	0,004	0,004	0,003	0,004	0,004	0,003	0,003	0,003	0,003	0,005	0,005	0,005	0,004	0,003	0,005	0,004	0,004	0,003
Mg	1,826	1,814	1,805	1,828	1,830	1,827	1,819	1,819	1,819	1,819	1,802	1,812	1,796	1,790	1,801	1,807	1,790	1,801	1,801	1,807
Ca	0,001	0,002	0,000	0,002	0,000	0,000	0,001	0,001	0,001	0,001	0,002	0,001	0,002	0,002	0,002	0,002	0,002	0,002	0,002	0,002
Na	0,000	0,000	0,000	0,000	0,000	0,000	0,000	0,000	0,000	0,000	0,000	0,000	0,000	0,000	0,000	0,000	0,000	0,000	0,000	0,000
K	0,000	0,000	0,000	0,000	0,000	0,000	0,000	0,000	0,000	0,000	0,000	0,000	0,000	0,000	0,000	0,000	0,000	0,000	0,000	0,000
Ni	0,007	0,008	0,008	0,006	0,007	0,008	0,000	0,000	0,000	0,000	0,004	0,009	0,007	0,008	0,009	0,005	0,008	0,009	0,009	0,005
Cr	0,000	0,000	0,002	0,000	0,000	0,000	0,000	0,001	0,001	0,001	0,000	0,000	0,000	0,000	0,000	0,000	0,000	0,000	0,000	0,000
totale	3,039	3,035	3,005	3,029	3,051	3,048	3,026	3,029	3,029	3,029	2,999	3,020	3,007	3,007	3,005	3,014	3,007	3,005	3,005	3,014
Fo	90,31	90,19	90,53	90,28	90,07	90,45	90,54	90,25	90,25	90,25	89,94	89,47	89,53	89,37	89,94	90,05	89,37	89,94	89,94	90,05
Fa	9,69	9,81	9,47	9,72	9,93	9,55	9,46	9,75	9,75	9,75	10,06	10,53	10,47	10,63	10,06	9,95	10,63	10,06	10,06	9,95

Appendix 1: Major element composition of olivines

Sample Area	MGP1d Wh											
	Area 2 3	Area 2 4	Area 3 3	Area 4 2	Area 4 3	Area 5 3	Area 6 3	Area 6 3	Area 8 3	Area 8 3	Area 8 3	Area 8 3
point	ol											
phase	rim	core										
rim/core	Wh											
Host rock												
SiO ₂	39,35	39,48	39,75	39,65	39,51	39,20	38,86					
TI ₂ O	0,01	0,00	0,00	0,00	0,00	0,00	0,00					
Al ₂ O ₃	0,00	0,00	0,00	0,00	0,00	0,00	0,00					
FeO	16,96	17,94	17,68	17,83	17,31	17,52	17,40					
MnO	0,25	0,24	0,35	0,30	0,14	0,23	0,20					
MgO	43,66	44,02	43,83	43,47	43,67	43,48	43,62					
CaO	0,07	0,03	0,06	0,02	0,07	0,06	0,07					
Na ₂ O	0,00	0,00	0,00	0,00	0,00	0,00	0,00					
K ₂ O	0,00	0,00	0,00	0,00	0,00	0,00	0,00					
NiO	0,15	0,20	0,27	0,15	0,14	0,20	0,23					
Cr ₂ O ₃	0,02	0,00	0,00	0,00	0,04	0,03	0,02					
Tot	100,47	101,91	101,94	101,42	100,88	100,72	100,40					
Si	0,972	0,975	0,982	0,980	0,976	0,968	0,960					
Ti	0,000	0,000	0,000	0,000	0,000	0,000	0,000					
Al6	0,000	0,000	0,000	0,000	0,000	0,000	0,000					
Fe2	0,350	0,371	0,365	0,368	0,358	0,362	0,359					
Mn	0,005	0,005	0,007	0,006	0,003	0,005	0,004					
Mg	1,608	1,621	1,614	1,601	1,608	1,601	1,606					
Ca	0,002	0,001	0,002	0,001	0,002	0,002	0,002					
Na	0,000	0,000	0,000	0,000	0,000	0,000	0,000					
K	0,000	0,000	0,000	0,000	0,000	0,000	0,000					
Ni	0,003	0,004	0,005	0,003	0,003	0,004	0,005					
Cr	0,000	0,000	0,000	0,000	0,000	0,000	0,000					
totale	2,941	2,977	2,976	2,958	2,950	2,942	2,937					
Fo	82,10	81,39	81,54	81,29	81,81	81,56	81,71					
Fa	17,90	18,61	18,46	18,71	18,19	18,44	18,29					

Appendix 2: Major element composition of clinopyroxenes

Sample Area	MGP2b Lh														
	Area 2							Area 3							
	1	2	3	1	3	4	1	1	2	3	1	7	8	1	2
point	cpx 1	cpx 1	cpx 2	cpx 1	cpx 1	cpx 2	cpx 2	cpx 1	cpx 1	cpx 1	cpx 1	cpx 1	cpx 1	cpx 1	cpx 1
phase	core	rim	core	core	rim	core	rim	core	rim	rim	rim	core	core	core	core
rim/core	Lh	Lh	Lh	Lh	Lh	Lh	Lh	Lh	Lh	Lh	Lh	Lh	Lh	Lh	Lh
Host rock	Lh	Lh	Lh	Lh	Lh	Lh	Lh	Lh	Lh	Lh	Lh	Lh	Lh	Lh	Lh
SiO ₂	52.43	52.94	53.63	52.52	52.73	52.81	52.59	53.12	52.35	52.33	52.78	52.58	52.22	52.76	52.46
TiO ₂	0.17	0.05	0.08	0.12	0.14	0.26	0.39	0.39	0.27	0.19	0.28	0.18	0.27	0.31	0.3
Al ₂ O ₃	4.06	4.07	3.21	4.17	3.99	4.12	3.79	4.01	4.17	3.96	4.04	4.01	4.52	3.84	3.92
Fe ₂ O ₃	0.15	0.06	0.4	0.59	0.5	0.43	0.48	0.15	0.55	0.54	0.26	0.52	0.14	0.38	0.29
FeO	2.78	2.72	2.67	2.53	2.19	2.23	2.46	2.76	2.54	2.37	2.76	2.2	2.8	2.53	2.63
MnO	0.15	0.23	0.09	0.14	0.07	0.12	0.18	0.12	0.09	0	0.11	0.03	0.04	0.09	0.05
MgO	16.68	16.75	17.5	16.76	16.85	16.93	17.2	16.75	16.88	16.6	16.8	16.81	16.63	16.79	16.8
CaO	20.95	21.15	21.49	21.29	21.55	21.3	21.26	21.01	21.03	21.59	21.05	21.49	21.06	21.49	21.02
Na ₂ O	0.81	0.78	0.81	0.99	1	1.02	0.86	0.99	1.01	0.99	0.91	1.02	0.77	0.92	0.91
K ₂ O	0	0	0.01	0.03	0	0	0	0.01	0	0	0.02	0	0.01	0.02	0
Cr ₂ O ₃	1.03	1.2	0.59	1.33	1.19	0.88	0.78	1.44	1.2	1.45	1.21	1.35	1.26	0.97	1.02
Tot	99.22	99.95	100.5	100.5	100.2	100.1	99.99	100.8	100.1	100	100.2	100.2	99.71	100.1	99.4
Si	1.913	1.919	1.928	1.893	1.902	1.905	1.902	1.911	1.892	1.895	1.907	1.898	1.898	1.908	1.909
Ti	0.005	0.001	0.002	0.003	0.004	0.007	0.011	0.011	0.007	0.005	0.008	0.005	0.007	0.008	0.008
Al	0.175	0.174	0.136	0.177	0.17	0.175	0.162	0.17	0.178	0.169	0.172	0.171	0.194	0.164	0.168
Fe III	0.004	0.002	0.011	0.016	0.014	0.012	0.013	0.004	0.015	0.015	0.007	0.014	0.004	0.01	0.008
Fe II	0.085	0.082	0.08	0.076	0.066	0.067	0.074	0.083	0.077	0.072	0.083	0.066	0.085	0.076	0.08
Mn	0.005	0.007	0.003	0.004	0.002	0.004	0.006	0.004	0.003	0	0.003	0.001	0.001	0.003	0.002
Mg	0.907	0.905	0.938	0.9	0.906	0.91	0.927	0.898	0.909	0.896	0.905	0.904	0.901	0.905	0.911
Ca	0.819	0.821	0.828	0.822	0.833	0.823	0.824	0.81	0.814	0.838	0.815	0.831	0.82	0.833	0.82
Na	0.057	0.055	0.056	0.069	0.07	0.071	0.06	0.069	0.071	0.07	0.064	0.071	0.054	0.064	0.062
K	0	0	0	0.001	0	0	0	0	0	0	0.001	0	0	0.001	0
Cr	0.03	0.034	0.017	0.038	0.034	0.025	0.022	0.041	0.034	0.042	0.035	0.039	0.036	0.028	0.029
SumCa	4	4	4	4	4	4	4	4	4	4	4	4	4	4	4
Al iv	0.087	0.081	0.072	0.107	0.098	0.095	0.098	0.089	0.108	0.105	0.093	0.102	0.102	0.092	0.091
Al vi	0.096	0.096	0.086	0.101	0.099	0.104	0.089	0.088	0.1	0.093	0.093	0.097	0.098	0.092	0.093
Al vi r	0.088	0.092	0.065	0.07	0.072	0.08	0.063	0.081	0.07	0.064	0.08	0.068	0.091	0.071	0.078
Mg M1	0.799	0.798	0.834	0.805	0.817	0.816	0.825	0.791	0.806	0.81	0.798	0.814	0.787	0.813	0.806
Mg M2	0.109	0.107	0.104	0.096	0.089	0.095	0.102	0.108	0.103	0.086	0.108	0.09	0.114	0.092	0.105
Fe2+ M1	0.075	0.073	0.072	0.068	0.06	0.06	0.066	0.073	0.068	0.065	0.074	0.06	0.074	0.069	0.071
Fe2+ M2	0.01	0.01	0.009	0.008	0.006	0.007	0.008	0.01	0.009	0.007	0.01	0.007	0.011	0.008	0.009

Appendix 2: Major element composition of clinopyroxenes

Sample Area	MGP2b2 Lh										MGPIb Hz											
	Area 3		Area 4		Area 5		Area 6		Area 6		Area 6		Area 6		Area 2		Area 3		Area 5		Area 6	
	6	3	3	4	1	2	3	4	5	6	3	10	1	2	4	1	2	4	1	2	4	4
point	cpx 1	cpx 2	cpx 2	cpx 2	cpx 1	cpx 1	cpx 1	cpx 1	cpx 1	cpx 1	cpx 2	cpx 2	cpx 1	cpx 2	cpx 2	cpx 1	cpx 1	cpx 1	cpx 1	cpx 2	cpx 2	cpx 2
rim/core	core	core	rim	core	rim	core	rim	core	rim	core	core	core	rim	core	rim	core	core	core	core	core	core	core
Host rock	Lh	Lh	Lh	Lh	Lh	Lh	Lh	Lh	Lh	Lh	Lh	Lh	Lh	Lh	Lh	Lh	Lh	Lh	Lh	Lh	Lh	Lh
SiO ₂	52.76	52.23	52.06	51.54	52.53	51.77	52.58	51.93	51.7	51.11	51.46	50.03										
TiO ₂	0.29	0.27	0.26	0.23	0.22	0.18	0.26	0.16	0.28	0.23	0.34	0.28										
Al ₂ O ₃	3.98	3.88	3.95	4.31	3.68	3.55	3.68	3.22	3.47	3.59	4.42	4.06										
Fe ₂ O ₃	0.18	0.52	0.31	0.42	0.62	0.7	0.35	0.68	0.74	0.81	0.3	0.86										
FeO	2.5	2.18	2.42	2.56	2.1	2.27	2.55	2.33	2.17	1.95	2.6	1.89										
MnO	0.05	0.15	0	0.04	0.12	0.06	0.05	0.15	0.12	0.09	0.12	0.12										
MgO	16.66	16.74	16.5	16.55	17.01	17.11	16.83	17.16	17.14	17.18	16.24	16.26										
CaO	21.27	21.27	21.1	21.09	21.56	21.28	21.42	21.24	21.06	21.31	20.92	21.16										
Na ₂ O	0.93	1	0.96	0.83	0.98	0.83	0.86	0.81	0.92	0.76	0.89	0.93										
K ₂ O	0.01	0.02	0	0	0	0.01	0.01	0.01	0	0.01	0.02	0										
Cr ₂ O ₃	0.92	1.32	1.26	1.2	1.01	1.03	0.89	1.2	1.14	0.87	1.24	1.19										
Tot	99.55	99.58	98.82	98.76	99.83	98.79	99.47	98.89	98.74	97.91	98.55	96.79										
Si	1.917	1.898	1.907	1.89	1.901	1.895	1.913	1.901	1.893	1.885	1.892	1.87										
Ti	0.008	0.007	0.007	0.006	0.006	0.005	0.007	0.004	0.008	0.006	0.009	0.008										
Al	0.17	0.166	0.171	0.186	0.157	0.153	0.158	0.139	0.15	0.156	0.192	0.179										
Fe III	0.005	0.014	0.008	0.011	0.017	0.019	0.01	0.019	0.021	0.023	0.008	0.024										
Fe II	0.076	0.066	0.074	0.078	0.063	0.069	0.077	0.071	0.066	0.06	0.08	0.059										
Mn	0.002	0.005	0	0.001	0.004	0.002	0.002	0.005	0.004	0.003	0.004	0.004										
Mg	0.902	0.906	0.901	0.904	0.918	0.933	0.912	0.936	0.935	0.944	0.89	0.906										
Ca	0.828	0.828	0.828	0.828	0.836	0.834	0.835	0.833	0.826	0.842	0.824	0.847										
Na	0.066	0.07	0.068	0.059	0.069	0.059	0.061	0.057	0.065	0.054	0.063	0.067										
K	0	0.001	0	0	0	0	0	0	0	0	0.001	0										
Cr	0.026	0.038	0.036	0.035	0.029	0.03	0.026	0.035	0.033	0.025	0.036	0.035										
SumCa	4	4	4	4	4	4	4	4	4	4	4	4										
Al iv	0.083	0.102	0.093	0.11	0.099	0.105	0.087	0.099	0.107	0.115	0.108	0.13										
Al vi	0.097	0.092	0.094	0.099	0.092	0.086	0.089	0.076	0.083	0.086	0.1	0.098										
Al vi r	0.087	0.064	0.077	0.076	0.058	0.048	0.07	0.039	0.042	0.041	0.084	0.049										
Mg M1	0.806	0.817	0.805	0.802	0.832	0.836	0.818	0.839	0.837	0.851	0.791	0.829										
Mg M2	0.097	0.09	0.096	0.102	0.085	0.098	0.095	0.098	0.098	0.095	0.1	0.076										
Fe2+ M1	0.068	0.06	0.066	0.07	0.058	0.062	0.069	0.064	0.059	0.054	0.071	0.054										
Fe2+ M2	0.008	0.007	0.008	0.009	0.006	0.007	0.008	0.007	0.007	0.006	0.009	0.005										

Appendix 2: Major element composition of clinopyroxenes

Sample Area	MGP1b Hz						MGP1c Hz						MGP3b Hz															
	Area 7		Area 8		Area 8		Area 1		Area 1		Area 4		Area 4		Area 4		Area 5		Area 5		Area 5		Area 5					
	3	1	2	3	1	2	4	1	2	4	1	2	7	8	1	2	7	8	1	2	7	8	1	2	7	8		
point	cpx 1	cpx 1	cpx 1	cpx 1	cpx 1	cpx 2	cpx 2	cpx 2	cpx 2	rim	rim	rim	rim	rim	rim	rim	rim	rim	rim	rim	rim	rim	rim	rim	rim	rim	rim	
phase	core	core	core	core	core	core	core	core	core	rim	rim	rim	rim	rim	rim	rim	rim	rim	rim	rim	rim	rim	rim	rim	rim	rim	rim	
rim/core	Hz/Lh	Hz/Lh	Hz/Lh	Hz/Lh	Hz/Lh	Hz	Hz	Hz	Hz	Hz	Hz/Lh	Hz/Lh	Hz/Lh	Hz/Lh	Hz/Lh	Hz/Lh	Hz/Lh	Hz/Lh	Hz/Lh	Hz/Lh	Hz/Lh	Hz/Lh	Hz/Lh	Hz/Lh	Hz/Lh	Hz/Lh	Hz/Lh	
Host rock	52,85	53,05	51,83	52,9	52,45	52,25	52,58	52,45	52,25	52,58	53,47	53,48	53,51	53,17	53,8	54,05	53,77	53,97	53,71	53,38	53,38	53,38	53,38	53,38	53,38	53,38	53,38	
SiO ₂	0,17	0,11	0,13	0,13	0,28	0,31	0,28	0,28	0,31	0,28	0,1	0,1	0,14	0,09	0,07	0	0,09	0,09	0,17	0,08	0,08	0,08	0,08	0,08	0,08	0,08	0,08	
TiO ₂	3,53	3,21	3,47	3,1	3,46	4,13	3,57	3,46	4,13	3,57	2,34	1,75	2,55	2,45	2,07	2,14	2,36	2,23	2,34	2,31	2,31	2,31	2,31	2,31	2,31	2,31	2,31	
Al ₂ O ₃	0,4	0,18	0,53	0,37	0,48	0,24	0,67	0,48	0,24	0,67	0,39	0,34	0,37	0,43	0,4	0,09	0,11	0,45	0,37	0,56	0,56	0,56	0,56	0,56	0,56	0,56	0,56	
Fe ₂ O ₃	3,65	3,43	3,21	3,42	2,64	2,85	2,47	2,64	2,85	2,47	2,68	2,47	2,88	2,8	2,87	2,87	2,91	2,39	2,65	2,62	2,62	2,62	2,62	2,62	2,62	2,62	2,62	
FeO	0,06	0,07	0,04	0,16	0,1	0,07	0,14	0,1	0,07	0,14	0,09	0,1	0,09	0	0,09	0,14	0,07	0,08	0,12	0,02	0,02	0,02	0,02	0,02	0,02	0,02	0,02	
MnO	16,41	16,95	16,72	16,82	16,49	16,34	16,76	16,49	16,34	16,76	17,24	17,47	17,24	17,14	17,67	17,17	17,08	17,69	17,31	17,24	17,24	17,24	17,24	17,24	17,24	17,24	17,24	
MgO	21,15	20,77	20,97	21,12	21,29	21,05	21,17	21,29	21,05	21,17	21,32	21,82	21,12	21,13	21,19	21,21	21,1	21,38	21,17	21,5	21,5	21,5	21,5	21,5	21,5	21,5	21,5	21,5
CaO	0,94	0,8	0,78	0,81	1,05	0,95	1,15	1,05	0,95	1,15	0,92	0,71	0,94	0,94	0,81	0,88	0,91	0,96	1	0,97	0,97	0,97	0,97	0,97	0,97	0,97	0,97	
Na ₂ O	0,01	0	0	0	0	0	0	0	0	0	0	0	0,02	0,04	0	0	0	0	0	0	0	0	0	0	0	0	0	
K ₂ O	1,07	0,91	1,06	0,92	1,32	1,38	1,36	1,32	1,38	1,36	1,06	1,02	1,31	1,25	0,59	1,05	1,26	0,95	1,12	1,19	1,19	1,19	1,19	1,19	1,19	1,19	1,19	
Cr ₂ O ₃	100,2	99,48	98,74	99,75	99,57	99,57	100,2	99,57	99,57	100,2	99,61	99,26	100,2	99,42	99,6	99,6	99,66	100,2	99,97	99,87	99,87	99,87	99,87	99,87	99,87	99,87	99,87	99,87
Tot	1,916	1,933	1,904	1,925	1,91	1,903	1,901	1,91	1,903	1,901	1,943	1,951	1,936	1,937	1,953	1,965	1,955	1,946	1,944	1,935	1,935	1,935	1,935	1,935	1,935	1,935	1,935	
Si	0,005	0,003	0,004	0,004	0,008	0,008	0,008	0,008	0,008	0,008	0,003	0,003	0,004	0,002	0,002	0	0,002	0,002	0,005	0,002	0,002	0,002	0,002	0,002	0,002	0,002	0,002	
Ti	0,151	0,138	0,15	0,133	0,148	0,177	0,152	0,148	0,177	0,152	0,1	0,075	0,109	0,105	0,089	0,092	0,101	0,095	0,1	0,099	0,099	0,099	0,099	0,099	0,099	0,099	0,099	
Al	0,011	0,005	0,015	0,01	0,013	0,007	0,018	0,013	0,007	0,018	0,011	0,009	0,01	0,012	0,011	0,002	0,003	0,012	0,01	0,015	0,015	0,015	0,015	0,015	0,015	0,015	0,015	
Fe III	0,111	0,104	0,099	0,104	0,081	0,087	0,075	0,081	0,087	0,075	0,081	0,076	0,087	0,085	0,087	0,087	0,089	0,072	0,08	0,079	0,079	0,079	0,079	0,079	0,079	0,079	0,079	
Fe II	0,002	0,002	0,001	0,005	0,003	0,002	0,004	0,003	0,002	0,004	0,003	0,003	0,003	0	0,003	0,004	0,002	0,002	0,004	0,001	0,001	0,001	0,001	0,001	0,001	0,001	0,001	
Mn	0,887	0,921	0,915	0,912	0,895	0,887	0,903	0,895	0,887	0,903	0,934	0,95	0,93	0,93	0,956	0,93	0,925	0,95	0,934	0,931	0,931	0,931	0,931	0,931	0,931	0,931	0,931	0,931
Mg	0,821	0,811	0,825	0,823	0,83	0,822	0,82	0,83	0,822	0,82	0,83	0,853	0,819	0,825	0,824	0,826	0,822	0,826	0,821	0,835	0,835	0,835	0,835	0,835	0,835	0,835	0,835	
Ca	0,066	0,057	0,056	0,057	0,074	0,067	0,081	0,074	0,067	0,081	0,065	0,05	0,066	0,066	0,057	0,062	0,064	0,067	0,07	0,068	0,068	0,068	0,068	0,068	0,068	0,068	0,068	
Na	0	0	0	0	0	0	0	0	0	0	0	0	0	0,001	0,002	0	0	0	0	0	0	0	0	0	0	0	0	
K	0,031	0,026	0,031	0,026	0,038	0,04	0,039	0,038	0,04	0,039	0,03	0,029	0,037	0,036	0,017	0,03	0,036	0,027	0,032	0,034	0,034	0,034	0,034	0,034	0,034	0,034	0,034	
Cr	4	4	4	4	4	4	4	4	4	4	4	4	4	4	4	4	4	4	4	4	4	4	4	4	4	4	4	
SumCa	0,084	0,067	0,096	0,075	0,09	0,097	0,099	0,09	0,097	0,099	0,057	0,049	0,064	0,063	0,047	0,035	0,045	0,054	0,056	0,065	0,065	0,065	0,065	0,065	0,065	0,065	0,065	
Al iv	0,088	0,081	0,084	0,078	0,085	0,094	0,089	0,085	0,094	0,089	0,065	0,045	0,065	0,065	0,062	0,062	0,062	0,065	0,064	0,064	0,064	0,064	0,064	0,064	0,064	0,064	0,064	
Al vi	0,067	0,071	0,054	0,058	0,058	0,081	0,053	0,058	0,081	0,053	0,043	0,027	0,045	0,042	0,041	0,057	0,056	0,04	0,044	0,034	0,034	0,034	0,034	0,034	0,034	0,034	0,034	
Al vi r	0,789	0,803	0,809	0,809	0,81	0,787	0,815	0,81	0,787	0,815	0,84	0,863	0,827	0,831	0,851	0,832	0,823	0,853	0,837	0,843	0,843	0,843	0,843	0,843	0,843	0,843	0,843	
Mg M1	0,098	0,117	0,106	0,103	0,085	0,099	0,088	0,085	0,099	0,088	0,094	0,087	0,103	0,1	0,106	0,098	0,102	0,097	0,097	0,089	0,089	0,089	0,089	0,089	0,089	0,089	0,089	
Mg M2	0,098	0,091	0,087	0,092	0,073	0,077	0,067	0,073	0,077	0,067	0,073	0,069	0,077	0,076	0,078	0,078	0,079	0,065	0,072	0,072	0,072	0,072	0,072	0,072	0,072	0,072	0,072	
Fe2+ M1	0,012	0,013	0,011	0,012	0,008	0,01	0,007	0,008	0,01	0,007	0,008	0,007	0,01	0,009	0,01	0,009	0,01	0,007	0,008	0,008	0,008	0,008	0,008	0,008	0,008	0,008	0,008	
Fe2+ M2	0,012	0,013	0,011	0,012	0,008	0,01	0,007	0,008	0,01	0,007	0,008	0,007	0,01	0,009	0,01	0,009	0,01	0,007	0,008	0,008	0,008	0,008	0,008	0,008	0,008	0,008	0,008	

Appendix 3: Major element composition of orthopyroxenes

Sample	MGP2b Lh											MGP2b2 Lh											MGP1b Hz																									
	Area 2			Area 6			Area 8			Area 1			Area 2			Area 7			Area 7			Area 7			Area 8																							
	5	6	4	5	4	5	10	11	11	9	10	4	4	5	6	7	6	7	2	1	4	2	1	4	2	1	4																					
point	55,6	0,03	2,75	55,5	0,05	2,77	56,1	0,06	2,84	56,2	0,06	2,81	56,2	0,08	2,85	56,5	0,06	2,69	56,5	0,06	2,71	55,7	0,06	2,91	55,2	0,02	2,76	55,2	0,07	2,83	55,5	0,16	2,73	55,8	0	2,3	55	0	2,3	55,6	0,04	2,61						
phase	opx	opx	opx	opx	opx	opx	opx	opx	opx	opx	opx	opx	opx	opx	opx	opx	opx	opx	opx	opx	opx	opx	opx	opx	opx	opx	opx	opx	opx	opx	opx	opx	opx	opx	opx	opx	opx	opx	opx	opx	opx	opx						
rim/core	rim	rim	rim	rim	rim	rim	rim	rim	rim	rim	rim	rim	rim	rim	rim	rim	rim	rim	rim	rim	rim	rim	rim	rim	rim	rim	rim	rim	rim	rim	rim	rim	rim	rim	rim	rim	rim	rim	rim	rim	rim	rim	rim	rim	rim			
Host rocl	Lh	Lh	Lh	Lh	Lh	Lh	Lh	Lh	Lh	Lh	Lh	Lh	Lh	Lh	Lh	Lh	Lh	Lh	Lh	Lh	Lh	Lh	Lh	Lh	Lh	Lh	Lh	Lh	Lh	Lh	Lh	Lh	Lh	Lh	Lh	Lh	Lh	Lh	Lh	Lh	Lh	Lh	Lh	Lh	Lh			
SiO ₂	55,6	0,03	2,75	55,5	0,05	2,77	56,1	0,06	2,84	56,2	0,06	2,81	56,2	0,08	2,85	56,5	0,06	2,69	56,5	0,06	2,71	55,7	0,06	2,91	55,2	0,02	2,76	55,2	0,07	2,83	55,5	0,16	2,73	55,8	0	2,3	55	0	2,3	55	0	2,3	55,6	0,04	2,61			
TiO ₂	0,29	0,03	2,75	0,28	0,05	2,77	0,21	0,06	2,81	0,21	0,06	2,81	0,21	0,06	2,85	0,21	0,06	2,69	0,21	0,06	2,71	0,21	0,06	2,91	0,21	0,02	2,76	0,21	0,07	2,83	0,21	0,16	2,73	0,21	0	2,3	0,21	0	2,3	0,21	0,04	2,61						
Al ₂ O ₃	5,56	0,14	33,9	4,96	0,13	34,3	5,59	0,17	33,9	5,76	0,16	33,5	5,83	0,11	33,5	5,66	0,17	33,9	5,66	0,16	33,9	5,53	0,16	33,9	5,53	0,16	33,9	5,49	0,18	34,2	5,66	0,18	34,2	5,66	0,18	34,2	5,66	0,18	34,2	5,66	0,18	34,2	5,66	0,18	34,2	5,66	0,18	34,2
FeO	0,14	0,13	33,9	0,13	0,13	33,9	0,16	0,11	33,5	0,16	0,11	33,5	0,11	0,11	33,5	0,11	0,11	33,9	0,11	0,11	33,9	0,11	0,11	33,9	0,11	0,11	33,9	0,11	0,11	34,2	0,11	0,18	34,2	0,11	0,18	34,2	0,11	0,18	34,2	0,11	0,18	34,2	0,11	0,18	34,2	0,11	0,18	34,2
MnO	33,9	0,94	99,9	34,3	0,99	99,7	33,9	0,94	99,9	33,5	0,94	99,9	34	0,99	99,7	33,9	0,94	99,9	33,9	0,94	99,9	33,9	0,94	99,9	33,9	0,94	99,9	33,9	0,94	99,9	34,2	0,94	99,9	34,2	0,94	99,9	34,2	0,94	99,9	34,2	0,94	99,9	34,2	0,94	99,9			
MgO	0,94	0,09	99,9	0,99	0,09	99,7	0,94	0,09	99,9	0,94	0,09	99,9	0,99	0,09	99,7	0,94	0,09	99,9	0,94	0,09	99,9	0,94	0,09	99,9	0,94	0,09	99,9	0,94	0,09	99,9	0,94	0,09	99,9	0,94	0,09	99,9	0,94	0,09	99,9	0,94	0,09	99,9	0,94	0,09	99,9			
CaO	0	0	0	0	0	0	0	0	0	0	0	0	0	0	0	0	0	0	0	0	0	0	0	0	0	0	0	0	0	0	0	0	0	0	0	0	0	0	0	0	0	0						
Na ₂ O	0	0	0	0	0	0	0	0	0	0	0	0	0	0	0	0	0	0	0	0	0	0	0	0	0	0	0	0	0	0	0	0	0	0	0	0	0	0	0	0	0	0						
K ₂ O	0	0	0	0	0	0	0	0	0	0	0	0	0	0	0	0	0	0	0	0	0	0	0	0	0	0	0	0	0	0	0	0	0	0	0	0	0	0	0	0	0	0						
Cr ₂ O ₃	0,7	0,61	99,9	0,51	0,52	99,7	0,52	0,53	99,9	0,54	0,51	99,9	0,54	0,51	99,9	0,54	0,51	99,9	0,54	0,51	99,9	0,54	0,51	99,9	0,54	0,51	99,9	0,54	0,51	99,9	0,54	0,51	99,9	0,54	0,51	99,9	0,54	0,51	99,9	0,54	0,51	99,9						
Tot	99,9	1,92	99,9	101	1,92	99,7	100	1,94	101	101	1,93	100	101	1,93	100	101	1,93	101	101	1,93	101	100	1,92	99,9	99,8	1,91	99,4	99,4	1,91	100	99,4	1,91	100	99,4	1,91	100	99,4	1,91	100									
Si	1,92	0	0	1,91	0	0	1,94	0	1,93	1,93	0	1,94	1,93	0	1,93	1,94	0	1,94	1,93	0	1,94	1,92	0	1,92	1,91	0	1,91	1,91	0	1,91	1,91	0	1,91	1,91	0	1,91	1,92	0	1,92									
Ti	0	0	0	0	0	0	0	0	0	0	0	0	0	0	0	0	0	0	0	0	0	0	0	0	0	0	0	0	0	0	0	0	0	0	0	0	0	0	0									
Al	0,11	0,11	0,11	0,12	0,11	0,12	0,12	0,11	0,12	0,11	0,12	0,11	0,12	0,11	0,12	0,11	0,12	0,11	0,11	0,12	0,11	0,12	0,11	0,12	0,11	0,12	0,11	0,12	0,11	0,12	0,11	0,12	0,11	0,12	0,11	0,12	0,11	0,12	0,11									
Fe III	0,01	0,01	0,01	0	0	0	0	0	0	0	0	0	0	0	0	0	0	0	0	0	0	0	0	0	0	0	0	0	0	0	0	0	0	0	0	0	0	0	0									
Fe II	0,16	0,14	0,16	0,16	0,17	0,17	0,17	0,17	0,17	0,17	0,16	0,17	0,17	0,16	0,17	0,17	0,16	0,17	0,17	0,16	0,17	0,16	0,15	0,16	0,16	0,16	0,16	0,16	0,16	0,16	0,16	0,16	0,16	0,16	0,16	0,16	0,16	0,16	0,16									
Mn	0	0	0	0	0,01	0,01	0	0,01	0	0	0,01	0,01	0	0,01	0,01	0	0,01	0,01	0	0,01	0,01	0,01	0,01	0,01	0,01	0,01	0,01	0,01	0,01	0,01	0,01	0,01	0,01	0,01	0,01	0,01	0,01	0,01	0,01									
Mg	1,74	1,76	1,75	1,74	1,74	1,72	1,74	1,72	1,74	1,74	1,74	1,73	1,74	1,73	1,73	1,74	1,74	1,73	1,74	1,73	1,73	1,75	1,75	1,75	1,75	1,75	1,75	1,75	1,75	1,75	1,75	1,75	1,75	1,75	1,75	1,75	1,75	1,75	1,75									
Ca	0,04	0,04	0,03	0,04	0,04	0,04	0,04	0,04	0,04	0,04	0,04	0,04	0,04	0,04	0,04	0,04	0,04	0,04	0,04	0,04	0,04	0,03	0,03	0,03	0,04	0,04	0,04	0,04	0,04	0,04	0,04	0,04	0,04	0,04	0,04	0,04	0,04	0,04	0,04									
Na	0	0	0	0	0	0	0	0	0	0	0	0	0	0	0	0	0	0	0	0	0	0	0	0	0	0	0	0	0	0	0	0	0	0	0	0	0	0	0									
K	0	0	0	0	0	0	0	0	0	0	0	0	0	0	0	0	0	0	0	0	0	0	0	0	0	0	0	0	0	0	0	0	0	0	0	0	0	0	0									
Cr	0,02	0,02	0,01	0,01	0,01	0,01	0,01	0,01	0,02	0,01	0,01	0,02	0,02	0,02	0,02	0,01	0,01	0,02	0,01	0,01	0,02	0,01	0,01	0,01	0,01	0,01	0,01	0,01	0,01	0,01	0,01	0,01	0,01	0,01	0,01	0,01	0,01	0,01	0,01									
SumCa	4	4	4	4	4	4	4	4	4	4	4	4	4	4	4	4	4	4	4	4	4	4	4	4	4	4	4	4	4	4	4	4	4	4	4	4	4	4	4									
Al iv	0,08	0,09	0,08	0,07	0,07	0,07	0,07	0,07	0,07	0,07	0,07	0,07	0,07	0,07	0,07	0,07	0,07	0,07	0,07	0,07	0,07	0,08	0,08	0,08	0,09	0,09	0,09	0,09	0,09	0,09	0,09	0,09	0,09	0,09	0,09	0,09	0,09	0,09	0,09									
Al vi	0,05	0,05	0,05	0,05	0,05	0,05	0,05	0,05	0,05	0,05	0,05	0,05	0,05	0,05	0,05	0,05	0,05	0,05	0,05	0,05	0,05	0,05	0,05	0,05	0,05	0,05	0,05	0,05	0,05	0,05	0,05	0,05	0,05	0,05	0,05	0,05	0,05	0,05	0,05									
Al vi r	0,03	0,03	0,04	0,04	0,04	0,06	0,04	0,06	0,04	0,04	0,05	0,05	0,04	0,05	0,05	0,04	0,04	0,04	0,04	0,04	0,04	0,04	0,04	0,04	0,04	0,04	0,04	0,04	0,04	0,04	0,04	0,04	0,04	0,04	0,04	0,04	0,04	0,04	0,04									
Mg M1	0,86	0,87	0,86	0,86	0,86	0,85	0,86	0,85	0,86	0,86	0,86	0,85	0,86	0,86	0,85	0,86	0,86	0,86	0,86	0,86	0,86	0,86	0,86	0,86	0,87	0,87	0,87	0,87	0,87	0,87	0,87	0,87	0,87	0,87	0,87	0,87	0,87	0,87	0,87									
Mg M2	0,88	0,89	0,88	0,88	0,88	0,87	0,88	0,87	0,88	0,88	0,88	0,88	0,88	0,88	0,88	0,88	0,88	0,88	0,88	0,88	0,88	0,88	0,88	0,88	0,88	0,88	0,88	0,88	0,88	0,88	0,88	0,88	0,88	0,88	0,88	0,88	0,88	0,88	0,88									
Fe2+ M1	0,08	0,07	0,08	0,08	0,08	0,09	0,08	0,09	0,08	0,08	0,08	0,08	0,08	0,08	0,08	0,08	0,08	0,08	0,08	0,08	0,08	0,08	0,08	0,08	0,08	0,08	0,08	0,08	0,08	0,08	0,08	0,08	0,08	0,08	0,08	0,08	0,08	0,08	0,08									
Fe2+ M2	0,08	0,07	0,08	0,08	0,08	0,09	0,08	0,09	0,08	0,08	0,08	0,08	0,08	0,08	0,08	0,08	0,08</																															

Appendix 3: Major element composition of orthopyroxenes

Sample Area	MGPIb Hz						MGPIc Hz															
	Area 2		Area 3		Area 6		Area 2		Area 3		Area 3		Area 3		Area 4		Area 4		Area 4		Area 4	
	1	2	1	3	1	3	1	3	1	3	1	3	1	3	1	3	1	3	1	3	1	3
point	opx	opx	opx	opx	opx	opx	opx	opx	opx	opx	opx	opx	opx	opx	opx	opx	opx	opx	opx	opx	opx	opx
rim/core	core	core	core	core	core	core	core	core	core	core	core	core	core	core	core	core	core	core	core	core	core	core
Host rock	Hz	Hz	Hz	Hz	Hz	Hz	Hz	Hz	Hz	Hz	Hz	Hz	Hz	Hz	Hz	Hz	Hz	Hz	Hz	Hz	Hz	Hz
SiO ₂	55,7	54,3	55,1	55,9	55,4	55,5	55,7	56,8	56,2	56,8	56,7	55,8	56,4	57,1	57,2	56,2	56,2	56,2	56,2	56,2	56,2	56,2
TiO ₂	0	0	0	0,03	0,04	0,04	0,09	0	0,08	0,03	0,05	0,06	0,05	0,02	0,01	0	0,04	0,08	0,08	0,08	0,08	0,08
Al ₂ O ₃	2,28	2,4	2,52	2,45	2,53	2,51	2,54	1,39	1,62	1,59	1,84	1,9	1,78	1,95	1,82	1,86	1,68	2,14	1,83	1,83	1,83	1,83
Fe ₂ O ₃	0,29	0,58	0,35	0,38	0,43	0,42	0,22	0,36	0,35	0,17	0,29	0,04	0,32	0,36	0,31	0,23	0,2	0,43	0,43	0,43	0,43	0,43
FeO	7,01	6,9	6,87	7,26	7,37	7,39	7,47	5,67	5,7	5,57	5,98	6,29	5,71	5,46	5,89	5,88	6	5,92	5,92	5,92	5,92	5,92
MnO	0,08	0,1	0,17	0,23	0,12	0,11	0,09	0,24	0,05	0,1	0,15	0,15	0,24	0,1	0,08	0,13	0,18	0,15	0,15	0,15	0,15	0,15
MgO	33,3	32,7	33	33,2	32,9	33,1	32,8	34,8	34,7	34,5	34,1	34	34,6	34,3	34,7	34,7	34	34,3	34,3	34,3	34,3	34,3
CaO	0,81	0,91	0,79	0,95	0,9	0,88	0,9	0,72	0,82	0,92	0,87	0,85	0,91	0,85	0,96	0,9	0,92	0,91	0,91	0,91	0,91	0,91
Na ₂ O	0	0	0	0	0	0	0	0	0	0	0	0	0	0	0	0	0	0	0	0	0	0
K ₂ O	0	0,04	0	0	0,04	0	0	0	0	0	0	0	0,02	0	0,01	0	0	0,03	0,03	0,03	0,03	0,03
Cr ₂ O ₃	0,47	0,52	0,53	0,54	0,6	0,52	0,56	0,26	0,47	0,3	0,43	0,46	0,39	0,52	0,58	0,49	0,4	0,51	0,51	0,51	0,51	0,51
Tot	99,9	98,4	99,3	101	100	100	100	100	100	99,9	99,9	101	99,8	100	102	101	100	100	100	100	100	100
Si	1,93	1,91	1,92	1,92	1,92	1,92	1,93	1,95	1,94	1,95	1,94	1,95	1,94	1,93	1,94	1,95	1,94	1,93	1,93	1,93	1,93	1,93
Ti	0	0	0	0	0	0	0	0	0	0	0	0	0	0	0	0	0	0	0	0	0	0
Al	0,09	0,1	0,1	0,1	0,1	0,1	0,1	0,06	0,07	0,07	0,08	0,07	0,08	0,07	0,07	0,07	0,07	0,07	0,07	0,07	0,07	0,07
Fe III	0,01	0,02	0,01	0,01	0,01	0,01	0,01	0,01	0,01	0,01	0,01	0	0,01	0,01	0,01	0,01	0,01	0,01	0,01	0,01	0,01	0,01
Fe II	0,2	0,2	0,2	0,21	0,21	0,21	0,22	0,16	0,16	0,16	0,17	0,18	0,16	0,16	0,17	0,17	0,17	0,17	0,17	0,17	0,17	0,17
Mn	0	0	0,01	0,01	0	0	0	0,01	0	0	0	0,01	0	0	0,01	0	0	0	0	0	0	0
Mg	1,72	1,72	1,72	1,7	1,7	1,7	1,69	1,78	1,78	1,77	1,76	1,74	1,76	1,78	1,76	1,76	1,74	1,76	1,76	1,76	1,76	1,76
Ca	0,03	0,03	0,03	0,04	0,03	0,03	0,03	0,03	0,03	0,03	0,03	0,03	0,03	0,03	0,04	0,04	0,03	0,03	0,03	0,03	0,03	0,03
Na	0	0	0	0	0	0	0	0	0	0	0	0	0	0	0	0	0	0	0	0	0	0
K	0	0	0	0	0	0	0	0	0	0	0	0	0	0	0	0	0	0	0	0	0	0
Cr	0,01	0,01	0,02	0,02	0,02	0,01	0,02	0,01	0,01	0,01	0,01	0,01	0,01	0,01	0,01	0,01	0,01	0,01	0,01	0,01	0,01	0,01
SumCa	4	4	4	4	4	4	4	4	4	4	4	4	4	4	4	4	4	4	4	4	4	4
Al iv	0,07	0,09	0,08	0,08	0,08	0,08	0,07	0,05	0,06	0,05	0,06	0,05	0,06	0,06	0,06	0,05	0,06	0,07	0,07	0,07	0,07	0,07
Al vi	0,04	0,04	0,05	0,04	0,04	0,04	0,04	0,03	0,02	0,03	0,03	0,03	0,03	0,03	0,03	0,03	0,03	0,03	0,03	0,03	0,03	0,03
Al vi r	0,03	0,01	0,03	0,02	0,02	0,02	0,03	0,01	0,01	0,02	0,02	0,03	0,01	0	0,01	0,02	0,02	0,01	0,01	0,01	0,01	0,01
Mg M1	0,85	0,86	0,85	0,85	0,84	0,85	0,84	0,9	0,89	0,89	0,88	0,87	0,89	0,88	0,88	0,88	0,87	0,88	0,88	0,88	0,88	0,88
Mg M2	0,87	0,86	0,86	0,85	0,86	0,86	0,86	0,89	0,89	0,88	0,88	0,87	0,88	0,88	0,88	0,88	0,88	0,88	0,88	0,88	0,88	0,88
Fe2+ M1	0,1	0,1	0,1	0,1	0,11	0,11	0,11	0,08	0,08	0,08	0,09	0,09	0,08	0,08	0,09	0,08	0,09	0,09	0,09	0,09	0,09	0,09
Fe2+ M2	0,1	0,1	0,1	0,11	0,11	0,11	0,11	0,08	0,08	0,08	0,09	0,09	0,08	0,08	0,09	0,08	0,09	0,09	0,09	0,09	0,09	0,09

Appendix 3: Major element composition of orthopyroxenes

Sample	MGP1g Hz										MGP3b Hz									
	Area 2		Area 2		Area 3		Area 4		Area 5		Area 5		Area 2		Area 2		Area 2			
	1	2	3	4	1	2	1	2	1	2	3	4	5	6	7	8	9	1	2	7
point	opx	opx	opx	opx	opx	opx	opx	opx	opx	opx	opx	opx	opx	opx	opx	opx	opx	rim	opx	opx
phase	core	core	core	rim	core	core	core	core	core	core	core	core	core	core	core	core	core	rim	core	core
rim/core	Hz	Hz	Hz	Hz	Hz	Hz	Hz	Hz	Hz	Hz	Hz	Hz	Hz	Hz	Hz	Hz	Hz	Hz	Hz	Hz
Host rocl	Hz	Hz	Hz	Hz	Hz	Hz	Hz	Hz	Hz	Hz	Hz	Hz	Hz	Hz	Hz	Hz	Hz	Hz	Hz	Hz
SiO ₂	54,4	54,3	54,5	54,1	54,5	54,5	54,4	54,3	55	55	54,8	54,8	54,9	54,5	55,3	54,2	54,7	56,8	56,8	57
TiO ₂	0,21	0,13	0,26	0,27	0,19	0,22	0,12	0,27	0,17	0,2	0,21	0,05	0,11	0,13	0,03	0,17	0,11	0,05	0,02	0,05
Al ₂ O ₃	3,1	3,03	3,32	3,18	3,25	3,16	2,97	3,18	2,96	2,95	2,77	2,83	2,98	3,07	3,02	2,88	2,96	1,69	1,64	1,52
Fe ₂ O ₃	0,42	0,47	0,69	0,47	0,59	0,33	0,5	0,48	0,34	0,32	0,19	0,45	0,36	0,4	0,31	0,45	0,29	0,05	0,16	-0,03
FeO	8,93	8,96	9,26	9,3	8,87	9,04	8,86	9,05	8,83	9,17	8,72	8,75	8,73	8,92	8,77	9,54	8,65	5,86	5,96	5,7
MnO	0,17	0,16	0,19	0,21	0,22	0,23	0,19	0,2	0,13	0,25	0,15	0,2	0,26	0,21	0,17	0,18	0,24	0,17	0,19	0,08
MgO	31,5	31,5	31,9	31,2	31,9	31,3	31,6	31,5	31,8	31,6	31,5	31,8	31,7	31,5	31,8	30,9	31,6	34,1	34,3	34,4
CaO	0,87	0,88	0,82	0,9	0,83	0,87	0,86	0,88	0,88	0,9	0,87	0,91	0,94	0,93	0,95	0,95	0,9	0,94	0,92	0,88
Na ₂ O	0	0	0	0	0	0	0	0	0	0	0	0	0	0	0	0	0	0	0	0
K ₂ O	0,02	0,02	0	0	0,01	0	0	0	0,01	0	0	0	0	0	0,02	0,03	0	0	0,01	0,01
Cr ₂ O ₃	0,38	0,41	0,28	0,43	0,36	0,39	0,26	0,28	0,46	0,47	0,47	0,47	0,42	0,48	0,48	0,41	0,41	0,53	0,54	0,51
Tot	100	99,9	101	100	101	100	99,8	100	101	101	99,8	100	100	100	101	99,7	99,9	100	101	100
Si	1,9	1,9	1,89	1,9	1,89	1,91	1,91	1,9	1,91	1,91	1,92	1,91	1,91	1,91	1,92	1,91	1,92	1,96	1,95	1,96
Ti	0,01	0	0,01	0,01	0,01	0,01	0	0,01	0	0,01	0,01	0	0	0	0	0	0	0	0	0
Al	0,13	0,13	0,14	0,13	0,13	0,13	0,12	0,13	0,12	0,12	0,11	0,12	0,12	0,13	0,12	0,12	0,12	0,07	0,07	0,06
Fe III	0,01	0,01	0,02	0,01	0,02	0,01	0,01	0,01	0,01	0,01	0,01	0,01	0,01	0,01	0,01	0,01	0,01	0	0	-0
Fe II	0,26	0,26	0,27	0,27	0,26	0,27	0,26	0,27	0,26	0,27	0,26	0,26	0,25	0,26	0,25	0,28	0,25	0,17	0,17	0,16
Mn	0,01	0,01	0,01	0,01	0,01	0,01	0,01	0,01	0	0,01	0	0,01	0,01	0,01	0,01	0,01	0,01	0,01	0,01	0
Mg	1,64	1,64	1,64	1,63	1,65	1,63	1,65	1,64	1,65	1,64	1,65	1,65	1,65	1,64	1,64	1,62	1,65	1,75	1,75	1,76
Ca	0,03	0,03	0,03	0,03	0,03	0,03	0,03	0,03	0,03	0,03	0,03	0,04	0,04	0,04	0,04	0,04	0,03	0,04	0,03	0,03
Na	0	0	0	0	0	0	0	0	0	0	0	0	0	0	0	0	0	0	0	0
K	0	0	0	0	0	0	0	0	0	0	0	0	0	0	0	0	0	0	0	0
Cr	0,01	0,01	0,01	0,01	0,01	0,01	0,01	0,01	0,01	0,01	0,01	0,01	0,01	0,01	0,01	0,01	0,01	0,01	0,02	0,01
SumCa	4	4	4	4	4	4	4	4	4	4	4	4	4	4	4	4	4	4	4	4
Al iv	0,1	0,1	0,11	0,1	0,11	0,09	0,1	0,1	0,09	0,09	0,08	0,09	0,09	0,09	0,09	0,09	0,09	0,05	0,05	0,04
Al vi	0,05	0,05	0,06	0,05	0,06	0,05	0,06	0,06	0,05	0,05	0,05	0,05	0,05	0,05	0,05	0,05	0,05	0,03	0,03	0,02
Al vi r	0,03	0,03	0,02	0,03	0,03	0,04	0,03	0,03	0,03	0,03	0,04	0,03	0,03	0,03	0,04	0,03	0,04	0,02	0,02	0,02
Mg M1	0,81	0,81	0,81	0,81	0,82	0,81	0,82	0,81	0,82	0,81	0,82	0,82	0,82	0,81	0,81	0,81	0,82	0,88	0,88	0,88
Mg M2	0,83	0,83	0,83	0,82	0,83	0,83	0,83	0,83	0,83	0,83	0,83	0,83	0,83	0,83	0,83	0,82	0,83	0,88	0,88	0,88
Fe2+M1	0,13	0,13	0,13	0,14	0,13	0,13	0,13	0,13	0,13	0,13	0,13	0,13	0,13	0,13	0,13	0,14	0,13	0,08	0,09	0,08
Fe2+M2	0,13	0,13	0,13	0,14	0,13	0,13	0,13	0,13	0,13	0,14	0,13	0,13	0,13	0,13	0,13	0,14	0,13	0,08	0,09	0,08

Appendix 3: Major element composition of orthopyroxenes

Sample point phase rim/core	MGP2a Du																			
	Area 5		Area 5		Area 5		Area 5		Area 5		Area 5		Area 5		Area 5		Area 5		Area 5	
Host rocl	Du	opx	Du	opx	Du	opx	Du	opx	Du	opx	Du	opx	Du	opx	Du	opx	Du	opx	Du	opx
SiO ₂	55,3	54,9	55,4	51,2	55,1	54,6	54,7	55,1	55,2	55,2	55,2	55,5	55,1	54,8	54,6	55,2	54,4	55,2	54,6	54,6
TiO ₂	0,06	0,06	0	0,48	0,02	0,08	0	0,05	0,03	0,06	0	0,05	0,09	0,03	0,08	0,03	0	0,04	0	0,04
Al ₂ O ₃	4,41	3,24	3,16	0,91	3,02	3,06	3,03	3,04	3,14	3,15	3,16	3,16	3,08	3,17	3,26	3,13	3,34	3,17	3,18	3,18
Fe ₂ O ₃	0,64	0,33	0,31	4,17	0,16	0,31	0,36	0,22	0,23	0,31	0,18	0,26	0,51	0,42	0,16	0,53	0,39	0,56	0,56	0,56
FeO	5,16	5,81	5,9	-0,62	6,1	5,82	5,84	6,03	5,96	5,98	6,11	5,84	5,85	5,62	5,96	5,71	5,95	5,53	5,53	5,53
MnO	0,12	0,2	0,14	0,21	0,15	0,2	0,16	0,2	0,09	0,11	0,16	0,13	0,15	0,2	0,17	0,21	0,18	0,18	0,18	0,18
MgO	31,4	33,4	33,2	27,4	33	33,2	33,3	33,3	33,3	33,5	33,4	33,6	33,4	33,4	33,4	33,3	33,4	33,6	33,7	33,7
CaO	1,69	0,84	1,46	17,8	0,88	0,85	0,85	0,79	0,82	0,76	0,76	0,85	0,8	0,83	0,79	0,86	0,8	0,82	0,82	0,82
Na ₂ O	0,54	0	0	0,3	0	0	0	0	0	0	0	0	0	0	0	0	0	0	0	0
K ₂ O	0,66	0,01	0,02	0,08	0,06	0	0,02	0,01	0	0,02	0	0,01	0	0	0	0	0	0	0	0
Cr ₂ O ₃	0,28	0,29	0,28	0,57	0,34	0,28	0,33	0,28	0,33	0,24	0,26	0,29	0,22	0,21	0,37	0,36	0,35	0,4	0,4	0,4
Tot	100	99,1	99,9	103	98,8	98,4	98,5	99	99,2	99,3	99,5	99,1	99,2	98,5	99,2	98,8	99,6	99,1	99,1	99,1
Si	1,9	1,91	1,92	1,76	1,93	1,91	1,91	1,92	1,92	1,92	1,92	1,92	1,92	1,9	1,91	1,92	1,9	1,91	1,9	1,9
Ti	0	0	0	0,01	0	0	0	0	0	0	0	0	0	0	0	0	0	0	0	0
Al	0,18	0,13	0,13	0,04	0,12	0,13	0,13	0,13	0,13	0,13	0,13	0,13	0,13	0,13	0,13	0,13	0,14	0,13	0,13	0,13
Fe III	0,02	0,01	0,01	0,11	0	0,01	0,01	0,01	0,01	0,01	0,01	0,01	0,01	0,01	0,01	0	0,01	0,01	0,02	0,02
Fe II	0,15	0,17	0,17	-0,02	0,18	0,17	0,17	0,18	0,17	0,17	0,18	0,17	0,17	0,16	0,17	0,16	0,17	0,17	0,16	0,16
Mn	0	0,01	0	0,01	0	0,01	0,01	0,01	0,01	0	0	0,01	0	0	0,01	0,01	0,01	0,01	0,01	0,01
Mg	1,61	1,73	1,71	1,4	1,72	1,73	1,73	1,73	1,73	1,73	1,73	1,73	1,73	1,74	1,74	1,73	1,74	1,73	1,75	1,75
Ca	0,06	0,03	0,05	0,66	0,03	0,03	0,03	0,03	0,03	0,03	0,03	0,03	0,03	0,03	0,03	0,03	0,03	0,03	0,03	0,03
Na	0,04	0	0	0,02	0	0	0	0	0	0	0	0	0	0	0	0	0	0	0	0
K	0,03	0	0	0	0	0	0	0	0	0	0	0	0	0	0	0	0	0	0	0
Cr	0,01	0,01	0,01	0,02	0,01	0,01	0,01	0,01	0,01	0,01	0,01	0,01	0,01	0,01	0,01	0,01	0,01	0,01	0,01	0,01
SumCa	4	4	4	4	4	4	4	4	4	4	4	4	4	4	4	4	4	4	4	4
Al iv	0,1	0,09	0,08	0,24	0,07	0,09	0,09	0,08	0,08	0,09	0,08	0,08	0,08	0,1	0,09	0,08	0,1	0,09	0,1	0,1
Al vi	0,1	0,06	0,06	0,01	0,06	0,06	0,06	0,06	0,06	0,06	0,06	0,06	0,06	0,06	0,06	0,06	0,06	0,06	0,06	0,06
Al vi r	0,08	0,04	0,05	-0,21	0,05	0,04	0,04	0,05	0,05	0,04	0,05	0,05	0,03	0,04	0,05	0,04	0,05	0,04	0,03	0,03
Mg M1	0,82	0,85	0,85	1,08	0,85	0,86	0,86	0,85	0,85	0,85	0,85	0,85	0,86	0,86	0,85	0,86	0,85	0,86	0,86	0,86
Mg M2	0,82	0,88	0,86	0,32	0,87	0,88	0,88	0,88	0,88	0,88	0,88	0,88	0,88	0,88	0,88	0,88	0,88	0,88	0,88	0,88
Fe2+ M1	0,08	0,08	0,09	-0,01	0,09	0,08	0,08	0,09	0,09	0,09	0,09	0,09	0,08	0,08	0,08	0,08	0,08	0,08	0,08	0,08
Fe2+ M2	0,07	0,09	0,09	-0	0,09	0,09	0,09	0,09	0,09	0,09	0,09	0,09	0,09	0,09	0,09	0,09	0,09	0,09	0,09	0,09

Appendix 3: Major element composition of orthopyroxenes

Sample Area	MGP2a Du																
	Area 5 line 3																
point	opx																
rim/core	Du																
Host rock	Du																
SiO ₂	55,3	54,9	55,4	51,2	55,1	54,6	54,7	55,1	55,2	55,5	54,6	54,8	54,6	55,2	54,4	55,2	54,6
TiO ₂	0,06	0,06	0	0,48	0,02	0,08	0	0,05	0,03	0,06	0	0,05	0,09	0,03	0,08	0,03	0
Al ₂ O ₃	4,41	3,24	3,16	0,91	3,02	3,06	3,03	3,04	3,14	3,15	3,16	3,17	3,26	3,13	3,34	3,17	3,18
Fe ₂ O ₃	0,64	0,33	0,31	4,17	0,16	0,31	0,36	0,22	0,23	0,31	0,18	0,26	0,51	0,42	0,16	0,53	0,39
FeO	5,16	5,81	5,9	-0,62	6,1	5,82	5,84	6,03	5,96	5,98	6,11	5,84	5,85	5,62	5,96	5,71	5,95
MnO	0,12	0,2	0,14	0,21	0,15	0,2	0,16	0,16	0,2	0,09	0,11	0,16	0,13	0,15	0,2	0,17	0,21
MgO	31,4	33,4	33,2	27,4	33	33,2	33,2	33,3	33,3	33,5	33,5	33,4	33,6	33,4	33,3	33,4	33,6
CaO	1,69	0,84	1,46	17,8	0,88	0,85	0,85	0,79	0,82	0,76	0,76	0,85	0,8	0,83	0,79	0,86	0,8
Na ₂ O	0,54	0	0	0,3	0	0	0	0	0	0	0	0	0	0	0	0	0
K ₂ O	0,66	0,01	0,02	0,08	0,06	0	0,02	0,01	0	0,02	0	0,01	0	0	0	0	0
Cr ₂ O ₃	0,28	0,29	0,28	0,57	0,34	0,28	0,33	0,28	0,33	0,24	0,26	0,29	0,22	0,21	0,37	0,36	0,35
Tot	100	99,1	99,9	103	98,8	98,4	98,5	99	99,2	99,3	99,5	99,1	99,2	98,5	99,2	98,8	99,1
Si	1,9	1,91	1,92	1,76	1,93	1,91	1,91	1,92	1,92	1,92	1,92	1,92	1,9	1,91	1,92	1,9	1,91
Ti	0	0	0	0,01	0	0	0	0	0	0	0	0	0	0	0	0	0
Al	0,18	0,13	0,13	0,04	0,12	0,13	0,13	0,13	0,13	0,13	0,13	0,13	0,13	0,13	0,13	0,14	0,13
Fe III	0,02	0,01	0,01	0,11	0	0,01	0,01	0,01	0,01	0,01	0,01	0,01	0,01	0,01	0	0,01	0,01
Fe II	0,15	0,17	0,17	-0,02	0,18	0,17	0,17	0,18	0,17	0,17	0,18	0,17	0,16	0,17	0,16	0,17	0,16
Mn	0	0,01	0	0,01	0	0,01	0,01	0,01	0,01	0	0	0,01	0	0	0,01	0,01	0,01
Mg	1,61	1,73	1,71	1,4	1,72	1,73	1,73	1,73	1,73	1,73	1,73	1,73	1,74	1,74	1,73	1,74	1,73
Ca	0,06	0,03	0,05	0,66	0,03	0,03	0,03	0,03	0,03	0,03	0,03	0,03	0,03	0,03	0,03	0,03	0,03
Na	0,04	0	0	0,02	0	0	0	0	0	0	0	0	0	0	0	0	0
K	0,03	0	0	0	0	0	0	0	0	0	0	0	0	0	0	0	0
Cr	0,01	0,01	0,01	0,02	0,01	0,01	0,01	0,01	0,01	0,01	0,01	0,01	0,01	0,01	0,01	0,01	0,01
SumCa	4	4	4	4	4	4	4	4	4	4	4	4	4	4	4	4	4
Al iv	0,1	0,09	0,08	0,24	0,07	0,09	0,09	0,08	0,08	0,09	0,08	0,08	0,1	0,09	0,08	0,1	0,09
Al vi	0,1	0,06	0,06	0,01	0,06	0,06	0,06	0,06	0,06	0,06	0,06	0,06	0,06	0,06	0,06	0,06	0,06
Al vi r	0,08	0,04	0,05	-0,21	0,05	0,04	0,04	0,05	0,05	0,04	0,05	0,05	0,03	0,04	0,05	0,04	0,03
Mg M1	0,82	0,85	0,85	1,08	0,85	0,86	0,86	0,85	0,85	0,85	0,85	0,86	0,86	0,86	0,85	0,86	0,86
Mg M2	0,82	0,88	0,86	0,32	0,87	0,88	0,88	0,88	0,88	0,88	0,88	0,88	0,88	0,88	0,88	0,88	0,88
Fe2+ M1	0,08	0,08	0,09	-0,01	0,09	0,08	0,08	0,09	0,09	0,09	0,09	0,08	0,08	0,08	0,09	0,08	0,08
Fe2+ M2	0,07	0,09	0,09	-0	0,09	0,09	0,09	0,09	0,09	0,09	0,09	0,09	0,09	0,08	0,09	0,08	0,08

Appendix 4: Major element composition of spinels

Sample Area	MGP2b Lh												MGP2b2 Lh											
	Area 2		Area 6		Area 6		Area 8		Area 8		Area 8		Area 1		Area 1		Area 1		Area 2					
	1	2	1	2	1	2	1	2	1	2	1	2	1	2	1	2	1	2	3	4				
point	Sp _{epx}																							
phase	rim	core	rim	rim																				
rim/core	Lh	Lh																						
Host rock																								
SiO ₂	0,04	0,08	0,02	0,07	0,06	0,15	0	0,02	0	0,02	0	0	0,02	0	0,04	0,01	0,04	0,07	0,01	0,01	0,01	0,01		
TiO ₂	0,27	0,21	0,21	0,11	0,43	0,23	0,14	0,47	0,06	0,47	0,06	0,06	0,06	0,06	0,24	0,19	0,28	0,28	0,31	0,31	0,23	0,23		
Al ₂ O ₃	34,91	35,65	35,19	34,75	35,86	36,55	36,29	35,32	36,33	36,33	36,33	36,33	36,33	35,36	34,89	35,15	35,3	35,3	35,74	35,74	35,17	35,17		
Fe ₂ O ₃	2,2	3,09	3,44	3,31	2,62	2,68	3,24	2,55	3,77	3,77	3,77	3,77	3,77	3,24	3,69	2,9	2,8	2,8	3,14	3,14	3,58	3,58		
FeO	11,68	10,78	10,81	11,23	11,43	11,78	11,29	11,82	11,49	11,49	11,49	11,49	11,49	11,55	11,1	11,33	11,49	11,49	11,39	11,39	9,58	9,58		
MnO	0,23	0,17	0,17	0,15	0,22	0,03	0,26	0,13	0,15	0,15	0,15	0,15	0,15	0,24	0,19	0,18	0,15	0,15	0,11	0,11	0,19	0,19		
MgO	16,67	17,17	17,2	16,84	17,04	17,38	17,04	16,75	17,05	17,05	17,05	17,05	16,9	16,95	17,03	16,99	16,99	17,32	17,32	18,18	18,18	18,18		
Cr ₂ O ₃	32,69	31,06	31,43	32,21	31,46	31,82	30,97	31,45	30,93	30,93	30,93	30,93	32,2	32,07	32,45	32,41	32,41	32,34	32,34	32,85	32,85	32,85		
NiO	0	0,22	0	0,19	0,23	0	0	0	0	0	0	0	0	0,22	0,29	0,16	0,22	0,22	0,11	0,11	0,2	0,2		
Tot	98,69	98,43	98,46	98,86	99,35	100,62	99,23	98,51	99,78	99,78	99,78	99,78	99,99	99,38	99,52	99,71	99,71	100,46	100,46	99,99	99,99	99,99		
Si	0,001	0,002	0,001	0,002	0,002	0,004	0	0,001	0	0,001	0	0	0,001	0	0,001	0,002	0,002	0	0	0	0	0		
Ti	0,006	0,005	0,005	0,002	0,009	0,005	0,003	0,01	0,001	0,001	0,001	0,001	0,005	0,004	0,006	0,006	0,006	0,007	0,007	0,005	0,005	0,005		
Al	1,19	1,211	1,198	1,183	1,21	1,215	1,224	1,204	1,22	1,22	1,22	1,22	1,191	1,182	1,188	1,191	1,191	1,194	1,194	1,176	1,176	1,176		
Fe	0,05	0,07	0,07	0,07	0,06	0,06	0,07	0,06	0,08	0,08	0,08	0,08	0,07	0,08	0,06	0,06	0,06	0,07	0,07	0,08	0,08	0,08		
Fe II	0,28	0,26	0,26	0,27	0,27	0,28	0,27	0,29	0,27	0,27	0,27	0,27	0,28	0,27	0,27	0,27	0,27	0,27	0,27	0,23	0,23	0,23		
Mn	0,006	0,004	0,004	0,004	0,005	0,001	0,006	0,003	0,004	0,004	0,004	0,004	0,006	0,005	0,004	0,004	0,004	0,003	0,003	0,005	0,005	0,005		
Mg	0,719	0,738	0,74	0,725	0,727	0,731	0,726	0,722	0,724	0,724	0,724	0,724	0,719	0,726	0,728	0,724	0,724	0,732	0,732	0,769	0,769	0,769		
Cr	0,748	0,708	0,717	0,736	0,712	0,71	0,7	0,719	0,697	0,697	0,697	0,697	0,727	0,729	0,735	0,733	0,733	0,725	0,725	0,737	0,737	0,737		
Ni	0	0,005	0	0,004	0,005	0	0	0	0	0	0	0	0,005	0,007	0,004	0,005	0,005	0,002	0,002	0,005	0,005	0,005		
Cr/Cr+Al	0,3858	0,3688	0,3746	0,3833	0,3704	0,3686	0,364	0,3739	0,3635	0,3635	0,3635	0,3635	0,3792	0,3814	0,3824	0,3811	0,3811	0,3777	0,3777	0,3852	0,3852	0,3852		
Mg/BIV	0,7137	0,7364	0,7363	0,7251	0,7227	0,724	0,7243	0,7141	0,723	0,723	0,723	0,723	0,7185	0,7279	0,725	0,7223	0,7223	0,7286	0,7286	0,7683	0,7683	0,7683		
Fe II/BIV	0,2807	0,2595	0,2596	0,2713	0,272	0,2753	0,2694	0,2827	0,2734	0,2734	0,2734	0,2734	0,2757	0,2674	0,2707	0,2741	0,2741	0,2688	0,2688	0,2272	0,2272	0,2272		
Fe III/TRIV	0,0241	0,0337	0,0375	0,0362	0,0286	0,0287	0,035	0,028	0,0404	0,0404	0,0404	0,0404	0,035	0,0401	0,0315	0,0304	0,0304	0,0337	0,0337	0,0384	0,0384	0,0384		
Cr/TRIV	0,3765	0,3564	0,3605	0,3695	0,3598	0,358	0,3513	0,3634	0,3488	0,3488	0,3488	0,3488	0,3659	0,3661	0,3703	0,3695	0,3695	0,3649	0,3649	0,3704	0,3704	0,3704		
Al/TRIV	0,5995	0,6099	0,6019	0,5943	0,6116	0,6132	0,6138	0,6086	0,6108	0,6108	0,6108	0,6108	0,5991	0,5938	0,5982	0,6001	0,6001	0,6014	0,6014	0,5912	0,5912	0,5912		
mg#	71,78	73,95	73,93	72,77	72,65	72,45	72,90	71,63	72,56	72,56	72,56	72,28	73,13	72,81	72,81	72,49	72,49	73,04	73,04	77,18	77,18	77,18		
cr#	38,59	36,89	37,47	38,35	37,06	36,88	36,41	37,40	36,36	36,36	36,36	37,93	38,15	38,25	38,12	38,12	37,78	37,78	37,78	38,53	38,53	38,53		

Appendix 4: Major element composition of spinels

Sample Area	MGP2b2 Lh												MGP1b Hz						MGP1c Hz			
	Area 4		Area 4		Area 5		Area 7		Area 7		Area 7		Area 2		Area 6		Area 7		Area 1		Area 2	
	1	6	1	6	1	2	1	2	1	2	1	2	5	5	2	5	4	4	5 repeat	1	1	2
point	Sp _{epx}																					
phase	core	rim	core	core	core	core																
rim/core	Lh																					
Host rock	Lh																					
SiO ₂	0,08	0	0,06	0,05	0,08	0,06	0,08	0,06	0,08	0,03	0,03	0,03	0,03	0,03	0,09	0,1	0,05	0,1	0,07	0	0,07	0
TiO ₂	0,31	0,3	0,32	0,26	0,25	0,34	0,21	0,33	0,21	0,33	0,21	0,33	0,21	0,33	0,29	0,28	0,34	0,26	0,43	0,42	0,43	0,42
Al ₂ O ₃	34,95	34,74	34,35	34,55	34,42	34,16	34,1	34,87	34,1	34,87	34,1	34,87	34,1	34,87	28,72	28,88	27,78	27,43	27,32	26,29	27,32	26,29
Fe ₂ O ₃	3,47	3,41	3,69	4,14	3,74	3,25	3,5	3,55	3,5	3,55	3,5	3,55	3,5	3,55	9,48	9,61	9,97	10,46	6,5	6,69	6,5	6,69
FeO	11,56	11,08	10,93	11,11	11,15	11,63	11,11	11,26	11,11	11,26	11,11	11,26	11,11	11,26	15,18	15,09	15,03	15,35	13	13,36	13	13,36
MnO	0,07	0,18	0,27	0,13	0,21	0,08	0,15	0,1	0,15	0,1	0,15	0,1	0,15	0,18	0,21	0,14	0,22	0,26	0,26	0,14	0,26	0,14
MgO	17,03	16,96	17,09	17,04	16,89	16,59	16,67	16,99	16,67	16,99	16,67	16,99	16,67	16,99	13,83	14,09	13,74	13,58	15,14	14,87	15,14	14,87
Cr ₂ O ₃	32,41	32	32,57	31,88	31,91	32,23	31,94	31,83	31,94	31,83	31,94	31,83	31,94	31,83	31,8	32,24	32,01	32,33	36,67	37,96	36,67	37,96
NiO	0,29	0,21	0,34	0,27	0,21	0,26	0,31	0,26	0,31	0,26	0,31	0,26	0,31	0,26	0,28	0,26	0,28	0,26	0,21	0,25	0,21	0,25
Tot	100,17	98,88	99,62	99,44	98,86	98,60	98,07	99,22	98,07	99,22	98,07	99,22	98,07	99,22	99,85	100,76	99,34	100,00	99,60	99,98	99,60	99,98
Si	0,002	0	0,002	0,001	0,002	0,002	0,002	0,001	0,002	0,001	0,002	0,001	0,002	0,001	0,003	0,003	0,002	0,003	0,002	0	0,002	0
Ti	0,007	0,007	0,007	0,006	0,005	0,007	0,005	0,007	0,005	0,007	0,005	0,007	0,005	0,007	0,007	0,006	0,008	0,006	0,01	0,009	0,01	0,009
Al	1,176	1,182	1,163	1,171	1,173	1,17	1,173	1,183	1,173	1,183	1,173	1,183	1,173	1,183	1,014	1,01	0,99	0,975	0,963	0,93	0,963	0,93
Fe	0,07	0,07	0,08	0,09	0,08	0,07	0,08	0,08	0,08	0,08	0,08	0,08	0,08	0,08	0,21	0,21	0,23	0,24	0,15	0,15	0,15	0,15
Fe II	0,28	0,27	0,26	0,27	0,27	0,28	0,27	0,27	0,27	0,27	0,27	0,27	0,27	0,27	0,38	0,37	0,38	0,39	0,33	0,34	0,33	0,34
Mn	0,002	0,004	0,007	0,003	0,005	0,002	0,004	0,002	0,004	0,002	0,004	0,002	0,004	0,002	0,005	0,005	0,004	0,006	0,007	0,004	0,007	0,004
Mg	0,725	0,73	0,732	0,73	0,728	0,718	0,725	0,729	0,725	0,729	0,725	0,729	0,725	0,729	0,618	0,623	0,619	0,61	0,675	0,665	0,675	0,665
Cr	0,731	0,73	0,74	0,725	0,73	0,74	0,737	0,724	0,737	0,724	0,737	0,724	0,737	0,753	0,756	0,765	0,77	0,867	0,9	0,867	0,9	
Ni	0,007	0,005	0,008	0,006	0,005	0,006	0,007	0,006	0,007	0,006	0,007	0,006	0,007	0,007	0,007	0,006	0,007	0,006	0,005	0,006	0,005	0,006
Cr/Cr+Al	0,3834	0,3819	0,3887	0,3823	0,3834	0,3875	0,3858	0,3797	0,3858	0,3797	0,3858	0,3797	0,3858	0,3875	0,4261	0,4281	0,4359	0,4415	0,4737	0,492	0,4737	0,492
Mg/BIV	0,7229	0,7286	0,7311	0,7298	0,7259	0,7163	0,725	0,7272	0,725	0,7272	0,725	0,7272	0,725	0,7272	0,6161	0,6213	0,6174	0,6084	0,6703	0,6625	0,6703	0,6625
Fe II/BIV	0,2754	0,267	0,2623	0,2671	0,269	0,2818	0,2713	0,2703	0,2713	0,2703	0,2713	0,2703	0,2713	0,2703	0,3794	0,3734	0,379	0,386	0,3231	0,3339	0,3231	0,3339
Fe III/TRIV	0,0376	0,0373	0,0402	0,0451	0,041	0,0358	0,0386	0,0388	0,0386	0,0388	0,0386	0,0388	0,0386	0,0388	0,1079	0,1084	0,1144	0,1197	0,074	0,0763	0,074	0,0763
Cr/TRIV	0,369	0,3676	0,3731	0,365	0,3676	0,3737	0,3709	0,365	0,3709	0,365	0,3709	0,365	0,3709	0,3802	0,3818	0,386	0,3886	0,4387	0,4544	0,4387	0,4544	
Al/TRIV	0,5934	0,5951	0,5867	0,5898	0,5913	0,5905	0,5962	0,5962	0,5905	0,5962	0,5905	0,5962	0,5905	0,5962	0,5119	0,5099	0,4995	0,4916	0,4873	0,4693	0,4873	0,4693
mg#	72,42	73,17	73,59	73,21	72,97	71,77	72,78	72,89	72,78	72,89	72,78	72,89	72,78	72,89	61,88	62,46	61,96	61,19	67,48	66,48	67,48	66,48
cr#	38,36	38,20	38,89	38,24	38,35	38,77	38,60	37,99	38,60	37,99	38,60	37,99	38,60	37,99	42,63	42,83	43,61	44,16	47,39	49,21	47,39	49,21

Appendix 4: Major element composition of spinels

Sample Area	MGP4b Hz												MGP1h Du							
	Area 3		Area 4		Area 4		Area 4		Area 5		Area 6		Area 7		Area 7		Area 7		Area 1	
	4	4	5	6	4	4	5	6	4	9	1	2	1	2	11	12	21	22	3	3
point	Sp _{epx} core	Sp _{epx} rim	Sp _{epx} core	Sp _{epx} rim	Sp _{epx} rim	Sp _{epx} core	Sp _{epx} core	Sp _{epx} rim	Sp _{epx} rim	Sp _{epx} core	Sp _{epx} rim	Sp _{epx} core	Sp _{epx} core	Sp _{epx} core						
rim/core	Hz	Hz	Hz	Hz	Hz	Hz	Hz	Hz	Hz	Hz	Hz	Hz	Hz	Hz	Hz	Hz	Hz	Hz	Hz	Hz
Host rock	0,03	0,07	0,07	0,07	0,03	0,03	0,01	0,01	0,05	0,07	0,02	0,01	0,02	0,01	0,03	0,09	0,03	0,04	0,03	0,03
SiO ₂	0,2	0,13	0,19	0,14	0,14	0,14	0,2	0,21	0,25	0,25	0,22	0,16	0,22	0,16	0,18	0,17	0,17	0,17	0,36	0,36
TiO ₂	33,45	33,72	34,01	34,19	34,64	34,64	34,85	34,36	34,41	34,41	34,61	34,35	34,61	34,35	33,91	33,86	33,41	33,78	29,25	29,25
Al ₂ O ₃	3,63	3,73	3,82	3,79	4,55	4,55	4,03	4,14	2,66	4,04	4,04	3,74	4,04	3,74	4,09	3,42	4,1	4,3	6,58	6,58
Fe ₂ O ₃	10,4	9,96	10,28	9,96	9,65	9,65	9,79	9,88	10,05	10,17	10,17	10,17	10,17	10,17	9,94	10,14	10,12	9,51	12,18	12,18
FeO	0,1	0,19	0,1	0,11	0,15	0,15	0,24	0,13	0,15	0,12	0,12	0,21	0,12	0,21	0,09	0,22	0,15	0,24	0,14	0,14
MnO	17,35	17,5	17,61	17,63	18,04	18,04	17,82	17,79	17,58	17,82	17,82	17,51	17,82	17,51	17,73	17,64	17,4	17,85	15,61	15,61
MgO	33,89	33,08	33,51	32,85	32,45	32,45	32,26	32,55	33,07	32,87	32,87	33,25	32,87	33,25	33,23	33,98	33,32	33,22	34,09	34,09
Cr ₂ O ₃	0,25	0,15	0,28	0,27	0,18	0,18	0,23	0,26	0,17	0,15	0,15	0,35	0,15	0,35	0,23	0,19	0,25	0,3	0,28	0,28
NiO	99,29	98,53	99,87	99,01	99,83	99,83	99,42	99,36	98,42	100,01	100,01	99,74	99,43	99,74	99,43	99,71	98,95	99,41	98,52	98,52
Tot	0,001	0,002	0,002	0,002	0,001	0,001	0	0,001	0,002	0,002	0,001	0	0,001	0,002	0,001	0,003	0,001	0,001	0,001	0,001
Si	0,004	0,003	0,004	0,003	0,003	0,003	0,004	0,005	0,005	0,005	0,005	0,003	0,005	0,003	0,004	0,004	0,004	0,004	0,008	0,008
Ti	1,138	1,151	1,147	1,16	1,164	1,164	1,175	1,161	1,172	1,172	1,162	1,159	1,162	1,159	1,148	1,144	1,139	1,143	1,03	1,03
Al	0,08	0,08	0,08	0,08	0,1	0,1	0,09	0,09	0,06	0,06	0,09	0,08	0,09	0,08	0,09	0,07	0,09	0,09	0,15	0,15
Fe	0,25	0,24	0,25	0,24	0,23	0,23	0,23	0,24	0,24	0,24	0,24	0,24	0,24	0,24	0,24	0,24	0,24	0,23	0,3	0,3
Fe II	0,002	0,005	0,002	0,003	0,004	0,004	0,006	0,003	0,004	0,004	0,003	0,005	0,003	0,005	0,002	0,005	0,004	0,006	0,004	0,004
Mn	0,746	0,755	0,751	0,756	0,766	0,766	0,759	0,76	0,757	0,757	0,757	0,747	0,757	0,747	0,759	0,753	0,75	0,764	0,695	0,695
Mg	0,773	0,758	0,758	0,748	0,731	0,731	0,729	0,738	0,755	0,74	0,74	0,753	0,754	0,753	0,754	0,77	0,762	0,754	0,805	0,805
Cr	0,006	0,003	0,006	0,006	0,004	0,004	0,005	0,006	0,004	0,003	0,003	0,008	0,003	0,008	0,005	0,004	0,006	0,007	0,007	0,007
Ni	0,4046	0,3968	0,3979	0,3919	0,3858	0,3858	0,383	0,3885	0,3919	0,3891	0,3891	0,3936	0,3891	0,3936	0,3966	0,4023	0,4008	0,3974	0,4387	0,4387
Cr/Cr+Al	0,7465	0,7544	0,7514	0,7573	0,7664	0,7664	0,76	0,7601	0,7543	0,7553	0,7553	0,7504	0,7553	0,7504	0,7591	0,752	0,7512	0,7654	0,693	0,693
Mg/BIV	0,251	0,2409	0,2462	0,24	0,23	0,23	0,2342	0,2368	0,2421	0,2418	0,2418	0,2445	0,2387	0,2445	0,2387	0,2426	0,2451	0,2287	0,3034	0,3034
Fe II/BIV	0,0396	0,0409	0,0414	0,0413	0,0489	0,0489	0,0435	0,0449	0,0292	0,0435	0,0435	0,0404	0,0444	0,0404	0,0444	0,0371	0,0449	0,0467	0,0746	0,0746
Fe III/TRIV	0,3886	0,3806	0,3814	0,3757	0,367	0,367	0,3663	0,3711	0,3805	0,3722	0,3722	0,3777	0,3789	0,3777	0,3789	0,3874	0,3828	0,3789	0,406	0,406
Cr/TRIV	0,5719	0,5785	0,5772	0,583	0,5841	0,5841	0,5901	0,584	0,5903	0,5843	0,5843	0,5818	0,5843	0,5818	0,5766	0,5755	0,5723	0,5744	0,5194	0,5194
Al/TRIV	74,83	75,79	75,32	75,93	76,91	76,91	76,44	76,24	75,71	75,74	75,74	75,42	75,71	75,42	76,07	75,61	75,39	76,98	69,55	69,55
mg#	40,47	39,70	39,80	39,20	38,60	38,60	38,32	38,86	39,21	38,92	38,92	39,38	39,21	39,38	39,67	40,24	40,09	39,76	43,89	43,89
cr#																				

Appendix 4: Major element composition of spinels

Sample Area	MGP1h Du												MGP2a Du															
	Area 1			Area 2			Area 4			Area 1			Area 3			Area 4			Area 1			Area 3			Area 4			
	4	9	10	1	3	Sp _{epx} rim	Sp _{epx} core	1	2	3	6	1	5	6	1	6	7	1	2	3	4							
Host rock	Du	Du	Du	Du	Du	Du	Du	Du	Du	Du	Du	Du	Du	Du	Du	Du	Du	Du	Du	Du	Du	Du	Du	Du	Du	Du	Du	Du
SiO ₂	0,01	0,07	0,07	0,04	0,04	0,03	0,06	0,12	0,03	0,03	0,05	0,05	0,05	0,03	0,03	0,03	0,05	0,03	0,12	0,03	0,05	0,03	0,03	0,03	0,01	0,05	0,03	0,03
TiO ₂	0,32	0,33	0,33	0,27	0,39	0,53	0,5	0,48	0,52	0,73	0,75	0,73	0,73	0,81	0,76	0,76	0,73	0,76	0,48	0,52	0,75	0,76	0,81	0,77	0,77	0,8	0,73	0,73
Al ₂ O ₃	29,47	27,84	28,81	22,46	22,83	21,59	21,81	21,89	21,4	24,87	24,87	25,87	26,05	25,51	26,05	25,51	25,87	26,05	21,4	24,87	24,87	25,87	26,05	25,51	25,64	25,69	25,06	25,06
Fe ₂ O ₃	7,01	5,93	6,69	7,34	7,33	6,4	5,48	5,82	6,2	5,83	6,2	6,17	5,97	5,91	5,97	5,91	6,17	5,97	6,2	5,83	6,2	6,17	5,97	5,91	5,94	5,4	5,12	5,12
FeO	11,84	14,3	12,38	13,43	13,35	14,37	14,68	14,56	13,82	14,27	14,27	13,83	13,89	13,36	13,89	13,36	13,83	13,89	13,82	14,27	14,27	13,83	13,89	13,36	13,69	14	13,95	13,95
MnO	0,19	0,19	0,22	0,08	0,27	0,2	0,19	0,17	0,27	0,23	0,23	0,28	0,2	0,24	0,2	0,24	0,28	0,2	0,27	0,23	0,23	0,28	0,2	0,24	0,23	0,18	0,16	0,16
MgO	15,82	14,25	15,7	14,23	14,56	13,68	13,41	13,64	13,79	14,3	14,3	14,47	14,58	14,79	14,58	14,79	14,47	14,58	13,79	14,3	14,3	14,47	14,58	14,79	14,76	14,58	14,27	14,27
Cr ₂ O ₃	33,76	36,26	35,3	40,81	41,43	42,2	42,21	42,35	42,36	39,2	39,2	37,44	37,62	37,92	37,62	37,92	37,44	37,62	42,36	39,2	39,2	37,44	37,62	37,92	38,63	38,77	38,81	38,81
NiO	0,27	0,31	0,18	0,14	0,21	0,12	0,07	0,18	0,24	0,17	0,17	0,25	0,2	0,14	0,2	0,14	0,25	0,2	0,24	0,17	0,17	0,25	0,2	0,14	0,19	0,26	0,16	0,16
Tot	98,69	99,48	99,68	98,80	100,40	99,12	98,41	99,21	98,63	99,67	99,67	99,09	99,30	98,71	99,30	98,71	99,09	99,30	98,63	99,67	99,67	99,09	99,30	98,71	99,87	99,73	98,28	98,28
Si	0	0,002	0,002	0,001	0,001	0,001	0,002	0,004	0,001	0,002	0,002	0,002	0,002	0,001	0,001	0,001	0,002	0,001	0,001	0,002	0,002	0,002	0,001	0,001	0	0,002	0,001	0,001
Ti	0,007	0,007	0,007	0,006	0,009	0,012	0,012	0,011	0,012	0,012	0,017	0,017	0,017	0,019	0,017	0,019	0,017	0,017	0,012	0,017	0,017	0,017	0,017	0,019	0,017	0,018	0,017	0,017
Al	1,034	0,986	1,006	0,818	0,817	0,789	0,802	0,799	0,786	0,889	0,889	0,925	0,929	0,914	0,929	0,914	0,925	0,929	0,786	0,889	0,889	0,925	0,929	0,914	0,91	0,914	0,906	0,906
Fe	0,16	0,13	0,15	0,17	0,17	0,15	0,13	0,14	0,15	0,13	0,13	0,14	0,14	0,14	0,14	0,14	0,14	0,14	0,15	0,13	0,13	0,14	0,14	0,14	0,13	0,12	0,12	0,12
Fe II	0,29	0,36	0,31	0,35	0,34	0,37	0,38	0,38	0,36	0,36	0,36	0,35	0,35	0,34	0,35	0,34	0,35	0,35	0,36	0,36	0,36	0,35	0,34	0,34	0,34	0,35	0,36	0,36
Mn	0,005	0,005	0,006	0,002	0,007	0,005	0,005	0,004	0,007	0,006	0,006	0,007	0,005	0,006	0,005	0,006	0,007	0,005	0,007	0,006	0,006	0,006	0,005	0,006	0,006	0,005	0,004	0,004
Mg	0,702	0,638	0,693	0,655	0,659	0,632	0,624	0,629	0,64	0,647	0,647	0,654	0,657	0,67	0,657	0,67	0,654	0,657	0,64	0,647	0,647	0,654	0,657	0,67	0,662	0,655	0,652	0,652
Cr	0,794	0,861	0,826	0,997	0,995	1,035	1,042	1,036	1,043	0,94	0,94	0,898	0,899	0,911	0,899	0,911	0,898	0,899	1,043	0,94	0,94	0,898	0,899	0,911	0,92	0,925	0,941	0,941
Ni	0,006	0,007	0,004	0,003	0,005	0,003	0,002	0,004	0,006	0,004	0,004	0,006	0,005	0,003	0,005	0,003	0,006	0,005	0,006	0,004	0,004	0,006	0,005	0,003	0,005	0,006	0,004	0,004
Cr/Cr+Al	0,4345	0,466	0,451	0,5493	0,549	0,5673	0,5648	0,5647	0,5704	0,5139	0,5139	0,4925	0,492	0,499	0,492	0,499	0,4925	0,492	0,5647	0,5139	0,5139	0,4925	0,492	0,499	0,5026	0,503	0,5095	0,5095
Mg/BIV	0,7009	0,637	0,689	0,6525	0,6558	0,6259	0,6165	0,6226	0,6355	0,6373	0,6373	0,6463	0,648	0,66	0,648	0,66	0,6463	0,648	0,6355	0,6373	0,6373	0,6463	0,648	0,66	0,6538	0,6468	0,6432	0,6432
Fe II/BIV	0,2943	0,359	0,305	0,3455	0,3373	0,3689	0,3786	0,373	0,3574	0,3569	0,3569	0,3466	0,347	0,334	0,347	0,334	0,3466	0,347	0,3574	0,3569	0,3569	0,3466	0,347	0,334	0,3404	0,3486	0,3527	0,3527
Fe III/TRIV	0,0791	0,068	0,075	0,0859	0,0846	0,0757	0,0653	0,0688	0,0736	0,0679	0,0679	0,0717	0,069	0,069	0,069	0,069	0,0717	0,069	0,0736	0,0679	0,0679	0,0717	0,069	0,069	0,0685	0,0625	0,0601	0,0601
Cr/TRIV	0,4001	0,435	0,417	0,5021	0,5025	0,5243	0,528	0,5259	0,5284	0,479	0,479	0,4572	0,458	0,465	0,458	0,465	0,4572	0,458	0,5284	0,479	0,479	0,4572	0,458	0,465	0,4681	0,4716	0,4789	0,4789
Al/TRIV	0,5208	0,498	0,508	0,412	0,4129	0,4	0,4068	0,4053	0,398	0,4531	0,4531	0,4711	0,473	0,466	0,473	0,466	0,4711	0,473	0,4068	0,4531	0,4531	0,4711	0,473	0,466	0,4633	0,4659	0,4611	0,4611
mg#	70,42	63,97	69,32	65,38	66,03	62,91	61,95	62,54	64,00	64,10	64,10	65,09	65,16	66,36	65,16	66,36	65,09	65,16	64,00	64,10	64,10	65,09	65,16	66,36	65,77	64,98	64,58	64,58
cr#	43,46	46,64	45,12	54,94	54,91	56,74	56,50	56,49	57,05	51,40	51,40	49,27	49,22	49,94	49,22	49,94	49,27	49,22	57,05	51,40	51,40	49,27	49,22	49,94	50,27	50,32	50,96	50,96

Appendix 4: Major element composition of spinels

Sample Area	MGPId Wh							
	Area 4 3	Area 4 4	Area 5 2	Area 6 2	Area 8 1	Area 8 1	Area 8 2	Area 8 2
point	sp	sp	Sp _{epx} core	Sp _{epx} core	sp	sp	sp	sp
phase	Hz	Hz	Hz	Hz	core	core	Hz	Hz
rim/core								
Host rock								
SiO ₂	0	0	0,09	0,02	0	0	0,06	0,06
TiO ₂	0,38	0,44	0,49	0,49	0,69	0,69	0,57	0,57
Al ₂ O ₃	48	48,16	48,48	45,4	45,52	45,52	47,16	47,16
Fe ₂ O ₃	4,65	4,72	3,56	4,26	4,84	4,84	4	4
FeO	15,28	15,46	15,21	16,01	15,73	15,73	16,06	16,06
MnO	0,1	0,27	0,17	0,17	0,1	0,1	0,15	0,15
MgO	15,83	15,84	16	15,06	15,5	15,5	15,39	15,39
Cr ₂ O ₃	15,2	15,51	15,3	17,79	17,28	17,28	15,98	15,98
NiO	0,21	0,23	0,21	0,24	0,22	0,22	0,13	0,13
Tot	99,65	100,63	99,52	99,44	99,89	99,89	99,50	99,50
Si	0	0	0,002	0,001	0	0	0,002	0,002
Ti	0,008	0,009	0,01	0,01	0,014	0,014	0,012	0,012
Al	1,557	1,55	1,569	1,496	1,491	1,491	1,54	1,54
Fe	0,1	0,1	0,07	0,09	0,1	0,1	0,08	0,08
Fe II	0,35	0,35	0,35	0,37	0,37	0,37	0,37	0,37
Mn	0,002	0,006	0,004	0,004	0,002	0,002	0,004	0,004
Mg	0,649	0,645	0,655	0,627	0,642	0,642	0,635	0,635
Cr	0,331	0,335	0,332	0,393	0,379	0,379	0,35	0,35
Ni	0,005	0,005	0,005	0,005	0,005	0,005	0,003	0,003
Cr/Cr+Al	0,1752	0,1776	0,1747	0,2081	0,2029	0,2029	0,1852	0,1852
Mg/BIV	0,6472	0,642	0,6495	0,6239	0,6356	0,6356	0,6285	0,6285
Fe II/BIV	0,3505	0,3517	0,3465	0,3721	0,362	0,362	0,368	0,368
Fe III/TRIV	0,0485	0,0489	0,0373	0,0453	0,0513	0,0513	0,0423	0,0423
Cr/TRIV	0,1667	0,1689	0,1682	0,1987	0,1925	0,1925	0,1773	0,1773
Al/TRIV	0,7848	0,7822	0,7945	0,7561	0,7562	0,7562	0,7804	0,7804
mg#	64,86	64,61	65,21	62,63	63,71	63,71	63,07	63,07
cr#	17,53	17,77	17,48	20,82	20,30	20,30	18,53	18,53

Sample Area point phase	MGP2b												MGP2b2																					
	Area 1		Area 6		Area 7		Area 8		Area 1		Area 2		Area 2		Area 3		Area 3		Area 3		Area 3													
	1	cp2	3	cp2	1	cp2	1	cp2	12	cp2	1	cp1	2	cp2	3	cp2	8	cp1	1	cp1	2	cp2	3	cp1	4	cp2	6	cp1	8	cp2				
SiO ₂			52,52	52,73	53,12	52,78	52,58	52,22	52,22	52,46	52,9	53,66	52,76																					
TiO ₂			0,12	0,14	0,39	0,28	0,18	0,27	0,3	0,3	0,26	0,27	0,29																					
Al ₂ O ₃			4,17	3,99	4,01	4,04	4,01	4,52	3,92	3,92	3,91	3,4	3,98																					
Fe ₂ O ₃			0,59	0,5	0,15	0,26	0,52	0,14	0,29	0,29	0,08	0,11	0,18																					
FeO			2,53	2,19	2,76	2,76	2,2	2,8	2,63	2,63	2,63	2,83	2,5																					
MnO			0,14	0,07	0,12	0,11	0,03	0,04	0,05	0,05	0,01	0,12	0,05																					
MgO			16,76	16,85	16,75	16,8	16,81	16,63	16,8	16,8	16,72	17,18	16,66																					
CaO			21,29	21,55	21,01	21,05	21,49	21,06	21,02	21,02	21,22	21,22	21,27																					
Na ₂ O			0,99	1	0,99	0,91	1,02	0,77	0,91	0,91	0,88	0,85	0,93																					
K ₂ O			0,03	0	0,01	0,02	0	0,01	0	0	0	0	0,01																					
Cr ₂ O ₃			1,33	1,19	1,44	1,21	1,35	1,26	1,02	1,02	1,09	0,56	0,92																					
Tot			100,47	100,21	100,76	100,22	100,19	99,71	99,4	99,4	99,7	100,2	99,55																					
Ba	5,4	0	0	0	1,57	0	0	0,65	0	1,39	0,33	0	1,42																					
Th	14,2	0	10,4	0	0	0	2,12	3,29	0	2,75	2,35	0	3,06																					
Nb	1,21	1,58	0	1,11	0,701	0,701	0,926	1,15	0,701	0,898	0,669	0,631	0,757																					
La	3,84	4,69	4,14	4,25	3,69	3,02	3,77	4,24	4,24	3,7	3,42	3,74	4,28																					
Ce	9,1	11,3	10,5	10,8	8,22	8,58	9,86	0	0	9,89	9,1	9,56	8,45																					
Sr	97,4	0	0	0	95,7	92,8	96,9	124	123	102	98	102	101																					
Nd	5,66	7,43	6,35	5,95	4,38	0	4,93	9,05	9,32	5,89	4,95	5,37	4,45																					
Zr	21,3	21,5	19,6	18	19,4	19	21,7	31,4	28,6	20,7	18,4	16,4	19,1																					
Sm	1,49	2,34	2,12	2,28	1,73	0,93	1,54	3,08	3,08	1,82	1,25	0,66	1,31																					
Eu	0,45	0,41	0,636	0,74	0,38	0,28	0,37	0	0	0,57	0,59	0,32	0,46																					
Ti	1694	1565	1452	1432	1455	1479	1726	1290	1290	1295	1330	1276	1479																					
Gd	1,6	0	1,67	0	1,34	0	1,19	1,66	1,66	2,88	0,72	1,48	0																					
Dy	1,99	1,43	1,7	0,99	1,24	0	1,62	2,13	2,39	1,92	1,4	1,8	1,97																					
Er	1,4	0,79	1,36	0,78	1,32	0,79	1,04	1,03	1,46	0	0,83	0,39	1,44																					
Yb	1,54	1,01	1,42	0	1,2	1,4	0	1,03	1,62	1,25	1,25	0,71	1,33																					
Lu	0,26	0,18	0	0	0,224	0	0	0	0,23	0,182	0,165	0	0																					

Appendix 5: Trace element composition of clinopyroxenes

Sample Area	MGP2b2										MGP1b					
	Area 4 3	Area 4 6	Area 4 1	Area 5 3	Area 5 7	Area 5 1	Area 6 4	Area 6 6	Area 6 3	Area 7 10	Area 7 11	Area 7 19	Area 1 1	Area 2 4	Area 6 2	Area 7 3
point	cpx2	cpx2	cpx2	cpx2	cpx2	cpx1	cpx1	cpx1	cpx2	cpx2	cpx2	cpx2	cpx2	cpx2	cpx2	cpx2
phase																
SiO ₂	52,23			52,06		52,53	51,93	51,11	51,46	50,03				52		52,85
TiO ₂	0,27			0,26		0,22	0,16	0,23	0,34	0,28				0,05		0,17
Al ₂ O ₃	3,88			3,95		3,68	3,22	3,59	4,42	4,06				3,45		3,53
Fe ₂ O ₃	0,52			0,31		0,62	0,68	0,81	0,3	0,86				0,52		0,4
FeO	2,18			2,42		2,1	2,33	1,95	2,6	1,89				3,26		3,65
MnO	0,15			0		0,12	0,15	0,09	0,12	0,12				0,12		0,06
MgO	16,74			16,5		17,01	17,16	17,18	16,24	16,26				16,51		16,41
CaO	21,27			21,1		21,56	21,24	21,31	20,92	21,16				21,09		21,15
Na ₂ O	1			0,96		0,98	0,81	0,76	0,89	0,93				0,82		0,94
K ₂ O	0,02			0		0	0,01	0,01	0,02	0				0		0,01
Cr ₂ O ₃	1,32			1,26		1,01	1,2	0,87	1,24	1,19				1,01		1,07
Tot	99,58			98,82		99,83	98,89	97,91	98,55	96,79				98,83		100,24
Ba	1,91	0	0,01	0	0,65	0,4	1,21	0	0	0,04	1,88	0	1,17	4,13	0	0
Th	4,35	3,06	0	1,88	1,29	2,35	2	0	10,7	0	0	0	8,12	0	4,82	8,59
Nb	0,799	0,743	0,884	0,823	0,912	0,662	0,547	0,519	0	0,934	0,645	0,463	0,687	0,07	0,393	0,168
La	4,18	12,6	4,17	3,85	4,13	3,64	3,61	3,95	4,58	3,79	4,45	0	5,98	5,78	5,55	4,84
Ce	13	33,6	14	9,08	13,4	9,81	8,01	9,17	0	9,86	0	13	0	14,8	12,6	13,2
Sr	111	261	122	101	120	98,6	90,11	102	113	103	130	114	0	0	106,3	99,6
Nd	9,29	20,5	10,4	6,26	9,82	6,21	0	5,84	8,34	5,73	9,72	8,48	9,87	7,29	8,13	5,77
Zr	26,9	85,5	29,5	23,4	30,4	17,1	8,8	12,6	28,9	21,5	33,5	25,9	6,19	5,14	5,75	6,89
Sm	2,67	4,08	2,36	1,56	3,33	1,57	0	0,92	0	1,65	2,92	2,4	0	2,48	0	1,41
Eu	0,68	0	0,87	0,5	0,8	0,32	0,51	0,21	0	0,31	0	0	0	0,49	0,81	0,643
Ti	1181	2160	1292	1563	1318	1275	1105	1092	1414	1558	1234	1197	923	890	1003	958
Gd	2,28	0	2,13	0	0	0	1,6	0	0	1,72	2,19	0	1,82	1,97	3,23	2,67
Dy	0	0	2,55	0	2,7	1,81	1,71	0	0	2,12	2,09	2,99	3,17	2,73	0	3,72
Er	0	0	1,18	1,22	0	1,24	0	0,98	0	1,38	1,12	1,15	0	0	0	2,7
Yb	0,8	1,62	1,31	0	0	0,95	0	0,62	1,15	1,25	1,08	0	2,84	1,94	2,37	0
Lu	0	0,34	0	0	0	0	0,138	0	0	0,177	0	0	0	0	0	0

Sample	MGP1c		MGP3b						MGP4b							
	Area 1	Area 1	Area 3	Area 4	Area 5	Area 6	Area 7	Area 1	Area 1	Area 2	Area 2	Area 3	Area 4	Area 5	Area 6	Area 8
point	1	2	2	2	8	6	2	3	3	2	5	1	1	2	4	1
phase	cp2	cp2	cp1	cp2	cp1	cp2	cp1	cp1	cp2	cp1						
SiO ₂	52,45	52,25	53,48	53,17	53,38	53,46	53,48					52,62		52,52	52,86	
TiO ₂	0,28	0,31	0,1	0,09	0,08	0,05	0,11					0,25		0,17	0,19	
Al ₂ O ₃	3,46	4,13	1,75	2,45	2,31	2,49	2,69					4,2		4,08	4,07	
Fe ₂ O ₃	0,48	0,24	0,34	0,43	0,56	0,34	0,14					0,54		0,42	0,34	
FeO	2,64	2,85	2,47	2,8	2,62	2,64	2,85					2,31		2,12	2,22	
MnO	0,1	0,07	0,1	0	0,02	0,03	0,03					0,05		0,09	0,12	
MgO	16,49	16,34	17,47	17,14	17,24	17,1	17,01					17,14		16,98	16,76	
CaO	21,29	21,05	21,82	21,13	21,5	21,28	21,04					21,02		20,96	21,28	
Na ₂ O	1,05	0,95	0,71	0,94	0,97	0,96	0,92					1,03		1,03	1,04	
K ₂ O	0	0	0	0,02	0	0,01	0					0		0	0	
Cr ₂ O ₃	1,32	1,38	1,02	1,25	1,19	1,09	1,45					1,36		1,43	1,33	
Tot	99,57	99,57	99,26	99,42	99,87	99,45	99,71					100,52		99,8	100,21	
Ba	0	0	1,95	1,24	0,56	0,57	0					5,1		0,66	2,17	0,71
Th	4,71	8,24	2,35	4	2,35	1,29	0					0		2,35	0	0,706
Nb	1,22	1,09	0,421	0,421	0,042	0,252	0,309					0,421		1,28	0,112	1,29
La	7,3	7,87	5,56	6,8	6,26	6,45	6,66					5,94		5,1	6,12	5,69
Ce	21,3	25,3	13,81	0	16,79	17,3	0					14,6		12,7	0	15,3
Sr	176	162	160	190	181	177	200					0		112	0	0
Nd	14,4	21	0	9,85	8,01	8,03	11,51					8,16		9,69	8,55	8,96
Zr	55	65,6	11,5	17,8	15,3	16,6	21					5,85		7,42	6,79	5,79
Sm	4,64	4,11	2,04	2,37	1,42	2,61	0					0		0	0	0
Eu	1,51	1,11	0,39	0,5	0	0,66	0					0		0,8	0,98	0,38
Ti	1463	0	631	861	725	753	933					913		897	799	807
Gd	4,52	0	1,37	1,42	0	1,12	0					2,26		0	0	1,56
Dy	0	0	1,6	1,35	1,93	1,18	2,04					0		1,25	0	2,2
Er	2,28	0	0,8	0,82	0	0	0,92					0		0	0	0
Yb	2,51	1,93	0	0,67	1	0	0,99					0		1,4	2,61	0
Lu	0,38	0,22	0	0	0	0	0					0		0	0	0

Appendix 6: Trace element composition of orthopyroxenes

Sample Area	MGP2b		MGP2b2		MGP1b		MGP1c		MGP1g				
	Area 2	Area 5	Area 1	Area 2	Area 3	Area 7	Area 8	Area 3	Area 4	Area 3	Area 4	Area 5	Area 5
	6	2	1	9	2	2	4	1	4	1	1	4	3
point phase	opx1												
SiO ₂	55,53		56,51		55,79	55,55	57,22	56,75		54,51	54,38	54,82	54,8
TiO ₂	0,05		0,08		0	0,04	0	0		0,19	0,12	0,05	0,21
Al ₂ O ₃	2,77		2,71		2,28	2,61	1,68	1,39		3,25	2,97	2,83	2,77
Fe ₂ O ₃	0,38		0,01		0,29	0,4	0,29	0,36		0,59	0,5	0,45	0,19
FeO	4,96		5,9		7,01	7,36	5,88	5,67		8,87	8,86	8,75	8,72
MnO	0,13		0,14		0,08	0,19	0,18	0,24		0,22	0,19	0,2	0,15
MgO	34,29		33,91		33,25	32,84	34,69	34,79		31,85	31,62	31,77	31,53
CaO	0,99		0,95		0,81	0,9	0,9	0,72		0,83	0,86	0,98	0,91
Na ₂ O	0		0		0	0	0	0		0	0	0	0
K ₂ O	0		0		0	0	0	0		0,01	0	0	0
Cr ₂ O ₃	0,61		0,54		0,47	0,54	0,4	0,26		0,36	0,26	0,47	0,47
Tot	99,71		100,75		99,89	100,32	101,17	100,19		100,68	99,76	100,33	99,75
Sc	27,9	25,8	24,2	24,6	25	24	20,7	10,8	16,5	17,2	21	17,4	20,1
Ti	408	508	490	519	300	357	294	248	358	1306	1081	743	1286
V	98	101	101	103	82	81	62	36	39	48	63	63	62
Ni	710	727	752	769	729	751	1635	754	718	461	558	548	541
Sr	0,19	0,59	0,17	0,33	0,19	0,46	0,54	0,61	0,66	0,36	0,57	0,53	0,52
Zr	1,3	0,93	1,13	0,94	0,97	1,28	1,12	2,01	2,26	5,54	5,04	4,67	4,74
Nb	0,45	0,11	0,45		0,445	0,27		0,32	0,31			0,1	0,455
Ba	0,28	0,65	0,61	0,38		0,61		0,94	0,715		0,65	0,72	0,53
La	0,12	0,06	0,345		0,21	0,19	0,17	0,14	0,18	0,14		0,18	0,18
Ce	0,15	0,22	0,35	0,28	0,25	0,225	0,33	0,115	0,24	0,45	0,55	0,48	0,465
Nd		0,62	1,35	1,25	0,61	0,45			1,26	0,7	0,8	0,69	0,72
Sm	0,32	0,35	0,63	0,59	0,45	0,31	0,4	0,61	0,675	0,35	0,4	0,33	0,34
Eu	0,19	0,18	0,29	0,25		0,225		0,29		0,17	0,21	0,18	
Gd	0,81	0,82		1	1,05	1,09	1,27	1,21	1,25	0,65	0,86	0,79	0,75
Dy	1,06	1,09	1,31	1,07	1,32	1,37	1,51	1,23	1,28	0,85	1,195	1,079	1
Er	0,69	0,71	0,84	0,69	0,86	0,89		0,75	0,74	0,6	0,81	0,78	0,71
Yb	0,7	0,72	0,82	0,725	0,88	0,9		0,74	0,72	0,61	0,81	0,77	0,72
Lu			0,12	0,1	0,13	0,135	0,14	0,12	0,12			0,12	0,11
Th	0,185	0,12	0,125		0,165	0,13	0,195	0,11	0,11	0,1			0,19

Appendix 6: Trace element composition of orthopyroxenes

Sample Area point phase	MGP3b		MGP4b		MGP1h		MGP2a					
	Area 12	Area 6	Area 1	Area 4	Area 2	Area 8	Area 5	Area 1	Area 4	Area 5	Area 5	
	opx1	opx1	opx1	opx1	opx1	opx1	opx1	opx2	opx2	opx2	opx2	opx2
SiO ₂	56,89	57,01		55,76								
TiO ₂	0	0,05		0,03								
Al ₂ O ₃	1,48	1,37		2,82								
Fe ₂ O ₃	0,27	0,18		0,2								
FeO	5,72	5,86		5,02								
MnO	0,22	0,19		0,06								
MgO	34,61	34,52		34,24								
CaO	0,89	0,89		0,89								
Na ₂ O	0	0		0								
K ₂ O	0	0		0								
Cr ₂ O ₃	0,44	0,49		0,71								
Tot	100,52	100,56		99,73								
Sc	20,6	20,2	21,1	22,1	8,9	9,9	22,5	25,2	24			
Ti	331	377	314	435	254	217	635	362	400			
V	59	64	78	86	30	28	39	51	50			
Ni	705	705	777	768	707	677	682	814	711			
Sr	0,32	0,46	0,65	0,36	0,58	0,29	1,26	0,96	0,81			
Zr	1,02	1,33	1,52	2,43	1,27	2,64	21,4	17,5	20			
Nb	0,44	0,345	0,145	0,395	0,34	0,42	0,12		0,36			
Ba	0,72	0,8	0,69	0,69	0,62				0,46			
La	0,16	0,35	0,27	0,4					0,34			
Ce	0,37	0,45	0,274	0,38	0,275	0,345	0,25	0,205	0,34			
Nd	0,4	0,61	0,35	0,35	0,46	0,39	0,75	0,605	0,5			
Sm	0,21	0,32	0,17	0,18	0,28	0,22	0,42	0,41	0,37			
Eu	0,11	0,16	0,115	0,115			0,23		0,21			
Gd	0,5	0,73	0,4	0,47	0,53	0,45		0,78	0,81			
Dy	0,56	0,77	0,49	0,6	0,67	0,58	1,095	1	1,02			
Er	0,36	0,53	0,325	0,385	0,41	0,36	0,69	0,68	0,67			
Yb	0,35	0,52	0,33	0,39	0,39	0,36	0,7	0,69	0,68			
Lu	0,055	0,08	0,05	0,06		0,055	0,1	0,1	0,11			
Th	0,16	0,155		0,125					0,155			

Appendix 7: P-T estimates for Estancia Sol de Mayo xenoliths

Sample Lithology Area	MGP2b Lherzolite			MGP2b2 Lherzolite			MGP1b Harzburgite						MGP3b Harzburgite			
	Area 2	Area 6	Area 8	Area 2	Area 1	Area 7	Area 2	Area 3	Area 5	Area 6	Area 7	Area 8	Area 4	Area 4	Area 5	Area 7
Spot	Cpx	7	3	6	8	3	10	2	1	2	4	3	3	2	8	2
	Opx	6	5	11	9	4	5	1	2	1	3	2	4	3	6	4
	OI	4	8	8	5	8	5	3	3	4	3	5	6	9	9	5
TK T°C		1329	1284	1300	1299	1314	1216	1314	1281	1268	1265	1275	1290	1285	1290	1277
		1055	1011	1026	1026	1041	943	1041	1008	995	992	1002	1017	1012	1017	1003
P Kbar		33	20	38	16	18	3	18	2	-5	-2	1	3	15	16	5
		108	67	124	54	59	11	59	8	-16	-8	5	11	49	51	18
Depth Km																

Appendix 7: P-T estimates

Sample	MGP4b Hz						
Lithology	Harzburgite						
Area	Area 3	Area 4	Area 5	Area 7	Area 7	Area 7	Area 7
Spot	1	7	1	10	3		
	6	9	6	14	6		
	1	2	6	8	15		
TK	1317	1300	1311	1313	1326		
T _c	1044	1027	1037	1040	1053		
P Kbar	13	11	2	13	-10		
Depth Km	44	38	6	42	-32		

Appendix 8: Sr-Nd systematics from six Patagonian localities

Sample	Cerro Rio Chubut		Cerro de los Chenques							
	CH 8		PM 12-15	PM 12-26	PM 12-12	PM 12-13	PM 12-17	PM 12-19	PM 12-48	
Rb			0,56	0,93	0,49	0,45	0,60	0,67	0,54	
Sr			68	88	62	68	99	74	85	
$^{87}\text{Sr}/^{86}\text{Sr}$	0,703873		0,703463	0,703696	0,702736	0,703417	0,704077	0,702704	0,703988	
2σ	0,000008		0,000008	0,000008	0,000009	0,000011	0,000011	0,000011	0,000009	
Nd			2,9	4,1	4,3	3,7	4,2	4,9	4,3	
Sm			1,0	1,0	1,8	1,4	2,0	2,0	1,4	
$^{147}\text{Sm}/^{144}\text{Nd}$			0,207552	0,141309	0,258362	0,233496	0,291797	0,244851	0,203867	
$^{143}\text{Nd}/^{144}\text{Nd}$	0,512902		0,51289	0,512734	0,513038	0,512848	0,512723	0,513087	0,512696	
2σ	1,60E-05		6,00E-06	9,00E-06	0,000018	0,00002	0,000022	0,000017	0,000019	

Sample	Gobernador Gregores						Cerro Clark		
	PM 23-1	PM 23-6	PM 23-16	DUB 1g	DUB 3g	DUB 2g	PM 24-22	PM 24-27	PM 24-32
Rb	0,22	0,21	0,10				0,101	0,172	0,295
Sr	258	444	452	194	333	234	46	186	67
⁸⁷ Sr/ ⁸⁶ Sr	0,703073	0,703046	0,703128	0,703259	0,703245	0,703345	0,703432	0,703236	0,704297
2σ	0,000013	0,000009	0,000011	0,000007	0,000009	0,000001	0,000009	0,000001	0,000009
Nd	23,83	35,96	37,26	13,3	24,14	27,83	3,80	9,76	3,26
Sm	6,90	9,59	8,16	2,9	5,29	7,43	1,53	2,21	1,16
¹⁴⁷ Sm/ ¹⁴⁴ Nd	0,174639	0,160854	0,132006	0,131510	0,132169	0,161021	0,242365	0,136262	0,214308
¹⁴³ Nd/ ¹⁴⁴ Nd	0,512904	0,512947	0,512865	0,512872	0,512866	0,512807	0,512867	0,512915	0,512774
2σ	0,000007	9,00E-06	1,10E-05	5,00E-06	6,00E-06	5,00E-06	0,000002	1,00E-05	1,10E-05

Sample	Cerro Fraile					Pali Aike				
	CF 6A	CF 8	CF 10	CF 13	CF 14	PA 1	PA 2	PA 5	PA 8	PA 13
Rb					0,01					
Sr	21,3		84,3		1,27					
$^{87}\text{Sr}/^{86}\text{Sr}$	0,703416	0,703351	0,703309	0,703232	0,703439	0,703246	0,703197	0,703338	0,703216	0,703464
2σ	0,000007	0,000013	0,000008	0,000009	0,000001	0,000008	0,000001	0,000001	0,000001	0,000001
Nd	2,708		1,38		0,38					
Sm	0,770		0,405		0,33					
$^{147}\text{Sm}/^{144}\text{Nd}$	0,171525		0,177321		0,529662					
$^{143}\text{Nd}/^{144}\text{Nd}$	0,512922		0,513223	0,512886	0,513529	0,512911	0,51284	0,512894	0,512986	0,512939
2σ	0,000024		0,000135	0,000017	0,000044	1,00E-05	8,00E-06	9,00E-06	9,00E-06	1,20E-05